University of Kentucky Doctoral Dissertations   Graduate School

2011

INTERACTIONS AND EFFECTS OF BIOMOLECULES ON AU NANOMATERIAL SURFACES

Manish Sethi
University of Kentucky, sethimani@gmail.com

ABSTRACT OF DISSERTATION

Manish Sethi

The Graduate School

University of Kentucky

2011

INTERACTIONS AND EFFECTS OF BIOMOLECULES

ON

AU NANOMATERIAL SURFACES

ABSTRACT OF DISSERTATION

A dissertation submitted in partial fulfillment of the

requirements for the degree of Doctor of Philosophy in the

College of Arts and Sciences

at the University of Kentucky

By

Manish Sethi

Lexington, Kentucky

Director: Dr. Marc R. Knecht, Professor of Chemistry

Lexington, Kentucky

2011

ABSTRACT OF DISSERTATION

INTERACTIONS AND EFFECTS OF BIOMOLECULES ON AU
NANOMATERIAL SURFACES

Au nanoparticles are increasingly being used in biological applications. Their use is of interest based upon their unique properties that are achieved at the nanoscale, which includes strong optical absorbances that are size and aggregation state dependent. Such absorbances can be used in sensitive chemical/biological detection schemes where bioligands can be directly attached to the nanoparticle surface using facile methods. Unfortunately, a number of complications persist that prevent their wide-scale use. These limitations include minimal nanoparticle stability in biological-based media of high ionic strength, unknown surface functionalization effects using simple biomolecules, and determining the binding motifs of the ligands to the nanoparticle surface. This situation can be further complicated when employing shaped materials where crystallographic facets can alter the binding potential of the bioligands. We have attempted to address these issues using traditional nanoparticle functionalization techniques that are able to be characterized using readily available analytical methods. By exploiting the optical properties of Au nanomaterials, we have been able to determine the solution stability of Au nanorods in a buffered medium and site-specifically functionalized Au nanomaterials of two different shapes: spheres and rods. Such abilities are hypothesized to be intrinsic to the bioligand once bound to the surface of the materials. Our studies have focused mainly on simple amino acids that have demonstrated unique assembly abilities for the materials in solution, resulting in the formation of specific patterns. The applications for such capabilities can range from the use of the materials as sensitive biochemical sensors to their directed assembly for use as device components.

Manish Sethi

9/30/2011

INTERACTIONS AND EFFECTS OF BIOMOLECULES

ON

AU NANOMATERIAL SURFACES

By

Manish Sethi

Dr. Marc R. Knecht
Director of Dissertation

Dr. John E. Anthony
Director of Graduate Studies

9/30/2011
Date

RULES FOR USE OF DISSERTATIONS

Unpublished dissertations submitted for the Doctor's degree and deposited in the University of Kentucky Library are as a rule open for inspection, but are to be used only with due regard to the rights of the authors. Bibliographical references may be noted, but quotations or summaries of parts may be published only with the permission of the author, and with the usual scholarly acknowledgements.

Extensive copying or publication of the dissertation in whole or in part also requires the consent of the Dean of Graduate School of the University of Kentucky.

A library that borrows this dissertation for use by its patrons is expected to secure the signature of each user.

<u>Name</u>   <u>Date</u>

_____

_____

_____

_____

_____

_____

_____

_____

_____

DISSERTATION

Manish Sethi

Graduate School

University of Kentucky

2011

INTERACTIONS AND EFFECTS OF BIOMOLECULES
ON
AU NANOMATERIAL SURFACES

DISSERTATION

A dissertation submitted in partial fulfillment of requirements for the degree of Doctor of
Philosophy in the college of Arts and Sciences,
University of Kentucky

By

Manish Sethi

Lexington, KY

Director Dr: Marc R. Knecht, Professor of Chemistry

University of Kentucky

Lexington, KY

2011

To my daughter, Anika

ACKNOWLEDGEMENTS

List of Tables

List of Figures

List of Schemes

Chapter 1: Introduction

1.1 Introduction to Nanotechnology

A nanometer is one-billionth of a meter, where the definition of nanotechnology, according to the National Nanotechnology Initiative (NNI), is the understanding and control of matter at dimensions between 1 and 100 nm where unique phenomena enable novel applications not feasible when working with bulk materials or single atoms or molecules.[1] Nanomaterials are defined as the structures at the nanoscale, which could be either naturally occurring (e.g. volcanic ash, sea spray, smoke) or synthetically engineered (e.g. nanoparticles, nanotubes, nanoplates).[1] Since, nanoparticle sizes range from 1-100 nm, they are considered as the bridge between atomic/molecular structures and their bulk counterparts. Although nanomaterials have the same chemical composition as the bulk materials, they have remarkably different physico-chemical properties that can be attributed to their larger surface to volume ratio and the quantum confinement effects. Nanoscale material synthesis involves two fundamental approaches: top down and bottom up. Designing materials by breaking down larger, higher order structures to the nanoscale is known as the top down approach (e.g. micropatterning and photolithography techniques). Conversely, self organization of component building blocks such as atoms, ions and/or molecules that orderly assemble to produce higher order nanostructures is known as the bottom up approach (e.g. synthesis of polymers and nanocrystal growth).[2]

1.2 Metallic Nanoparticles: Properties and Characterization

From thermodynamics, the formation of metallic nanoparticles involves the generation of growth species produced by supersaturation via reduction, nucleation that is

initiated when the supersaturation reaches a critical value above the solubility of the reduced species, and the subsequent growth and termination processes that produce the final sized nanoparticles.[2] For the synthesis of metallic nanoparticles, a bottom-up method generally used is the reduction of metal salts/complexes to produce colloidal dispersions that are capped by a surface passivant.[3-6] Certain key constituents for metal nanoparticle synthesis include a metal salt/complex, a reducing agent that produces the zero-valent metallic colloidal dispersion of varied sizes depending upon the type of reagent used, and a chosen ligand that binds to the nanoparticle surface and hinders their agglomeration.[2-5]

It is known that nanoparticles possess a large surface to volume ratio, thus they attain enormous surface energy, making them thermodynamically unstable.[2] The necessity to reduce the overall surface energy drives the nanoparticle aggregation process;[2-5] however, surface passivants bound to the nanoparticle shields them from each other by providing steric and/or electrostatic stabilizing factors. Steric stability is generally provided by polymeric surface passivants that bind to the nanoparticle surface and sterically prevent them from agglomerating.[7-9] On the other hand, electrostatic stabilization is provided by highly charged molecules bound to the nanoparticle surface that repel each other in solution by electrostatic forces that arise from the surface charge.[10] For example, for the synthesis of Au nanoparticles, one of the most commonly used method involves the use of trisodium citrate (reductant and passivant) that reduces chloroauric acid at 100 °C and subsequently binds to the nanoparticle surface, which stabilizes the colloidal suspension for months by providing the electric surface charges required for electrostatic stabilization.[11-13]

In a solution, both the charges, comprised of nanoparticle surface ligands and the appropriate counter ions co-exist that maintains the overall neutrality of the system. Due to the affinity of the charged ligand, it attaches to the nanoparticle surface. This causes non-homogeneous distribution of ions in the proximity of the solid surface that leads to the formation of a charge double layer around the nanoparticle structure: inner Stern layer and the outer Gouy layer (also called diffuse double layer); both the layers are separated by the Helmholtz plane as shown in Scheme 1.1.[2,10] As a result, the total interaction between nanoparticles is comprised of the sum of attractive van der Waals forces and repulsive electrostatic forces described by DLVO theory (named after Derjaguin, Landau, Venvey and Overbeek).[14] When the nanoparticles are distantly separated, they do not experience any forces (attractive or repulsive); however, as they move closer to each other due to Brownian motion, they experience a net repulsive force due to the partial overlap of the charge double layer.[2,14] The repulsive force is dependent upon the concentration of the counter ions. When the counter ion concentration is increased, it reduces the electrostatic repulsion force, which may get subdued by the attractive van der Waals forces between the nanoparticle metal surfaces.[2,14] This can cause the aggregation and/or destabilization of the nanoparticle,[2,14] which is likely undesirable based upon the chosen application of the system.

Although factors such as solvent, solution conditions (e.g. temperature, pH etc.), and the presence of other salts can play a role in controlling the size of the nanoparticles, the global parameters controlling the size are the amount and type of reducing agent and the surface passivant used.[2] In general, when a stronger reductant is used, a faster reaction rate ensues that favors the formation of smaller nanoparticles.[15] This is due to the
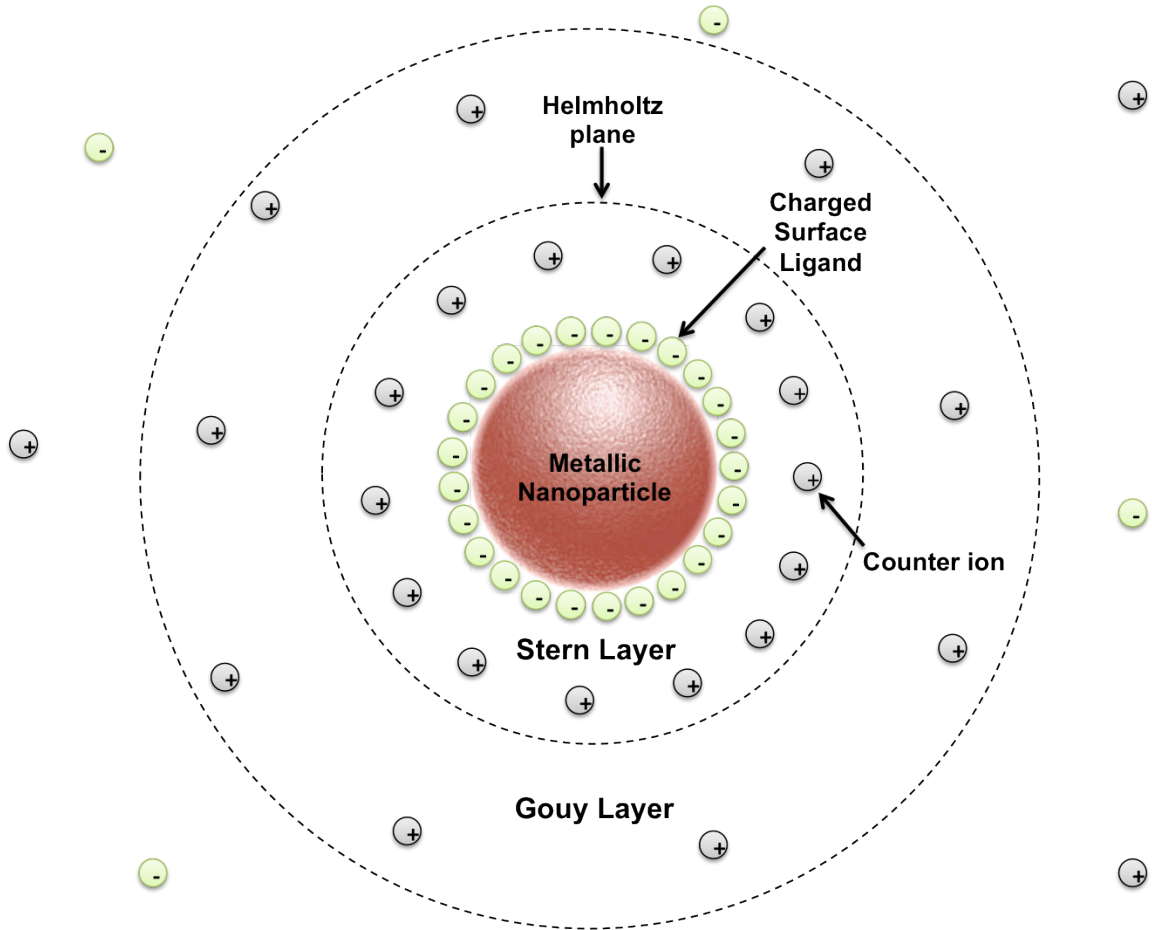
Scheme 1.1 Charge double layer on nanoparticle surface comprising of a Stern layer and Gouy layer

fact that a stronger reagent is able to increases the rate at which supersaturation of the metal atoms is reached and thus, produce a greater number of nucleation sites. This depletes the metal precursors available for the growth of nanoparticles, and thus, leads to formation of smaller particles. The surface passivant with the higher surface affinity can also lead to formation of smaller nanostructures.[3,16] A strongly adsorbed passivant is likely to cover the nanoparticle more extensively and thus not only sequester growth sites, but also impede the diffusion of the growth species towards these sites from the surrounding medium. Similarly, higher ratios of either the reducing agent and/or the surface passivant to the precursor molecules can lead to formation of smaller nanostructures.[17] The surface passivant also governs the point of growth termination of the nanoparticles by eventually occupying all growth sites and making them inaccessible to the metal building blocks in the surrounding medium.[2,17]

Controlled ligand place exchange reactions can be attributed to their lability i.e propensity of a ligand to dissociate from the surface. For example, citrate-capped Au nanoparticles can undergo place exchange reactions with Cys or other thiol-based molecules, displacing citrate from the nanoparticle surface.[18] This process is thermodynamically favored as the thiol group has a very high affinity for Au, releasing a large surface-binding free-energy of the order of 40 kcal/mol.[19,20] A study on the desorption and the self-exchange process of alkanethiols has reported the attainment of a pseudo-steady-state, incomplete desorption/exchange plateau;[20] this provides evidence of the limited desorption capability and the strong affinity of thiol groups to the Au surface. Nanoparticle solubility can also be changed from non-polar to polar by exchanging methylene terminated ligands with alcohol or carboxyl groups.[21,22] The production of

mixed monolayers of the ligands by partial ligand exchange can further impart interesting properties to nanoparticle surfaces.[22-27] For instance, a mixture of octylthiol and 11-thioundecanoic acid on Au nanoparticles can provide control over their assembly based upon the pH value of the solution. This causes the formation of aggregated structures at low pH due to the hydrogen bonding between COOH groups and independent nanoparticles are present at high pH due to the negatively charged terminal COO^- groups.[24] Mirkin and colleagues have used citrate-capped Au nanoparticles for cellular delivery after modifying the nanoparticle surface with thiol-capped DNA molecules such that the DNA displace citrate molecules and the complex thus created is targeted to the cell surface.[28-31]

Most of the properties unique to nanoparticles can be attributed to their substantial surface energy, large fraction of surface atoms, and quantum confinement (with change of electronic and optical properties when the particle size is of the magnitude of the wave function of the electrons); these properties are a direct effect of their small size and high surface to volume ratio.[2] For example, due to the large fraction of surface atoms and high surface energy, nanoparticles have significantly lower melting points or phase transition temperatures than their bulk counterparts.[32-34] Further, it was observed that not only the melting point of metallic nanoparticles such as Au,[32] Cu,[35] Sn,[36] In,[37] Pb,[38] and Bi[38] is significantly lower than bulk materials, but this temperature also decreases for smaller sized materials.[2] In general, the mechanical strength of nanoparticles is also one to two orders of magnitude higher than the bulk, which is due to the direct effect of the reduced probability of crystal defects; most of the nanoparticles are known to possess single crystals with a fewer structural defects.[2,39,40]

Nanoparticles possess certain unique optical properties due to their two fundamental characteristics: their small size that causes the increase in the spacing of the energy levels and the surface plasmon resonance (SPR) capabilities.[1,17] SPR is defined as the collective excitation and oscillation of the conduction electrons that behaves like a nearly free electron-plasma in the form of an electromagnetic wave along the boundary between a metal and the medium in which they are suspended.[2,22,41-46] Depending upon the size, the SPR is generated only when the nanoparticles are irradiated and are smaller than the wavelength of the incident light.[2,22] Plasmons are electromagnetic waves composed of surface electrons that absorb the light at a resonant frequency relative to the lattice of positive ions and propagate in parallel at the interface of the metal and the medium/dielectric (Figure 1.1).[2,22,41] To that effect, it is a dipolar excitation created with a certain frequency of the incident photons on the particle surface comprising the negatively charged free electrons and positively charged lattice. The energy of the incident resonant photons is absorbed in causing the vibrations/oscillations of the metal lattice and scattered by the re-emission of resonant photons in all directions,[2,22,41] thus the SPR is composed of both absorption and scattering components. In order to understand the different coloration of nanoparticles and their size dependence, Mie theory presents an analytical solution based upon Maxwell's equations to explain the extinction coefficient of spherical particles, which is given by the sum of their scattering and absorption coefficients.[2,22,42,47] The optical properties of the nanoparticles are also the result of the effect of quantum confinement.[2,11,22,42] For example, a few metallic nanoparticles (like Au and Ag) can produce varying shades of different colors depending upon their size, which in turn, are generally different from the color of the bulk metal
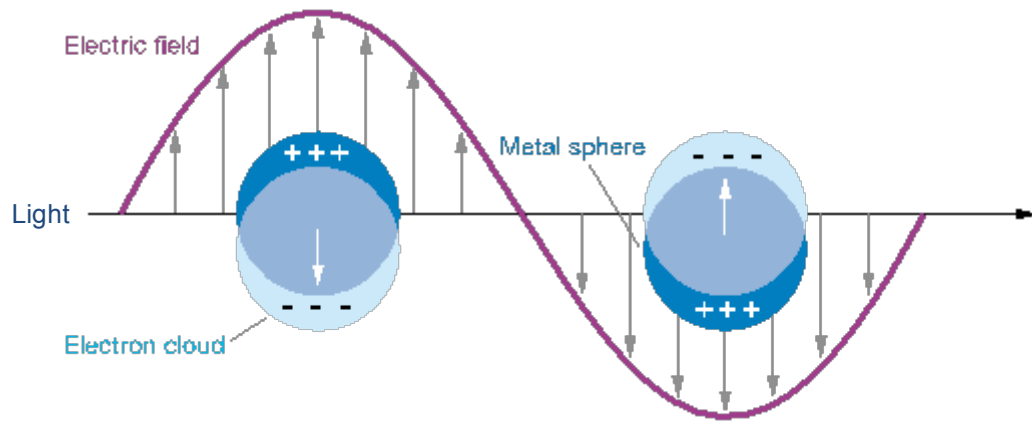
Figure 1.1 Schematic diagram illustrating a localized surface plasmon

material.[2,11,22,42] The SPR energy is also directly dependent upon the free electron density and the surrounding medium.[2,22,41] Since the plasmon resonance is created at the interface of the metal and external medium, it is highly sensitive to the physico-chemical changes at the nanoparticle surface.[2,22,41,43-46] To that end, the oscillation of the electrons has to match the impulse of the plasmon and is affected by the surface interactions and the number of adsorbed and desorbed molecules.[2,22,41,43-46] This forms the basis for many optical spectroscopy techniques such as surface-enhanced Raman scattering (SERS), UV-vis, infrared, and other surface-enhanced spectroscopic processes, and for procedures in life sciences such as biosensing.[2,22,41,43-46]

The surface plasmons of Au nanoparticles of sizes between 10-20 nm are typically centered around 520 nm as observed using UV-vis spectroscopy.[22,23,48-51] A red shift in the absorption band (λ_{max}) is observed when the size of the nanoparticles is increased (Figure 1. 2). For example, for particles of 9, 22, 48, and 99 nm, a λ_{max} of 517 nm, 521 nm, 533 nm, and 575 nm, respectively, are observed.[52] These results are attributed to electromagnetic retardation, which can be explained on the basis of increased nanoparticle size providing greater distance/area for electrons to oscillate.[52] At the same time, Au nanoparticles with an average size of < 3.2 nm were observed to possess a sharp decrease in the intensity of the surface plasmon band, which is attributed to the onset of quantum size effect leading to dampening of the surface plasmon mode due to the scattering of conduction electrons.[22,53-55] Further, the aggregation state of the nanoparticles can also affect the SPR such that there occurs a collective oscillation of the electrons on different nanoparticle metal surfaces present in close proximity. This can cause the appearance of new absorption resonance peaks (in the case of asymmetric
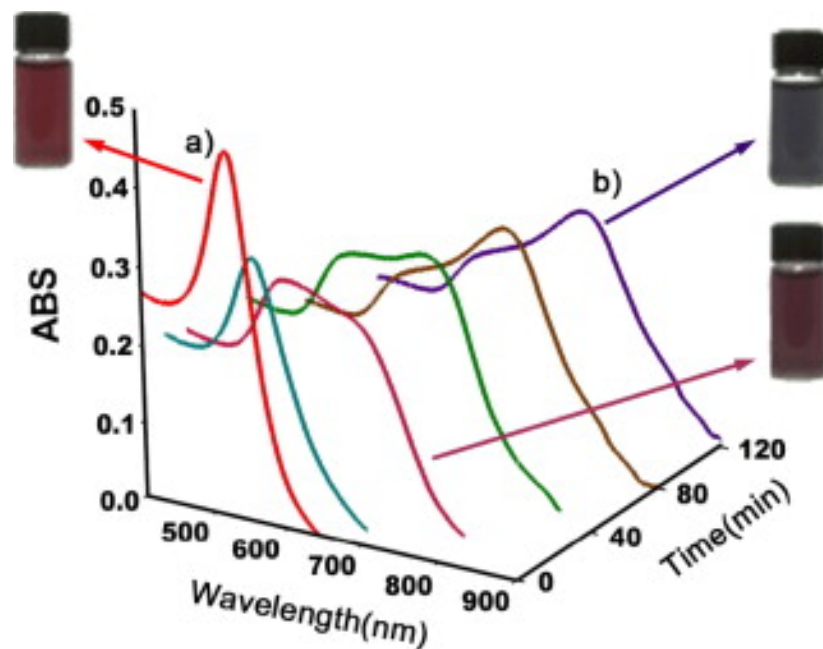
Figure 1.2 Pictures and the UV-vis spectra of the 15 nm Au nanoparticles showing different colors corresponding aggregation states. (a) demonstrates unaggregated nanoparticles with characteristic surface plasmon ~ 520 nm and (b) shows red shifting of surface plasmon with time along with change in color from red to darker red to blue that is characteristic of the increase in the presence of the aggregated nanostructures.[56]

Reproduced with permission from ref 56, copyright Elsevier B.V.

assembly) and/or shifting/broadening of peaks (in the case of random assembly) as observed by UV-vis spectroscopy.[2,22,23,41,43-46,48,49,56]

These unique optical/plasmonic properties of nanomaterials are also directly dependent upon shape and structure. For example, nanorods have similar surface properties as nanospheres as they possess a metallic core and surface passivating ligands, but these minor shape differences drive significant alterations in their optical properties.[22] Nanorods are one-dimensional, asymmetrical structures with a longitudinal and transverse axis as opposed to zero-dimensional nanospheres, such that their size is defined by their aspect ratio (AR) given by the ratio between the lengths of the two axes. Based upon their shape, nanorods possess unique photonic properties; for example, they exhibit two surface plasmon resonances: the transverse surface plasmon (TSP) corresponding to the transverse axis and the longitudinal surface plasmon (LSP) corresponding to the longitudinal axis. While the TSP remains fixed e.g. ~520 nm for Au and ~ 410nm for Ag,[2] the LSP of the nanorods varies across the visible to near-IR region depending upon the aspect ratio of the materials and their aggregation states (Figure 1.3).[57] In general, the LSP undergoes a red shift into the near-IR with an increase in aspect ratio.[2,50,58,59] Other properties of nanorods that distinguish them as compared to other shapes of the same material include higher extinction constants for visible and near-IR radiation, enhanced fluorescence intensity due to the increased surface electron density, enhanced thermal stability and mechanical strength due to the lower probability of finding a crystalloid imperfection, and lower melting points due to their high surface energy.[2,22]
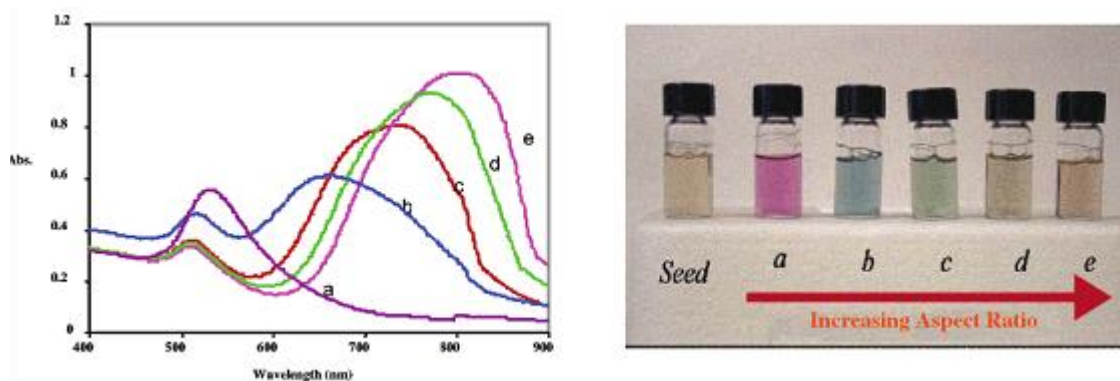
Figure 1.3 Optical spectra (left), and photographs of (right) aqueous solutions of Au nanorods of various aspect ratios. Seed sample: aspect ratio 1; sample a, aspect ratio 1.35±0.32; sample b, aspect ratio 1.95±0.34; sample c, aspect ratio 3.06±0.28; sample d, aspect ratio 3.50±0.29; sample e, aspect ratio 4.42±0.23.[57]

Reproduced with permission from ref 57, copyright ACS Publications.

1.3 Sources of Biomolecules for Nanoparticles Synthesis

1.3.1 Biomineralization and biomolecules derived from organisms

Most nanofabrication techniques such film deposition, electrospinning, laser ablation, chemical vapor deposition, and various lithography techniques use extremely harsh conditions and are fairly limited on various aspects in the production of nanostructures.[22,60] Biological systems, on the other hand, produce beautiful and ornate structures, often in a hierarchical fashion, with complex functionality by a simple process of incorporating minerals in distinct patterns at the nanoscale.[60] This phenomenon of incorporating and processing minerals associated with organisms is known as biomineralization. Nature exhibits materials with optimized properties produced by using simple precursor molecules in a highly energy efficient manner. For the technology to advance, learning from nature, thus, becomes an important aspect. The idea of mimicking biological syntheses (biomimetics) comes from the knowledge of the process of biomineralization and the assembly of nanostructured inorganic components into hierarchical superstructures.[61]

There are numerous examples of nanostructures synthesized by nature using biomolecules. A variety of inorganic-based compositions such as Fe_3O_4, SiO_2, Ag, Au, and CdS nanoparticles are known to be synthesized by microorganisms.[61] Magnetotactic bacteria that utilize earth's magnetic field for alignment and migration do so by producing structurally defined Fe_3O_4 or Fe_3S_4 nanoparticles that are aligned along the length of the bacteria in organelles called magnetosomes (Figure 1.4).[62-66] Biomolecules specialized in synthesizing such structures generally are peptides and proteins that are found to play a major role in directing and assisting their formation like storage and
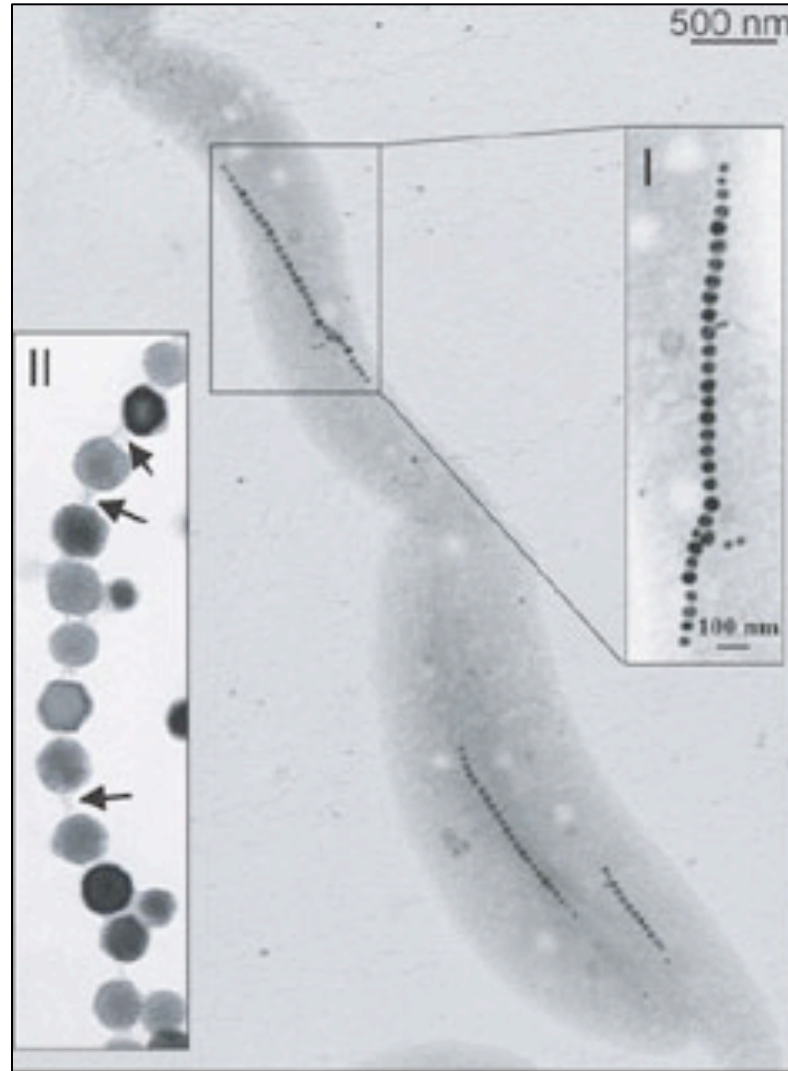
Figure 1.4 TEM image displaying Fe$_3$O$_4$ (magnetic) nanoparticles arranged in linear fashion in a magnetotactic bacteria.[66]

Reproduced with permission from ref 66, copyright Nature Publishing Group.

stabilization of iron in magnetotactic bacteria that is primed by the ferritin protein.[64,67-73] Mn, Cu, Fe and Au deposits have been found in certain bacteria while $Ca_3(PO_4)_2$ and $CaCO_3$ in vertebrates are involved in bone formation.[62,74] A variety of fish fabricate structures known as otoliths, or "ear stones", within the inner ear that are sensitive to gravity and linear acceleration.[65,68] Other organism use calcium carbonate crystals, including mollusks, to produce external shells that may either contain a single distinct crystalline form of calcium carbonate, such as aragonite, or may contain segregated layers of calcite and aragonite.[67] SiO_2 spicules are produced by marine sponges that have similar traits to optical fibers and have demonstrated light-guiding characteristics.[65,70,71,75-77] Other SiO_2 processing organisms are diatoms that generate a frustule, or cell wall, composed almost entirely of SiO_2, which is made from silicic acid (Figure 1.5).[72,73,78] The formation of frustules in diatoms requires polycondensation reactions between silicic acid molecules and a hydroxyl-rich β-sheet protein template.[79]

Since, proteins are known to play the most prominent role in the processes of biomineralization, it seems obvious to focus on protein and peptide extraction for the *in vitro* reactions for nanoparticle synthesis. Indeed researchers have isolated proteins and peptides from various biological sources to produce inorganic nanostructures *in vitro* that are not only specific for those materials, as determined from the source of the peptides, but were also found to be useful in synthesizing non-natural materials. Silicatein proteins, for example, that are used for the synthesis of SiO_2 spicules in sponges can induce the formation of SiO_2, TiO_2, and GaO_2 on the benchtop.[76-81] The proteinaceous cage structures of proteins such as apoferritin, heat-shock proteins, and virus capsids are useful for the synthesis of nanomaterials as they can act as size-constraining reaction chambers.
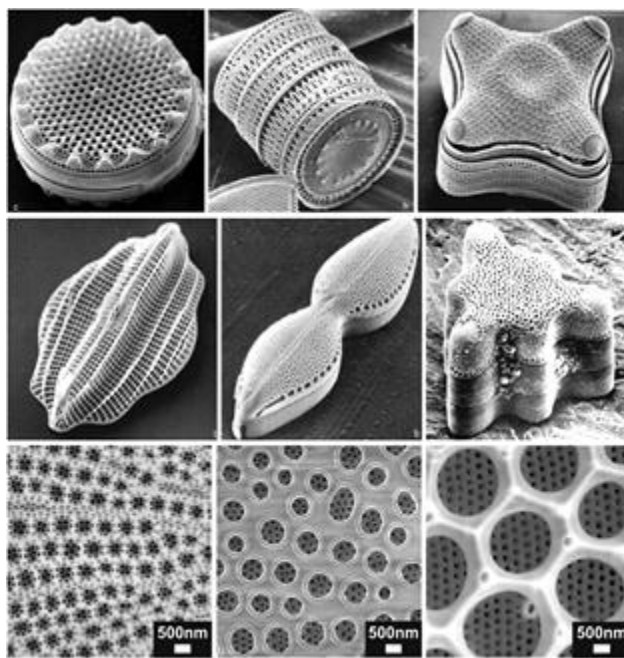
Figure 1.5 SEM images of SiO₂ on the cell walls of different diatom species, displaying a variety of shapes and patterns.[65]

Reproduced with permission from ref 65, copyright ACS Publications.

For instance, apoferritin can be used for the synthesis of Fe_3O_4 and Co_3O_4 nanoparticles by incubating apoferritin with Fe or Co ions in the presence of an oxidizing agent like H_2O_2; however, these protein cages support the production of only limited materials compositions.[65]

While proteinaceous cages are useful for the size confinement of various nanomaterials, there are numerous examples of regular proteins being used for the synthesis of Au nanoparticles that include BSA (bovine serum albumin), silk proteins, and even some enzymes.[65,80-84] One of the most common proteins used for the synthesis of Au materials is BSA, which is known to possess a high affinity for Au due to the large number of Cys, Tyr, and charged residues within the protein structure.[80-84] Burt *et al.* used $NaBH_4$ as a reducing agent in the presence of BSA to synthesize Au nanoparticles of < 2 nm where BSA was determined to be conjugated to the Au surface through its Cys residues.[84] In another instance, Au^{3+} ions were also reduced via UV irradiation in the presence of BSA to form larger Au nanospheres (7.7 ± 0.9 nm).[81] Notice that the UV-vis irradiation method produces bigger size nanoparticles as compared to the reduction by $NaBH_4$. This is mainly due to the fact that $NaBH_4$ is a stronger reductant and thus, as explained earlier, stronger reducing agents produce smaller size nanoparticles. Another protein that has been shown to produce Au nanoparticles is fibroin, purified from silk worm silk.[85] Fibroin contains a large number of Tyr residues that are postulated to reduce Au^{3+} ions to Au nanoparticles producing ~15 nm size nanoparticles coated with a thick (~15 nm) protein layer.[85] Shankar and colleagues used lemongrass extracts and synthesized Au nanoprisms in moderate yield while a more distinct production the same structures has recently been demonstrated by Xie and colleagues using green algae

cellular extracts.[86,87] In this work, the researchers found that a protein (that they named gold shape-directing protein (GSP)) was reducing, shape-directing, and dispersing the nanoparticles and was capable of producing prism- and polygonal-shaped Au nanoparticles in high yield (~90%).[87]

While the use of biomineralizing proteins and peptides isolated from organisms is capable of preparing a set of interesting materials, there are several drawbacks to their widespread use, including difficulty in isolating large quantities of peptide, requirement of specialized facilities to grow the organisms, and the limitations in improving the functionality/properties of the available biomolecules.[65] At the same time, a lack of inorganic material's diversity in nature provides few technologically important compositions that can be readily biomineralized; for example few known naturally occurring peptides are available for reducing certain industrially important materials like certain toxic heavy metals. Protein modifications via recombinant DNA technology has been used to overcome many of these difficulties like isolation large quantities of protein/peptide; however, the number of peptides and proteins produced and derived from living organisms is limited by the number of biomineralizing sequences known.[72,73,88-91] As a result, to overcome the limitations that exist in nature, other methods have been employed to isolate new materials directing peptides for specific nanoparticle syntheses and applications.

1.3.2 Phage Display Technology

Phage display can be used to isolate peptides for specifically desired materials. It is the process of displaying peptides or proteins on the surface of a bacteriophage. Bacteriophage, commonly known as phage are viruses that parasitize bacteria, and, like

other viruses, consist of an outer proteinaceous shell known as a capsid that encloses the viral genetic material. Since, phages display peptides on their capsid (coat protein) surface, this structural property can be exploited for generating a combinatorial library to isolate peptide sequences for various technological advances. Phage display technology is the outcome of recombinant DNA technique in which the foreign DNA is introduced into the phage vector and is allowed to express on one of the surface protein of the virus, thus, forming a chimeric protein structure (described later).[92]

A typical phage display technology employs filamentous bacteriophage such as the M13 because unlike the lytic phage, these bacteriophage use lysogeny as their path to replicate and assemble without killing their host cells. The M13 possesses a simple structure composed of multiple copies of a single major coat protein, pVIII, that shields the viral genome and constitutes the main viral filamentous structure, along with five copies of each of the minor coat proteins pIII, pVI, pVII and pIX located at each end of the filament.[93,94] Although any coat protein can be used to display the foreign peptide, the most commonly employed method is to fuse the foreign sequences to the amino terminus of pIII or pVIII; proteins are usually displayed from pIII.[93,94]

In a typical phage display combinatorial library, ~10^9 different phages containing random dodecamer peptides are present. These peptides can be displayed at the amino termini of pIII, which are then incubated with the target material in a process called biopanning.[95,96] The phage that display peptides having an affinity for the target material bind to the surface while those lacking affinity are removed by extensive washing.[95] To release the bound phage, the sample is dispersed in a low pH buffer that may partially denature the peptides and disrupt the peptide/material interactions.[95] The selected viruses

19

are then amplified by infecting them into *E. coli* where they are allowed to replicate their corresponding gene for the selected peptide. This marks the end of the first round of the biopanning process. Additional screening rounds are carried out by re-incubating the previously selected and replicated phage pool with the target, followed by their release with an increasingly stringent washing solution in order to exclude lower affinity target binders.[95,97] Each round of selection increases the affinity of the target binding peptides that are isolated to generate a library of sequences with differing degrees of affinity. After the final round of selection, the individual phage clones are analyzed to determine the sequence of the target binding peptide.[95] Chemically synthesized peptides can then interact with an appropriate precursor solution that may facilitate the synthesis of the target material.[95,98]

While the stringent washing steps can typically remove weaker bound phage, it is known that certain viruses remain bound to the surface of the target material even after the last elution step and are thus absent from the sequences obtained. These phage likely display peptides with the highest affinity for the target surface; therefore, new methods must be employed for isolation of the DNA of the phage to elucidate sequences of the strongest binding biomolecules. In one such approach, the unreleased phage are ruptured while bound to the target surface and their released DNA is amplified via the Polymerase Chain Reaction (PCR) method (Scheme 1.2).[61] The amplified DNA can then be analyzed to determine the peptide sequence displayed by the phage to ascertain the strongest binding materials.[61,95] Even the PCR method, however, is time consuming as it generates fragments of phage DNA, which require additional rounds of panning.[96] To address this issue, another similar method of the phage display technique was developed exploiting

Combinatorial
phage library ≈ 10^9

target species

elution
(pH, temp)

Phage rupture
to release DNA

Identification of
peptide sequence

PCR amplification of
phage DNA
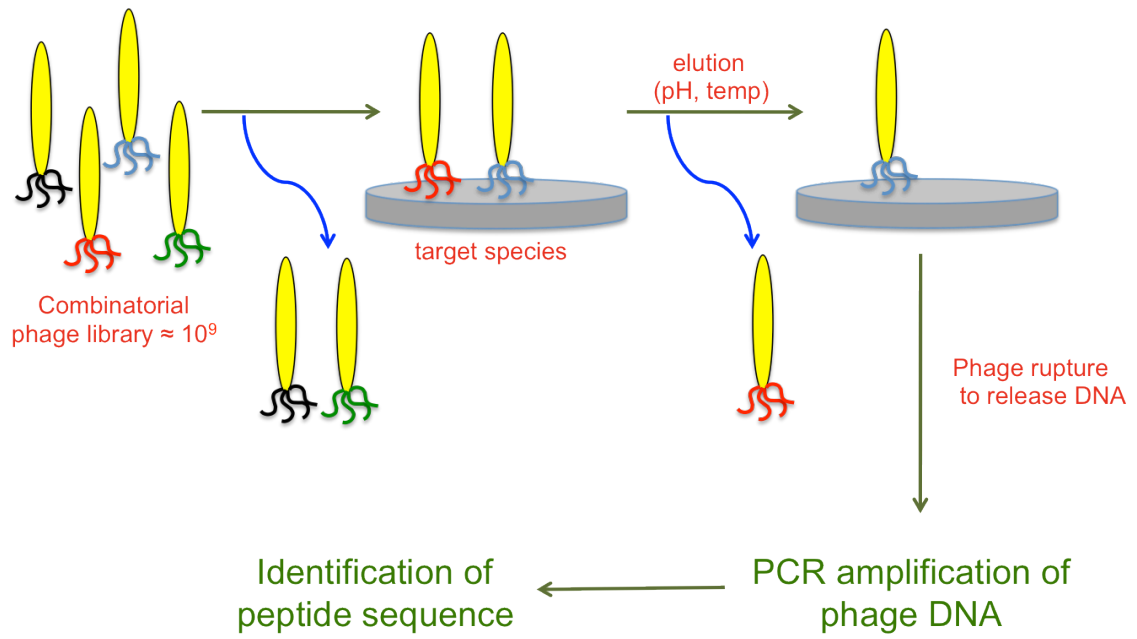
Scheme 1.2 Phage display technique demonstrating biopanning process.

the Rolling Circle Amplification (RCA) method of the phages.[96] RCA is the process of unidirectional genomic replication employed by some viruses such that from circular genomic DNA/RNA, long continuous DNA strands are synthesized. These continuous strands are then cut at specific sites and ligated to produce multiple copies of the circular DNA. The phage that remain bound to the target surface can be subjected to RCA which can then be directly transformed into *E. coli* to obtain individual clones for the sequence determination.[96] This method can, thus, reduce the amount of DNA manipulation along with increasing the effectiveness and speed of phage display technology.[96]

1.3.3 Peptide Mediated Nanoparticle Synthesis

1.3.3.1 Au nanoparticles

Phage display technology is one of the most widely used methods for isolating new peptides with high surface affinities for target inorganic nanomaterials. Brown and colleagues were the first to demonstrate the synthesis of Au nanoparticles using peptide-mediated approaches by developing and screening a library displayed on *E. coli* cells.[99] Of the 50 repeating polypeptides identified that were added to solutions containing Au^{3+} ions and sodium ascorbate (a reducing agent), three sequences were found to increase the growth of nanoparticles and to control the morphology of the resulting Au crystals.[99,100] By analyzing the crystallization process, these peptides were found to act catalytically by acidifying the local solution encompassing the Au nanoparticle precursors.[99] By increasing the number of tandem repeats of the polypeptides, a greater control of the nanoparticle growth was achieved.[99] The peptides were found to be neither covalently bound to the surface nor incorporated into the growing Au crystals, suggesting that the

peptide is not forming a composite material.[99] The effects of pH and the concentration of

Au^{3+} on the morphology and size of the Au nanocrystals formed in the presence of one of

these peptides (MS14-(MHGKTQATSGTIQS)) were determined by Wang *et al.*[101]

Monodisperse Au nanospheres were produced in the presence of the peptide such that the

average size of the nanoparticles decreased with an increase in the solution pH or a

decrease in the Au^{3+} concentration.[101]

A3 peptide (AYSSGAPPMPPF) has been used for the fabrication of Au

nanoparticles in a variety of synthetic approaches.[102-104] The A3 peptide was initially

identified to synthesize Ag nanoparticles using phage display technology where it was

originally known as AG3.[61,98] The peptide's amino acids have been shown to interact

with metal surfaces via hydrophobic or hydrogen-bonding interactions.[104,105] Certain

other peptides such as FLG (DYKDDDDK), GSH (γ-ECG) and HRE (AHHAHHAAD)

are also known to synthesis Au nanoparticles.[65] The FLG (or the FLAG tag epitope),

HRE (or the histidine-rich epitope, derived from the histidine-rich protein II (HRP II) of

the malarial parasite *Plasmodium falciparum*), and GSH peptides are the epitopes

recognized by antibodies.[65,106] This property makes them even more significant as the

they can be easily eluted with the nanoparticles following the *in situ* nanoparticle

growth.[102-104] It was supposed that the peptides such as A3 and FLG could synthesize Au

nanoparticles in the absence of a reducing agent where Tyr in the sequence would act as

the main reductant, while the peptides like GSH and HRE with no Tyr needed the aid of

sodium borohydride as a reducing agent.[102-104] It was, however, later discovered that Tyr

played a minor role, if any, in the reduction process; the HEPES buffer itself caused the

reduction of the Au^{3+} ions to form Au nanoparticles, while the peptides act as the surface

passivant.[107] The HRE peptide has a particular significance as they are rich in His residues; this property can be used to conjugate HRE-produced Au nanoparticles to Ni^{2+}-nitrilotriacetic acid (Ni-NTA) functionalized surfaces, a direct application of which can be in biomedical diagnoses and treatments.[104] The HRE peptide can also direct the synthesis of Au-coated nanotubes.[108,109]

1.3.3.2 Other noble metal nanoparticles:

Utilizing a phage-displayed peptide library method, Naik *et al.* were the first to identify peptides (AG3 (AYSSGAPPMPPF) and AG4 (NPSSLFRYLPSD)) capable of binding and reducing Ag^+ ions and directing the formation of Ag nanoparticles and nanoplatelets (two dimensional plate-like structures).[61,98] The Ag nanoparticles produced were found to be various shapes (hexagonal, spherical, and triangular) and of a size range from 60–150 nm.[61,98] Bassindale *et al.* found two additional peptides, Ag-22 (TVPPKAPRSSDL) and Ag-28 (LTRPNHGNTVDT), using the RCA-based phage display method that were able to synthesize Ag nanoparticles.[61,96,110,111] Tightly bound phages that could not be washed off even after five washes were amplified using RCA.[61,96,110,111] These peptides exhibited the ability to synthesize specifically shaped Ag nanoparticles, such that, Ag-22 exhibited triangular, quadrangular and spherical shapes, while Ag-28 produced relatively uniformly spherical nanoparticles with an average diameter of 20–50 nm.[61,96,110,111] Another peptide (TBP-1, RKLPDAPGMHTW) identified through phage display technology against titanium was found to be cross-reactive for Ag nanoparticles.[61,96,110,111] TBP-1 produced slightly larger Ag nanoparticles (300-500 nm) as compared to the AG4 peptide.[111] High aspect ratio Ag nanostructures were synthesized by Yu and colleagues forming polygonal Ag nanoparticles on the

surface of the AG4-functionalized bolaamphiphile nanotubes that were used as scaffolds.[112]

As compared to Au or Ag nanoparticles, there are fewer examples of the peptide-directed synthesis of Pt and Pd nanoparticles are known.[65] Yu *et al.* reported such synthesis using a short peptide (HPGAH) that was able to produce dispersed Pt nanoparticles under acidic conditions and continuous Pt nanotubes under basic pH conditions.[113] In a biomimetic approach, the peptide was immobilized on template nanotubes where it recognized and anchored Pt^{2+} ions on the template leading to the Pt nanotube formation by nucleating Pt nanocrystals on the template nanotubes.[113] Song *et al.* were able to synthesize Pt nanowire structures by using as molds the inside of diphenylalanine nanotubes such that they produced porous Pt–nanoparticle peptide–nanostructure composites.[65,114] The HRE peptide has also been known to synthesize spherical Pt nanoparticles of about 3 nm in size.[94] Similar results were obtained by Bassindale *et al.* such that they used phage-display library to screen Pt-binding peptide (Pt-41) and produced roughly spherical Pt nanoparticles observed to be 3-4 nm in size.[85,96]

Similar to Pt nanoparticles, different peptides under diverse conditions can lead to the synthesis of the various shaped Pd nanoparticles. For instance, a peptide known generally for the synthesis of silica structures (R5-(SSKKSGSYSGSKGSKRRIL)) has also been shown to be useful for Pd nanoparticles synthesis.[115] It was observed that different nanoparticle shapes could be produced simply by changing the Pd: peptide ratio such that spherical, linear or networks of Pd nanoparticles were produced at Pd: peptide ratios of 60, 90, or 120, respectively; nonetheless all of the structures produced were

found to be catalytically active with minor difference in their efficiencies.[115] The Pd2 (NFMSLPRLGHMH) and Pd4 (TSNAVHPTLRHL) peptide sequences are two of the few well known peptides for the synthesis of Pd nanoparticles in the presence of $NaBH_4$ as a reducing agent.[116] Biomimetic synthesis of Pd nanoparticles has been reported using the Pd4 peptide such that water-soluble, peptide-functionalized Pd nanoparticles of 1.9 ± 0.3 nm in diameter were produced.[116] These nanoparticles were shown to possess high catalytic activity driving Stille C–C coupling reactions under aqueous conditions at room temperature.[116]

1.3.3.3 Nanoparticle Synthesis using Chimeric Peptides

Chimera are protein/peptide fusions that are created by combining the sequences of two or more separate proteins/peptides into a single sequence to enhance, combine, or change their properties.[65] The engineered peptides possess unique functions that can be used for the synthesis of inorganic nanoparticles otherwise difficult to synthesize with the desired properties by using the single peptide alone. The Ag-reducing AG4 peptide fused to the C-terminus of the light-chain ferritin (LCF) protein as shown by Kramer *et al.* paved the way to explore the potential of chimeric cage-like proteins for materials synthesis.[65,101,117,118] AG4 was displayed in the internal cavity of the LCF protein that was used to nucleate and control the growth of nanoparticles within its core.[118] Ag nanoparticles generated with the AG4 peptide free in solution possessed an average diameter of 102 ± 28 nm, however, Ag nanoparticles with an average diameter of 7 ± 1 nm were produced when synthesized by the chimeric LCF-AG4-based peptide cages due to the size constrain provided by the LCF protein.[65,101,117] Dai *et al.* produced a chimeric peptide by fusing a Cu_2O-precipitating peptide (CN225 – RHTDGLRRIAAR) with the

primary structure of the DNA-binding protein TraIi1753.[119] While the native TraIi1753 protein did not possess the ability to induce the formation of Cu_2O materials, the chimeric TraIi1753/CN225 peptide could fabricate 2 nm Cu_2O nanoparticles upon exposure to a CuCl-bearing aqueous precursor solution.[119] These Cu_2O nanoparticles were coated with a protein shell that further led to their spontaneous assembly on circular DNA fragments due to the presence of the TraIi1753 domain of the chimeric peptide.[119] Sano and colleagues synthesized a fusion peptide of apoferritin with minTBP-1peptide that possesses the titanium metal-binding affinity and TiO_2- and SiO_2-precipitation activities.[110,120-124] The chimeric apoferritin cages provided the scaffold to limit the multifunctional nanoparticle composite size by a process now known as Biomimetic Layer-by-Layer assembly (BioLBL).[121,124]

Chimeric peptides can also be used to synthesize multimetallic nanoparticles. For example, production of Pd@Au possessing a core-shell (with Au core and Pd shell) hybrid nanostructure was first demonstrated by Slocik and Naik through the use of two peptides: the A3, specific for the synthesis and stabilization of Au nanoparticles, and Flg, which contains potential binding sites for Pd and Pt.[125] The peptides were fused together to form a single sequence (Flg-A3 or A3-Flg, depending upon which peptide is present at the N-terminus). In most cases Au nanoparticles were coated with much smaller Pd nanoparticles with an average diameter of ~3 nm, decorating the Au surface; a smaller number of monometallic Pd nanoparticles (1–3 nm) independent of the Au species were also observed by TEM analysis.[125] Approximately 7–28 Pd nanoparticles were observed per Au core in comparison to the estimated number of 12–18 Flg–A3 surface peptides which template the Au surface to serve as Pd^{4+} ion bind sites.[125] The bimetallic

nanoparticles were found to be composed of about 24.4 wt% Pd and 75.6 wt% Au by energy dispersive spectroscopy analysis.

McMillan and colleagues used chimeric peptides for the syntheses of other bimetallic nanoparticles.[126] A polyhistidine (His10) sequence was engineered in an inner cavity of the heat-shock protein (TF55β) to increase its solvent accessibility.[126] This enabled the chimeric TF55β-His10 protein to preferentially bind to Pd^{2+} ions in its core in the presence of either Ni^{2+} or Co^{2+} ions and, respectively yielded NiPd or CoPd nanocrystals of approximately 2 nm in size.[126] These results show that not only are peptides useful for the synthesis of metal nanoparticles, they can also be modified and engineered to obtain desired novel properties.

1.4 Peptide and Amino Acid Interactions with Inorganic Surfaces

1.4.1 Peptide interactions

Most current peptide-mediated nanoparticle approaches are based on the fabrication of inorganic nanostructures and/or the various applications of the materials with little regards to the biotic/abiotic surface interactions. There exists little homology between the different peptides that are known to bind to the same target species. At the same time the amino acid compositional specificity of the peptides does not appear to be consistent for the target nanostructures i.e. there can occur multiple targets for the same peptide despite of no obvious similarity between the two e.g. R5 is specific for both SiO_2 and Pd. Recent information has been established about the way biomolecules interact with two dimensional surfaces of inorganic solids in terms of both experimental and theoretical evidence.[43,46,127-132] Peelle *et al.* designed homo-hexamers of all 20 natural amino acids in order to study their binding ability to materials (II-VI semiconductors

such as CdS, CdSe, ZnS, ZnSe, as well as Au).[133] Only a few were shown to possess binding capabilities. For example, hexa-His (H6) was able to bind to all five materials studied, while Trp (W6), Cys (C6), and Met (M6) possessed variable affinity for single-crystalline ZnS and ZnSe and polycrystalline Au surfaces.[133]

Another library of peptides used interdigitated sequences of the general form XHXHXHX (where H is His and X is one of the 20 common amino acids (e.g. AHAHAHA)).[133] The library was subsequently generated in order to examine the contribution of neighboring amino acids to the His binding ability.[133] Further, a study of subtle sequence changes to the binding behavior of the materials-directing peptides towards the surfaces of the materials was conducted.[133] While Ala had little influence on the inorganic binding activity of the designed peptides, Gly, Lys, Arg, His, Trp, Cys, and Met were observed to enhance the binding affinity.[133] On the other hand, acidic, hydrogen-bond forming (i.e. polar), and hydrophobic amino acids were found to down-modulate the binding activity of the interdigitated peptides.[133] Though some binding trends could be generalized, most of the 20 amino acids were found to have a unique modulation effect.[133] As a result, this study showed that material specificity and affinity can be controlled by minor sequence changes in terms of spatial proximity of the certain amino acids, providing a minor degree of predictability to design material-specific binding biomolecules.[133]

A peptide sequence can also play a direct role in controlling the structure and properties of a resultant nanoparticle. For example, while the Pd nanoparticles synthesized using peptide the Pd4 possess a diameter of 1.9 ± 0.3 nm, its His substituted analog peptides, A6 (TSNAV*A*PTLRHL), A11 (TSNAVHPTLR*A*L) and A6,11

(TSNAV*A*PTLR*A*L) containing Ala substitutions for His at positions 6 and/or 11. This lead to the production of Pd nanoparticles of diameters around 2.2 ± 0.4 nm, 2.4 ± 0.5 and 3.7 ± 0.9 nm, respectively.[134] Further, by making such subtle changes in the peptide Pd4 sequence, catalytic efficiency of the Pd nanoparticles was found to be increased.[134] This was an interesting finding because it was earlier thought that His not only plays a critical role in controlling the formation of the Pd nanoparticles but was considered to be responsible for the attachment of the Pd4 peptide to the nanoparticle surface.[134] At the same time it shows that minor changes in the peptide sequence can significantly alter the structure-function relationship between peptide-nanoparticle surface interactions.

To study the adsorption kinetics of an engineered Au binding peptide (GBP1 - MHGKTQATSGTIQS) on a Au surface, Quartz Crystal Microbalance (QCM), along with SPR was used.[135] In QCM, two conducting films are deposited on either side of the quartz crystal across which an alternating current is applied that excites the crystal into a resonating state that oscillates at a particular frequency.[135] The technique is sensitive to the amount of adsorbed materials on the crystal surface and can be used to monitor the adsorption of molecules.[135] Both QCM and SPR are similar techniques in terms of their high sensitivity to the adsorption and desorption of molecular species on solid substrates in aqueous solution; however, each method measures different physical phenomena.[135] While QCM is a mechanical measurement technique that detects the total amount (or mass) of the molecule present on the surface, SPR measures the optical properties of the adsorbent.[135] Though SPR also detects the amount of the molecule, it is sensitive to the uniformity of the coverage of surface, whereas QCM cannot discern the specific coverage pattern of the adsorbing species.[135] Using the two techniques, Sarikaya and colleagues

studied the effects of 3R-GBP1 (MHGKTQATSGTIQS)$_3$, that was designed to possess a triple repeat of the sequence of GBP1.[135] The triple-repeat motif was used in an anticipation to increase the surface affinity of the peptide. QCM analysis of the binding to a Au surface was fit using a simple exponential curve whereas SPR analysis demonstrated biexponential behavior. Interestingly, the two equilibrium values of the kinetic processes isolated from the different techniques were similar in magnitude.[135] The differences in the fits likely arose from binding to the polycrystalline Au surface. By using a polycrystalline target, different surface topologies, facets, and defects are typically presented that may alter peptide binding capabilities. From this analysis, a rapid binding process was elucidated where 90% of the metallic surface was covered within 20 min with a binding energy on the order of -8.0 kcal/mol.[135] On the basis of the amino acid sequence, it is possible that surface binding can occur through the thioether group of Met, the multiple amine groups of His and Lys, and the hydroxyl functionalities of Thr and Ser.

Clearly, the 3R-GBP1 peptide has been shown to possess higher binding affinity for the material's surface. Surprisingly, however, in recent results, the effects of repeating the sequence three times in a single peptide to increase the surface-binding strengths have demonstrated varying results depending upon the target surface.[132] In some instances, increased surface affinity was observed; however, in other cases, minimal binding changes were noted. A modified SPR method was used to investigate the binding kinetics and the specific affinity of the two different forms of peptides: cyclic (*c*) and linear (*l*). The peptides that were studied included Pt binding septapeptides (*c*-PtBP1 – (CPTSTGQAC) and *c*-PtBP2 – (CQSVTSTKC)), quartz-binding dodecapeptides (*l*-

QBP1 – (RLNPPSQMDPPF) and *l*-QBP2 – (QTWPPPLWFSTS)) and the Au-binding peptide (*l*-GBP1) selected using phage or cell surface display libraries.[132] SPR spectroscopy generally uses a Au surface, but here it was modified to contain a thin film of the material of interest (SiO_2 or Pt) on Au for the quantitative analysis of their respective peptides.[132] The binding kinetics of all the peptides were studied and compared with their triple repeat sequences that were engineered to contain three copies of the same original sequences. It was hypothesized that with the increased number of binding domains, there would be a general increase in the binding affinity with all the peptides studied; however, it was observed that the binding strength of the peptides varied with the increase of sequence repeat units with no general trend.

The adsorption rate of the tandem repeats of the sequence of QBP1 was an order of magnitude faster than the single moiety leading to an increase in its binding energy, while no change was observed in the binding energy of QBP2 as a function of increased number of repeats.[132] Similarly, the triple-repeat form of GBP1 was found to be twice as fast and possessed slightly higher adsorption rates and energies as compared to its single repeat counterpart.[132] The Pt binding peptides (PtBP1 and PtBP2) in their *l*- were studied as 1 - and 3 - tandem repeat sequences. While the *c*-PtBP1 was found to possess 20 times higher adsorption rate as compared to the linear form, the 3*l*-PtBP1 (the three repeat from) possesses free-energy of adsorption similar to that of single repeat form.[132] On the other hand, the adsorption kinetics of *l*-PtBP2 was found to be several times faster than the *c*-form, while the free energy of adsorption of 3*l*-PtBP1 is considerably higher than the single repeat form.[132] Clearly, the results obtained from PtBP1 were opposite to those

observed with PtBP2 and the results obtained with all the peptides did not lead to any universal behavior for the peptides that could be based upon their sequence only.

Although the exact mechanism of the adsorption behavior of peptides onto solid surfaces is not clear, the observed differences in the binding behavior of the peptides could be attributed to the conformational changes between the *c*- and *l*-forms and the single and three repeat polypeptides.[132] The CD experiments indicated the presence of extended helical polyproline type II (PPII) secondary structure in the peptides containing Pro, Ala, and Gln like PtBP1.[132] While the *l*-PtBP1 can adopt some degree of PPII structure, the *c*-PtBP1 does not; at the same time, since PtBP2 lacks these amino acids, the differences between the binding behavior to Pt of the *l* and *c*-forms of PtBP2 do not follow that of PtBP1.[132] This clearly shows that the secondary structure of peptide has a direct effect on its binding affinity towards the particle surface that differs from one peptide to another.

Sarikaya and colleagues also noted how primary and secondary structures of a peptide can manipulate its functions and adsorption behavior to Au nanoparticles.[127] Two different peptide sequences, named AuBP1 (WAGAKRLVLRRE) and AuBP2 (WALRRSIRRQSY), that exhibited the highest Au-binding affinity were selected from a library of the Au-binding peptides and synthesized in two different forms: cyclic and linear.[127] The cyclic forms [*c*-AuBP1 – (CGPWAGAKRLVLRREGPC) and (*c*-AuBP2 – (CGPWALRRSIRRQSYGPC)] were constructed using bridged terminal Cys constrained loops. In order to analyze their adsorption behavior and to quantify their metal-binding affinity, all four Au-binding peptides were subjected to SPR analysis, circular dichroism (CD), and computational molecular modeling studies.[127] Whereas the binding affinity and

the adsorption behavior of both the *c*- and *l*-forms of AuBP1 were found to be quite similar, the affinity of the *c*-version of AuBP2 was an order of magnitude higher than the *l*-form. The main reason for the discrepancy was the difference in the molecular structures of the peptides.[127] Three of them (both forms of the AuBP1 and the *c*-AuBP2) had similar structures, while the *l*-AuBP2 had substantially different structure as revealed by CD experiments and molecular modeling.[127]

To study the effects of peptide's structural conformation on the their ability to adhere to the nanoparticle surface, crystallographic surface recognition was performed by conformational analysis of various Pt-binding septapeptides [containing strong binders, SD152 (PTSTGQA) and SD60 (QSVTSTK); moderate binders, SD128 (LGPSGPK); and weak binders, SD1 (APPLGQA) and SD6 (LNDGHNY)] that were isolated using a phage display library. It was revealed that multiple protrusions called polypods occurred in the peptide structure.[128] Further, it was found that these protrusions played an important role as being the points of contact to the surface such that they spatially correspond well with the crystallographic metal surfaces.[128] The protrusions were observed to be more prominent in strong surface binders as compared to the weak binders.[128] Further, even the strong binders possessing different sequences had significant disparity in their conformations on the metal surfaces.[128] These experiments revealed that it is not just the amino acid sequence but also the conformational orientation of the peptides that can play an important role in imparting them different characteristic properties.

The peptide's structure and conformation not only affects the affinity but also their adsorption kinetics on the materials' surfaces. Adsorption can be of two types,

chemisorption and physisorption, both of which can be guided by one or more of the following forces: hydrophobic, electrostatic, and/or hydrogen bonding interactions, which, in turn, depends upon the amino acid composition.[132] Interestingly, different conformations of the same peptide having significantly different adsorption behaviors suggests that the molecular conformation also has an effect on the molecular recognition, as shown earlier by the CD experiments of the AuBP1 and AuBP2.[43,127] For the GBP1, it was further deduced that the conformational change of the triple-repeat form of GBP1 could lead to the relaxation of the peptide that may result in the lattice matching with the underlying crystal surface of the solid.[132] Hydrophilicity of QBP1 and hydrophobicity QBP2 could be the reasons for the slower adsorption and desorption rates and thus, the higher binding constant and binding energy of QBP2 than that of QBP1.[132] An explanation of the biexponential and stronger binding behavior of 3-repeat GBP1, *l*-PtBP1, 3-repeat *l*-PtBP2, and *l*-QBP2 could be the formation of a network structure of isolated "islands" of the peptides on the solid surfaces.[132] Nonetheless, the binding behavior of the peptides is governed by the differences in the adsorption and desorption rates leading to equilibrium that in turn is controlled by their three dimensional conformation.[132] At the same time, it is likely that the main factor in controlling the binding behavior is ultimately the amino acid sequence on which the electrostatics and secondary structures of the peptides depends, and which can dictate the type of conformation (*l* or *c*) to have higher or lower binding affinities.

1.4.2   Amino acid Interactions

While it is known that peptides interact with nanomaterial surfaces due to their structure and amino acid composition, little information is known about the types of

interactions of the individual amino acids on the three-dimensional surface. Different amino acids have different effects on nanoparticle synthesis, structure, and applications.[65] Shao *et al.*, for instance, demonstrated that Asp can initiate and control the syntheses of Au nanoparticles at room temperature.[136] It was shown that Asp could act as both the reducing and the surface passivating agent giving rise to polygonal Au nanoplatelets with average edge length of 590 nm for hexagonal nanoplates and 840 nm for truncated triangular nanoplates.[136] Lys and Trp, on the other hand, produced highly monodisperse spherical Au nanoparticles with average sizes of 6 ± 2 nm and 60 ± 5 nm, respectively.[136] At the same time, when Au nanoparticles were synthesized using Arg, a wide range of size distribution with diameter 10 ± 5 nm was obtained and that with Tyr, spherical and rod-shaped particles were produced.[136] While previous studies have shown that Lys produces Au nanoparticles only in the presence of $NaBH_4$ as the reductant, in the studies conducted by Shao *et al.* it was revealed that Lys is able to synthesize Au nanoparticles without any external reducing agent under slightly different conditions.[136,137]

Bhargava *et al.* synthesized Au nanoparticles with the help of Tyr, glycyl-L-Tyr and Arg, all which produced nanoparticles with wide range of particle size distributions (5-40 nm, 5-30 nm and 15-50 nm, respectively).[138] While both Tyr and glycyl-L-Tyr along with Arg produced similar structures with particles comprised of multiply twinned crystals, Arg also produced highly anisotropic particles with platelike morphologies.[138] A broad particle size distribution suggests a relatively large nucleation time interval.[139] Since, these amino acids produced Au nanoparticles with a broad size range, it indicates that the nucleation process exhibited by them is different from the burst nucleation of

36

citrate, in which the nucleation of the nanoparticles starts immediately after the citrate addition and completes in a short time interval.[138,139]

Cys is known to have an inherent ability to bind to divalent metal ions and naturally has a widespread presence in the structural motifs of various proteins e.g. zinc fingers.[140] When the outer surface of Tobacco Mosaic Virus (TMV) was engineered in order to display additional Cys residues, it was able to synthesize Pt nanoparticles on the protein surface.[141] The thiol group of Cys is known to bind with Au and other noble metals based on hard soft acid base (HSAB) theory and is also suggested to be a source of electrons for the reduction of Au ions during Au nanoparticle synthesis by the use of Cys.[65,142,143] The large number of Cys residues in BSA provides it the ability to synthesize and bind to Au nanoparticles via the thiol group.[65,84] Aryal *et al*. spectroscopically identified the S-Au interaction in Cys-capped Au nanoparticles by using UV–vis, Raman, NMR, and FT-IR spectroscopies.[144] For the study, the Au nanoparticles were synthesized using Cys as the surface passivating agent and $NaBH_4$ as the reducing agent with subsequent aging for ~12 h.[144] Using UV-vis spectroscopy, it was observed that the nanoparticles initially produced a peak of 512 nm, which red shifted with broadening over the time period; during the same time, the solution color changed from ruby-red into blue while the nanoparticles remained stable for up to two months.[144] FT-IR spectra results indicated a shift in the position of the COO^- and NH_3^+ stretching frequencies, which could be attributed to the change in their dipole moment when Cys binds to metal surface with high electron density. Further, the disappearance of the S-H band in the spectra of the Cys/Au complex confirmed the S-Au interaction, which was indicated to be covalent-like by the absence of S-H in the Raman spectra.[144]

Hong *et al.* used density functional theory (DFT) calculations of selected single amino acids that constitute, in part, the sequences of the Flg and A3 peptides. Here they found that specific side-chain binding affinities to Au and Pd surfaces may exist because of a combination of molecular-level effects.[46] The DFT results were found to be consistent with the experimental trend.[46] In the case of charged/polar residues, a stronger binding affinity was observed over nonpolar residues, which could be attributed to charge transfer leading to the higher attraction between the molecules and the inorganic surfaces.[46] The relative order of affinity (Ser, Pro, and Val for a Au surface) was dictated by the amino acid polarizability such that the affinity of Ser > Pro > Val.[46] Further, it was determined that the affinity of a peptide is not only determined by the sequence of the peptide but also by the solvent.[46] By studying the effects of changing solvent conditions, it was found that only Asp retained its adhesion to the Au surface in DMSO, while the other amino acids could not bind to the Au surface when DMSO was used as the solvent in place of water.[46] On the other hand, Lys and Arg showed reversed adhesion characteristics to the Au surface in HEPES buffer as compared to when present in the aqueous solvent.[46] Hoefling *et al.* calculated the interaction free energy for all twenty standard amino acids on Au surface. It was found that aromatic amino acids possessed the highest Au binding affinity followed by sulfur containing which, in turn is followed by positively charged amino acids, while polar, aliphatic and negatively charged amino acids possessed the lowest affinity in the order.[145] Obviously, the amino acids possess binding affinities that vary based upon the side chains; however, when collected into peptides, it is likely that there may occur multiple interactions that can range from

cooperative to antagonistic and even multidentate binding that can control the surface affinity.[146,147]

Amino acids and peptides not only interact with the nanoparticle surface but also provide them unique properties based upon such interactions. These properties can be employed for a variety of applications in the fields of medicine, electronics and energy. In many cases, the amino acids and peptides act as both the surface passivating agents as well as templates that can help synthesize specifically shaped nanostructures. In certain other cases, they make nanoparticles accessible to interact with molecules of interest and thus taking a indirect part in chemical reactions.[148] While there are numerous peptide and amino acid-based nanoparticle applications, two such applications have been discussed in the next section where the peptides have a clear role in delivering the nanoparticle attributes.

1.5 Applications of Bio-derived Nanoparticles

1.5.1 Enzyme Mimics

Peptide-mediated approaches have been used to design a multitude of different functional structures for applications such as enzyme mimics and biosensors. One such system comprised of an integrated one-component CdS–Pt nanoparticle system constructed by Slocik and Naik. CdS and CdS–Pt nanoparticle conjugates were prepared by a peptide-stabilization method by addition of Cd^{2+} and S^{2-} ions to peptide using an aqueous approach.[148,149] A Cys-modified multifunctional FlgA3C peptide (DYKDDDDKPAYSSGAPPMPPFC) that acted as a biotemplate for CdS, generated a system that could be used to template Pt nanoparticles by addition of Pt^{2+} and $NaBH_4$. This formed a platform comprising of catalytic Pt^0 nanoparticles on the surface, a

39

sandwiched peptide coat, and photoactive CdS nanoparticles at the center. (Figure 1.6).[148] The peptide-based method served as an inorganic mimic of the enzyme nitrate reductase for the reduction of nitrate (NO_3^-) to nitrite (NO_2^-).[148] The CdS–Pt system was found to be so robust that it even outperforms the native nitrate reductase enzyme in catalytic activity by more than 23-fold.[148]

The peptide interface performs additional functions beyond acting as a template and passivating ligand for the synthesis of the CdS-Pt nanoparticles.[148] It imposes a close proximity between the Pt and CdS nanoparticles for effective electron transfer in the absence of an electron mediator, thus making the process extremely fast and efficient. The peptide also takes an active part in the reaction process by acting as a separate sacrificial electron donor via the Tyr residues that are known to have redox properties in a number of biochemical processes such as in photosystem II (PS-II). Within the peptide, the Tyr residues can provide electrons for the trapped holes (h+) (as in PS-II) on CdS nanocrystal, which appear as a result of the catalytic reaction as shown in Figure 1.6.[148] Furthermore, the peptide aids in the production of smaller sized CdS nanoparticles, leading to their increased stability and resistance to aggregation in solution which can help in formation of higher electronic band gaps of the nanocrystals.[148,150,151] The peptide not only leads to increased nanoparticle stability but also increases the range of reactivity for these biomimetic materials. The catalytic activity was found to be further increased by a factor of four by increasing the temperature to about 75°C, due to more photoexcited electrons that become available for the reaction from the enhanced electron diffusion, versus a complete loss of activity for the thermally denatured enzyme.[148]
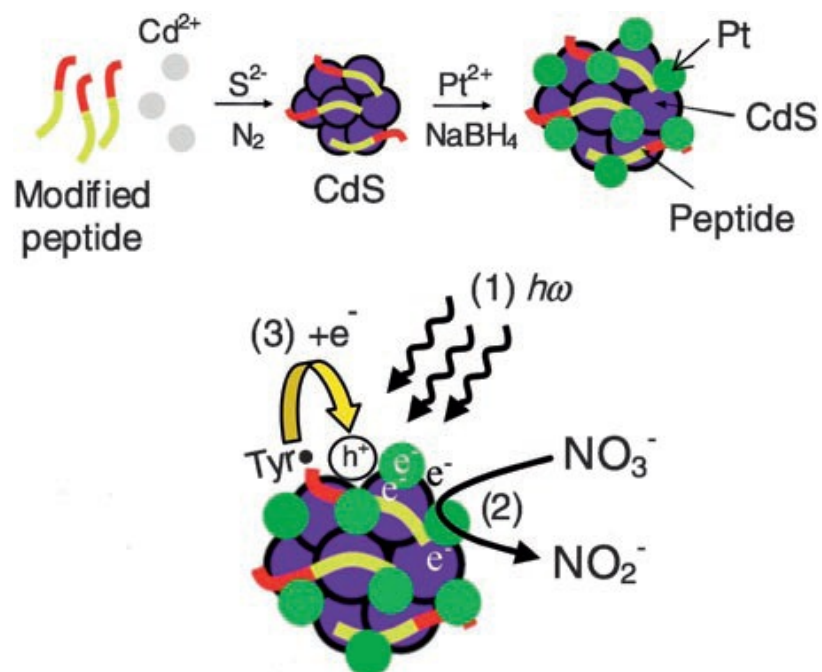
Figure 1.6 Synthesis of CdS-Pt nanoparticle conjugates by using FlgA3C peptide. The complex was shown to mimic the catalytic activity of the enzyme nitrate reductase.[148]

Reproduced with permission from ref 148, copyright John Wiley and Sons.

1.5.2 Biological sensors

Although, most colorimetric Au nanoparticle sensing strategies have used nucleic acids as the sensing element, [48,65,152-157] Naik and colleagues synthesized peptide-functionalized Au nanoparticles using the previously discussed Flg-A3 peptide as a colorimetric sensor for detection of metal ions.[158] The peptide has an acidic pI (3.9) imparting a net negative charge onto the Au nanoparticle surface that prevents their aggregating.[158] The amino terminus Flg domain that contains charged and aromatic residues is involved in the complexation of secondary metal ions,[158] while the A3 peptide domain binds to the Au surface.[158] Initially, the Au nanoparticles were cherry red, but a rapid color change was observed with the addition of metal ions such as Co^{2+}, Hg^{2+}, Pb^{2+}, Pd^{2+}, and Pt^{2+}.[158] (Figure 1.7) At the same time, the SPR absorption spectrum of the nanoparticles red shifted and broadened due to the metal ion induced aggregation of the nanoparticles; a distinct color and SPR peak were observed for each metal ion species such that unaggregated materials produced a peak at ~ 524 nm, while Co^{2+}, Hg^{2+}, Pb^{2+}, Pd^{2+}, and Pt^{2+}-based aggregation shifted the peak to 593 nm, 580 nm, 614 nm, 617 nm, and 542 nm, respectively.[158] Although the nanoparticles were not selective for a particular metal ion, the colorimetric response was specific and reproducible for a particular metal ion species each having their own optical signature that depends upon the interparticle spacing and aggregate size.[158] The difference in the colorimetric response was attributed to the way the peptide interacted with the metal ions leading to different aggregation levels of the Au nanoparticles and thus different color in the presence of different metal ions.
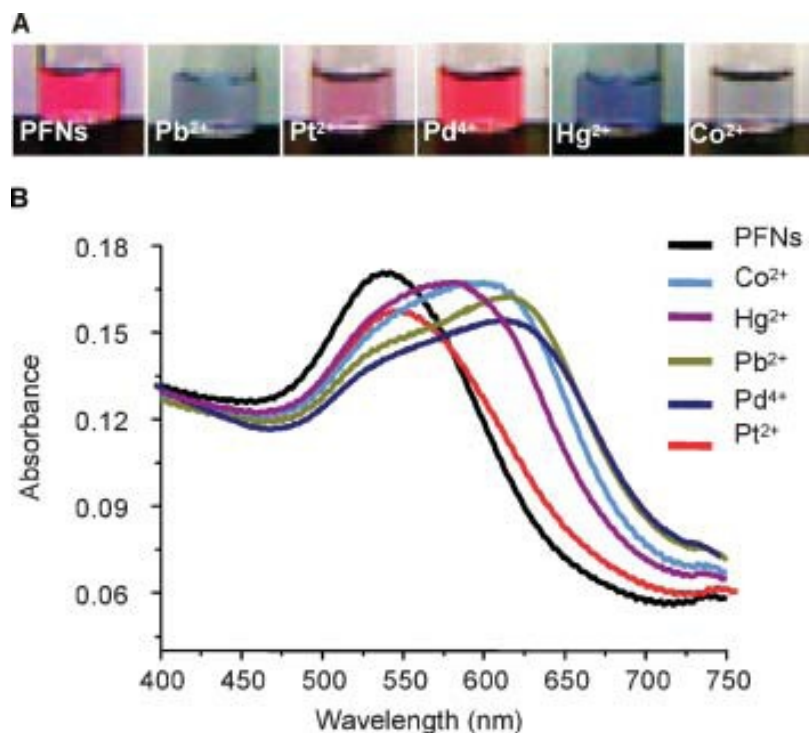
Figure 1.7 Characteristic colorimetric response of the peptide functionalized Au nanoparticles in the presence of different heavy metal ions.[158]

Reproduced with permission from ref 158, copyright John Wiley and Sons.

1.6 Summary and Conclusions

Metal nanoparticles are synthesized by reducing their precursor salts with a reducing agent and then stabilizing them with a surface-passivating agent by the steric and/or repulsive electrostatic interaction. Nanoparticles have distinct structure-function relationships and physico-chemical properties as compared to their bulk counterparts. Most of these properties can be attributed to their small size, providing a large surface to volume ratio. The surface properties are generally highly dependent upon the shape and size. While most nanomaterial synthesis procedures require harsh chemical conditions, biology uses simple inorganic precursors to produce complex nanomaterials in a hierarchical fashion and in a highly energy efficient manner. Biomimetics is a tool to overcome this barrier while learning form nature for the synthesis of the nanomaterials. There are numerous examples where biological systems synthesize nanomaterials using specialized biomolecules, most commonly being proteins or smaller peptides. Natural proteins/peptides are limited not only in terms of their availability but also their ability to synthesize non-natural nanostructures. As a result, artificial means to obtain peptides for the synthesis of various nanomaterials are being utilized. Phage display technology is the most commonly used method to obtain short peptides that can direct the synthesis of the nanoparticles. The peptides, thus identified can provide specific properties to the target material against which they are obtained. Different peptides identified through this combinatorial method to a target material appear to have little homology and, at the same time, little is known about the type of interactions that are present between amino acids of the sequence and the nanoparticles. Although some computational and experimental studies have been conducted to address this issue, most of them employ two-dimensional

surfaces, which can be quite dissimilar from the three-dimensional nanoparticle structures in solution. In order to understand the amino acid interactions with the nanomaterials on a three-dimensional surface, we employed Au nanoparticles and nanorods to study their interactions with various amino acids. Based upon different assembly patterns that were obtained from different amino acids, and with the use of UV-vis spectroscopy, DLS and TEM, specific amino acid surface interactions were elucidated. The results obtained could one day be used for the *de novo* peptide synthesis to obtain "tailor-made" peptides rather than random sequences obtained by the combinatorial methods.

Chapter 2: Mechanism of Arginine-Based Assembly of Au Nanoparticles leading to Chain Structure Formation

2.1. Overview of Study

Biomacromolecules represent new structures employed for the fabrication, assembly, and subsequent use of nanomaterials for a variety of applications. By genetically selecting for the binding abilities of these bio-based molecules, generation of materials with enhanced and environmentally sound properties is possible. Unfortunately, the level of understanding as to how the biomolecules bind and arrange on the nanomaterials surface is incomplete. Recent experimental and theoretical results suggest that the binding ability is dependent upon the peptide composition, sequence, and structure; however, these results were obtained for two-dimensional surfaces of the targeted inorganic material. Changing of the sample from two-dimensional targets to in solution three-dimensional nanomaterials presents a challenge, as the level of analytical characterization for the latter system is minimal. This chapter presents studies on the interactions between Au nanoparticles and the amino acid arginine (Arg) that is able to bind to the surface of Au nanoparticles in a segregated pattern, which produces an electric dipole across the structure. Increasing concentrations of Arg to citrate capped Au nanoparticles results in the formation of branched linear chains of the spherical nanomaterials. Further study confirms the mechanism of assembly and demonstrates the unique reaction conditions that can be used to directly control the assembly rate, and thus the size of the final superstructure that is produced. The assembly rate was directly modulated by the Arg:Au nanoparticle ratio, the temperature of the system, and the dielectric of the solvent, all of which can be used in combination to control the process.

These effects were monitored using UV-vis spectroscopy, transmission electron microscopy, and dynamic light scattering. The final results suggest that incomplete substitution of the original citrate surface passivant with the amino acid occurs, leading to surface segregation of the two species. This segregation effect produces a dipole across the Au nanoparticle surface to drive the linear assembly of the materials in solution. It is suggested that the second step of the assembly process, the formation of nanoparticle chains controlled by Brownian motion, controls the overall assembly rate and thus the size and orientation of the final superstructure. These results are important as they lay the basis for the subsequent use of this technique for the possible fabrication of electronic device components, as well as for use as assays to probe nanomaterials surface structures.

2.2. Introduction

The use of nanomaterials for commercial and industrial applications is becoming increasingly important. These applications rely upon the enhanced properties that are achieved by the quantum confinement effects that are observed at the nanoscale, which can dramatically alter the activity of the structure as compared to their bulk counterparts.[143,159-162] Such effects are evident with Au nanoparticles that possess vibrant plasmon bands and surfaces that are easily functionalized with a variety of ligands ranging from oligonucleotides to hydrophobic chains.[143] The surface functionalization is typically achieved using thiol-based chemistries, wherein the thiol is either used to passivate growing Au nanoparticles in solution[163-165] or they are place-exchanged onto the surface of preformed Au nanostructures.[166,167] A prime example of the latter situation is the exchange of a variety of thiolated ligands onto the surface of citrate capped Au nanoparticles, which has been used to display proteins, oligonucleotides, organometallic

complexes, as well as many other species.[29,167-171] The surface display of these ligands is critical to their subsequent function. This can be especially true for different applications such as catalysis and nanoparticle assembly where the ligands possess a significant degree of control over the activity.[48,58,115,116,172-175] For instance, for catalytically active nanomaterials, the ligands must present a sufficient metallic surface to solution from which the reaction is processed while maintaining the nanoparticle stability.[116,173-175] For a different capability, nanoparticle assembly, the ligands must be designed in such a way that controlled assembly of the component structures is achieved without the formation of bulk or uncontrolled aggregates.[176-178] To address this issue, many groups have employed asymmetric surface functionalization techniques wherein certain ligands are specifically localized at a single region on the nanoparticle surface from which assembly can only occur via these ligands.[29,31,179] While such techniques do produce a level of control for the organization process, the synthetic strategies used to achieve the required surface display can be complicated and the assembly of the materials can be limited to a single site, which can minimize the complexity of the final structure.

For many years, numerous synthetic strategies have been developed for the production of nanomaterials of various compositions using judiciously selected ligands.[65,143,173,175] Unfortunately, the ligand set must be designed initially to achieve materials that are fully stable in solution against aggregation, which can minimize the subsequent activity of the structures by poisoning or disrupting the inorganic surface. As an alternative, biomimetic strategies have been developed that are modeled on biological routes towards inorganic materials production, which have been developed over millennia of evolution.[65,123,180] In this case, many organisms employ protein/peptide-

mediated methods to nucleate, grow, and direct the activity of inorganic nanostructures for a variety of applications including protection against predation, structural support, or as bioremediation mechanisms.[65,180-182] While the number of biologically observed inorganic minerals is limited, phage display techniques[98,116,183-190] have been used to isolate peptides with the ability to produce nanomaterials of technologically interesting compositions such as $BaTiO_3$,[191] $FePO_4$,[184] and Pd.[116] Here, mixing of the peptide with appropriate precursors can initiate and modulate the growth of their respected materials, which are usually controlled by binding of the peptide to the growing nanoparticle surface.[107] For instance, using the Pd4 peptide, production of nearly monodisperse Pd nanoparticles is achieved, which can be used as highly reactive C-coupling catalysts.[116] The activities of these bio-inspired nanomaterials are likely controlled by the peptide surface, which dictates the nanoparticle interactions in solution. Unfortunately, little chemical information is known about the surface of these three-dimensional structures in solution. Using two-dimensional surfaces to study the biomolecules binding to their target materials, many groups have shown that the amino acid composition, the sequence, and the geometrical structure of the peptide contribute to the surface binding ability, especially for sequences that possess Au, Pd, and Pt binding activities.[48,127,128,132,135,146,168,192-194] It is envisioned that by constraining the peptides into specific orientations, the chemical moieties of the amino acid side chains will be displayed in such a fashion that optimal binding will occur as the peptide approaches the growing inorganic materials.

While the two-dimensional binding studies are quite useful in understanding how individual peptides bind to the surface from a sequence/conformation effect, limited

49

information is known about how biomolecules interact with each once bound to the surface. Recent analyses using alkyl thiols have demonstrated that when a mixture of ligands is present on a three-dimensional surface, spontaneous surface segregation of these ligands can occur, which appears to be thermodynamically controlled.[48,195-201] This indicates that while the initial binding of the molecules may happen in a random fashion, the ligands can adjust their positions/orientations once attached to achieve a more stable configuration. Such events may be observed for complex biomolecules on the surface of nanomaterials via interactions between two or more of the molecules on the surface.[48,172,202] As a result of these non-covalent inter-ligand forces, the biomolecules may align, segregate, or be specifically oriented in some fashion to minimize the energetics of the system while maintaining particle stability.[48] At present, such results for biomolecules are only sparsely studied due to the complexity of monitoring three-dimensional colloidal systems in solution as such studies are typically beyond the limits of detection of readily available analytical techniques.

In this study, direct experimental evidence concerning the interactions and surface segregation of the amino acid Arg with Au nanoparticles in solution is demonstrated, as shown in Scheme 2.1. This system was selected as the Arg side chain has been implicated as possessing binding capabilities to inorganic substrates[203] and has been observed in many materials binding peptides, especially those isolated for Au surfaces.[204-207] To study this process, various concentrations of the amino acid were added to aqueous solutions of citrate-capped 15 nm Au nanoparticles, which resulted in the self-assembly of the nanomaterials to form long, branching linear chains in solution. Evidence attained by
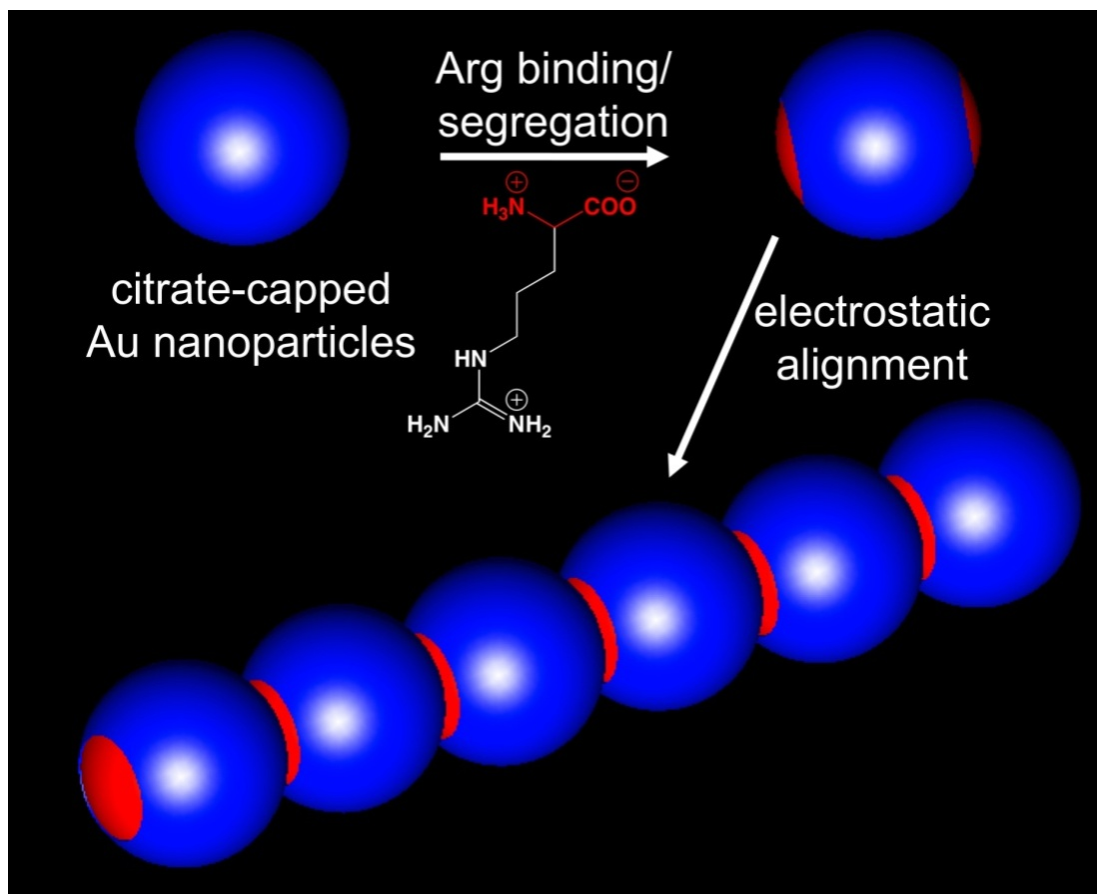
Scheme 2.1 Representative scheme for the formation of linear Au nanoparticle assemblies mediated by Arg.

UV-vis spectroscopy, transmission electron microscopy (TEM), and dynamic light scattering (DLS) indicate that the Arg partially replaces the citrate stabilizer, thus resulting in a mixed monolayer. The organized nanoparticle assembly process suggests that the Arg molecules self-segregate on the Au surface, resulting in negatively charged regions arising from the citrate molecules coexisting with neutral surface regions based upon the solvent exposed, zwitterionic head-groups of the amino acids. In response to the patchwork surface charge and the resultant nanoparticle dipole, formation of linear nanoparticle chains occurs by allowing nanoparticles to collide and interact at the neutral regions. This process is accelerated when higher Arg concentrations are present, which can result in nanoparticle degradation at extremely high Arg concentrations. Further, an in depth analysis focused on the mechanism of the assembly process mediated by Arg surface exchange reactions with citrate capped Au nanoparticles depicts that Arg first binds to the Au nanoparticle surface in a segregated fashion to form a patchy charged network from which the nanoparticle assembly process in solution can be achieved through electrostatic-based interactions. After Arg surface binding/segregation, the two particles must be within a critical interparticle distance and co-orient their charged surface regions towards one another to result in the observed directed/linear assembly. Nanoparticle movements in solution, which is mediated by Brownian motion, control these critical distance and orientation factors. Thus, the assembly process was studied by varying three specific parameters: the concentration of Arg in solution, the temperature of the assembly process, and the dielectric of the solvent. By judicious selection of these conditions, the process can be directly modulated to control the rate of assembly. Overall, the results indicate that the limiting step of the process is at the level of particle

motion/orientation rather than the ligand exchange reaction, which is anticipated to be rapid. These results are important for four key reasons. First, the results suggest specific binding modes and motifs based upon amino acids and their interactions, which may translate to similar arrangements for metal binding peptides to explain metallic solvent accessibility. Second, this study provides a direct route for experimental evidence on the surface interactions between biomolecules and three-dimensional nanomaterials in solution, which is typically difficult to attain. Third, by using these methods, the rate of assembly can be readily controlled; therefore, it may be possible to direct the size and orientation of the final self-assembled structure in solution. Such a level of control may make it possible to design and grow specifically selected lengths, shapes, and orientations of nanoparticle superstructures for use as components in complex devices at the nanoscale. Fourth, this method also represents a unique strategy to biologically control the fabrication of linear assemblies of nanoparticles that are challenging to organize due to the high degree of symmetry from the spherical species.[208] Such arrangements may prove useful for electronic and optical applications.

2.3. Methods

2.3.1. Chemicals.

HAuCl$_4$·3H$_2$O (99.999%), sodium citrate tribasic dehydrate (ACS reagent, ≥99.0%), and L-arginine (reagent grade, ≥ 98%) were purchased from Sigma-Aldrich (St. Louis, MO). Ethanol (95%, ACS grade) was purchased from Pharmco-AAPER (Shelbyville, KY). All chemicals were used as received. Milli-Q water (18 MΩ cm; Millipore, Bedford, MA) was used throughout.

2.3.2. Preparation of Citrate-Capped Au Nanoparticles.

Au nanoparticles were synthesized using the citrate reduction method.[209] Prior to the reaction, all glassware was thoroughly washed using aqua regia (3:1 HCl/HNO$_3$) and then fully rinsed with deionized water to remove any acidic species. For the reaction, a 50.0 mL aqueous solution of 1.00 mM HAuCl$_4$ was refluxed while vigorously stirring. Once refluxing of the solution was achieved, 5.00 mL of an aqueous 38.8 mM sodium citrate solution was added in a single injection. Immediately, the solution changed from pale yellow to colorless. The reaction was allowed to continue to reflux for 15.0 min and from which a final solution color of wine red was developed. After the reaction, the solution was allowed to cool to room temperature before use.

2.3.3. Arg-based Assembly of Citrate-Capped Au Nanoparticles.

For this analysis, various volumes of a 400 μM aqueous Arg stock solution were added in a 1.00 cm quartz cuvette, to result in final amino acid concentrations of 0, 20.0, 40.0, 80.0, 120, 160, and 200 μM. These concentrations were selected as they represent a 0-, 1.00×10^4-, 2.00×10^4-, 4.00×10^4-, 6.00×10^4-, 8.00×10^4-, and 1.00×10^5-fold excesses of Arg as compared to the Au nanoparticles, respectively. These samples are designated as 0, 10K, 20K, 40K, 60K, 80K, and 100K throughout the text, where K = 1000, e.g. 40K = 40,000 etc. The reaction volume was then diluted to 2.40 mL for each sample before adding 600 μL of the prepared Au nanoparticle solution to each cuvette. As a result, the final volume of the reaction solution was 3.00 mL with a 2.00 nM concentration of Au nanoparticles.[48] The reaction was allowed to proceed for 1.00 h while being monitored using UV-vis spectroscopy at various temperature and dielectric conditions as discussed below.

2.3.4. Analysis of the Solvent Dielectric.

To ascertain the effects of the solution condition, identical reaction analyses were completed as described above; however, various volumes of the aqueous solvent were replaced with EtOH. Three separate analyses were completed where 0.50 mL, 1.00 mL and 1.50 mL of the aqueous medium was replaced with EtOH at the appropriate temperature conditions. For each analysis, a control study was conducted simultaneously in neat water to ensure that the observed results were the effect of the lower dielectric solution based upon the added EtOH.

2.3.5. Analysis of the Reaction Temperature.

Each reaction condition described above was additionally studied as a function of temperature at 10.0 ^{o}C, 20.0 ^{o}C, 30.0 ^{o}C, 40.0 ^{o}C, 50.0 ^{o}C, 60.0 ^{o}C, and 70.0 ^{o}C. For this analysis, the UV-vis cuvette holder containing eight wells was thermally controlled using an Isotemp 3016S recirculating chiller (Fisher Scientific). After addition of the solvent and Arg solutions to the cuvettes, the mixtures were allowed to equilibrate with a set temperature value for 15.0 min before the addition of Au nanoparticles (600 µL). Immediately, after addition of the nanoparticle solution, UV-vis spectra were obtained for 1.00 h at 30.0 s intervals. Identical procedures were also employed for DLS analysis.

2.3.6. Characterization.

Time-resolved UV-vis spectra were obtained using an Agilent 8453 UV-vis spectrometer, employing 1.00 cm path length quartz cuvettes (Starna). Each cuvette was washed with aqua regia and rinsed with water prior to the analysis. All spectra were background subtracted against water, which is the main reaction solvent. While studying the effects of concentration alone at room temeperature over a period of 6.00 h, reaction

spectra were recorded at 10.0 min intervals. On the other hand, while studying the effects of all the three factors, i.e Arg concentration, temperature and ethanol over a period of 1.00 h, spectra were collected at 30.0 s intervals as the reaction occurred much faster. TEM images of the assembly process were obtained using a JEOL 2010F transmission electron microscope (TEM) having a resolution of 0.19 nm and operating at 200 kV. A total volume of 5.00 μL of the reaction solution was pipetted onto the surface of a 400 mesh Cu grid coated in a thin layer of carbon (EM Sciences) and allowed to dry in a desiccator. Similarly, like UV-vis, DLS analyses were conducted on a Zetasizer Nano ZS System (Malvern Inc.) at 1.00 h intervals over a total time of 6.00 h and at 1.00 min intervals over a total time of 1.00 h.

2.4. Results and Disscusion

Au nanoparticles with an average diameter of 15 nm were synthesized using the citrate reduction method,[13] and confirmed using UV-vis and TEM analyses (Figure 2.1). The particles possessed the expected plasmon resonance peak at 520 nm, which was used to dilute the nanoparticles to a concentration of 4.00 nM using the Beer-Lambert law. To 1.50 mL of the nanoparticles, various concentrations of Arg were added, resulting in a 0, 10K, 20K, 40K, 60K, 80K, or 100K fold excess of the amino acid with respect to the nanoparticles to achieve a final solution volume of 3.00 mL as discussed in the experimental section. This notation is subsequently used throughout the text to differentiate samples. The reactions were agitated initially and studied over a time period of 6.00 h to monitor changes in the nanoparticle stability at room temperature. To study the effects of temperature and the dielectric, the reactions were monitored for 1.00 h as
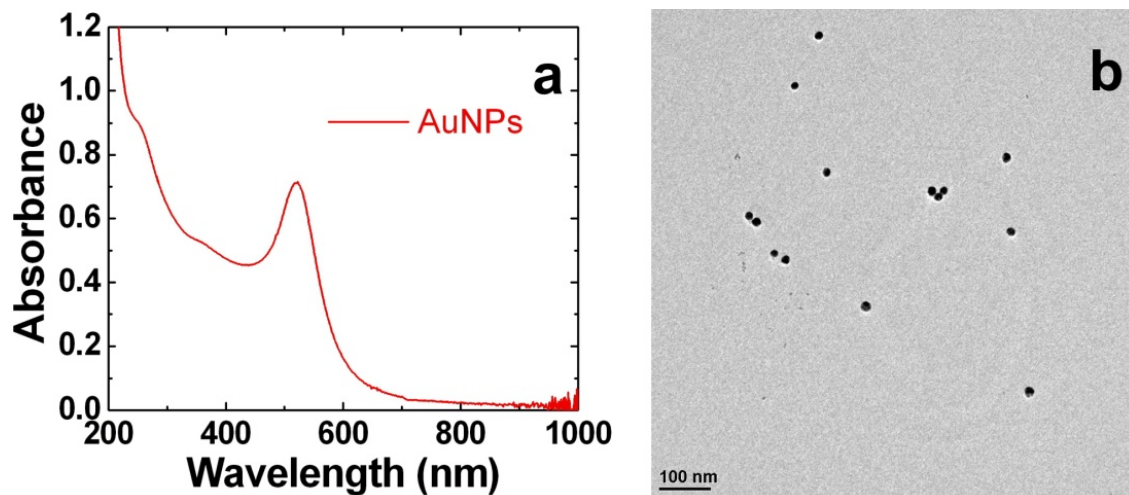
Figure 2.1 (a) UV-vis spectrum and (b) TEM image of the precursor citrate capped Au nanoparticles.

discussed later. Arg was initially selected based upon its known affinity for Au surfaces and its frequency in many materials binding peptides.[203,205,206] Figure 2.2 displays photographs of the reaction between the Au nanoparticles and Arg as they progressed over time demonstrating a distinct color change. Prior to addition of the amino acid, the solution for each reaction was the expected red color. Immediately after Arg addition, Figure 2.2a, this red color is maintained for most samples; however, the 80K materials demonstrated a change to a deeper red color and the 100K solution appeared purple. After 1.00 h of reaction time, Figure 2.2b, the 80K and 100K solutions are distinctly blue and the 60K reaction has become purple. For 0 and 20K, the original red color is observed while the 40K solution becomes darker red. The changes in color progressed after 4.00 h, as shown in Figure 2.2c, to where the 60K solution is now deeper purple and is approaching a blue color, while the 40K sample is purple. At this time point, the 0 and 20K samples have remained red and the 80K and 100K samples remained blue. The solution colors observed at 4.00 h visually remained constant after 6.00 h of reaction time (Figure 2.2d); however, a dramatic change is observed after   18.0 h, as shown in Figure 2.2e. While the control sample, 0, has maintained the initial cherry red color, the 20K sample has evolved to a deeper red. The 40K sample has become deep blue as compared to the previous time point, and samples with higher Arg concentrations display a dimming of the solution color intensity. Even as the resultant blue color is maintained for the 60K and 80K sample, it has become distinctly lighter in intensity as compared to the 6.00 h time point. A more dramatic effect was also observed for the 100K sample, where a blue/black precipitate is observed at the bottom of the vial, in combination with a pale blue solution.
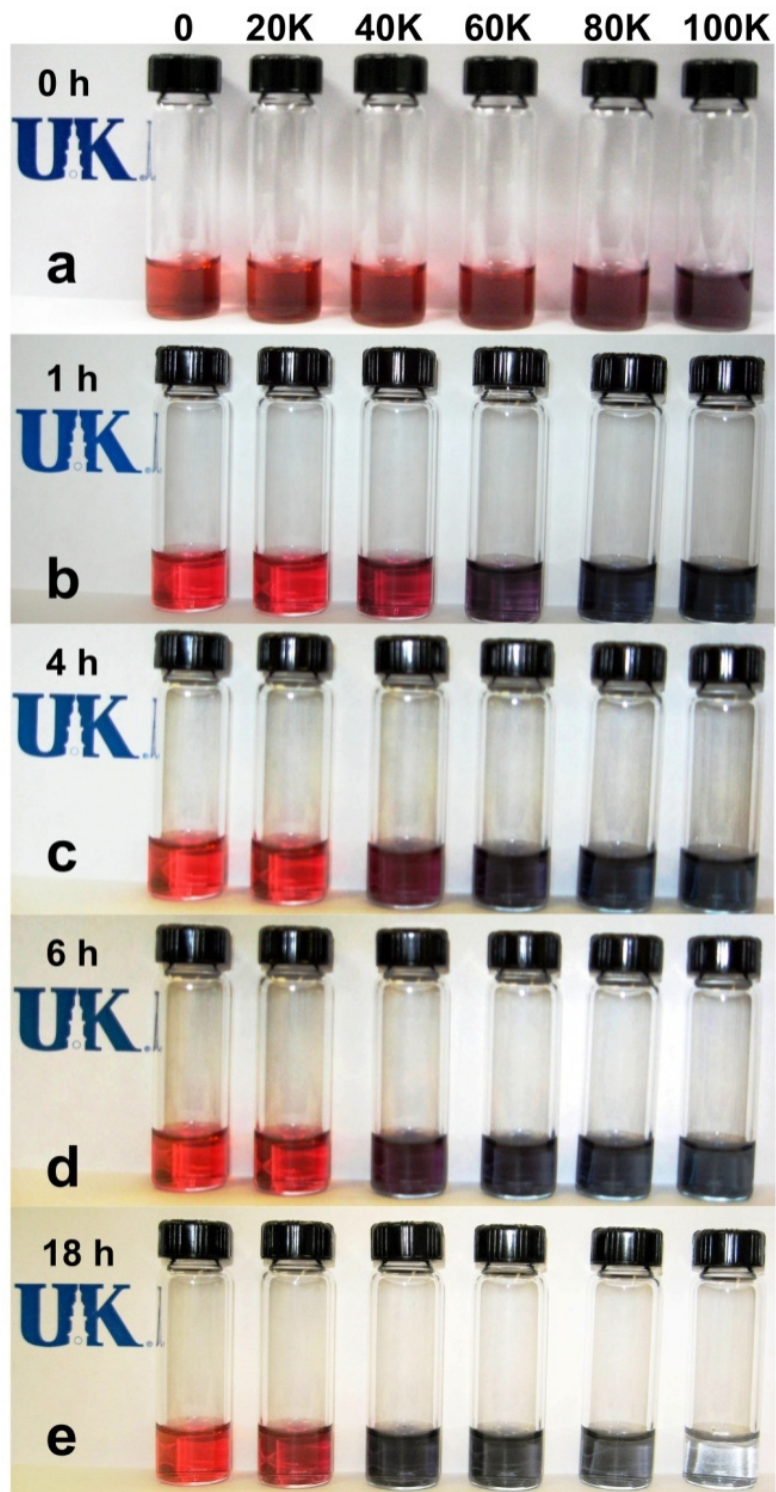
Figure 2.2 Photographs of the effect of Arg on Au nanoparticles at time intervals of (a) 0.0 h, (b) 1.0 h, (c) 4.0 h, (d) 6.0 h, and (e) 18.0 h.

Such visual observations of color changes are consistent with the aggregation of the Au nanoparticles in solution.[210-212] The distinct color changes from red to purple to blue and precipitation of the 100K sample are anticipated for changes in particle size from individual particles to larger aggregates. The color stability of the control sample suggests that the changes observed are directly associated with the Arg molecules in solution. Additionally, the noted differences in the rate of color change between the samples, from 20K to 100K, indicates that the nanoparticle aggregation is dependent upon the solution concentration of Arg, with faster rates arising for higher Arg concentrations. While these results suggest Arg-based aggregation, more quantitative analyses are required to determine the effects of the amino acid.

The aggregation process was initially analyzed using UV-vis spectroscopy. Such a technique is highly accurate to determine the assembly state of the material by shifts in their absorbance.[18,211,213,214] Figure 2.3 shows the spectral changes of the Au nanoparticles in response to Arg addition. Figure 2.3a specifically demonstrates that no change is observed in the spectrum of the Au nanoparticles over the period of 6.00 h in the absence of Arg. Additionally, at the lowest concentration of Arg studied, 10K (Figure 2.3b), no spectral shifts or secondary absorbance peaks are observed. As the Arg concentration is increased to 40.0 μM in the 20K sample, Figure 2.3c, definitive spectral changes are evident. Over a period of 6.00 h, the plasmon resonance peak at 520 nm of the individual Au nanoparticles decreases in intensity as a new absorbance centered at 665 nm increases. In this sample, no distinct peak is observed; however, the absorbance at higher wavelengths continually increases in a linear fashion. More distinctive changes are observed in the 40K sample, as shown in Figure 2.3d. For this sample, a well-
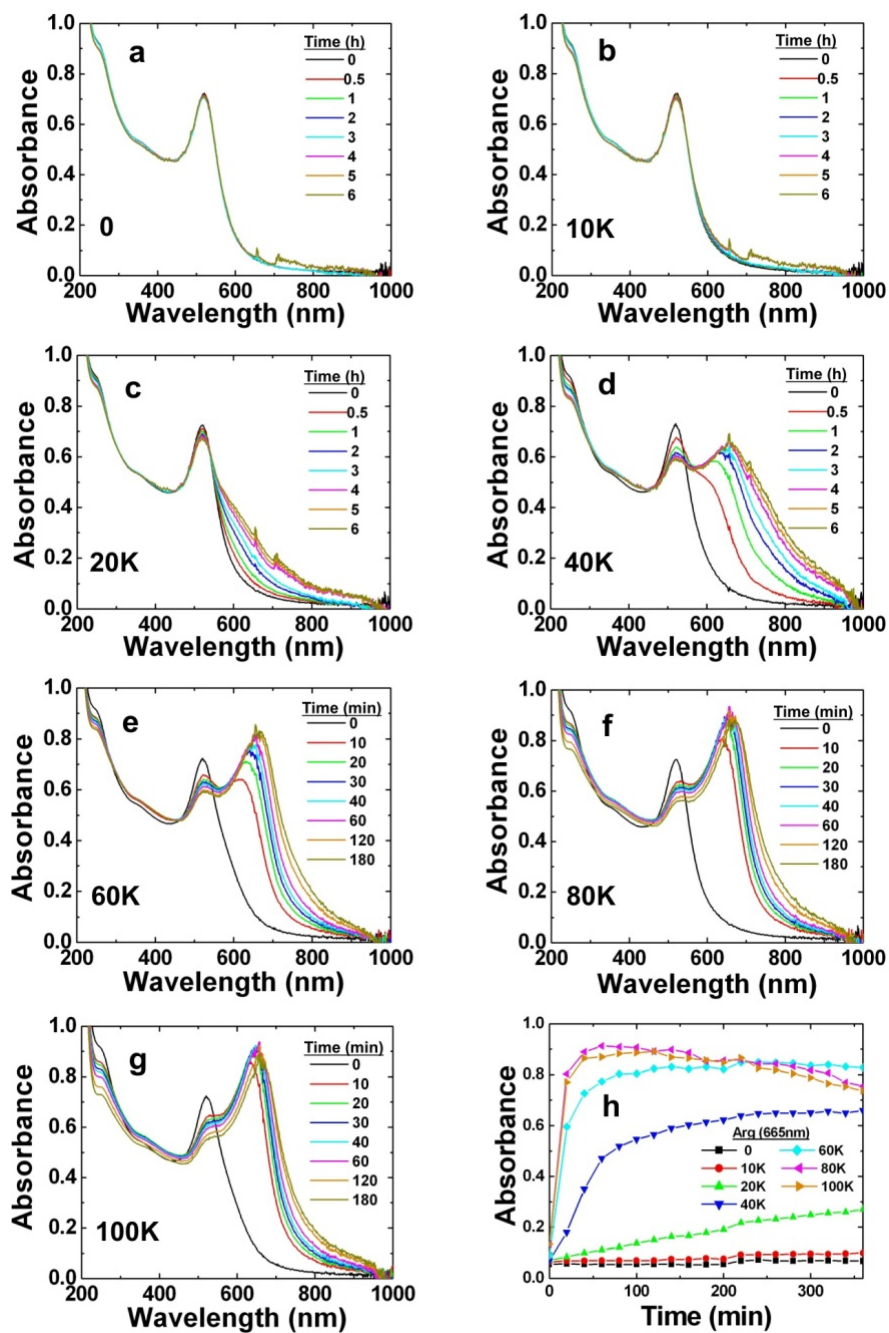
Figure 2.3 UV-vis analysis of the effects of Arg on Au nanoparticles for samples (a) 0, (b) 10K, (c) 20K, (d) 40K, (e) 60K, (f) 80K, and (g) 100K. Part (h) displays the time evolution for the production of the peak at 665 nm for all Arg concentrations studied.

resolved peak at 665 nm is developed as the initial 520 nm plasmon resonance decreases in intensity. This distinct peak is initially slightly broader than the original plasmon resonance, yet is easily resolved over the 6.00 h time scale. For samples of higher Arg concentrations, the rate of peak formation increases dramatically. For the 60K sample shown in Figure 2.3e, development of a strong and narrow absorbance at 665 nm is complete within 2.00 h. After this time point, no changes in the spectra are observed and both the 520 nm and 665 nm peak remain constant. For the 80K and 100K samples, Figures 2.3f and g, respectively, very similar results as to the 60K sample are observed, except faster rates of spectral change are noted. For both samples, growth of the 665 nm absorbance is terminated after 20.0 min, from which both peaks remain constant for ~40.0 min (1.00 h after reaction initiation). After this time point, the spectra demonstrate a progressive red shift and a decrease in intensity for the 665 nm peak. This change is accompanied by materials precipitation at time points greater than 8.00 h.

Figure 2.3h presents the growth of the 665 nm peak over the specified reaction time for all of the samples studied at the various Arg concentrations. It is evident that the growth rate of the new peak directly depends on the Arg concentration. For those samples with no spectral changes, 0 and 10K, no change in the absorbance at 665 nm is observed. For the 20K sample, a slow but consistent linear growth of the 665 nm absorbance is observed over 6.00 h. Note that for this sample, only a rising broad absorbance at higher wavelengths was observed and not a defined peak. Analysis of the 40K sample shows an initial increase in the absorbance at 665 nm, which eventually slows after 100 min post Arg addition. At this point, the growth rate decreases considerably; however, the intensity continues to increase over time. The 60K sample demonstrates a very fast growth rate,

which plateaus after 1.00 h. After this rapid initial growth, the 665 nm absorbance remains constant with no spectral changes observed for this sample. Similar results were obtained for both the 80K and 100K sample with fast absorbance intensity growths; however, this initial period was followed by a slow decrease in intensity over time. This diminishing factor is attributed to the precipitation of the materials as the reaction progressed. Indeed precipitation is observed for both samples, as shown in the image of Figure 2.2e. Interestingly, for all samples that displayed changes to their UV-vis spectra over time, while the initial 520 nm peak does decrease in intensity, its position remains constant over the entire analysis. Even when saturation of the peak at 665 nm is observed, suggestive of the termination of materials assembly, the 520 nm peak persists. As discussed below, this is likely due to the controlled aggregation process mediated by the Arg in solution.

While UV-vis analysis is commonly accepted to be sensitive to the aggregation/assembly state of the materials in solution, it is unable to discern the aggregate size, nor structural changes to the growing framework. To address any size changes in solution, whereby alleviating any possible drying effects, DLS analysis of the materials was conducted. These results are presented in Figure 2.4a, for all samples, with Figure 2.4b showing an expanded analysis for those materials studied with Arg concentrations below the 100K sample. For the 0 and 20K sample, black and red plots, respectively, no changes in the materials size is observed after 6.00 h. The material sizes remain constant around 20 nm, which is consistent with the hydrodynamic radius of the individual Au nanoparticles and the lack of or slow changes observed spectroscopically.[215] For the 40K sample, green plot, a linear increase from an initial size
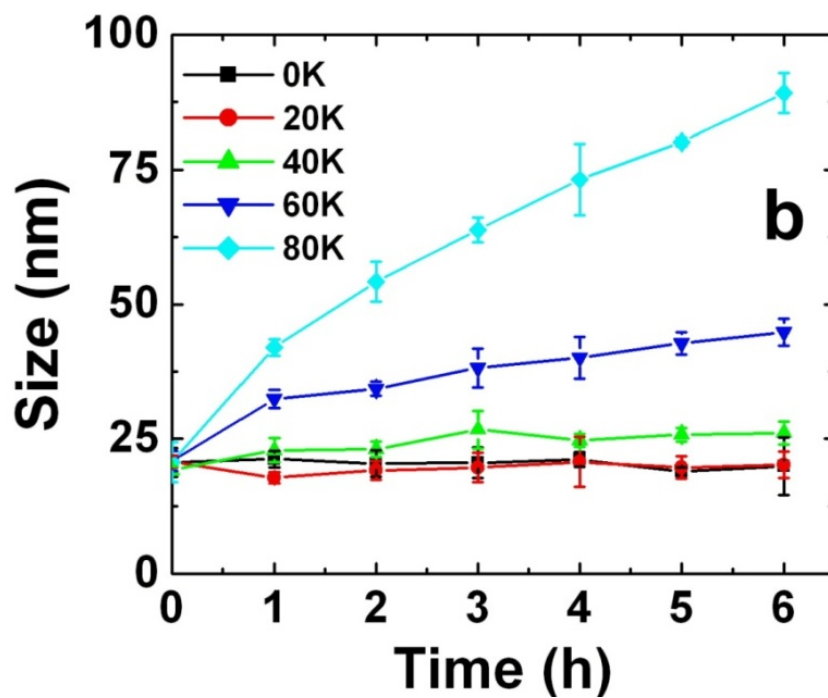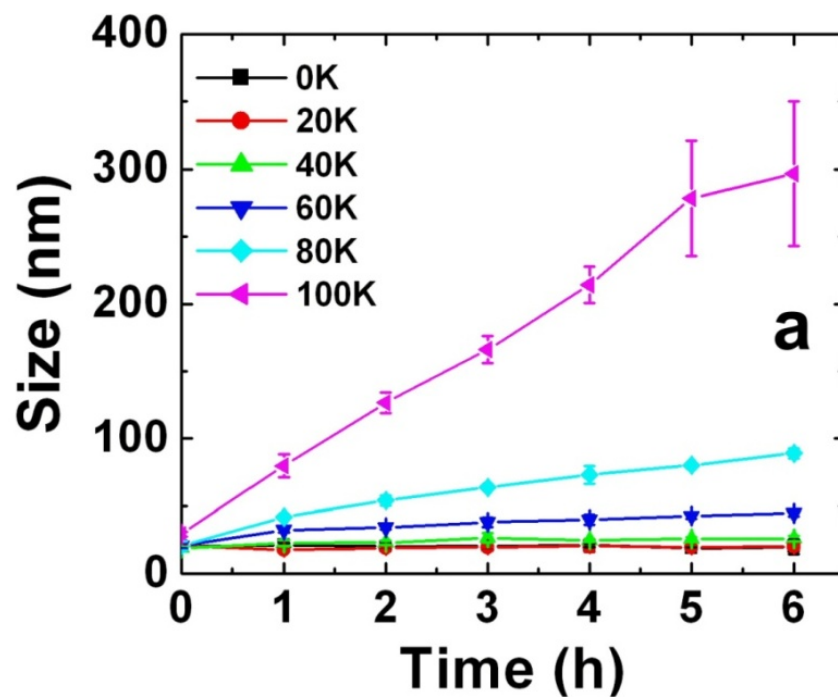
Figure 2.4 DLS analysis of Au nanoparticles in the presence of Arg over a time period of 6.00 h. Part (b) displays the analysis for all samples with Arg concentrations less than that used in the 100K sample.

of 19.1 nm to a size of 26.1 nm is achieved. At all time points, this sample possesses larger average aggregate sizes, as compared to samples with lower Arg concentrations, suggesting that a noticeable size shift is observed. At higher Arg concentrations, clear and linear size dependences are noted. For the 60K sample, plotted in royal blue, an increase in size is observed, which reaches an aggregate size of 44.8 nm after 6.00 h. This increasing trend is conserved for higher concentrations; however, faster rates of production of larger aggregates are observed for these materials. For the 80K sample, light blue plot, this consistent growth process is maintained and terminates in an aggregate size of 89.2 nm at the 6.00 h time point. Finally, analysis of the 100K growth process, plotted in pink, demonstrates the fastest rate for all of the materials studied. As a result, generation of a final aggregate size of 297 nm occurs in 6.00 h, which is considerably larger in size than all other aggregated species studied. While the DLS results indicate that assembly of the materials is occurring in solution, it is unable to determine if this process produces controlled final structures from the individual nanoparticle components. TEM analysis of the materials was thus conducted to ascertain the assembly state of the nanoparticles in response to Arg.

Based upon the above UV-vis results, which demonstrated a splitting of the plasmon resonance, a directed assembly mechanism appears to be mediating the process, which could result in a patterned nanoparticle structure. TEM grids were prepared 6.00 h post Arg addition for each sample from 0 – 100K from which the images attained from these samples. Analysis of multiple TEM images for each sample is shown in Figure 2.5 that classified the nanoparticles as either independent, linearly assembled, or other. Au nanoparticles were considered linearly assembled if three or more particles
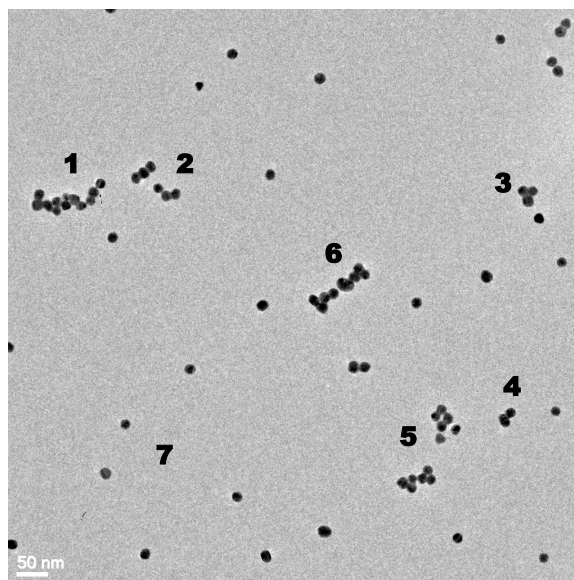
Figure 2.5 Representative TEM image of a sample used to demonstrate the method used to count and characterize the nanoparticles as independent, linear or other (non-linearly aggregated).

1. Shows that there are 12 nanoparticles in close proximity (< 1 nm distance apart) to each other such that 5 of them (on the right) are linear while the rest 7 of them (on the left) are non-linear (other).
2. Shows 3 nanoparticles in close proximity (< 1 nm distance apart) and they are linearly arranged.
3. Shows 3 nanoparticles in close proximity (< 1 nm distance apart) and they are non-linearly arranged, hence "other".
4. Shows only 2 nanoparticles in close proximity (< 1 nm distance apart), thus they are considered as "other".
5. Shows non-linear aggregates, hence "other".
6. Shows non-linear aggregates, hence "other".
7. Shows nanoparticles at distances > 1 nm apart, thus they are considered as independents.
   In this manner, a total of 100 particles were counted together on different TEM images to obtain the statistical data.

were aligned with an interparticle spacing of ≤1.0 nm; however, should the nanoparticles be observed in a random assembly or a non-assembled state, they were classified as either other or independent, respectively, using the process described in detail in Figure 2.5.

As expected, no assembly was observed for the 0 sample prepared in the absence of Arg, displayed in Figure 2.6a. Under these conditions, the Au nanoparticles remain independent and highly dispersed on the carbon grid surface. Similarly, for the 20K sample shown in Figure 2.6b, only small aggregated structures of the Au nanoparticles are observed. Surprisingly, short linear chains of Au nanoparticles were the dominant species observed for this sample. Approximately 3 – 10 nanoparticles could be seen in a linear arrangement, from which occasional chain clustering was also observed. In addition to these structures, an extensive number of independent and unassembled nanoparticles were also detected in this sample. Further analysis of the 40K sample, Figure 2.6c, demonstrated a higher degree of linear arrangements of Au nanoparticles. While long chains of the Au nanoparticles existed, branching points were apparent, which resulted in a network like organization of the linear chains into a superstructure. This larger structure could stretch to >1.00 μm in dimension. TEM imaging of the 60K sample, displayed in Figure 2.6d, indicated that this linear branching trend continued for higher concentrations of Arg. In this sample, larger controlled aggregated networks were apparent. This trend of increased aggregation continued for higher Arg concentrations, with a noticeably denser network prepared for the 80K sample. In this sample, presented in Figure 2.6e, while linear chains were observed at the 6.00 h time point, large regions of the sample were observed to be in a more uncontrolled aggregated structure of variable
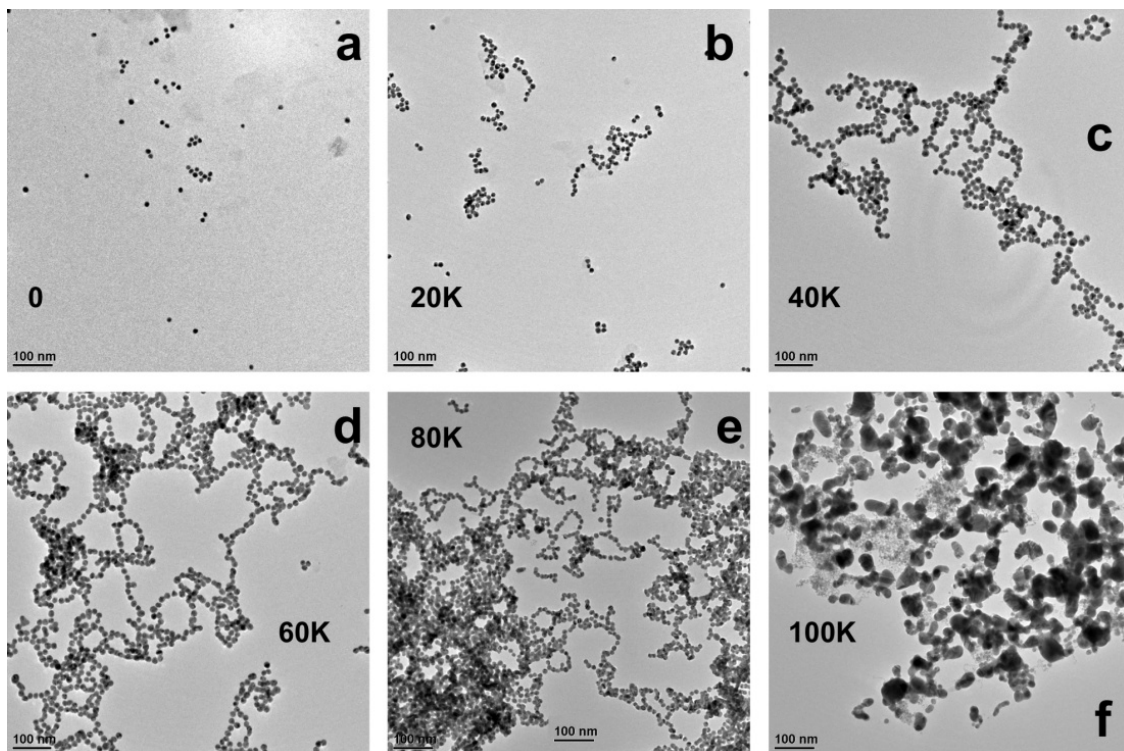
Figure 2.6 TEM micrographs of the Au nanostructures produced after 6.00 h of incubation with Arg for samples (a) 0, (b) 20K, (c) 40K, (d) 60K, (e) 80K, and (f) 100K.

sizes. This mixed type of aggregation is apparent in the TEM image where the linear chains are observed at the center of the image, while large uncontrolled aggregates are observed to surround the chains. Finally, only bulk, irregular Au structures were observed for the 100K sample 6.00 h post Arg addition (Figure 2.6f). No specific arrangement of these uncontrolled structures was discernable with only random orientations and arrangements observed for this sample.

While it appears to be evident that the Au nanoparticles indeed assemble in an organized linear manner in the presence of Arg, both the UV-vis and DLS data suggest that this process occurs over time, rather than in a single immediate step. To analyze this process, TEM images (Appendix I Figures A2.1 – A2.5) were acquired for each sample at 1.00 h time points during the 6.00 h reaction time. Note that for the 40K (Figure 2.7) sample both a solution color change from red to purple was observed over this time period, in addition to the formation of a distinct secondary assembled absorbance peak at 665 nm in the UV-vis analysis, thus it is discussed in detail. Prior to Arg addition, Figure 2.7a, no assembly of the materials is observed; however, after 1.00 h in the presence of Arg, small linear aggregates are noted, intermixed with individual Au nanoparticles, indicating that not all of the materials are assembled (Figure 2.7b). As the time progressed to 2.00 h in the presence of Arg, longer linear structures are observed, with a larger degree of branching as compared to the 1.00 h time point as shown in Figure 2.7c. Further analysis at 3.00 h, Figure 2.7d, displays the formation of larger aggregated structures where the development of a network arrangement of nanoparticles occurs. Linear regions of Au nanoparticles remain; however, it appears as if branching regions collide to form interconnects between the two chains. This growth process progresses for

69
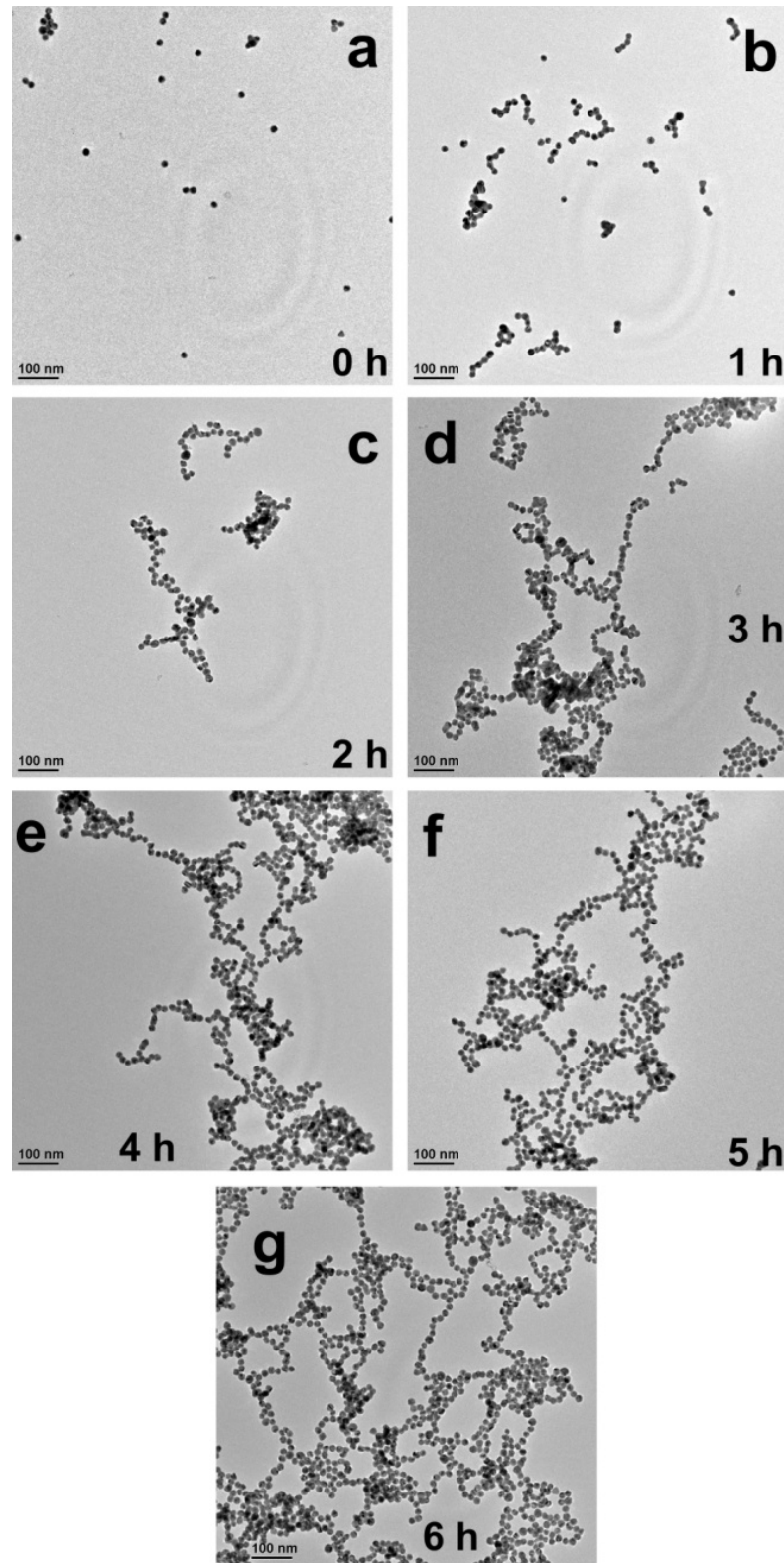
Figure 2.7 TEM analysis of the 40K Arg assembly process at time points of (a) 0.0 h, (b) 1.0 h, (c) 2.0 h, (d) 3.0 h, (e) 4.0 h, (f) 5.0 h, (g) 6.0 h.

the 4.00 h and 5.00 h time points, Figures 2.7e and f, respectively, where the networks continue to expand and become intermingled. Finally, at a time point of 6.00 h, Figure 2.7g, large extended networks of the branched, linearly arranged Au nanoparticles exist. The linear portions persist; however, these chains are branched and interconnected at distinct points to form a highly integrated network of linearly assembled Au nanoparticles. This imaging analysis appears to concur with the previous spectroscopic and scattering data suggesting a dynamic growth process occurring over time.

It is worth noting that we attempted to analyze these images to attain statistical information on the assemblies. We have already addressed the aggregate size in solution via DLS studies, which can be complicated by the aggregate architectures and solution index of refraction, but attaining information on the number of particles per chain can be difficult. While such results for the 40K sample at the shorter time points ($\leq$2.00 h) is possible, determining this value for the chained networks at longer times is challenging. For instance, at the 6.00 h time point of Figure 2.6g, neither a clear starting point nor a clear end point for the branched chain is able to be observed without a region from which the structure progresses. Indeed, certain parts of the chain do terminate throughout the structure; however, due to the bifurcated nature of the assembly, progression of the chain length can occur in other directions. As such, determining an exact number of nanoparticles per chain for such samples is complicated to impossible. As discussed below, the number of nanoparticles organized into linear chains versus other arrangements can be elucidated. This is used to isolate the effects of assembly conditions (*vide infra*). While other considerations such as shape and solvent effects do factor into the DLS analysis, these results are consistent with the changes in solution color, UV-vis

71

spectroscopic shifts, and the TEM-determined degree of assembly over time for all samples.

The observed nanoparticle assembly process, mediated by Arg in solution, is based upon the fundamental interactions between the nanoparticles and the amino acid molecules, which includes the binding strength of Arg to Au.[203] This oriented assembly is likely to be driven by the formation of a patchy, segregated mixed monolayer on the surface of the Au nanoparticles,[195,216] as presented in Scheme 2.1. This mixed surface is generated by incomplete ligand exchange of the initial negatively charged citrate surface passivant with the Arg. Based upon theoretical modeling, Arg binds to the surface of the Au nanoparticle via the guanidinium group of the side chain.[203] As a result, the zwitterionic head group is displayed to solution, which can drastically change the electronic nature of the nanoparticle surface. The pH value of the reaction is 7.02 after Arg addition; therefore, nearly all of the amino acid head groups are electronically neutral. Such changes to this layer are known to cause nanoparticle instability and lead to aggregation in solution by a minimization of the electrostatic repulsion between colloids.[153,195,216,217]

The formation of linear chains, rather than generation of a massive uncontrolled aggregate, is likely caused by the surface segregation of the two ligands on the nanoparticle. Such segregated patchy networks have previously been identified and studied using high resolution STM analysis of Au monolayer protected clusters.[218-221] In the present study, this segregation is driven by the electronic characteristics of the two surface ligands, citrate and Arg. It is known that zwitterionic species are able to form electrostatic networks when positioned in close proximity on three-dimensional

surfaces.[18,222-224] These regions are stabilized and promoted by the electrostatic network of interactions formed between the multiple cationic amines and anionic carboxylic acids placed in close proximity, thus resulting in Arg surface segregation on the Au nanoparticles. Discharging of the network, either by charge changes or shielding, can liberate the surface bound species;[18] however, under the present conditions, only the zwitterions are present. As such, the driving force to form this surface electrostatic network results in partitioning of the amino acids from the remaining citrate stabilizers, when a mixed monolayer is present, producing an anisotropic surface containing both neutral and negatively charged regions. As a result of this effect, an electronic dipole across the particle is generated, upon which the linear arrangement of these species can occur. In addition, branching is anticipated as multiple neutral regions are possible, thus resulting in a focal point for chain splitting from individual nanoparticles.

TEM evidence supports this dipole-based alignment mechanism through the specific interactions that occur between two nanoparticles of the linear chain. As shown in Figure 2.8, a linear network of Au nanoparticles is studied using the 40K system after 6.00 h. In the insert of a region of the nanoparticle superstructure, three Au nanoparticles are presented in which necking is observed between each of the three components. This necking process is initiated by the close proximity between the nanoparticles that is achieved by the dipole-based alignment over the electronically neutral regions of the nanoparticle surface. For this to occur, the distance between nanoparticles must be significantly minimized, which arises from a decrease in the electrostatic repulsion forces over these specific regions. These regions of low electrostatic repulsion are directly attributable to the patchy neutral regions of the amino acids on the nanoparticles.

73
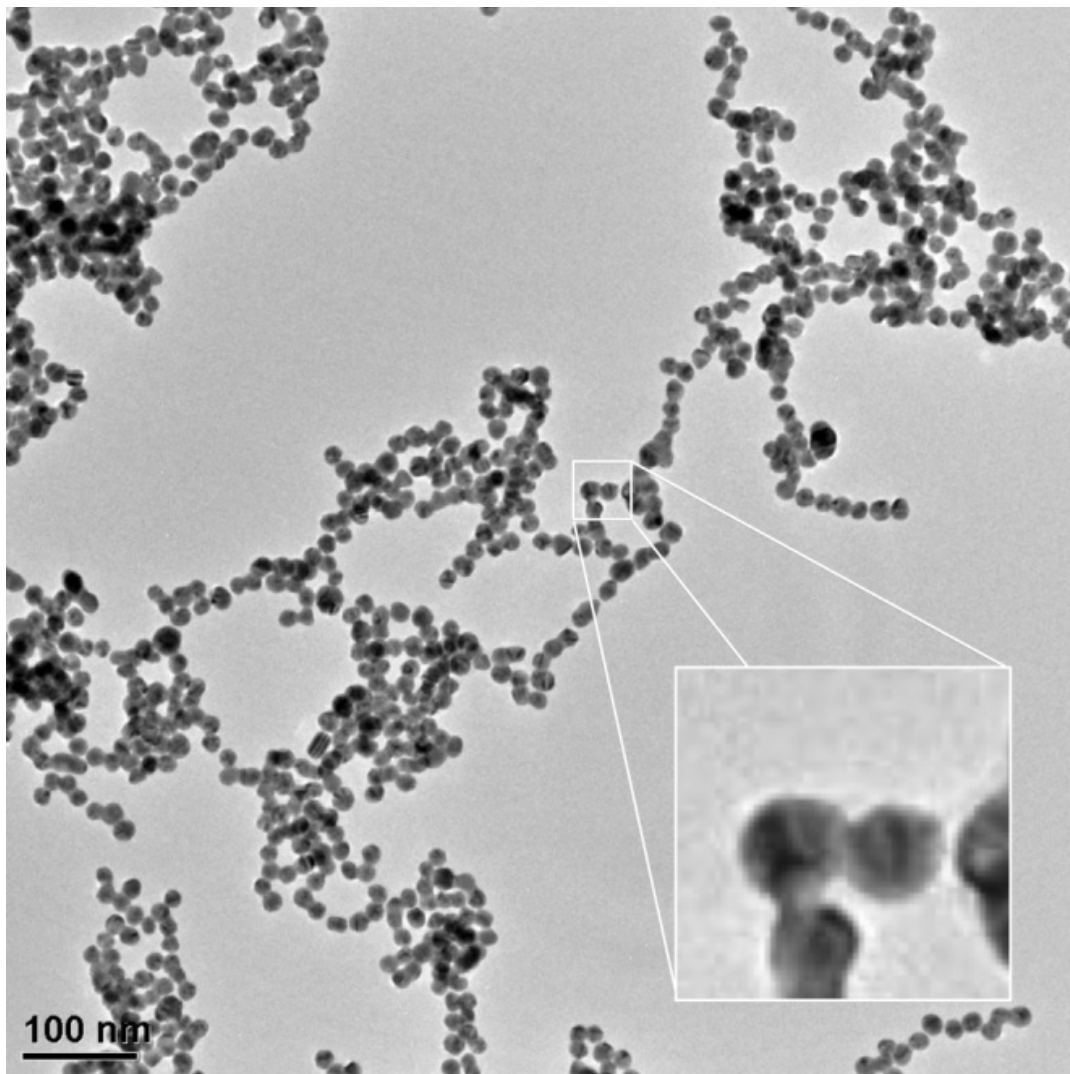
Figure 2.8 TEM image of the linear network of Au nanoparticles observed for the 40K sample at a time point of 6.00 h. The insert displays fused necks between three Au nanoparticles.

Furthermore, these fused nanoparticles suggest that the alignment occurs in solution to facilitate the necking process, as such actions are unlikely to proceed in the solid state.

Further evidence to support that the directed linear assembly occurs in solution, rather than from solvent evaporation during TEM sample preparation, arises from the UV-vis analysis. Prior to Arg addition, a single plasmon resonance is observed at 520 nm associated with the individual Au nanoparticles. As the ligand exchange process ensues to form the nanoparticle dipoles and subsequent linear chains, a new absorbance peak develops at 665 nm with an isosbestic point at 550 nm. Such a growth process is consistent with the fabrication of one-dimensional nanostructures in which a large degree of anisotropy arises from the linear chains.[18,153,214,225-228] As a result of this structure, interparticle plasmonic coupling can occur along the chain axis; however, the secondary transverse direction, which is maintained as the diameter of the Au nanoparticles, remains constant. Based on this arrangement, two plasmon resonance peaks would be expected arising from the two directions with the 520 nm peak associated with the transverse axis and the 665 nm peak arising from the longitudinal axis of the structures.[214,225] These results are similar to the absorbance spectrum of one dimensional plasmonic Au nanorods that possess a similar absorbance quality, observed both experimentally and theoretically.[18,214,225] Additionally, as the 520 nm peak is consistently positioned, this strongly suggests that growth of the particles occurs in a linear fashion rather than from all three dimensions. Such results are consistent with the end-to-end assembly of Au nanorods where the transverse plasmon peak remains constant and shifting of the longitudinal peak occurs based upon the assembly mechanism.[18,214,225] Taken together, the formation of a second absorbance band and the constant position of the 520 nm peak

indicate an in solution linear assembly process, whose results are consistent with the observed linear networks of Au nanoparticles.

An interesting result of this study indicated that the observed assembly process is directly controlled by the concentration of Arg in the solution. To that end, at low Arg concentrations of 40 µM (20K sample), the formation of short nanoparticle chains are observed after 6.00 h; however, when compared to the highest concentration of Arg employed in the 100K sample, 200 µM, rapid assembly is noted. This effect is attributed to the on-off equilibrium of the amino acid with the Au nanoparticle surface, which is a direct function of the Arg binding strength. At low Arg concentrations, the equilibrium is shifted towards ligand desorption and results in only small regions of the amino acid on the nanoparticle surface. As such, the assembly process is slow, thus leading to the minimal degree of assembly observed in the 20K sample. As the Arg concentrations increase to the levels used in the 100K sample, the on-off equilibrium is shifted towards surface adsorption, thus resulting in nanoparticles with a high Arg surface coverage, but with a very low surface charge. While this does indeed produce nanoparticle chains and superstructures at short time periods, as depicted in Figure 2.9a, bulk aggregation of these materials is noted after longer assembly times. This is due to the fact that the highly branched structures possess very little electrostatic repulsions between nanoparticles, which are required for stability,[217] thus generating necks between multiple nanoparticles. As this process ensues, small aggregate regions are observed after 3.0 h, Figure 2.9b, that eventually the organization mechanism continues over time to form large bulk aggregates as shown in Figure 2.9c. These undesirable bulk materials eventually precipitate, which can be avoided by selection of lower Arg concentration. While this effect allows for
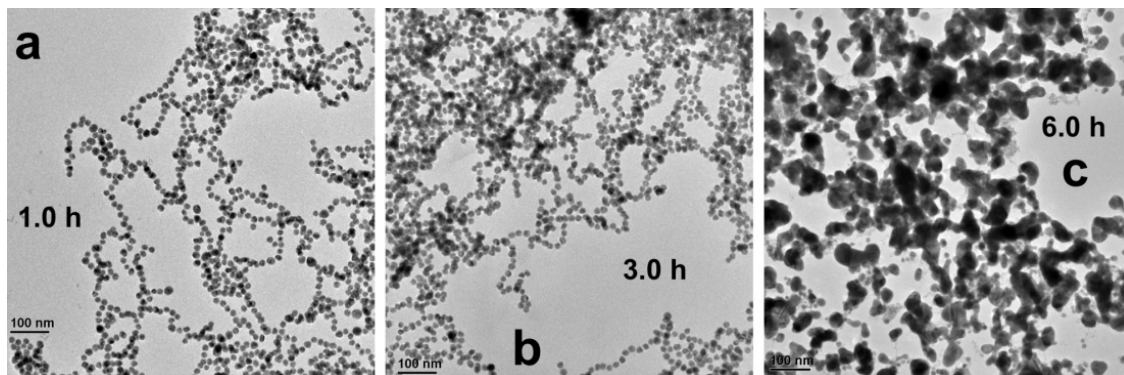
Figure 2.9 TEM micrographs of the 100K sample after (a) 1.0 h, (b) 3.0 h, and (c) 6.0 h. The degree of bulk formation increases as the reaction time progresses.

control of the final assembled network, its direct relationship with the side chain binding strength may be exploited for further comparisons between other amino acids for experimental determination of their intrinsic binding abilities with nanomaterials surfaces.

In order to further probe and validate the mechanism, Arg-based Au nanoparticle assembly process was monitored at different reaction temperatures between 10.0 °C and 70.0 °C using UV-vis spectroscopy. For this analysis, the system temperature was maintained employing a recirculating water bath, which minimized thermal fluctuations. As shown in Figure 2.10b, when the analysis was conducted at 30.0 °C, similar results were obtained as shown above. The UV-vis spectra of the reactions with different Arg concentrations are presented on the left, while a plot of the absorbance intensity at 665 nm as a function of time is shown on the right. When no Arg is added to the system, a single plasmon band from the independent Au nanoparticles is observed at 520 nm, which is consistent with particles of approximately 15 nm in diameter.[209] As the concentration of Arg in the reaction increases, the growth of a second peak at 665 nm is observed, which is associated with the formation of the linear, branched superstructures using Arg.[48]

Figure 2.10a displays the same analysis of Arg effects on Au nanoparticle assembly; however, the reaction temperature was lowered to 10.0 °C. At this temperature, a noticeable shift in the assembly rate was observed for all of the Arg concentrations studied. For the 40K samples and those at lower Arg concentration, no change was observed over the reaction time in the UV-vis spectra of the materials; no growth at 665 nm was demonstrated, which suggested that the materials remained unassembled at this
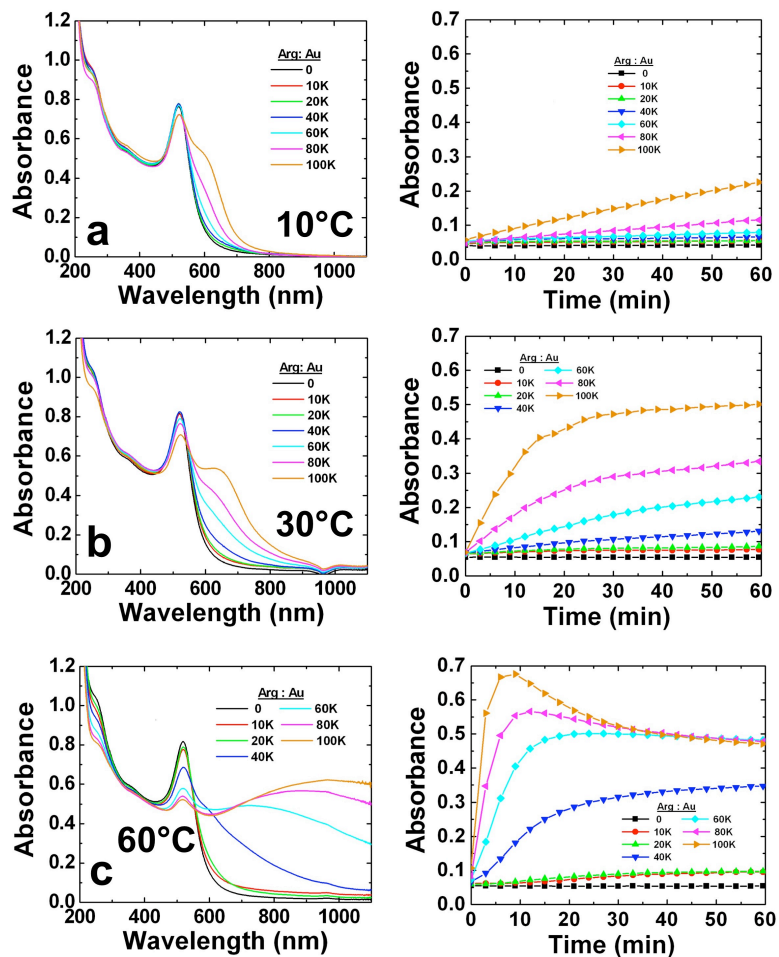
Figure 2.10 UV-vis analysis of the temperature effects on the Arg concentration dependent assembly of Au nanoparticles studied at (a) 10.0 °C, (b) 30.0 °C, and (c) 60.0 °C. The plots on the left demonstrate the UV-vis spectra obtained after 1.00 h of reaction for each Arg:Au nanoparticle ratio studied, while the plots on the right present the absorbance intensity of the 665 nm peak as a function of time.

temperature. It was not until the 60K sample that an observable shift in the optical properties of the Au nanoparticle was demonstrated. With this sample, a slight increase in the absorbance at 665 nm was observed, with no clear peak formation. A nearly identical result was observed for the 80K sample, as compared to the 60K sample; however, the absorbance intensity was greater over the specified time frame. The only sample at 10.0 °C that produced a semi-resolved peak shoulder at 665 nm was the 100K sample, where the growth of the assembled band did not reach saturation over the time of the analysis. For the 100K sample, while peak growth was evident, it resulted in only a linear absorbance growth over time that reached a final intensity that was significantly reduced as compared to the same analysis conducted at 30.0 °C.UV-vis studies of the reaction at a system temperature of 60.0 °C is presented in Figure 2.10c. For these reactions, a dramatic increase in the assembly rate is apparent as compared to the studies at the lower temperatures. No change is observed in the control study of Au nanoparticles in the absence of Arg, which indicates that the materials are stable at the elevated temperature. A noticeable increase in the absorbance was detected for both the 10K and 20K samples, above the background of the Au nanoparticles, at 665 nm, which suggests that some degree of assembly may be occurring for these materials at the higher temperature. As the concentration of Arg increased, a larger degree of assembly is demonstrated. For the 40K sample, the absorbance at 665 nm increases over time, to which the rate of the absorbance growth slows considerably after 25.0 min; however, an increase persists after this time point at a slower rate. For the 60K sample, saturation of the 665 nm peak intensity occurs at 15.0 min and the absorbance is maintained for the duration of the experiment. As the concentration of the amino acid is further increased to the 80K and

100K samples, the absorbance growth rate is initially rapid for the first 10.0 min; however, after this time point, the intensity begins to decrease. This effect is likely due to changes in the spectra that are observed and shown in the plot to the left due to the formation and precipitation of bulk materials. At 1.0 h, the 80K and 100K samples demonstrate broad absorbances that are red shifted in proportion to the Arg concentration: the higher the Arg concentration, the further to the red the peak is shifted. This suggests that larger chains and/or bulk-like materials develop as the reaction progresses, which may result from the increased rate of assembly. It is known that at higher Arg concentrations, bulk materials are prepared due to the extensive coverage of Arg on the nanoparticle surface, which minimizes the electrostatic stability of the materials in solution. Similar results are likely to occur at shorter time frames at lower Arg: Au nanoparticle ratios if the rate of assembly is increased at the higher temperatures. This would be observed with a decrease in the intensity of the 665 nm absorbance due to peak shifting and materials precipitation. Indeed, such results are observed as shown in Figure 2.10c.

TEM analysis of the materials at the different Arg concentrations as a function of reaction temperature is presented in Figure 2.11. Specifically, Figure 2.11b displays the results at 30.0 °C for the 0, 20K, 40K, and 80K samples. These Arg:Au nanoparticle ratios were chosen to demonstrate the results over a range of conditions to fully observe the effects of both Arg concentration and temperature. For the 0 control sample, only independent Au nanoparticles were observed on the TEM grid surface as anticipated. This conforms directly to the UV-vis results, which indicated that the nanoparticles remained independent as the 520 nm plasmon band remained unchanged. For the 20K
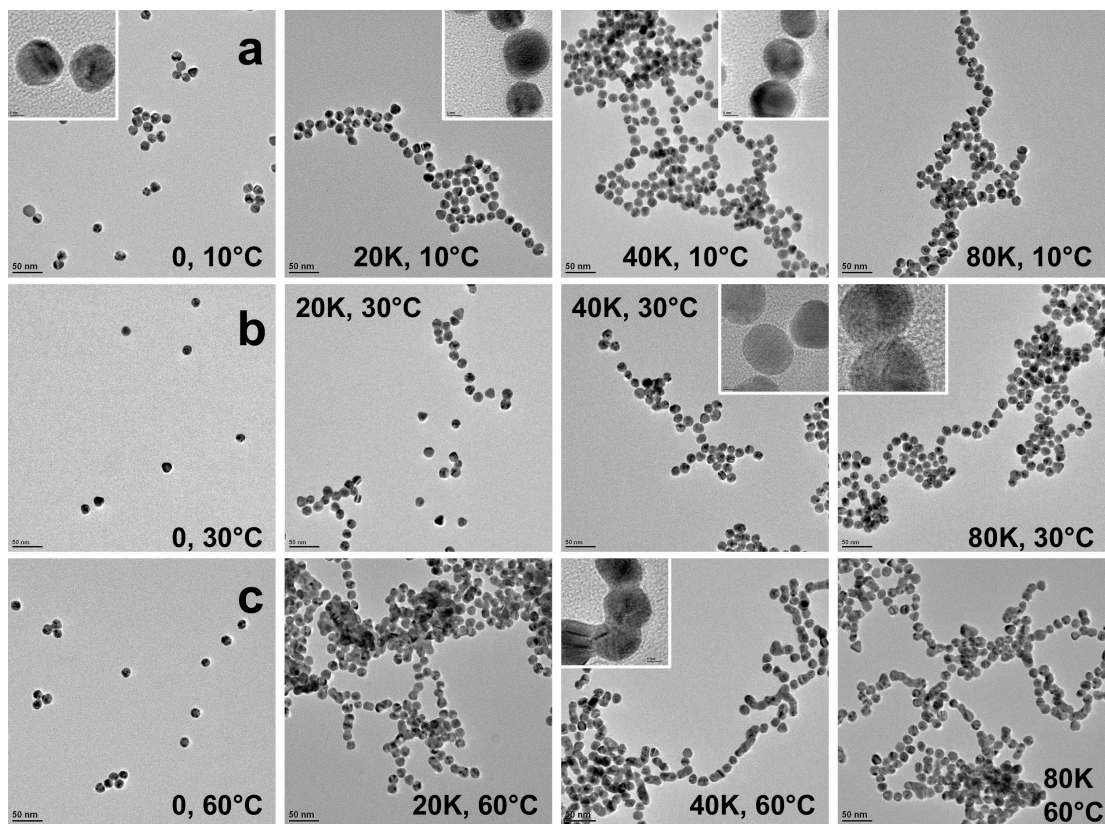
Figure 2.11 TEM analysis of the temperature effects on the assembly process employing Arg:Au nanoparticle ratios of 0, 20K, 40K, and 80K studied at (a) 10.0 °C, (b) 30.0 °C, and (c) 60.0 °C. TEM images were obtained after a reaction time of 1.00 h.

sample, two different sets of materials were observed: individual as well as short linear chains of Au nanoparticles. As the Arg:Au nanoparticle ratio increased in the 40K sample, a larger set of linear chains are observed with a degree of branching. Furthermore, as shown in the insert of the 40K sample, in the nanoparticle linear chained structures, while the materials are assembled in a controlled fashion, minimal to no necking is observed between the particles. For the 80K sample, larger linear structures are observed. In these samples, a high degree of branching is noted, as well as a degree of nanoparticle aggregation, which is demonstrated in the insert. The necking between particles occurs when two species are assembled in solution and the degree of repulsion at the assembled region is significantly minimized to allow for mixing of the metallic components. This is likely a function of the surface electronic dipole as an effect of the Arg display. Over time, as this process ensues, bulk materials precipitation would be anticipated. Indeed, a dark black precipitate is observed after allowing the reaction to proceed over night.

Figure 2.11a presents the TEM analysis of the materials studied at 10.0 °C. Consistent with the UV-vis results, no assembly was observed in the 0 control sample; however, at higher Arg: Au nanoparticle ratios, linear assembly was observed. For instance, in the 20K sample, linear chains were noted on the TEM grid surface. Furthermore, such effects were also observed at for the 40K and 80K samples with higher degrees of linear assembly and branching. These assembly results are similar to those observed for the same samples at 30.0 °C; however, they are inconsistent with the UV-vis results, which indicated a lack of assembly at low ratios with minimal degrees of assembly at the highest ratios. The observed TEM effects are likely due to TEM sample

preparation. For this, 5.00 μL of the reaction sample at 10.0 °C is pipetted onto the TEM grid surface and the solution is allowed to evaporate overnight in a desiccator in the refrigerator at 4.00 °C. While the temperature is maintained, due to the evaporation process, the particle concentration drastically increases over time, which causes the particles to come closer together. As a result, the particles could assemble during the evaporation process, thus resulting in the observed chain formation. Similar evaporation effects have previously been observed for Au nanorods, where the sample preparation process resulted in the formation of organized structures.[229] While the TEM results are unanticipated, DLS studies, discussed below, confirm minimal to no assembly for the nanoparticles in solution at 10.0 °C, which is consistent with the UV-vis analysis.

TEM examination of the assembly process of a temperature of 60.0 °C is displayed in Figure 2.11c. For these materials, a higher degree of bulk aggregation is observed, as compared to those samples studied at lower temperatures. From this analysis, the control again demonstrated independent Au nanoparticles in the absence of Arg. For the 20K sample, a large degree of assembly and some aggregation is observed to form Au agglomerates. The larger structures likely arise from the rapid assembly process, which could lead to the observed aggregation. For the 40K sample, linear branched Au nanoparticle chains are observed, with a significant degree of neck formation between the aligned particles. The HR-TEM insert demonstrates the formation of four interconnected particles that are linearly aligned with a significant degree of agglomerization between the species. The mixing of the metallic components of the particles is likely due to the surface electronic dipole and individual nanoparticle spacings that are maximized for neck formation at the elevated temperatures, as discussed above.

Similar effects are observed with the 80K sample where linear necked structures are observed with additional bulk like aggregates.

In addition to temperature effects, changes to the solvent dielectric are likely to alter the ability to assemble the Au nanoparticles in the presence of Arg. By lowering the dielectric of the solvent, the degree of charge shielding of the electronic dipole along the nanoparticle surface should be minimized, which would increase the rate of assembly; therefore, it is anticipated that the solvent dielectric and the rate of assembly should be inversely proportional. To study this factor, the Au nanoparticle surface exchange process was monitored for the 0, 20K, 40K, and 80K samples where 0.00, 0.50, 1.00, and 1.50 mL of the aqueous solvent was replaced with EtOH at 20.0 °C. As such, the dielectric of the solvent system should decrease for those samples that possess a higher volume of EtOH. The effects of lowering the solvent dielectric on the assembly and optical properties of the materials are shown in Figure 2.12. Specifically, the control analysis in the absence of Arg using the various volumes of EtOH is presented in Figure 2.12a. For these materials, no changes in the UV-vis spectra over 1.00 h are observed using the solvents of different dielectrics. This result is important as it indicates that the materials are stable in the various solutions and demonstrates that the EtOH does not induce the aggregation, linear or otherwise, of the materials, thus any changes observed for those reactions containing Arg in the presence of EtOH can be directly attributed to the effects of the amino acid.

Figure 2.11b displays the effects of decreasing the solvent dielectric for the 20K sample. For this analysis, as shown in the plot on the left, minimal to no changes in the UV-vis spectra of the 20K materials after 1.00 h in a solvent of pure water or with
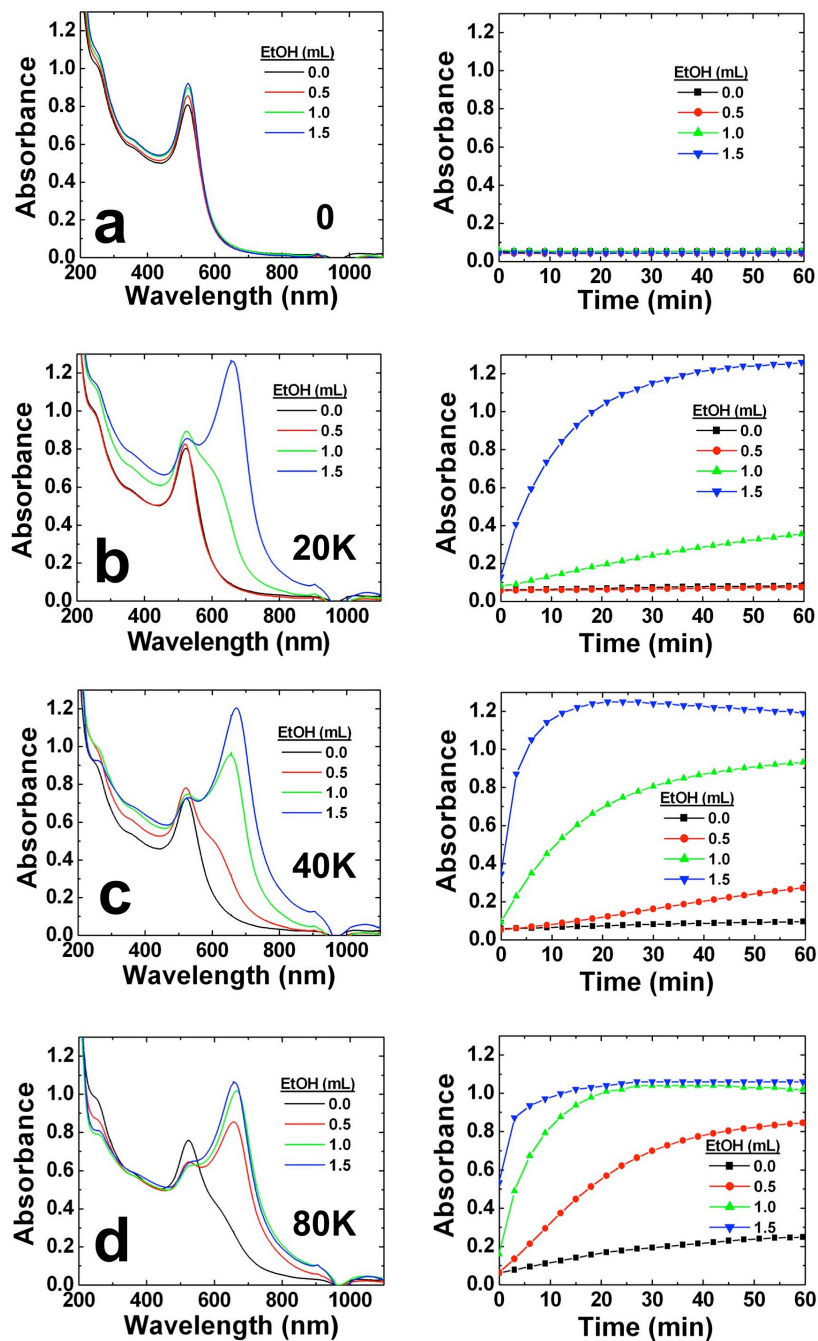
Figure 2.12 UV-vis analysis of the effects of the amount of EtOH added to the reaction system for the assembly of Au nanoparticles using the (a) 0, (b) 20K, (c) 40K, and (d) 80K samples. The plots on the left demonstrate the UV-vis spectra obtained after 1.00 h of reaction for each volume of EtOH studied, while the plots on the right present the absorbance intensity of the 665 nm peak as a function of time.

0.50 mL of EtOH are observed; only a single plasmon band at 520 nm is detected, which suggests that no assembly occurs from these reactions. When 1.00 mL of water is replaced with EtOH in the reaction, formation of the 665 nm assembled peak is observed for the 20K sample within the reaction time frame. For this analysis, the absorbance increases linearly over 1.00 h and results in the generation of an absorbance shoulder at the higher wavelength when the reaction is complete. Furthermore, when the amount of EtOH used in the reaction is increased to 1.50 mL, the rate of assembly is even faster. Under these conditions, a clear and sharp plasmon band is observed at 665 nm after 1.00 h that rapidly grows during the analysis. The peak continues to grow for approximately 30.0 min, after which it begins to saturate, indicating that the assembly process is nearly complete.

Further studies for the effect of solvent dielectric for the 40K and 80K sample demonstrated nearly identical results as compared to the 20K sample, only faster assembly rates of spectroscopic change were noted for the higher ratio analyses. As shown in Figure 2.12c, for the 40K studies, minimal assembly was observed from the water-only control sample; however, when 0.50 mL of EtOH was used in the reaction, a new peak shoulder was observed to grow over the time frame of the reaction. The shoulder intensity at 665 nm grew linearly throughout the reaction at a slower rate as compared to the reactions that possessed 1.00 and 1.50 mL of EtOH. For these reactions, the 665 nm absorbance grew rapidly in intensity and demonstrated distinct plasmon bands after 1.00 h (shown in the left panel of the figure). Again, the rate of assembly was directly related to the amount of EtOH in the solution; as the EtOH volume increased, the rate of assembly increased. For instance, with the reaction containing only 1.00 mL of

EtOH, 665 nm peak growth occurred linearly for the first 30.0 min of the reaction, but trailed off at a slower rate after this time point; however, for the reaction possessing 1.50 mL of EtOH, rapid linear peak growth occurred for the first 15.0 min and then was saturated at longer times points. Nearly identical results are achieved for the 80K sample, Figure 2.12d, with various concentrations of Arg, but the main difference was a faster rate of assembly as compared to those samples with lower Arg:Au nanoparticle ratios. Additionally, minor assembly was observed for the 80K reaction in the water only solution, consistent with the above described results, and a strong 665 nm absorbance was observed for all reactions completed in the presence of EtOH. The rate of assembly was again inversely proportional to the solvent dielectric, which decreases with higher EtOH concentrations, consistent with the 20K and 40K studies.

The combination of temperature and solvent dielectric effects for the assembly of Au nanoparticles for all of the Arg: Au nanoparticle ratios was further studied and is presented in Figure 2.13 for the results obtained using 1.00 mL of EtOH. The studies employing 0.500 mL and 1.50 mL of EtOH follow an identical trend with respect to temperature and are presented in the Appendix I, Figures A2.8 and A2.10. For the studies at 10.0 °C (Figure 2.13a), it is evident that the rate of Arg-mediated assembly in the presence of 1.00 mL of EtOH is increased as compared to the reactions studied using a water-only solvent (Figure 2.10a). With the addition of 1.00 mL of EtOH, all reactions at Arg: Au nanoparticle ratios ≥ 10K demonstrate a degree of nanoparticle assembly at10.0 °C. Even for the lowest ratio, 10K, an increase in the absorbance at 665 nm is observed that increases linearly during the reaction as compared to the 0 control. Again, the rate of absorbance growth follows a linear trend for the materials as a function of Arg
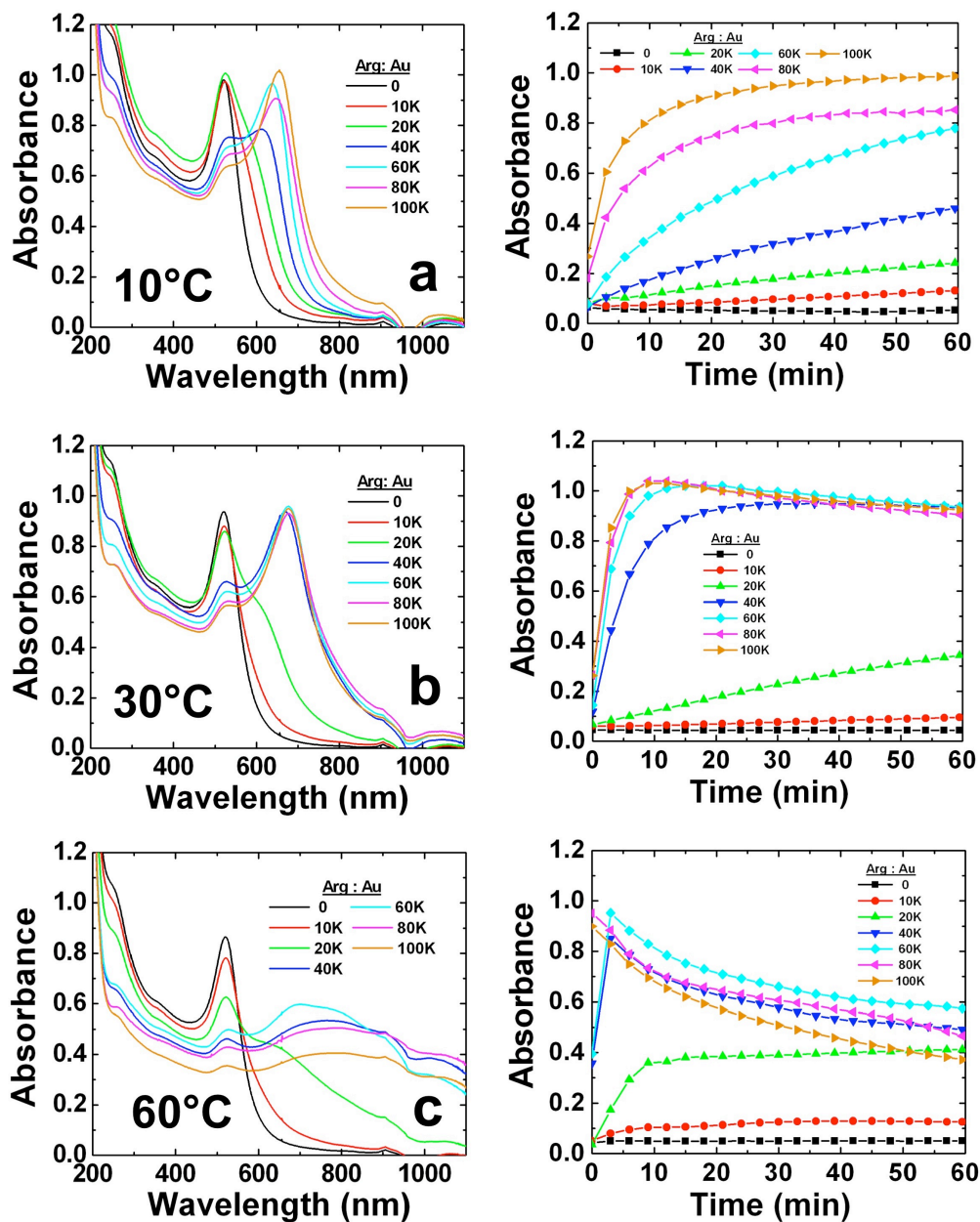
Figure 2.13 UV-vis analysis of the temperature effects on the Arg concentration dependent assembly of Au nanoparticles in the presence of 1.00 mL of EtOH studied at (a) 10.0 °C, (b) 30.0 °C, and (c) 60.0 °C. The plots on the left demonstrate the UV-vis spectra obtained after 1.00 h of reaction for each Arg:Au nanoparticle ratio studied, while the plots on the right present the absorbance intensity of the 665 nm peak as a function of time.

concentration to prepare the assembled structures. Furthermore, at the 1.00 h time point, sharp plasmon bands are observed for the materials at ratios $\geq$ 40K (left panel), which further indicate the rapid rate of assembly. Note that for the materials studied at the same temperature in the water-only solvent demonstrated minimal to no assembly and that even at the highest ratio, 100K, only a slight peak shoulder was observed.

The rates of assembly are further increased for the reactions at higher temperatures employing the solvent that contains 1.00 mL of EtOH. For the reactions studied at 30.0 °C (Figure 2.13b), assembly is observed for all samples that possess Arg and the rate of assembly increases for reactions with higher amino acid concentrations. For instance, for the 20K sample, an absorbance shoulder develops during the 1.00 h reaction time frame from which the intensity increases linearly. For all of the other samples with ratios $\geq$ 40K, the rate of assembly is rapid, which, after a certain time period, saturates at roughly the same absorbance value. In fact, at the end of the 1.00 h reaction time, all samples with ratios $\geq$ 40K demonstrate very similar UV-vis spectra with nearly identical 665 nm absorbance peaks, which suggests that the assembly rate is significantly increased for these samples, with minimal to no formation of bulk materials. For the reactions processed at 60.0 °C, presented in Figure 2.13c, the reaction rate is extremely fast and generates UV-vis spectra for the samples at ratios $\geq$ 20K that demonstrate broad red shifted spectra, indicative of large superstructures and/or bulk material formation. In fact, the reaction rate is so fast that the materials in the 80K and 100K samples are completely aggregated before their first UV-vis spectrum can be obtained, which is evident by the high absorbance value at 665 nm at the initial time point. Together, the observed UV-vis results suggest that the solvent dielectric can

significantly alter the rate of assembly such that as the dielectric decreases, the rate of Arg-based Au nanoparticle assembly increases.

TEM analysis of the 0, 20K, 40K, and 80K materials reacted for 1.00 h at 10.0 °C, 30.0 °C, and 60.0 °C in the presence of 1.00 mL of EtOH are displayed in Figure 2.14. For all of the materials, regardless of the reaction conditions, those systems processed in the absence of Arg produced independent Au nanoparticles only. Figure 2.14a specifically presents the TEM images of the materials studied at 10.0 °C. For the samples where Arg was present, branched linear chains are observed for all reactions. For the most part, nearly all of the nanoparticles tend to form linear chains regardless of the ratios; however, for the 20K sample, individual Au nanoparticles not aligned in chains are occasionally observed. For the materials studied at 30.0 °C (Figure 2.14b), a higher degree of nanoparticle assembly is noted as compared to the materials processed using the same Arg: Au nanoparticle ratio at 10.0 °C. For these materials, however, while most of the nanoparticles in the assembled state remained unagglomerated, meaning lacking neck formation between multiple particles, a degree of larger bulk-like aggregates were observed for the 80K reaction. When the analysis was studied at a temperature of 60.0 °C, shown in Figure 2.14c, branched linear chains were again observed, but a higher degree of nanoparticle necking and agglomeration was noted. For all samples, many of the nanoparticles demonstrated mixing of the metal atoms between particles to form the long linear structures, which were likely produced based upon the initial nanoparticle linear chain formation. This is again caused by the increased assembly rate and changes to the dipole shielding, which rapidly positions the nanoparticles in sufficiently close contact to allow for direct agglomerization between the materials.

91
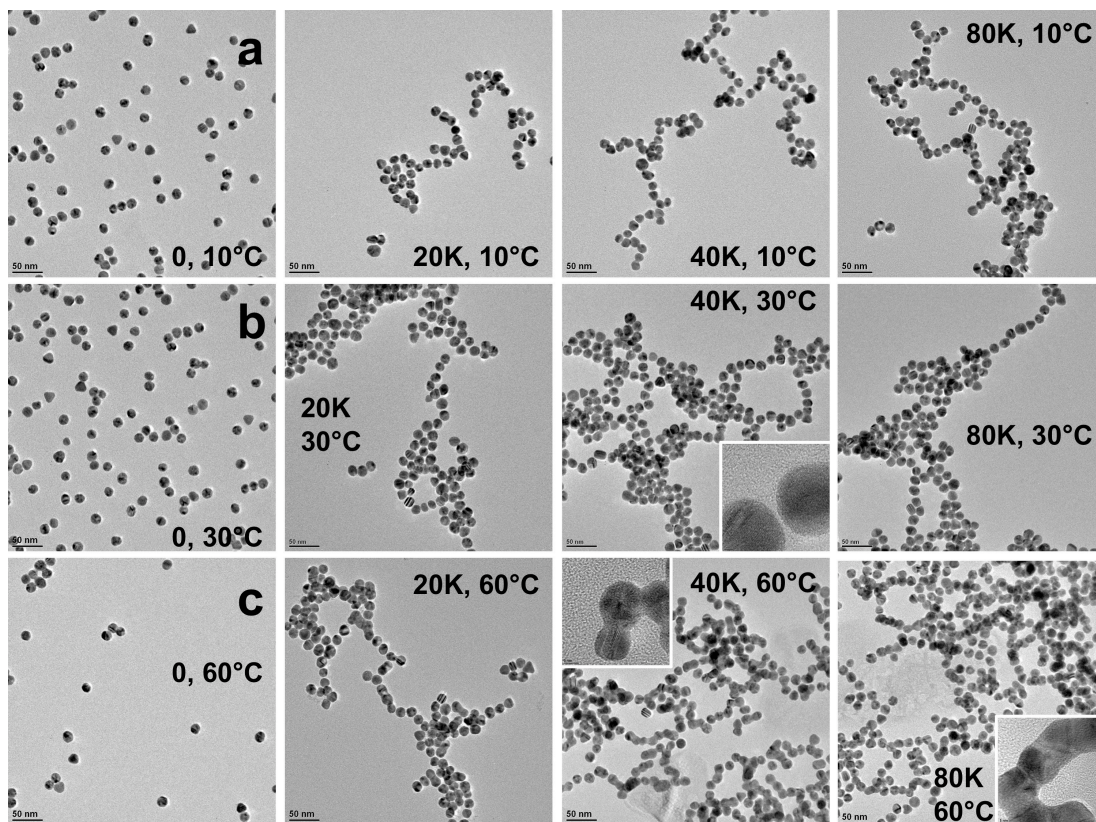
Figure 2.14 TEM analysis of the temperature effects on the assembly process in the presence of 1.00 mL of EtOH with Arg:Au nanoparticle ratios of 0, 20K, 40K, and 80K studied at (a) 10.0 °C, (b) 30.0 °C, and (c) 60.0 °C. TEM images were obtained after a reaction time of 1.00 h.

While the UV-vis and TEM results suggest that the Au nanoparticles are assembling in response to the effects of the Arg addition, DLS studies were conducted to confirm the aggregation state in solution. The overall analysis is plotted in Figure 2.15 for the 0, 20K, 40K, and 80K samples at 10.0 °C, 30.0 °C, and 60.0 °C with 0.00 mL to 1.50 mL of EtOH. Individual plots of the DLS studies at all reaction conditions are additionally presented in the Appendix I, Figures A2.11 – A2.13. Figure 2.15a specifically displays the results obtained at 10.0 °C. When considering the reactions processed using an aqueous-only solvent, the materials in the absence of Arg displayed a particle size of 17.5 nm, which is consistent with the 15.0 nm particle size observed via TEM. As the concentration of Arg increased, a small increase in the observed size occurred over the 1.00 h time point, with a maximum aggregate size of 31.5 nm for the 80K sample. This confirms that a small of degree assembly of the materials happens in solution at 10.0 °C, as is consistent with the UV-vis results. When the same reaction conditions were used with 0.50 mL EtOH, an increase in the aggregate dimensions was observed as compared to the results achieved for the water-only solvent. For instance, for the 20K, 40K, and 80K samples, aggregate sizes of 53.4 nm, 62.1 nm, and 103 nm, were noted at 1.00 h, respectively, as compared to the sizes of 22.5 nm, 26.1 nm, and 31.5 nm achieved in the water-based system. Both trends of increasing aggregate sizes for increasing Arg: Au nanoparticle ratios, as well as increasing sizes for solvents of lower dielectric constants (higher volumes of EtOH) was conserved for all samples across the analysis. As anticipated, based upon these trends, the 80K sample with 1.50 mL of EtOH produced the largest aggregate size of 2,438 nm at 10.0 °C.
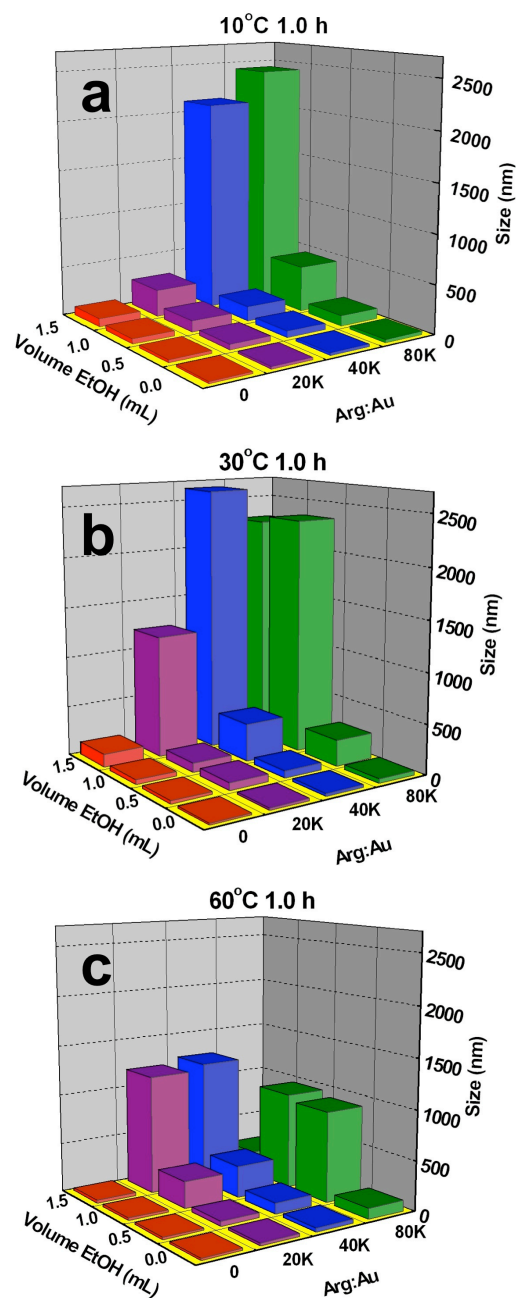
Figure 2.15 DLS-based determination of aggregate size in solution after 1.00 h. The three-dimensional graphs are plotted as functions of the Arg:Au nanoparticle ratio, volume of EtOH employed in the system, and the size of the aggregates achieved at temperatures of (a) 10.0 °C, (b) 30.0 °C, and (c) 60.0 °C.

DLS analysis of the Arg/Au nanoparticle system at a temperature of 30.0 °C is presented in Figure 2.15b, which displays similar sizing trends as compared to those observed at 10.0 °C. For materials studied under identical conditions of Arg:Au nanoparticle ratio and solvent composition, larger aggregate sizes were observed for the reactions processed at the higher temperature. For instance, for the 80K materials in an aqueous only solvent, an aggregate size of 45.6 nm was detected, as compared to the value of 31.5 nm achieved at 10.0 °C. Furthermore, the trends previously determined for the effects of Arg concentration and solvent dielectric were maintained; however, the size of the aggregate after 1.00 h for the 80K sample using 1.50 mL of EtOH (2283 nm) does not fit this trend as it is clearly smaller in size as compared to the 80K sample with 1.00 mL of EtOH (2348 nm) or the 40K sample with 1.50 mL of EtOH (2630 nm). This change from the anticipated trend is likely due to the formation of excessively large structures that precipitate from solution, thus leaving only smaller assembled materials dispersed in solution. Indeed, as shown in the Appendix I, Figure A2.12, the 80K sample in 1.50 mL EtOH shows an increasing aggregate size over time that maximizes to 3,035 nm at 40.0 min, after which the size decreases to 2,283 nm at 1.00 h. In addition, a black precipitate is also noted from this sample after 1.00 h. Further studies of the same set of materials at 60.0 °C (Figure 2.15c) demonstrates identical trends; however, a larger degree of materials assembly/aggregation followed by precipitation is observed. For this temperature, the reactions processed at 80K using 1.00 mL and 1.50 mL of EtOH and at 60K studied with 1.50 mL of EtOH showed precipitation due to the rapid assembly process, which resulted in the observed deviations from the expected sizes; the other

samples that were examined demonstrated anticipated aggregate sizes as dictated by the hypothesized trends.

From the results obtained, a few key trends can be elucidated that can assist in understanding the Au nanoparticle assembly process occurring in solution as a result of amino acid surface exchange. First, the rate of assembly is dependent upon the Arg:Au nanoparticle ratio such that as the concentration of the amino acid increases, a more rapid assembly process is observed to produce larger superstructures. Second, the temperature of the reaction system affects the process in such a way that as the temperature increases, the formation of branched linear structures occurs faster. Third, as the dielectric constant of the solvent employed in the reactions decreases, the rate of the assembly of the nanoparticles increases. Fourth, by combining the effects of temperature and solvent composition, the rates of assembly can be further maximized (i.e. by raising the temperature and lowering the solvent dielectric). Taken together, these results suggest that the second step of the amino acid-based assembly process presented in Scheme 2.1, which is mediated by Brownian motion, controls the overall mechanism and may be able to be manipulated by the reaction conditions to dictate the rate of assembly and aggregate size.

The initial temperature-based studies change the assembly process specifically by increasing the Brownian motion of the nanoparticles dispersed in solution. To that end, as the temperature increases, the velocity and tumbling of the particles increases as well.[230] As a result, the nanoparticles can more readily orient themselves, with respect to the electronic dipole of neighboring materials, and form the interactions responsible for nanoparticle alignment. In addition, by lowering the temperature, the Brownian motion of

the materials should significantly decrease,[230] thus the materials assembly process should be minimized or prevented, especially when approaching the freezing point of the solvent system. The observed results correspond to this theory, thus suggesting that the reaction temperature is directly affecting the second step of the process. A second possible temperature effect could alter the first step of the process, which could change the ability of the amino acids on the surface to segregate and form the charged network/electronic dipole required for assembly. In this event, at elevated temperatures, sufficient thermal energy would be available to overcome the thermodynamic stability of the electrostatic network between the amino acid residues, thus causing a scrambling of the surface patterns to form a mixed surface monolayer, which would disrupt the formation of the electronic dipole required for assembly. Previous results have demonstrated this effect for the electronic-based assembly and disassembly of nanomaterials.[231] Under this hypothesis, the assembly process should decrease at higher temperatures; however, this is the exact opposite of the observed trend, which suggests that the temperature effects do not alter the ability to form the surface segregated layer and electronic dipole. Furthermore, this also suggests that the electrostatic interactions of the amino acid residues to form this type of electronic network are relatively strong.

The effects of changing the solvent dielectric also is likely to change the ability of the nanoparticles to assemble at the second step by changing the shielding of the electronic dipole. By adding increasing volumes of EtOH, the dielectric constant of the solvent will decrease. As a result, the shielding of the charged patchy surface of the nanoparticles will decrease, which will enhance the electrostatic interactions between the individual particles in solution.[217] By increasing these interactions, the species will orient

quicker in a fashion that minimizes electrostatic repulsions, which is anticipated to occur through the assembly of the materials across the electronic dipole. This event has been directly observed by the studies presented using EtOH, thus suggesting that the Brownian motion and electronic character of the surface of the materials dictate the assembly rate. Furthermore, the combination of both temperature variations and solvent composition can be used to control the assembly process without interfering with each other. This suggests that by judiciously selecting the appropriate reaction conditions, a direct method to achieve nanoparticle chains of certain dimensions may be possible.

2.5. Summary and Conclusions

In summary, the ability to assemble Au nanoparticles into anisotropic linear assemblies through the specific interactions of the simple amino acid Arg has been demonstrated. In this model, Arg is able to displace the citrate surface passivant of 15 nm Au nanoparticles, producing a segregated ligand surface arrangement. As a result, a patchy charged surface on the Au nanoparticle is achieved, which induces the formation of an electronic dipole across the overall nanoparticle structure. From this dipole, linear assembly of the materials can occur to generate large branched superstructures of the materials in solution. The assembly process is dependent upon the concentration of the amino acid in solution, thus yielding larger assembly rates for higher solution concentrations. These effects are due to two intrinsic factors associated with the ligand/nanoparticle interactions: the actual binding strength of the amino acid and their subsequent arrangement on the nanoparticle surface.

These results may represent a way to experimentally compare biomolecular surface binding events using nanomaterials in solution where exploitation of the inherent

materials properties can occur, rather than by approximations employing two-dimensional surfaces or theoretical calculations. Such a fundamental level of understanding is desirable, as biomolecules are becoming increasingly important vehicles for the fabrication of functional nanomaterials. By a comparison of the nanoparticle assembly rates and their final architectures produced, direct information of the binding process from a variety of biomolecules ranging from simple amino acids to complex protein structures may be achievable. Additionally, the amino acid-based capping and assembly of Au nanoparticles has been extensively probed to elucidate the mechanism by which the formation of branched linear superstructures is achieved.

Understanding this event is important as determining how the individual surface and electronic structure of the materials affects their function is critical for the incorporation of such organization methods into *in situ* device fabrication or for use as sensitive assays or detection methods. At present, very little information is readily known about biomolecular interactions with dispersed, three-dimensional nanomaterials in solution due to instrumental limitations; therefore, new methods must be developed to monitor this process. These methods, such as the present technique, must be extensively characterized and validated to fully understand the mechanism at play and to comprehend the generated data to ensure correct results. Furthermore, the assembly ability of the materials in a linear fashion is also attractive for use as approaches to produce controlled arrangements of nanomaterials for electronic applications. As such, determining the method of assembly and developing techniques to control the process could prove to be highly important. From the results of the present study, it is indicated that the first step of the process, which incorporates Arg surface binding and self-segregation, is relatively

rapid and not easily perturbed; however, the second step of Brownian motion-based assembly can be directly manipulated by the reaction conditions. Changing of the reaction temperature or electronic shielding capability of the solvent can directly alter the rate of assembly, from which the size and orientation of the final prepared structure may be able to be manipulated. These results were confirmed via the optical (UV-vis) and scattering (DLS) properties of the Au nanoparticles, which is an additional attractive component as such characteristics can also be manipulated based upon the assembly of the materials.

This Chapter has been reproduced with permission from the following publication: copyright ACS publications

Sethi, M.; Knecht, M.R. Experimental Studies on the Interactions between Au Nanoparticles and Amino Acids: Bio-Based Formation of Branched Linear Structures, *ACS Appl. Mater. Interfaces* **2009**, *1*, 1270-1278.

Sethi, M.; Knecht, M.R. Understanding the Mechanism of Amino Acid-Based Au Nanoparticle Chain Formation, *Langmuir*, **2010**, *26*, 9860-9874.

Chapter 3: Employing Materials Assembly to Elucidate Surface Interactions of Amino Acids with Au Nanoparticles

3.1. Overview of Study

Biomolecule-directed growth and assembly of nanomaterials utilizes highly specific interactions to provide the exciting prospect of producing a new generation of precisely arranged, stimuli responsive, and reconfigurable nanoarrayed structures for a wide range of applications from catalysis to energy storage. With an objective to create a much needed fundamental understanding of the complex biotic/abiotic interfacial interactions, this chapter presents a systematic study of surface interactions of a series of amino acides with Au nanoparticles. We have employed our designed self-assembly-based method that monitors changes in the optical properties and aggregate size of Au nanoparticles in response to their binding with selected amino acid residues. These observations were used to derive information on the binding strength and ligand surface arrangement, where our experimental results follow previously derived computational trends in the surface affinities of the residues, thus suggesting that our approach can be used to assess the binding abilities and interligand interactions of biomacromolecules on nanomaterial surfaces.

3.2. Introduction

Biomolecule directed assembly of nanostructures provides new aproaches towards the synthesis and application of nanomaterials under ambient conditions.[65] In addition, the assembled nanoaggregates can be tailored to be reconfigurable to modulate a specific function and be responsive to an external stimulus using materials directing peptides isolated through biocombinatorial methods.[65] Using peptides,

nanostructures of various compositions have been fabricated including noble metals,[98,103,116,134,232-234] metal sulfides,[148,185,187] and metal oxides,[188-191] where the sequences bind to inorganic surfaces to control the growth and stability of the materials in solution. In addition, these materials have demonstrated functionalities for catalysis,[116,134,148,232,234] chemical and biological sensing,[235] energy storage,[184,188,233] and complex materials assembly.[236-238] Recent experimental and computational studies have demonstrated that peptides are able to bind inorganic materials in specific arrangements, which may control the functionality of the resulting structure.[127,128,132,134,145-147,168,192-194,239] Unfortunately, minimal information is known about how peptides and bio-ligands interact with the particle and other bound species, which could attenuate the functionality. To optimize the desired activity, the composition, structure, and interactions of the peptides in the ligand shell must be rationally designed and fully characterized.

A logical place to begin to understand peptide binding of nanomaterials is at the level of amino acids. Recent theoretical studies have been used to calculate amino acid binding energies for Au surfaces that demonstrate varied degrees of surface binding based upon the side chain.[145,192] Specifically, Hoefling *et al.* calculated the interaction free energy for all twenty standard amino acids with a Au(111) surface, which displayed a binding trend of aromatic > sulfur > positive > polar > aliphatic ~ negative.[145] Interestingly, the aromatic residues presented the strongest affinities over thiol-terminated cysteine (Cys); however, similar results have also been observed in peptide computational studies.[146] While amino acids possess binding affinities that

vary based upon the side chains, when collected into peptides, it is likely that cooperative and multidentate binding could occur to control the surface affinity.[146,147]

We have demonstrated as in the previous chapter that the amino acid arginine (Arg) can drive the linear assembly of citrate-capped Au nanoparticles.[48,240] This process is suggested to arise from a partial ligand displacement reaction, resulting in the segregation of Arg from the remaining citrate. Such a surface could arise from incomplete ligand exchange, leading to the formation of a patchy charged surface, as previously observed for other systems.[195,196,200] Ligand segregation is anticipated to be driven by the formation of an electrostatic network among the zwitterionic headgroups of the amino acids.[172,202,240] From this, a dipole would form across the nanoparticles that directs their assembly into linear superstructures. This process likely occurs in two steps after dipole formation: Au nanoparticle dimers are initially generated, after which the superstructures result from dimer oligomerization.[240] Based upon this mechanism and the affinities of amino acids for Au, it is reasonable that similar results could occur with other residues. Furthermore, the amino acid concentration for assembly would likely be dependent upon the binding strength, thus it may be possible to adapt this approach as a method to monitor ligand binding and structure on nanomaterial surfaces.

Here we present evidence that the assembly process is sensitive to the amino acid structure and can be used to extract important information concerning the biotic/abiotic interface. For this study, the stability and degree of aggregation for citrate-capped Au nanoparticles was monitored in the presence of four different amino acids: Cys, Arg, histidine (His), and alanine (Ala). These residues were chosen as

they span the affinity values for Au.[145] The formation of nanoparticle aggregates was resolved using time and temperature-based UV-vis spectroscopy, kinetic analysis of the assembly process, transmission electron microscopy (TEM), dynamic light scattering (DLS), and surface plasmon resonance (SPR) analysis. From these studies, it can be inferred that the assembly process is dependent upon partial ligand substitution *and* the individual binding strength of the residues. As such, the concentration at which the nanoparticle assembly is observed is inversely proportional to the surface affinities of the selected residues. This suggests that the binding capability of the ligands is dependent upon the amino acid structure, composition, and side chain functionality.

3.3. Methods

3.3.1. Chemicals

$HAuCl_4 \cdot 3H_2O$, sodium citrate tribasic dihydrate, L-arginine, L-histidine, and L-alanine were purchased from Sigma-Aldrich (St. Louis, MO). L-cysteine was purchased from SAFC (Lenexa, KS). All chemicals were used as received. Milli-Q water (18 MΩ cm; Millipore, Bedford, MA) was used throughout.

3.3.2. Preparation of Citrate-Capped Au Nanoparticles

Au nanoparticles were prepared by the citrate reduction method.[13] Before the reaction, all glassware was washed using aqua regia (3 HCl : 1 HNO_3) and then rinsed with deionized water. For the reaction, a 50.0 mL aqueous solution of 1.00 mM $HAuCl_4$ was refluxed while stirring. Once solution refluxing was achieved, 5.00 mL of an aqueous 38.8 mM sodium citrate solution was added. Immediately, the solution color changed from yellow to colorless. The reaction was refluxed for 15.0 min and a final

solution color of wine red was achieved. After the reaction, the solution was allowed to cool to room temperature prior using. Before each analysis, the Au nanoparticle samples were centrifuged at 5000 rpm for 2.00 min from which the supernatant was studied.

3.3.3. Reaction of citrate-capped Au nanoparticles and amino acids

Citrate-capped Au nanoparticles were prepared as previously described.[48,209,240] Aqueous stock solutions of Cys, His, and Ala were prepared at a concentration of 16.0 mM, while the Arg stock was prepared at a concentration of 50.0 mM. To a 1.00 cm pathlength quartz cuvette, 600 μL of the citrate-capped Au nanoparticles were added with various volumes of the amino acids to result in final concentrations of 0, 8, 20, 80, 200, 400, 2000, and 4000 μM for Cys, His, and Ala, which represented an amino acid:Au nanoparticle ratio of 0-, 4.00×10^3-, 1.00×10^4-, 4.00×10^4-, 1.00×10^5-, 2.00×10^5-, 1.00×10^6 and 2.00×10^6, respectively. To assist in identifying these samples, we have designated them as 0, 4K, 10K, 40K, 100K, 200K, 1000K, and 2000K, respectively, where 4K = 4,000, etc. For Arg, different amino acid concentrations were used due to differences in the assembly conditions: 0, 80, 200, 400, 800, 2000, 8000, and 16000 μM for Arg:Au nanoparticle ratios of 0, 4.00×10^4, 1.00×10^5, 2.00×10^5, 4.00×10^5, 1.00×10^6 and 4.00×10^6, 8.00×10^6, respectively. These samples are designated as 0, 40K, 100K, 200K, 400K, 1000K, 4000K, and 8000K, respectively. The final volume of the reaction was 3.00 mL, which was achieved by the addition of excess water as needed. The reaction proceeded for 6.00 h while being monitored using UV-vis spectroscopy at various temperatures.

3.3.4. Characterization

Employing 1.00 cm pathlength quartz cuvettes (Starna), time and temperature-resolved UV-vis spectra were obtained using an Agilent 8453 spectrometer. All spectra were background subtracted against water. The temperature of the UV-vis system was controlled by using an Isotemp 3016S recirculating chiller. TEM images of the assembly process were obtained using a JEOL 2010F electron microscope operating at 200 keV with a point-to-point resolution of 0.19 nm. To prepare the sample, a volume of 5.00 μL of the reaction solution was added onto the surface of a 400 mesh Cu grid coated in a thin layer of carbon (EM Sciences). The sample was taken from the solution phase prior to any precipitation of the reaction. The sample was allowed to dry in a desiccator overnight. DLS analyses were conducted on a Zetasizer Nano ZS System (Malvern Inc.) using their proprietary GP algorithm at selected time intervals from which the maximum intensity peak was used as a qualitative measure of the assembly size over time. For surface plasmon resonance, a home built SPR system employing Kretchman geometry was used. This set up allows for monitoring phase changes at the SPR coupling angle, which provides a major gain in the sensitivity as described previously.[241]

3.4. Results and Disscusion

To study aggregation-based changes, the plasmon band at 520 nm for 15 nm Au nanoparticles is exploited to monitor the binding and assembly of the materials in solution. Assembly of the nanoparticles at room temperature is demonstrated in Figure 3.1 using Arg. Consistent with the studies of Chapter 2,[48,240] the formation of linear chains was observed at Arg:Au nanoparticle ratios between 10K and 200K. This is noted in the UV-vis analysis by a decrease in the plasmon band intensity at

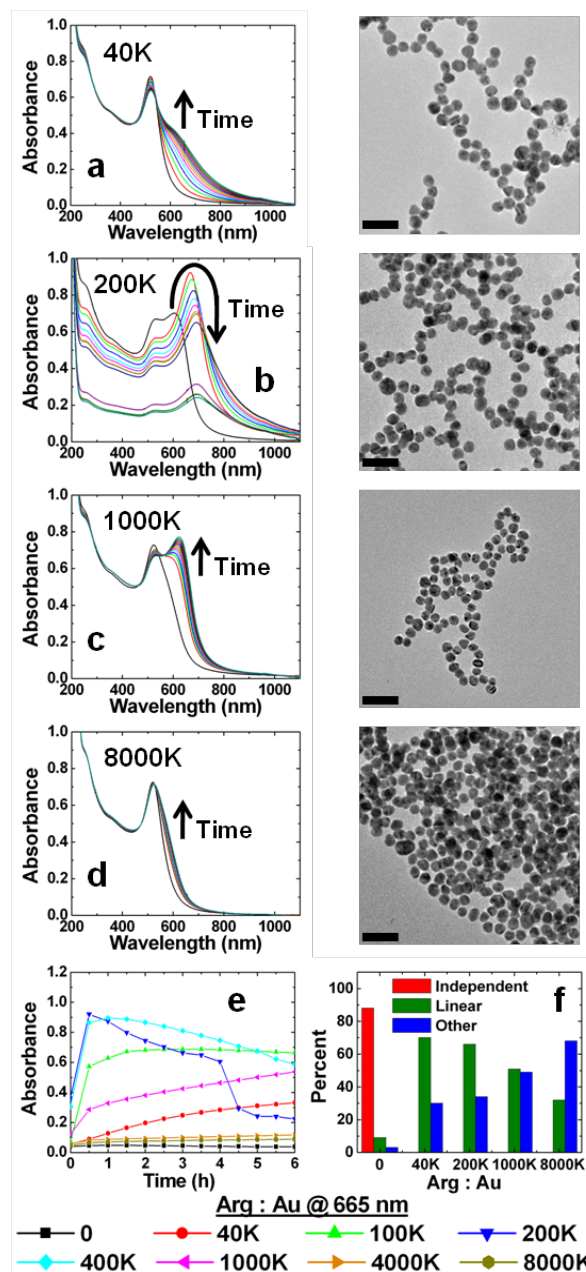**Figure 3.1 UV-vis and TEM analysis of the Arg-based assembly of Au nanoparticles at room temperature using Arg:Au nanoparticle ratios of (a) 40K, (b) 200K, (c) 1000K, and (d) 8000K (scale bar = 50 nm). Part (e) presents the absorbance intensity at 665 nm (legend below Figure for clarity), while part (f) presents a statistical analysis of the assembly state of the Au nanoparticles, as observed via TEM.**

520 nm, concurrent with the growth of a new absorbance at 665 nm. As shown in Figure 3.1a, when an Arg:Au nanoparticle ratio of 40K is employed, a peak shoulder is observed at 665 nm that grows in intensity over 6.00 h. TEM analysis of these materials at reaction completion demonstrates the formation of linear chains of nanoparticles. As the ratio is increased, the rate of 665 nm peak growth increased as well. Figure 3.1b demonstrates this effect using a ratio of 200K. Here, a rapid growth of the 665 nm peak occurs within 30.0 min, after which a red shifting and decrease in intensity is observed for the new peak. This is consistent with previous results that indicated that the 665 nm peak arises from Au nanoparticle dimers that then oligomerize to form Au nanoparticle chains, resulting in the red shift.[240] Surprisingly, when the Arg:Au nanoparticle ratio was further increased, the assembly rate decreased. As shown in Figure 3.1c for a ratio of 1000K, the formation of the 665 nm peak does occur; however, no red shift is evident. At higher ratios (Figure 3.1d), only minimal changes to the absorbance spectrum of the Au nanoparticles are observed, suggesting that little to no assembly occurred.

Figure 3.1e presents the absorbance intensity of the 665 nm peak for all Arg:Au nanoparticle ratios studied over the course of the assembly process. In the absence of Arg, no change in the intensity at 665 nm is observed; however, at 40K a steady increase is noted. The rate of this intensity growth continues to increase for the 100K sample, which reaches a maximum intensity that remains constant after 2.00 h. At a ratio of 200K, the 665 nm growth is very rapid, followed by a decrease due to the red shift. For this sample, a dramatic drop in the intensity is observed at 4.50 h due to precipitation of the materials. At subsequently higher ratios, the rate of the growth in

intensity at 665 nm decreases until a ratio of 4000K and higher, where minimal to no changes are observed.

TEM analysis of the materials at the different Arg:Au nanoparticle ratios is also presented in Figure 3.1. For these images, the solution sample was dried on the surface of a TEM grid, where increases in concentration and shear forces will be present.[240,242] Such effects can manipulate particle deposition on the grid surface, thus analysis of the TEM images to ascertain the number of particles in specific arrangements is used to determine the type of assembly in solution. Consistent with previous reports, at ratios between 40K and 200K, predominantly branched linear chains of nanoparticles are observed. Statistical analysis of multiple TEM images for each sample is shown in Figure 3.1f that classified the nanoparticles as either independent, linearly assembled, or other. From the analysis of ≥ 100 nanoparticles per sample, the 40K and 200K materials were preferentially linearly aligned; however, a shift towards random aggregate formation was observed at higher ratios when no assembly was indicated from UV-vis. This effect at the highest ratios is likely due to a combination of two factors: minimized electrostatic repulsion between the particles and TEM sample preparation that increases the nanoparticle concentration during drying. At high Arg:Au nanoparticle ratios, more Arg is likely to be on the surface, thus lowering the electrostatic repulsion between particles. As a result, the particles can come closer together during the drying process, which results in the formation of non-linear and random arrangements of materials on the TEM grid.

These results further help to resolve the effects of Arg on Au nanoparticle surfaces. At low ratios, partial displacement of the citrate most likely occurs, which is anticipated to be followed by the segregation of the two ligands. Arg is able to form an electrostatic network among the zwitterionic head group moieties that drives the segregation process,[48,172,240] resulting in the formation of an electric dipole across the Au nanoparticles. These neutral Arg patches are likely to be stochastically positioned on the nanoparticle surface, where the patch size directly correlates to the amino acid concentration used in the reaction. Once the dipole is generated, the materials can align in solution to give rise to linear aggregates. These assemblies are likely controlled by the magnitude of the dipole, the solution conditions, and the amount of nanoparticles in solution where higher Au nanoparticle concentrations facilitate the formation of larger structures. Furthermore, additional forces are likely important in maintaining the assembly state. For instance, entanglement of the surface interface between the two nanoparticles is likely to contribute to and help maintain the linearly assembled structures. Should this entanglement be minimal, the two nanoparticles could disengage to disrupt the assembled structure. Above a critical threshold, the amount of Arg bound to the surface has displaced a sufficient number of citrate ligands, thus lowering the intensity of the dipole, until complete surface coverage by the amino acid. At this point, minimal to no assembly is anticipated, as observed with the 8000K sample by UV-vis and DLS analysis (discussed below).

To determine if the assembly process can be used to compare ligand binding, additional amino acids were selected. Cys is a unique residue due to the terminal thiol moiety of the side chain. Hoefling *et al.* have computationally demonstrated that Cys

has a higher affinity for the Au surface than Arg;[145] therefore, the Cys:Au nanoparticle ratio required for assembly should be lower than Arg. Indeed, such results are presented in Figure 3.2 where Au nanoparticle assembly was evident at room temperature at a ratio of 4K. At this value, a rising absorbance is observed that is centered around 600 nm. This absorbance is slightly lower than that observed using Arg; however, the dielectrics at the surface of the nanoparticle are likely altered with the different amino acid ligands and the aggregated structure. The rate of assembly is maintained until a ratio of 10K, but above this point, the rate decreases. This is apparent in the time resolved graphs of Figures 3.2b-d, which presents the data for Cys:Au nanoparticle ratios of 40K, 100K, and 2000K, respectively.

Note that the rate of Cys-based assembly is lower than that for Arg, which is likely due to the mode of assembly, as discussed below. Additionally, the absorbance increase at 600 nm over time is shown in Figure 3.2e. Here, the most rapid assembly is observed from the 4K and 10K samples that levels off in intensity growth at ~3.00 h. After this time, little to no growth in the absorbance is observed. Furthermore, the maximum absorbance at 600 nm is observed with the 10K sample, while higher ratios demonstrate decreasing saturation intensities. This is consistent with the minimal to no assembly at higher ratios observed with Arg and suggests that the Au nanoparticle surface must be partially coated with the amino acid for assembly.

TEM analysis of the Cys-based system demonstrates different structures as compared to Arg. At all ratios, non-linear and randomly oriented Au nanoparticle aggregates were observed. This was surprising and is suggestive that dipole-based assembly is not employed using Cys. Based upon the TEM images for the 4K, 40K,

111
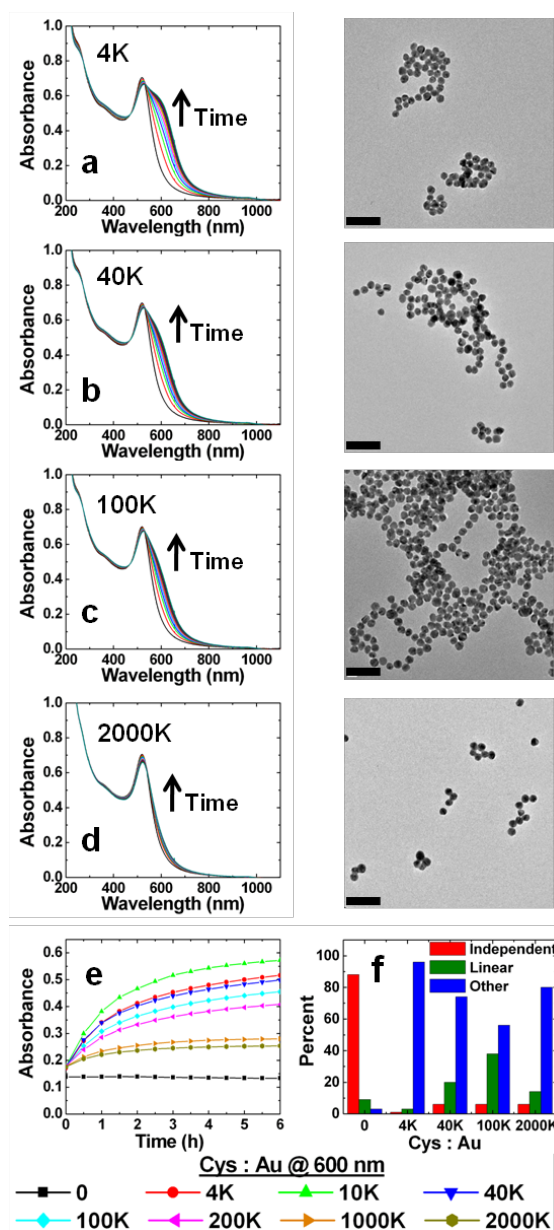
Figure 3.2 UV-vis and TEM analysis of the Cys-based assembly of Au nanoparticles at room temperature using Cys:Au nanoparticle ratios of (a) 4K, (b) 40K, (c) 100K, and (d) 2000K (scale bar = 50 nm). Part (e) presents the absorbance intensity at 600 nm (legend below Figure for clarity), while part (f) presents a statistical analysis of the assembly state of the Au nanoparticles, as observed via TEM.

100K, and 2000K samples, only a small fraction of the nanoparticles was arranged linearly, while the vast majority were randomly oriented (Figure 3.2f). DLS studies, discussed below, indeed demonstrate the formation of nanoparticle assemblies in solution where changes in the plasmon band are observed.

To further analyze the effects of amino acid structure, residues with weaker Au affinities (His and Ala) were studied. The analysis for His at room temperature is shown in the Appendix II, Figure A3.3, with the absorbance intensity plot presented in Figure 3.3a. For the His analysis, no assembly was evident at His:Au nanoparticle ratios <40K; however, for the 40K sample, a minor increase at 600 nm was noted. The rate of 600 nm growth increased until the 200K sample; however, above this ratio, a slower growth process was observed until minimal changes for the 2000K sample. TEM analysis of these materials also demonstrates the formation of randomized aggregates in solution in the presence of independent and linearly assembled particles (Appendix II, Figure A3.5). When the analysis was conducted using Ala at room temperature, no significant changes were noted in the UV-vis spectrum of the materials over the reaction time frame, regardless of the amino acid concentration. Figure 3.3b presents the 600 nm intensity plot for the Ala analysis, which displays a lack of notable absorbance increases. Furthermore, TEM analysis of materials (Appendix II, Figure A3.6) demonstrated independent Au nanoparticles for all samples, which was identical to the amino acid free control, thus suggesting that Ala was not able to bind the nanoparticle surface.

To compare the UV-vis changes as a function of the amino acid:Au nanoparticle ratio, Figure 3.4 plots the scattering-corrected absorbance intensities of
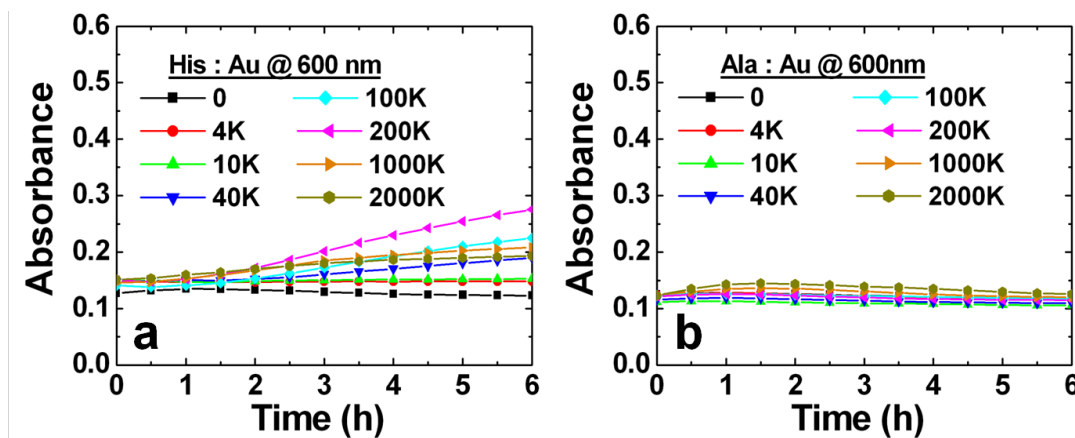
Figure 3.3 UV-vis intensity analysis at 600 nm for the room temperature assembly process employing (a) His and (b) Ala.
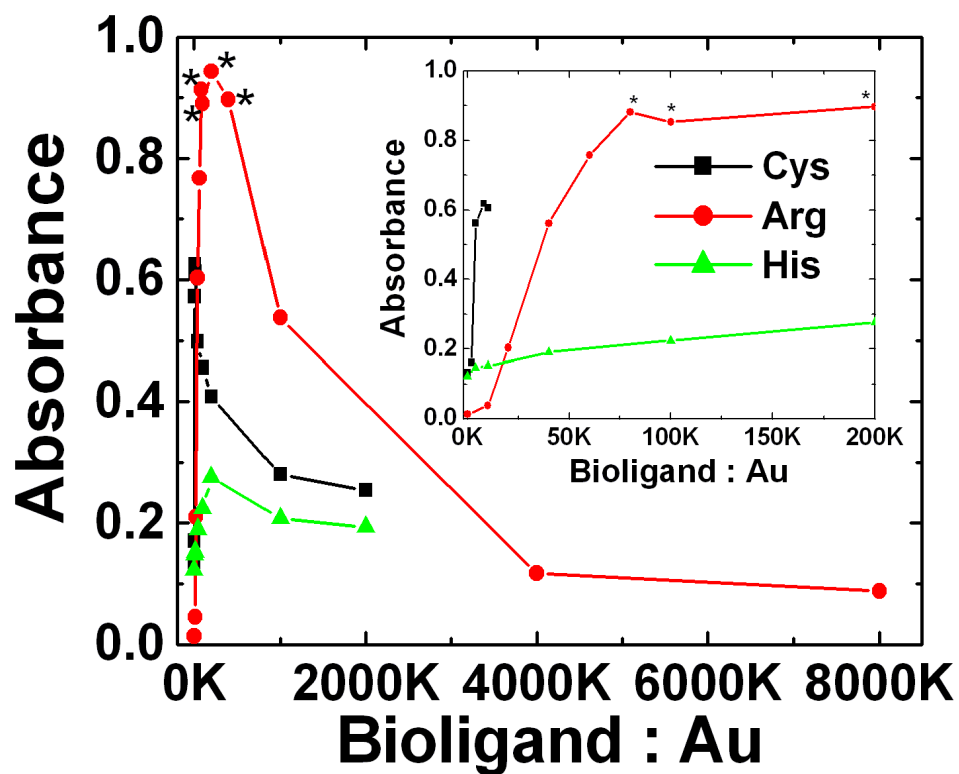
Figure 3.4 Comparison of the scatter-corrected, absorbance intensity of the formation of nanoparticle aggregates as a function of the amino acid:Au nanoparticle ratio at 6.00 h at room temperature. For the Cys and His samples, monitoring of the 600 nm peak is presented, while the intensity of the 665 nm peak for Arg samples is used. The insert presents the effects at low ratios where maximum assembly is reached. For Arg, the starred points were achieved at shorter time periods immediately prior to precipitation.

the Au nanoparticle aggregates at 600 nm for Cys and His, and 665 nm for Arg after 6.00 h. Due to precipitation in the 80K, 100K, 200K and 400K Arg samples at t < 6.00 h, the maximum absorbance prior to precipitation is presented, which represents the maximum degree of assembly in solution. Here, as the ratio increases, all of the systems demonstrate an increase in intensity; however, above a critical value, a decrease in the aggregated absorbance is observed. As anticipated, the ratio with the greatest absorbance intensity is observed to shift based upon the amino acid. The insert of Figure 3.4 presents an expanded analysis of the region of maximum assembly. For Arg, the maximum intensity for the aggregates was observed at 100K, while for the Cys, the ratios shifted to between 4K and 10K. This represents an ~10× decrease in the residue concentration for assembly. When considering His, the ratio for maximum assembly shifted to 200K, which is higher than both Arg and Cys. Note that while the shifts are present, the absolute intensity of the absorbance at these values differs. This is due to the size of the aggregates, which is controlled by the individual amino acid assembly as confirmed by DLS below. Overall, the shifts correspond well to the theoretically predicted Au affinities of the amino acids.[145]

DLS analysis, presented in Figure 3.5 for the reactions at room temperature (with the particle size distribution diagrams displayed in the Appendix II, Figures A3.8 – A3.11), was used to determine the degree of nanoparticle size and the degree of aggregation. This technique is performed in solution, thus avoiding the complications of TEM sample preparation; however, the reported values represent a qualitative analysis of the aggregation process. DLS is dependent upon the shape, size, dispersity, and hydrodynamic radius of the materials, all of which are unable to
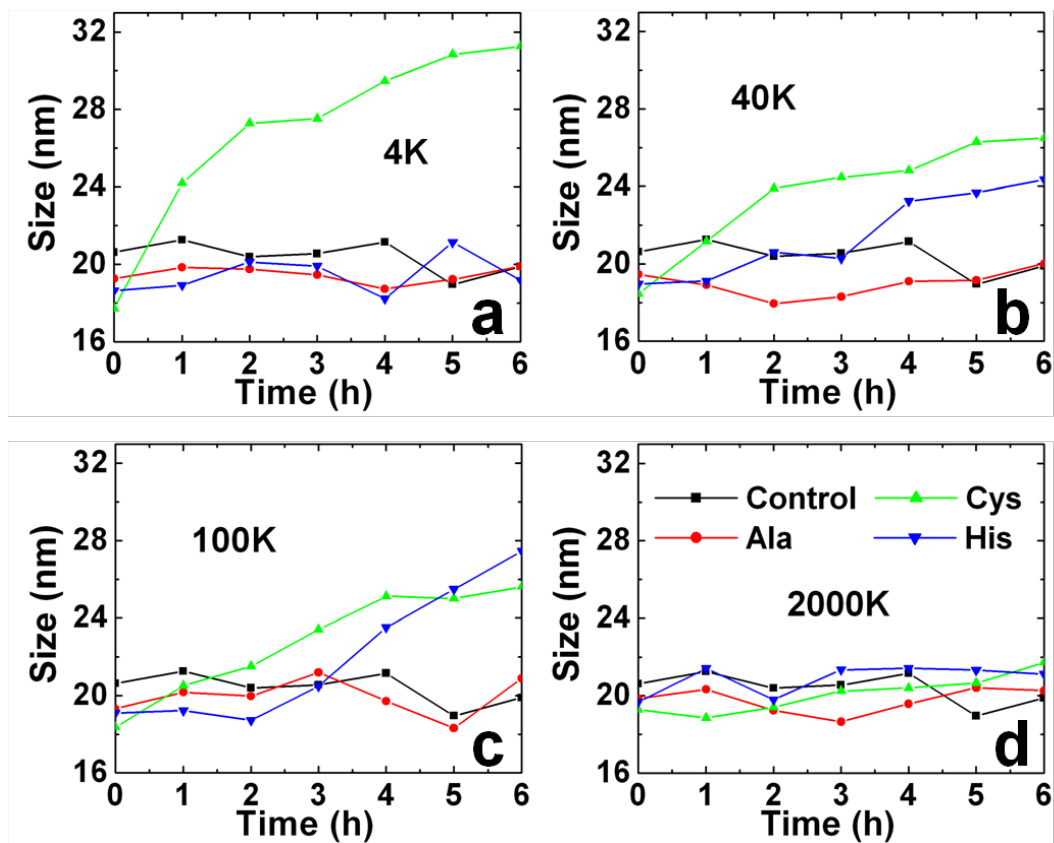
116

Figure 3.5 DLS analysis of the Au nanoparticle aggregate hydrodynamic size at room temperature in the absence of amino acids and in the presence of Cys, His, and Ala at amino acid:Au nanoparticle ratios of (a) 4K, (b) 40K, (c) 100K, and (d) 2000K.

be accurately measured for the present system. As a result, DLS can be used to compare the degree of aggregation between the samples, rather than as a quantitative analysis of aggregate size; however, such a study is important to confirm the assembly.Figure 3.5a presents the analysis for Ala, Cys, and His at a ratio of 4K where the values represent the maximum intensity peak. The DLS analysis for Arg, which results in larger aggregate sizes, is reported in Chapter 2 (Figure 2.4). and is presented in the Appendix II, Figure A3.7. The maximum peak intensity was used due to the formation of minor aggregates associated with histidine and citrate in solution (Appendix II, Figure A3.12) that skewed the Z-average value. Furthermore, changes in the DLS peak position associated with the nanoparticle aggregates is dependent upon the state of aggregation of the nanomaterials in solution, including nanoparticle dimers, trimers, higher ordered assemblies, and individual Au nanoparticles, whose concentrations are dependent upon the rate of assembly. As a result, shifts in the maximum peak intensity are indicative of aggregation and the assembly rate in solution. As a result, shifts in the maximum peak intensity are indicative of aggregation and the assembly rate in solution. At a ratio of 4K, the Cys sample demonstrates maximal aggregate sizes at 6.00 h with a hydrodynamic diameter of 31 nm. This value is higher than the individual nanoparticle as measured by TEM analysis (15 nm), and larger than the DLS control sample of citrate-capped Au nanoparticle (~20 nm). For Ala and His, particle sizes that were identical to the control were noted, indicating that no assembly occurred. When the amino acid:Au nanoparticle ratio was increased to 40K (Figure 3.5b), assembly was evident for the Cys and His samples. For the Cys system, an aggregate size of 26 nm was observed at

6.00 h, which is lower than the size noted at a ratio of 4K and is consistent with the UV-vis results. For the 40K His sample, particle aggregation is evident, resulting in the formation of structures with dimensions of ~24 nm after 6.00 h. Again, both the control and the Ala sample displayed no change in particle size. Note that these size increases are attributed to changes in the aggregation state, rather than simple changes in the hydrodynamic radius of individual particles; should these increased values arise from perturbations in the particle surface leading to changes in the hydrodynamic environment of the materials, an immediate size change would be observed that would be stable throughout the analysis as the ligand exchange process has been shown to be rapid in solution while the particle assembly step is rate limiting.[33] For the 100K ratio (Figure 3.5c), aggregation is still evident for the Cys and His systems, with sizes of ~26 nm and 27.5 nm, respectively; however, no change in aggregate size is again noted for the control and Ala systems. Finally, at the highest ratio (2000K; Figure 3.5d), no assembly is observed for any sample. Such results are fully consistent with the UV-vis analysis.

These results indicate that materials assembly occurs as a function of the amino acid structure and affinity for the Au surface, which follows theoretical trends.[145] For instance, based upon optical changes and particle size increases, the amino acids are able to induce maximum assembly at ratios of ~10K, 100K, and 200K for Cys, Arg, and His, respectively, suggesting that the residues are ordered by decreasing affinities. Furthermore, a lack of assembly in the presence of Ala is observed, which is indistinguishable from the amino acid-free control. This indicates that the side chain is likely responsible for the surface binding event. Ala apparently

119

does not bind to the nanoparticle surface, either through the methyl side chain or α–amine group. Primary amines do have an affinity for Au;[143] however, these results indicate that the single amine is unable to bind to the metallic surface alone. While this is somewhat surprising, it is not completely unexpected; the binding strength of Cys is significantly lower than comparable alkyl thiols,[145] suggesting that individual amino acids may possess inherently weaker affinities for materials surfaces.

To confirm the trend in surface affinity, an SPR study of amino acid binding of a Au surface was conducted at room temperature. In the beginning of the analysis (Figure 3.6), pure water was introduced to the sensor head and the captured signal served as the baseline. Then citrate, Ala, His, Arg, and Cys solutions of the same concentration (10.0 mM) were sequentially exposed to the sensor head (black arrow) with water flowed in between two analytes to confirm the binding of amino acid on the Au surface (red arrow). The data clearly show that the binding process for each of sample except Cys was fully reversible, suggesting that Cys possessed the strongest affinity to the Au surface. This is reasonable as the thiol group of Cys quickly forms a stable chemical interaction with the Au surface, which led to a large magnitude change of SPR signal that did not return to baseline. It is worth noting that small differences (5-10 units) in the baseline signals were observed before and after the injection of analytes, which can be attributed to the shot noise of the instrument and drift of the surrounding temperature. For the other analytes, an abrupt change of SPR signal was detected when the ligand solution was flowed over the surface. This change is caused by an increase in the absolute mass in the binding event (adhesion of molecule on the surface). This abrupt change was followed by a stabile signal,
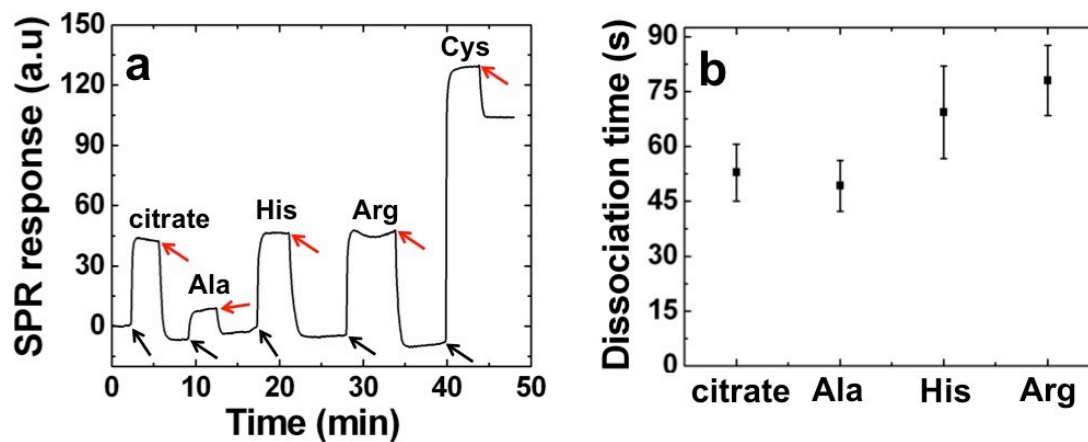
Figure 3.6 SPR analysis of surface binding at room temperature. Part (a) presents the SPR response curve for the sequential introduction of citrate, Ala, His, Arg and Cys solution (10mM) to the sensor surface, while part (b) displays the dissociation time of the analytes from the Au surface.

indicating an equilibrium rate of adsorption and desorption from the Au surface was achieved.

The equilibrium was shifted towards desorption when water was flowed through the system, leading to a rapid drop of SPR signal. The strength of the interaction between the molecules and the Au surface can be determined by the desorption rate (i.e. the time required for the signal to return to the baseline). A dissociation time of each analyte was determined by introducing different solutions onto the sensing films followed by water. Each set of experiments was repeated five times to achieve an average value as shown in Figure 3.6b. Here, it is readily shown that the strength of the interactions between the amino acids and the Au surface is Cys>Arg>His>citrate>Ala, which is consistent with the observations in the nanoparticle system. Note that the dissociation time for Ala is lower than for citrate, suggesting that Ala displacement of citrate on the surface of Au nanoparticles would be unfavored. Altough other interactions including hydrophilicity and electrostatics may play a role in the assembly pattern, all the UV-vis, DLS and TEM results obtained clearly indicate a direct corelation of the binding pattern with the SPR data and modeling.

While the amino acid binding of Au is likely dependent upon the side chain, it is apparent that different mechanisms are at play for the different residues. For instance, with Arg, linear branching chains are observed; however, for Cys, random assemblies are produced. Furthermore, the assembly rates for Arg are clearly faster based upon UV-vis and DLS results as compared to the Cys samples.[48,240] Arg is likely to employ a ligand induced dipole process, which has been shown to be rapid in

solution.[240] Since non-linear aggregates prevail with Cys, attempts to elucidate the assembly process were studied to more fully determine the differences associated with amino acid binding. To further characterize the effects of Cys, a kinetics-based analysis of the assembly was conducted at temperatures between 10.0 °C and 70.0 °C.

Figure 3.7 displays temperature effects on the Cys-based process over 2.00 h, as monitored by UV-vis. A shortened time frame was employed due to the rapid assembly at low temperatures. Figure 3.7a presents the process at 10.0 °C, which demonstrated rapid formation of the assemblies at Cys:Au nanoparticle ratios <200K. When the temperature was raised to 25.0 °C (Figure 3.7b), assembly occurred in solution similar to the 10.0 °C sample. Surprisingly, as the temperature was elevated to 40.0 °C (Figure 3.7c), a change in the assembly process was evident where the rate of growth at 600 nm was impeded. While assembly does occur, the process is clearly slower. This decrease in absorbance growth with increasing temperatures was continued at 70.0 °C, which is presented in Figure 3.7d. Here, only minor changes in the absorbance spectra for all samples at any ratio were observed. This demonstrates that as the temperature increases, the formation of nanoparticle assemblies decreases, which is in direct contrast to the trend previously observed for Arg-based assembly.[240] The TEM analysis of the assemblies at selected temperatures is presented in the Appendix II, Figure A3.16, which demonstrated randomly oriented structures, regardless of the temperature and ratio employed.

To confirm the UV-vis detected assembly process, DLS was completed at the selected temperatures (Figure 3.8). At 10.0 °C, formation of aggregated structures is observed with maximal sizes achieved with the 10K sample. Here, aggregates with an
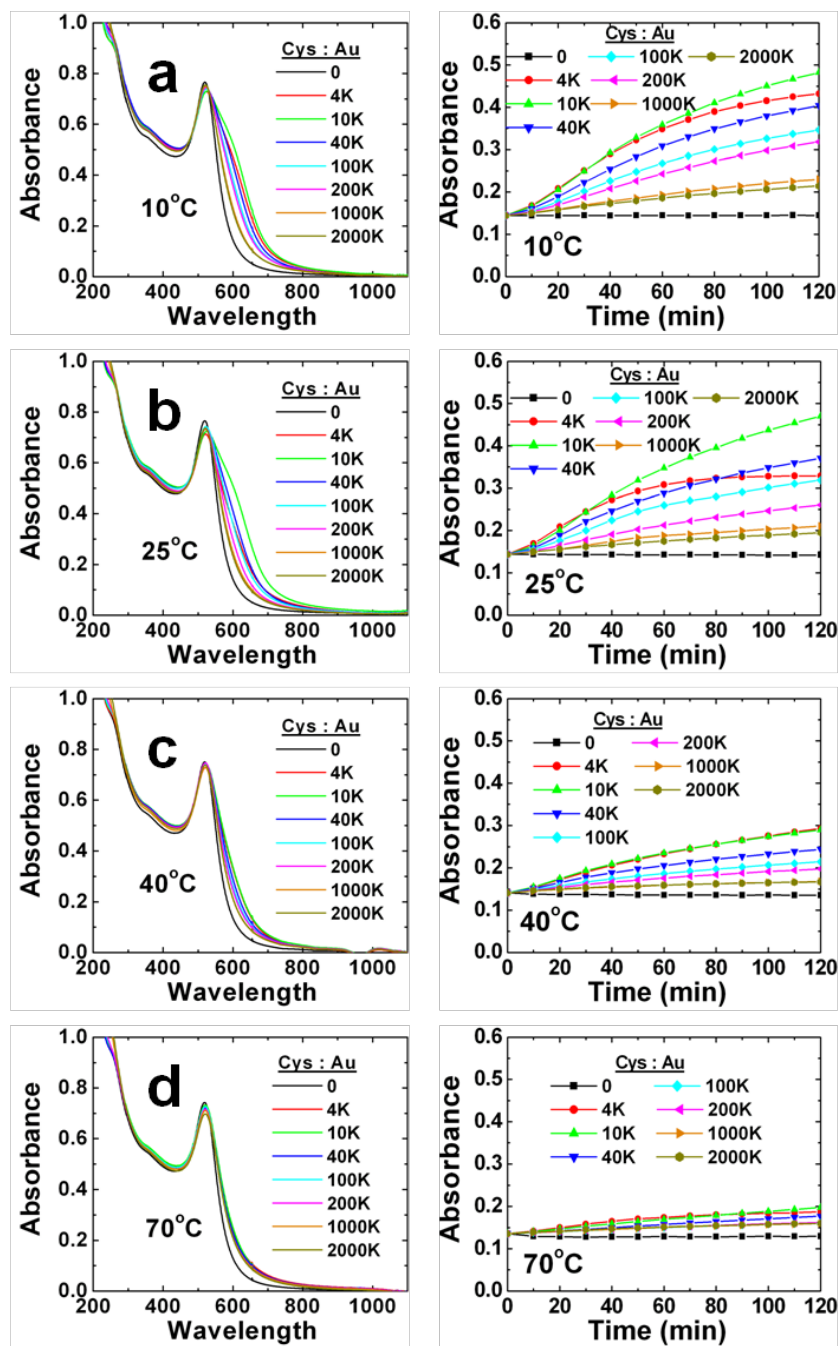
Figure 3.7 UV-vis analysis of reaction temperature effects on the Cys-mediated assembly of Au nanoparticles at a temperature of (a) 10.0 °C, (b) 25.0 °C, (c) 40.0 °C, and (d) 70.0 °C. The left panel displays the UV-vis spectra at 2.00 h, while the right panel displays the growth of the 600 nm absorbance as a function of time for all ratios studied.
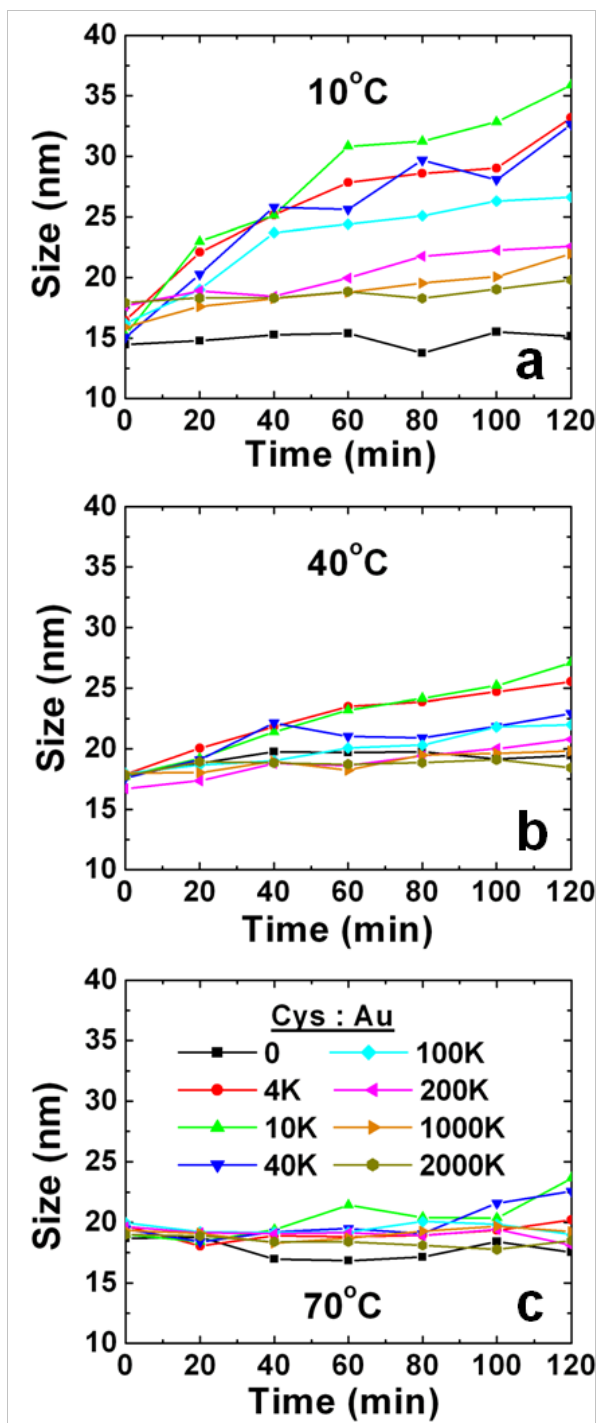
Figure 3.8 DLS analysis of the effects of reaction temperature on the Cys-mediated assembly of Au nanoparticles at temperatures of (a) 10.0 °C, (b) 40.0 °C, and (c) 70.0 °C.

average hydrodynamic diameter of ~36 nm were achieved after 2.00 h. Additionally, as the Cys:Au nanoparticle ratio is increased, the size of the structures decreased until an average size of ~20 nm results in the 2000K sample. At 40.0 °C (Figure 3.8b), a significant decrease in the aggregate size is observed. Here, maximal assemblies are observed with the 10K sample; however, the average hydrodynamic size decreased to ~27.5 nm. For the reactions at 70.0 °C (Figure 3.8c), no significant change in size is observed for any sample as compared to the control, suggesting that nanoparticle assembly is prevented. These results are consistent with the UV-vis analysis, demonstrating that the assembly rate decreases as temperature increases.

To achieve a quantitative analysis of the temperature effects on Cys-based assembly, a kinetic analysis of the UV-vis study was conducted. This process can be modeled using equation below[177,240] where the rate constant, k, is calculated based upon the plamson intensity.

$$k_{dim}t = \frac{\varepsilon(A_0 - A_t)}{A_0 A_t}$$

Here, A_0 and A_t represent the absorbance intensity of the Au nanoparticles at 520 nm before the reaction and at time t, respectively, while ε is the nanoparticle molar absorptivity constant, which is 3.6×10^8 M^{-1}cm^{-1}.[48]

From this analysis, the k-values at different temperatures are determined and are presented in Table 3.1. To achieve these values, the formation of nanoparticle assemblies must be clearly observed in both the UV-vis study and DLS analysis. Since no assembly was evident at 70.0 °C by DLS, no k-values were determined. At

Table 3.1 Second order rate constants for the Cys-based assembly of Au nanoparticles

Cys:Au NP Ratio	k $(M^{-1}s^{-1})$			
	10 °C	25 °C	40 °C	70 °C
4K	3087	3561	617	---
10K	2916	2769	502	---
40K	1724	1404	146	---
100K	1292	1090	72	---
200K	1079	592	---	---
1000K	613	823	---	---
2000K	903	---	---	---

10.0 °C, the maximum rate constants were achieved for the 4K and 10K samples that demonstrated the most rapid assembly, with values of 3087 $M^{-1}s^{-1}$ and 2916 $M^{-1}s^{-1}$, respectively. As the Cys:Au nanoparticle ratio was increased, decreasing k-values were achieved until a value of 903 $M^{-1}s^{-1}$ was observed for the 2000K sample. At 25.0 °C, similar values as compared to the 10.0 °C reactions were achieved. Under these conditions, a maximum rate of 3561 $M^{-1}s^{-1}$ was achieved for the 4K sample that decreased to 823 $M^{-1}s^{-1}$ for the 1000K sample. Further elevation of the temperature to 40.0 °C demonstrated significant decreases in the rate constants. For this temperature, the k-values varied from 617 $M^{-1}s^{-1}$ to 72 $M^{-1}s^{-1}$ for the 4K and 100K samples, respectively. Values for reactions at higher ratios were not determined due to the lack of assembly. This suggests a correlation between the temperature and assembly such that higher temperatures prohibit assembly, which is in contrast to the Arg mechanism that demonstrated increased assembly at elevated temperatures.[240]

Based upon the changes at the selected temperatures, the aggregation of Au nanoparticles by Cys likely follows the proposed mechanism of Scheme 3.1. In this process, citrate-capped Au nanoparticles are exposed to Cys, from which the amino acid binds to the surface via the thiol functionality to partially displace citrate. As sufficient numbers of Cys bind to the nanoparticle at indiscriminate locations, the zwitterionic headgroups will be displayed on the surface. Unlike Arg, it is likely that the Cys residues do not segregate from the remaining citrate. This is due to the stronger thiol binding of Cys to Au, in which the amino acids are locked in place, whereas with Arg, the weaker binding of the guanidinium group allows for movement of the residue on the surface to facilitate ligand segregation. By being locked in place,
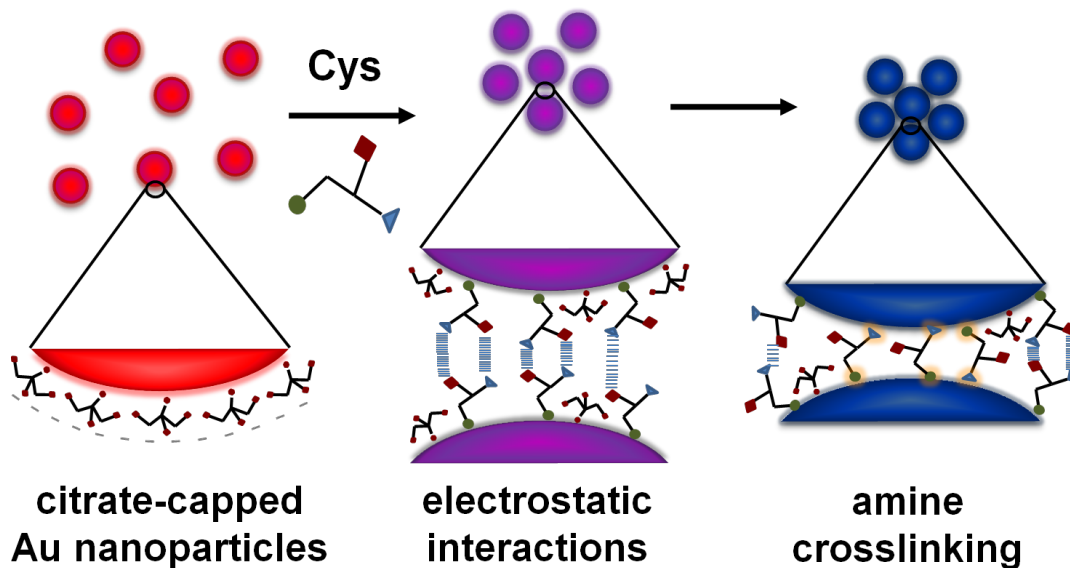
**Scheme 3.1 Representative scheme for the Cys-based assembly of Au nanoparticles. Note that Cys binding of the Au surface is stochastic in nature and no patterns are anticipated. First, Cys partially replaces citrate on the Au nanoparticles. Once bound, electrostatic interactions between the α–headgroups attracts the particles together to allow for crosslinking to occur via the multi-dentate binding of the exposed α–amines.**

no Cys-based electrostatic network can be formed; therefore, the uncoordinated zwitterionic head groups can electronically interact with other species in solution. To that end, electrostatic interactions of the cationic amine and anionic carboxylate between multiple amino acids on the surfaces of adjacent Au nanoparticles can be used to attract the species closer together to begin the assembly process.[231] Once a sufficient distance is achieved between the two particles, crosslinking can occur via binding of multiple amine groups to the second Au surface. Here, chelate-based binding of the amines is possible where multiple amines of the two Au surfaces can bind to the adjacent particle.[172] This is different as compared to the binding of a single amine of amino acids, where multidentate binding cannot occur. Once crosslinked, the materials are irreversibly bound in a non-organized motif to form the aggregated structure in a significantly different process as compared to the dipole-based method of Arg.

This mechanism corresponds well with the observed changes in the Cys assembly process. It is established that elevated temperatures disrupt interparticle electrostatic interactions, such as those initially between the surfaces of Au nanoparticles that initiates the assembly.[231] To that end, as the temperature is raised, the formation of the aggregates in solution should diminish, which was observed by both UV-vis and DLS. Furthermore, the lack of directional assembly is also consistent with this mechanism. By being locked in a single location, binding of cysteine along the entire nanoparticle surface occurs, thus preventing the formation of a dipole for linear assembly. As a result, random aggregates are observed based upon interparticle attractions along the entire particle surface. Additionally, since aggregate formation is

prevented at high Cys:Au nanoparticle ratios, this indicates that a mixed monolayer is required for assembly; should Cys cover the entire surface, no binding points would be available for amine crosslinking. Once the entire surface is passivated by Cys, this would position the zwitterionic headgroups in close proximity to form an electrostatic network.[172] As this occurs, the charge-based interactions between multiple materials would be diminished, which further indicates the necessity of a mixed ligand layer. As an effect of this multi-step, multi-interaction process, the rate of assembly is anticipated to be slower as compared to the Arg process where the magnitude of the dipole facilitates rapid assembly. Indeed, such results are observed where the assembly rate for the Cys reactions are two to three orders of magnitude lower than the Arg system and result in smaller aggregates.[240]

To probe this mechanism, two controls were performed. As shown in Figure 3.9a, the assembly process was studied at a Cys:Au nanoparticle ratio of 4K at a temperature of 70.0 °C, after which minimal changes in the UV-vis spectra was observed after 2.00 h. Next, the system was allowed to cool to room temperature. When the reaction was allowed to stand at room temperature for 2.00 h, a color change from red to purple was observed, with a sharp rise in absorbance at 600 nm, consistent with materials assembly. This study suggests that the elevated temperatures do indeed disrupt the initial electrostatic effects; however, cooling of the system can facilitate these interactions to form the aggregates. In the second experiment (Figure 3.9b), the materials were allowed to assemble at 10.0 °C for 2.00 h using the 4K system, which is evident by the growth of the 600 nm absorbance. Next, the reaction was heated to 70.0 °C for 2.00 h. Even after the prolonged exposure to the high temperature, no
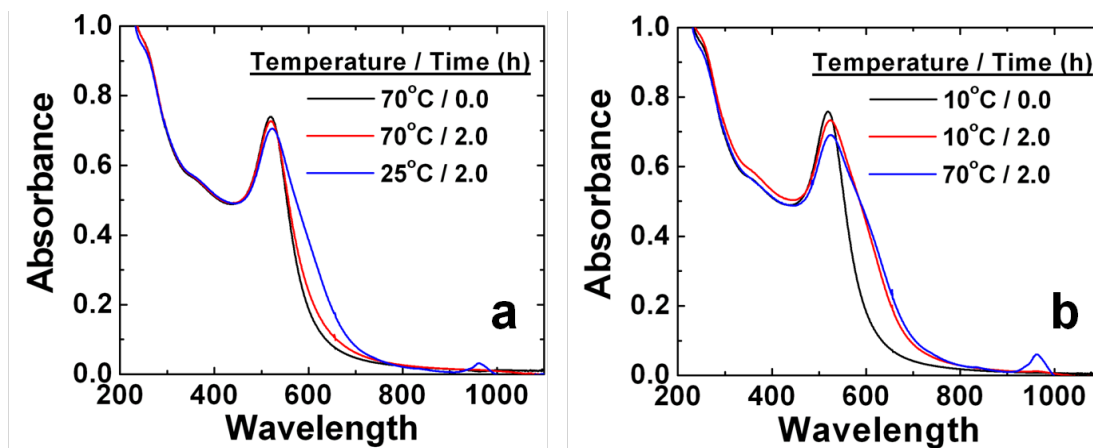
Figure 3.9 Control analysis of Cys-mediated assembly. For part (a), the black spectrum corresponds to the Au nanoparticles studied in the 4K Cys sample at 70.0 °C immediately after amino acid addition. The sample was maintained at 70.0 °C for 2.00 h (red spectrum) and then cooled to room temperature and allowed to react for 2.00 h (green spectrum). As is evident, materials assembly occurred after cooling to the lower temperature. For part (b), a similar analysis was conducted as in part (a); however, the reaction was studied initially (black spectrum) at 10.0 °C for 2.00 h (red spectrum), which allowed for assembly to occur. After this initial time at low temperatures, the sample was heated at 70.0 °C for 2.00 h (green spectrum). After heating, no disassembly of the materials is evident.

change in the assembly state was observed, indicating that a robust interaction exists between the two particles.

3.5. Summary and Conclusions

In conclusion, these results demonstrate that amino acids possess different binding affinities and surface structures for Au nanoparticles. To that end, the composition, identity, and binding strength of the residues work in combination to drive the assembly of Au nanoparticles, which can be monitored using available techniques such as UV-vis, SPR, and DLS. Using this approach, the strength of the interactions between the amino acid and nanoparticle dictate the concentration at which assembly is observed, which follows computationally derived trends.[145] This study represents a new step towards the development of chemical approaches to elucidating biomolecular interactions on nanomaterials, which may prove to be critical in the future design of highly active bio-directed structures for applications ranging from dynamic assembly to energy storage to diagnostics. From further studies using this approach extrapolated to other biomolecules, it may be possible to elucidate binding motifs, chelate effects, and important ligand structural effects that could allow for the rational design of peptides to control the morphology and activity of nanomaterials.

Chapter 4: Stability and Electrostatic Assembly of Au Nanorods for Use in Biological Assays

4.1. Overview of Study

The structure, stability, and aggregation potential of short Au nanorods under biological-based solution conditions has been studied. These attributes were probed using UV-vis spectroscopy, transmission electron microscopy, ζ-potential analysis, and dynamic light scattering. The stability and aggregation potential of the materials depended strongly upon both the purity of the solvent used to prepare Au nanorod solutions and other solutes added. When the Au nanorods were dissolved in Tris buffer at concentrations less than 10.0 mM, no aggregation was observed; however, when the solvent was comprised of Tris buffer with concentrations between 10.0 mM and 100 mM, significant aggregation of the materials occurred. This effect resulted in a dramatic broadening and shift in the absorbance maxima of the longitudinal surface plasmon resonance. At Tris buffer concentrations of > 100 mM, minimal to no aggregation of the materials in solution was observed. Such an ability is based upon electrostatic aggregation of the materials in solution mediated by the anions associated with the buffer system; at concentrations between 10.0 mM and 100 mM, the anions present electrostatically bind to the surface of the positively charged Au nanorods, resulting in crosslinking of the materials. At higher buffer concentrations, a sufficient number of anions are present in solution to template around the entire surface of each individual nanorod, in effect neutralizing the charge and producing an electronic double layer that prevents aggregation. Such studies are timely as they represent an analysis of the

134

stability and range of use of Au nanorods for biological-based applications where remarkable potential exists.

4.2. Introduction

Nanomaterials represent recently investigated targets for use in biological assays and detection schemes,[211,243-247] and for *in vivo* activities.[28,30,248-252] The interest in these materials lies in their individual properties that are highly distinctive as compared to their bulk counterparts.[165,212,253,254] These properties include significant fluorescence,[255-257] distinctive surface plasmon resonances,[254,258] large surface to volume ratios,[175,259] and simple surface functionalization.[165,166] One set of materials that has been intensely used for biological applications are Au nanoparticles. Au materials have been used as colorimetric sensors,[169,211] bio-delivery devices,[248,260] agents of photo induced cell destruction,[251,260,261] and cellular imaging materials.[262,263] Such materials are believed to be non-toxic[252,264] and can be taken up by cells with relative ease;[28,30,248,252,262,263] however, many groups have demonstrated the instability of Au nanoparticles in various ionic media.[265-267] Bio-based assays and applications of Au nanoparticles require their stability in high ionic strength buffer solutions, such as Tris, but little information is known about the effects of the buffer on the nanomaterials of interest. As a result of the solution conditions, nanoparticle aggregation and collapse can occur, resulting in release of Au^{3+} ions and/or precipitation of bulk material, both of which are undesirable. In order to avoid such events, specific conditions must be designed for the application and use of Au nanoparticles with biological systems.

Au nanorods have been investigated as alternatives to typical spherical Au nanoparticles due to their unique spectroscopic properties.[226-228,254,258] The rod-shaped

materials are synthesized using a variety of techniques, with the seed mediated method using the surfactant cetyltrimethylammonium bromide (CTAB) as the surface passivant being used most frequently due to the simple synthetic procedure.[227,228,268-270] As a result of the anisotropic shape, two plasmon resonances are present whose positions are dependent upon the nanorod's aspect ratio,[228,254,271] as compared to only one plasmon band observed with spherical Au nanoparticles.[212,258] The longitudinal surface plasmon (LSP) band typically absorbs light of wavelengths in the near-IR region of the electromagnetic spectrum[226] and is highly sensitive to the local environment surrounding the nanorod.[272-274] These properties make the application of Au nanorods for biological processes highly desirable. For instance, the degree of sensitivity of the LSP band allows for detection of binding of biological analytes based upon peak shifting of the band in solution.[273] Additionally, assembly of nanorods has been achieved using biological interactions resulting in end-to-end linkages of the rods to form chain-like species of varying length.[274,275]

For nearly all biological applications of Au nanorods, multiple steps are required for the functionalization and subsequent use of the materials, typically in aqueous solutions buffered at physiological pH.[247,249,273,275] After completion of each synthetic step, purification of the materials by centrifugation is commonly used to remove excess reagents followed by dissolving of the Au nanorod pellet in an appropriately buffered system for the subsequent reaction step. As the number of purification steps increases due to the complexity of the desired application, instability in the nanorod structure has been observed.[273,276] This instability is likely the result of driving the on-off equilibrium of the surfactant surface stabilizer towards desorption from the nanorod surface,[276] but little

information is known about the effect of the equilibrium on the nanorod structure. In fact, the stability of the Au nanorods in high-ionic strength solutions, such as those used for bio-based systems, is relatively unclear,[267] but aggregation/assembly of the nanorods as a result of particle concentration and solvent evaporation from solutions in water or ionic media has been noted.[229,277-279] While aggregation in the solid-state is of interest for specific applications that do not require solvation of the materials, understanding the aggregation and assembly of Au nanorods in high ionic strength buffer solutions is critical for their biofunctionalization and their further use in biological applications.

The study on the stability and aggregation of Au nanorods in biological-based solutions includes an analysis of the purification process and the effects of buffer concentration on the Au nanorods in solution. To study the nanorod stability, the material's structure and assembly in both the solid state and solution state from crude product to functionalizable material was probed through the use of UV-vis spectroscopy, transmission electron microscopy (TEM), and ζ-potential and light-scattering analyses. From this study, it was determined that minimization of centrifuge purification (less than two times) is required to prevent nanorod deformation. Additionally, it was observed through an analysis of the Au nanorods in Tris-buffered solutions at pH 7.42, that there occurs a direct aggregation of the materials as a result of the concentration of buffer in solution as shown in Scheme 4.1. At low buffer concentrations of <10.0 mM, the nanorods are independent species in solution, but at buffer concentrations between 10.0 and 100 mM, the materials quickly aggregate in response to the ions in solution. The assembly of the materials is likely mediated by the buffer anions causing electrostatic interactions between
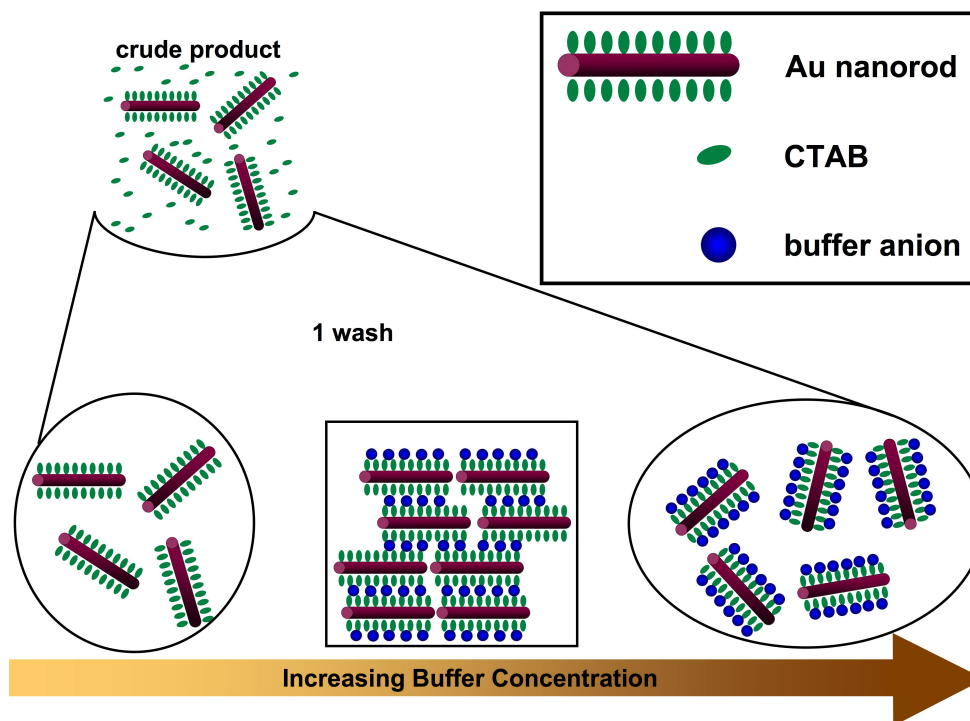
Scheme 4.1 Effects of Buffer Concentration on the Aggregation of Au Nanorods in Solution

multiple Au nanorods due to their cationically charged surfactant surface. Eventually, at buffer concentrations >100 mM, the rods do not self-assemble in solution and remain independent; at high buffer concentrations, a sufficient number of anions are present in solution to template along the surface of the polycationic nanorods, thus preventing the aggregation process by generating a stabilizing charged double layer along the Au nanorods.

4.3. Methods

4.3.1. Chemicals

$HAuCl_4 \cdot 3H_2O$ (99.999%) and CTAB (≥99.0%) were purchased from Sigma-Aldrich (St. Louis, MO). $NaBH_4$ (≥98%) was purchased from EMD (Gibbstown, NJ), ascorbic acid was purchased from J. T. Baker (Phillipsburg, NJ), $AgNO_3$ (ACS Grade) was purchased from BDH (VWR, Radnor, PA), and Tris buffer (THAM) was purchased from Fisher (Waltham, MA). All chemicals were used as received. Milli-Q water (18 MΩ· cm) (Millipore, Bedford, MA) was used throughout.

4.3.2. Characterization

UV-vis spectra were obtained on an Agilent 8453 UV-vis spectrometer using a 2.00 mm path length quartz cuvette (Starna). All spectra were background-subtracted against water, the solvent. TEM images were obtained using a JEOL 2010F transmission electron microscope operating at 200 kV with a point-to-point resolution of 0.19 nm. Samples were prepared on 400 mesh Cu grids coated with a thin layer of carbon (EM Sciences). The solution (5.00 μL) was pipetted onto the surface of the grid and allowed to dry in air. Solution-based ζ-potential and light-scattering analyses were completed on a Zetasizer Nano ZS System (Malvern Inc.).

4.3.3. Preparation of Au Seeds

Au nanorods were produced by the seed-mediated method previously described by Sau and Murphy.[228] First, 7.50 mL of a 100 mM CTAB solution in H_2O was added to a plastic conical centrifuge tube. To the CTAB, 250 μL of a 10.0 mM aqueous $HAuCl_4$ solution was added. The solution turned a deep orange color immediately upon addition, after which it was gently mixed by the inversion method three times. To this, 600 μL of a freshly prepared 10.0 mM $NaBH_4$ solution was added, changing the solution color to pale brown. The Au seeds were allowed to stand for 2.00 h prior to use to ensure complete Au-ion reduction.

4.3.4. Fabrication of Au nanorods

All Au nanorods were prepared using identical conditions, but varying the amount of Au seeds added in the final step results in changes to the particles' dimensions. For each synthesis, 4.75 mL of 100 mM CTAB, 200 μL of 10.0 mM $HAuCl_4$, 30.0 μL of 10.0 mM $AgNO_3$, and 32.0 μL of 100 mM ascorbic acid were added to a conical centrifuge tube. All solutions were added in the order listed followed by mixing of the solution by the inversion method after addition of each species. With the addition of the mild reductant, ascorbic acid, the deep orange solution turned clear and colorless upon mixing. Finally, either 2.00 μL or 4.00 μL of the Au seeds was added to the solution followed by gentle mixing for 1.00 min. The reaction was allowed to stand at 26 °C for 1.50 h before analysis. Purification of the product was performed using standard centrifugation techniques.[228] As demonstrated by TEM, an increase in the aspect ratio was observed for materials prepared from 4.00 μL of seeds as compared to those prepared using 2.00 μL.

4.3.5. Preparation of Buffers

Tris buffer was prepared by dissolving 1.21 g of tris(hydroxymethylamino)-methane in 100 mL of water to prepare a 100 mM stock solution. The solution was titrated with 1.00 M HCl until a constant pH value of 7.42 was obtained. Subsequently, stock solutions of low concentrations of Tris buffer, ranging from 2.00 to 80.0 mM, were obtained by dilution with water. The pH of each dilution was confirmed prior to use. An identical procedure was employed for the preparation of Tris buffer concentrations of 100-400 mM, except a 500 mM initial stock solution was used for the dilution preparation.

4.3.6. Buffer Stability Analysis.

After nanorod fabrication, 500 µL aliquots of the crude Au nanorod reaction product were placed into 1.70 mL microcentrifuge tubes. Twelve samples were prepared and then centrifuged at 14,600 rpm for 10.0 min to pellet the Au nanorods. The aqueous supernatant containing excess CTAB surfactant molecules was then extracted and discarded. From this point, the Au nanorod pellet was redissolved in 500 µL Tris buffer at various concentrations ranging from 2.00 mM to 400 mM at a pH of 7.42. For each analysis, a positive control dissolved in deionized H_2O was consistently performed to confirm the viability of each assay. Once dissolved, characterization of the aggregated state of the Au nanorods was conducted.

4.4. Results and Disscusion

4.4.1. Purification Stability of Au Nanorods

The structural stability of Au nanorods after multiple functionalization and purification steps is key to obtaining materials with desired properties. The material's

initial structure is susceptible to an exchange of surfactant bound to the metallic surface with free surfactant in solution,[276] similar to the equilibrium observed for Au monolayer protected clusters (MPCs).[165] Controlling the on-off equilibrium of the surfactant is key to maintaining particle stability since as the concentration of free surfactant molecules in solution decreases with increasing material purity and nanorod instability increases as well. This instability is the effect of driving the equilibrium towards release of the surfactant, thus causing nanoparticle degradation.

To maximize the nanorod purity without sacrificing structural stability, we analyzed the centrifugation purification method for Au nanorods of two different aspect ratios. These materials were classified as the 2.00 μL and 4.00 μL Au nanorod samples, as this is the volume of Au seeds required to produce the specific set of materials. Immediately after the reaction, the crude materials produced using 2.00 μL of the Au seeds possessed a LSP peak at 705 nm in the UV-vis spectra shown in Figure 4.1a. Additionally, a transverse plasmon resonance peak is observed at 520 nm and a third peak is present at 590 nm. The third peak is likely due to the "dog bone" shaped nanorods produced, *vide infra*, similar to results observed by Chilkoti and coworkers[280] and predicted by Xu and Cortie.[281] After the initial analysis, 1.00 mL of the crude materials was centrifuged to form a pellet and the supernatant was decanted. Subsequently, the deep blue pellet was redissolved in 1.00 mL of water and vortexed to ensure complete dissolution. UV-vis analysis of the once purified materials demonstrated an identical UV-vis spectrum as compared to the crude sample set. The materials were then washed a second time using the same procedure, which resulted in a sharp decrease in absorbance, as well as a blue shift of the longitudinal plasmon resonance peak by 3.00 nm. The
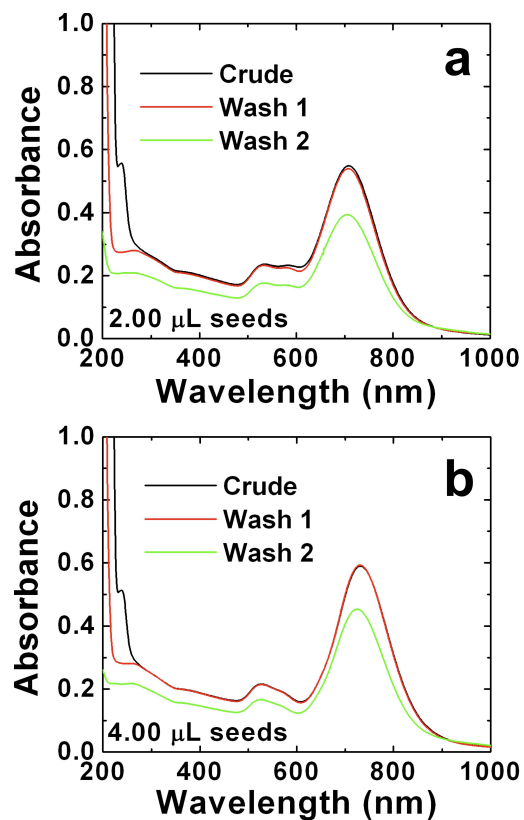
Figure 4.1 UV-vis analysis of the centrifugation purification of Au nanorods. Au nanorods were prepared using (a) 2.00 μL and (b) 4.00 μL of Au seeds. For this analysis, the black spectra correspond to the crude materials, while the red spectra represent the materials washed only once. The shifted green spectra correspond to the materials that were washed twice. Further purification analysis was unable to be performed due to bulk material formation after subsequent washes.

longitudinal plasmon peak is highly sensitive to changes in the material's structure,[254] which indicates that a change in the aspect ratio occurs after a second washing step. After a third washing procedure, an insoluble black pellet was obtained, suggestive of bulk material formation and lack of preservation of the Au nanorod structure.

Similar results were obtained for Au nanorods produced using 4.00 μL of Au seeds as shown in Figure 4.1b. The LSP resonance of the crude materials is red-shifted to 724 nm, as compared to the 2.00 μL Au nanorods, indicating that nanorods of different dimensions have been successfully prepared. Additionally, no change in the UV-vis spectra of the crude and once-washed materials is observed, consistent with the materials retaining their initial structure after one purification step. As observed with the 2.00 μL sample, a decrease in absorbance and a blue shift of 6.00 nm was observed for these nanorods, indicating that a change in the particle shape occurred. Finally, a black insoluble pellet was obtained after the second wash for all materials.

UV-vis analysis indicates that a change in particle shape and/or structure has occurred with increasingly purified samples based upon LSP peak shifting. To confirm this result, TEM images of the materials after the first and second washing steps were obtained. TEM images of the crude materials were unable to be obtained due to the high concentration of CTAB in solution. Figures 4.2a and b show images and a size-distribution analysis of the materials synthesized using 2.00 μL of Au seeds after the first and second rounds of purification, respectively. After one washing, the observed nanorods had dimensions of approximately 56.4 x 30.9 nm with an aspect ratio of 1.83. Such dimensions are slightly smaller than those reported previously by
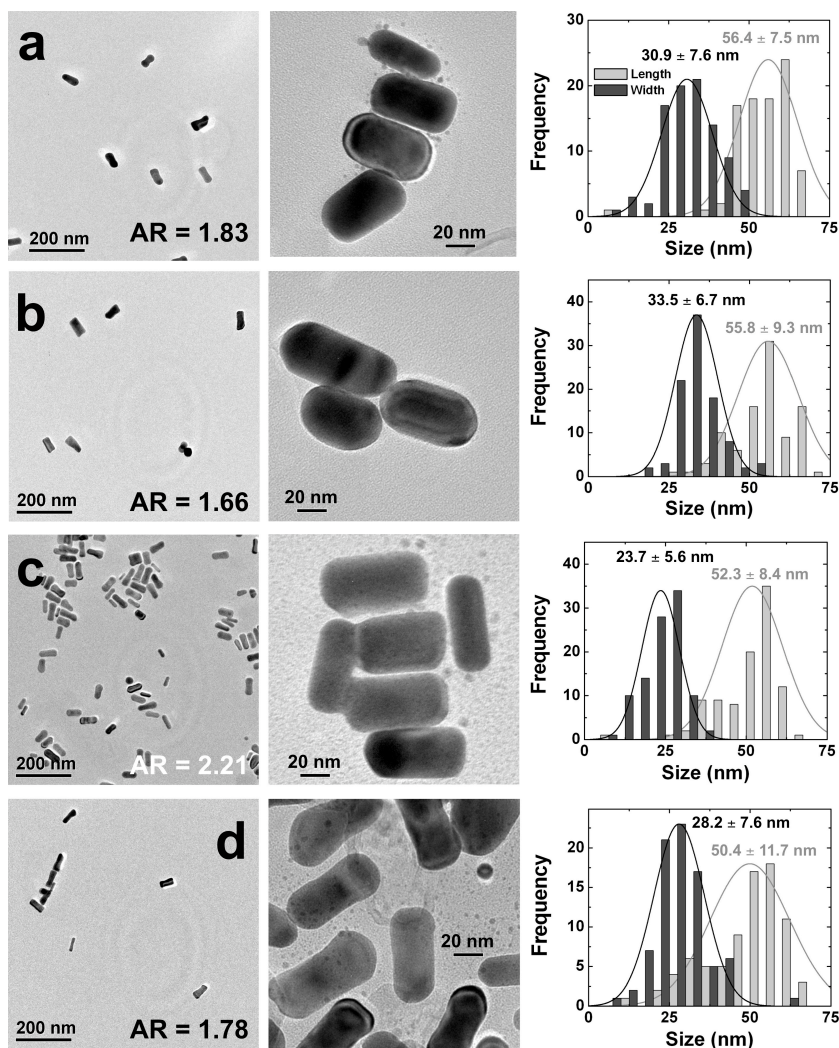
Figure 4.2 TEM and sizing analysis of the stability of Au nanorods during purification. Nanorods were prepared using 2.00 μL (a, b) and 4.00 μL (c, d) of Au seeds. The images in (a) and (c) were obtained after one round of purification, while the images in (b) and (d) were obtained after a second purification step. A low-resolution image is shown to the left, with a higher resolution image of the obtained nanorods presented in the middle, and a size-dimensional histogram of the materials shown at the right. While individual nanorods may possess similar sizes between samples, as is evident due to the material's dispersity, the average dimensions shift to produce a smaller aspect ratio after the second washing step.

145

Sau and Murphy.[228] After a second centrifuge-based washing step, the Au nanorods possessed dimensions of approximately 55.8 x 33.5 nm with an aspectratio of 1.66. A full-dimensional analysis of all the nanorods produced is shown in Table 4.1. As stated above, further purification steps were not taken due to bulk material formation. A decrease of 0.17 in the average aspect ratio of the Au nanorods is observed as the purity of the rods increases. The change in aspect ratio is likely due to particle deformation and aggregation as a result of changes in the purity of the sample; as the sample purity increases, the on-off equilibrium of the CTAB shifts to release the surfactant from the rod surface leading to particle aggregation.[254] Additionally, the decrease in aspect ratio is also spectroscopically observed (Figure 4.1a) by the blue shift in the UV-vis absorbance for the doubly-washed nanorod species, consistent with previous results for changes in the aspect ratio.[228] A similar trend for changes in the aspect ratio for increasingly pure nanorod samples is also observed for Au nanorods fabricated using 4.00 μL of Au seeds (Figures 4.2c and d). For these materials, after one round of washing, nanorods with approximate dimensions of 52.3 x 23.7 nm with an aspect ratio of 2.21 were obtained, while after a second round of washing, Au nanorods of 50.4 x 28.2 nm were observed with an aspect ratio of 1.78 (Table 4.1). This decrease in the aspect ratio is consistent with both the UV-vis results and the sizing analysis for the other nanorods presently studied.

With increasing purity, surfactant desorption is enhanced, which provides an exposed surface for particle aggregation. Particle aggregation can be observed directly by the changes in the average particle dimensions of the two sets of materials. Interestingly, while the overall rod structure appears to be maintained, both sets of

Table 4.1 Comparison of Au Nanorod Dimensions and Aspect Ratios with Increasing Levels of Purity

Au$_{seed}$	Wash 1			Wash 2		
(µL)	Length (nm)	Width (nm)	AR	Length (nm)	Width (nm)	AR
2.00	56.4 ± 7.5	30.9 ± 7.6	1.83	55.8 ± 9.3	33.5 ± 6.7	1.66
4.00	52.3 ± 8.4	23.7 ± 5.6	2.21	50.4 ± 11.7	28.2 ± 7.6	1.78

nanorods tend to preferentially grow outward along the longitudinal facets, which is the location of the highest density of surfactant molecules, rather than from the nanorod tips.[282] This is highly suggestive that surfactant desorption is key to the changes in the rod structure. These results are noteworthy as they demonstrate nanorod deformation based upon material purity, which will negatively alter their properties postfunctionalization. Changes in the materials structure subsequent to biomolecule functionalization will no doubt adversely affect their activity; therefore, minimizing the number of washing steps required for biological processing of the materials is required.
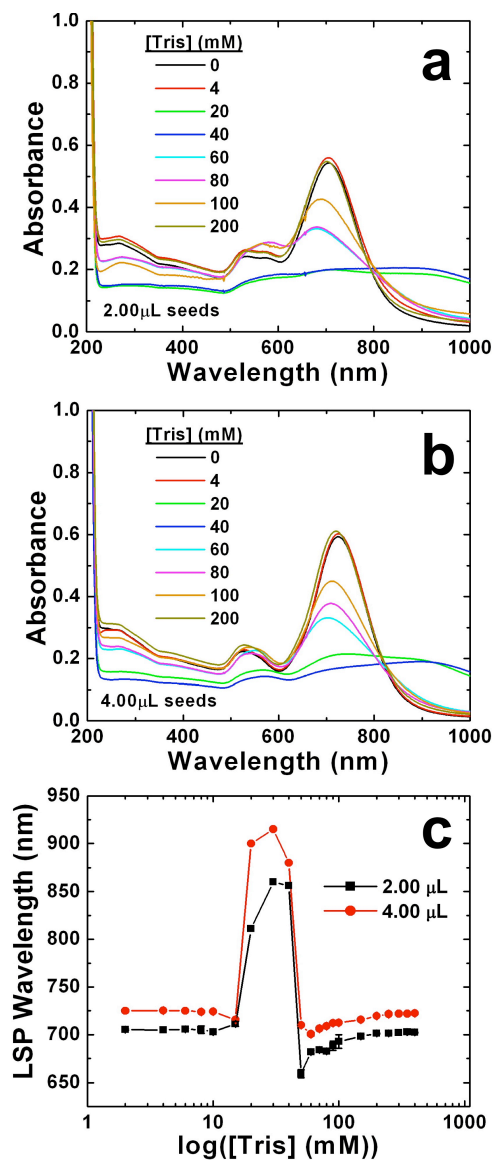
4.4.2. Effects of Tris Buffer Concentration

The use of Au nanorods for biological applications has been of increasing interest as their shape dependent properties are desired for applications as bio-inspired technologies and therapeutics.[226,247,251,252,273,283,284] For their controlled use in biological systems, the nanorods must be stable when dissolved in buffered solutions, typically at a physiological pH of 7.40. A typical biological buffer used at this pH value is Tris, which is usually present at high concentrations (50.0 – 100 mM) leading to a high ionic strength medium. El-Sayed and coworkers have previously demonstrated the assembly of Au nanorods in the solid-state by evaporation of the solvent from a Au nanorod solution containing 50.0 mM NaCl.[229] The driving force for the assembly and orientation of the rods on a TEM grid is likely to be solvent evaporation,[277-279] in conjunction with electrostatic interactions with the anions in solution, but electrostatic assembly of the materials in solution has not been reported. Such effects are fundamental to their functionalization and application in bio-based systems and assays, which are nearly

always performed in buffered solutions that contain high concentrations of ionic species, which may lead to undesired aggregation. Their stability needs to be high with a low degree of uncontrolled assembly to ensure maximum biofunctionalization and subsequent activity.

To determine the effects of buffered medium on Au nanorod stability, we studied the optical and assembly properties of the rods dissolved in various concentrations of Tris buffer at pH 7.42. Initially, 500 µL aliquots of the crude Au nanorods of the different aspect ratios were centrifuged once to remove excess CTAB. The materials were centrifuged only once to avoid the changes in the nanorod structure observed above. The individual pellets were then redissolved in 500 µL of an appropriate concentration of buffer in which they were immediately analyzed by UV-vis.

UV-vis analysis of the concentration effects of Tris buffer at pH 7.42 for Au nanorods prepared using 2.00 µL of seeds is shown in Figure 4.3a. A complete UV-vis analysis of these materials is presented in Appendix III (Figure A4.1). Note that these materials possessed an aspect ratio of 1.83. UV-vis spectroscopy was primarily used as it represents a powerful tool to determine the material's aggregation state by the peak position of the surface plasmon bands.[161,225,226,254,272] Initially, the nanorods dissolved in low concentrations of Tris buffer, <10.0 mM, demonstrated nearly identical spectra as the Au nanorods dissolved in water with a LSP resonance at 705 nm. A slight red shift of 5.00 nm by the LSP band was observed for the nanorods dissolved in 15.0 mM Tris. When the concentration of buffer is increased to 20.0 mM,

Figure 4.3 UV-vis analysis of the effects of the concentration of Tris buffer, pH 7.42, on Au nanorods in solution. Part (a) and (b) display the effects of individual buffer concentrations on the shifting of the LSP band of Au nanorods fabricated using 2.00 and 4.00 μL of Au seeds, respectively. Part (c) demonstrates the dependence of the LSP peak position upon the concentration of the Tris buffer used to dissolve the materials.

a dramatic red shift of the LSP to 810 nm is observed, with a significant broadening of the peak. This trend continues to 40.0 mM buffer where the LSP peak continues to red shift to approximately 865 nm (Figure 4.3a). As the concentration of buffer continues to increase, the LSP peak narrows and blue shifts to 665 nm for a buffer concentration of 50.0 mM and eventually is restored to 705 nm at buffer concentrations >100 mM. The overall LSP peak position is presented in Figure 4.3c, which clearly identifies the shifts in the position of the peak. A nearly identical trend was observed for nanorods prepared using 4.00 μL of Au seeds, as shown in Figure 4.3b, with the only difference arising for the initial position of the intrinsic LSP band, which is determined based upon the nanorod's dimensions and aspect ratio of 2.21.

Figure 4.3c shows an overall log plot of the position of the LSP band versus the buffer concentration for both sets of nanorods studied. From this analysis, it is evident that the position of the LSP peak for the two species is constant at low and high concentrations of buffer, less than 10.0 mM and greater than 100 mM, respectively, but that at concentrations between these two values, a significant shift of the peak is observed. All analyses were performed in triplicate, and each individual data point represents an average peak position for that sample. The peak position for the materials which demonstrated the largest degree of aggregation was selected as the center of the broad peak. As discussed previously, the LSP band is highly sensitive to the aggregation state of the nanorods as evidenced by shifting of the peak position. The shifting is caused by the close proximity of the nanorods with each other in the aggregated species, allowing for coupling of their individual plasmon resonances.[225] These shifts presently noted are likely to be caused by aggregation of

the materials in solution, which are possibly mediated by the anions present in the Tris buffer media.

To confirm that aggregation of the Au nanorods results in the observed optical changes of the particles, a set of specifically designed analytical characterization methods has been applied to the system. These methods include TEM in the solid state and ζ-potential and dynamic light-scattering (DLS) analyses, both of which are performed in solution. Based upon the UV-vis spectroscopic evidence, Au nanorods dissolved in Tris buffer of concentrations between 10.0 and 100 mM likely aggregate in solution. TEM analysis of the materials was the first characterization method employed as it allows for visualization of the aggregation state on the nanoscale level and changes in particle morphology; however, since this analysis is completed in the solid state, solution-based aggregation cannot be confirmed since solvent evaporation has been shown to lead to nanorod self-assembly.[229,277]

TEM images of both species of Au nanorods under investigation dissolved in various concentrations of Tris buffer are shown in Figure 4.4. Parts a and b of Figure 4.4 show the aggregation state of the nanorods prepared using 2.00 μL of Au seeds dissolved in 4.00 and 40.0 mM buffer, respectively. Attempts to obtain images from nanorods dissolved in buffer at concentrations >100 mM failed due to salt precipitation on the grid surface. Note that based upon UV-vis evidence aggregation of the nanorods is predicted at a buffer concentration of 40.0 mM, while the other species should remain unchanged. Indeed, such results are confirmed by the TEM images. The nanorods dissolved in 4.00 mM buffer demonstrated independent rods along the surface of the grid, consistent with lack of aggregation. For the nanorods
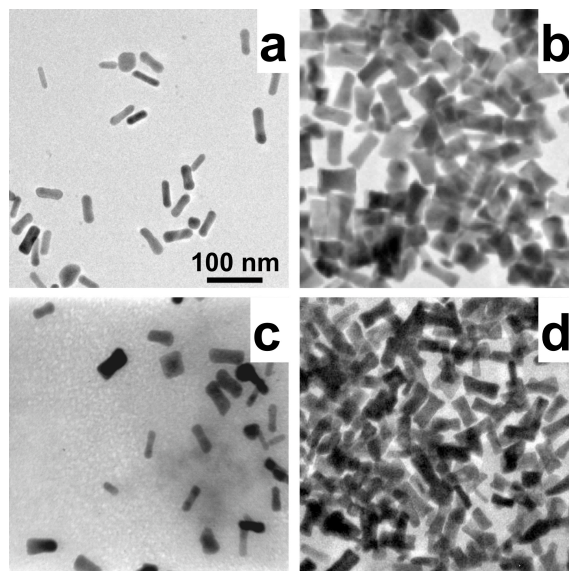
Figure 4.4 TEM images of the Au nanorods dissolved in Tris buffer. Parts (a) and (b) demonstrate the 2.00 μL Au nanorods dissolved in 4.00 and 40.0 mM Tris buffer, respectively, while parts (c) and (d) were obtained from the 4.00 μL Au nanorods dissolved in 4.00 and 40.0 mM buffer. Images obtained from nanorods dissolved in higher buffer concentrations were unable to be obtained due to salt precipitation on the TEM grid. The scale bar in part (a) is 100 nm and is representative for all images.

dissolved in 40.0 mM buffer, a dramatic change in particle morphology and aggregation state is clearly noted. For these materials, irregularly shaped species in which nanorods with transversally extended tips are observed. Most importantly, these materials are highly aggregated on the surface of the TEM grid. Due to this fact, images of individual nanorods could not be obtained; therefore, an accurate assessment of the particle size was not possible. Identical results were obtained for nanorods prepared using 4.00 μL of Au seeds, as shown in Figures 4.4c and d, suggestive of an aggregation/assembly process that is irrespective of particle dimensions. While this analysis is indicative of materials' aggregation, only a small fraction of the materials can be observed. Other methods are required that analyzethe materials in solution to confirm solution-based aggregation of the Au nanorods.

ζ-Potential and DLS analyses were used to confirm the aggregation state of the Au nanorods in solution. Such analytical methods are extremely powerful as they can be used to determine the properties of the nanorods in the reaction solution of interest. Since the materials possess a high net positive charge due to the surfactant stabilizer, ζ-potential analysis is a useful tool. Changes in the charge state of the surface, in combination with DLS based sizing analysis, can be used to pinpoint the aggregation behavior, and the mode of assembly, of the materials in solution. Analysis of the ζ-potential for the materials is shown in Table 4.2. A trend of decreasing potentials is determined for the materials as the concentration of the Tris buffer media is increased. Initially, the Au nanorods synthesized using 2.00 μL of seeds possessed a ζ-potential of 52.4 ± 1.8 mV, which is consistent with previous results.[252,285] This number steadily decreased to 2.50 ± 0.4 mV for the materials dissolved in 60.0 mM

Table 4.2 ζ-Potential and DLS Aggregate Size Comparisons for Au Nanorods Dissolved in Various Concentrations of Tris Buffer

[Tris]	2.00 μL Au nanorods		4.00 μL Au nanorods	
(mM)	ζ-potential (mV)	Size (nm)*	ζ-potential (mV)	Size (nm)*
0.00	52.4 ± 1.8	71.6 ± 6.9	50.4 ± 1.3	87.5 ± 13.7
4.00	30.3 ± 3.6	67.0 ± 21.4	36.8 ± 9.6	70.9 ± 15.6
20.0	9.58 ± 0.7	835.7 ± 41.5	12.1 ± 0.6	843.3 ± 190.1
60.0	2.50 ± 0.4	211.3 ± 60.3	-0.97 ± 1.5	145.6 ± 28.3
200	---	131.1 ± 56.0	---	114.2 ± 37.8
400	---	75.4 ± 21.7	---	85.9 ± 20.0

* Represents the size of hydrated species in solution, either nanorods or aggregates, as determined by DLS.

Tris buffer. Subsequent ζ-potential analysis of materials dissolved in higher buffer concentrations was limited as the high solution ionic concentration interfered with the analysis. A similar trend in ζ-potentials was observed for the second set of Au nanorods (fabricated using 4.00 μL of seeds). For this set of materials, a maximum ζ-potential of 50.4 ± 1.3 mV was observed for the materials dissolved in deionized water. Similar to the first set of Au nanorods, this value decreased linearly as the buffer concentration increased with the analysis unable to be completed at a buffer concentration >60.0 mM. Taken together, the trend in ζ-potentials demonstrates a minimization of the surface charge states, from highly positive to nearly neutral, indicating that the surface is able to electrostatically bind the anions present in solution.

Changes to the surface charge state are the likely result of electrostatic binding of buffer anions to the surface of the positively charged Au nanorods. Such interactions have previously been observed for other nanomaterials[286-288] and are driving forces for their selected growth. To determine if electrostatic assembly/aggregation of the materials is occurring in the present system, DLS analysis of the nanorods was completed. DLS analysis of the materials prepared using 2.00 μL of seeds dissolved in water, as listed in Table 4.2, demonstrated an average size of 71.6 ± 6.9 nm. This value represents the averaged dimensions of the anisotropic shape in solution, including the hydrodynamic radius of the particles. Additionally, such a result is consistent with previous results in the literature.[285] Further analysis of the same nanorods dissolved in 4.00 mM buffer presented the same average size, within the error of the measurement, indicating that the materials

in solution are independent. Such a result is consistent with the UV-vis data that demonstrates nearly identical spectra of these two species. The aggregate size for the materials dissolved in 20.0 mM Tris buffer demonstrates a large shift to 835.7 ± 41.5 nm, indicating a large proportion of the materials in solution are aggregated. Note that this species demonstrated a dramatic red shift of the LSP band with a significantly broad peak. As we steadily increase the concentration of the buffer, aggregate sizes begin to decrease to 211.3 ± 60.3 and 131.1 ± 56.0 nm for materials dissolved in 60.0 and 200 mM Tris buffer, respectively, until the restoration of nonaggregated species in solution is achieved at 400 mM buffer conditions (75.4 ± 21.7 nm). Each value possesses a degree of error that is associated with the dispersity in the material's dimensions and the dispersity in the aggregate size.

Identical aggregation behaviors were also noted for the Au nanorods prepared using 4.00 μL of Au seeds. When these materials were dissolved in water, a size of 87.5 ± 13.7 nm was obtained. As these materials are dissolved in a low concentration of buffer, 4.00 mM, no aggregation is evident from the obtained particle size of 70.9 ± 15.6 nm. When these materials are subsequently dissolved in 20.0 mM buffer, a large aggregate size of 843.3 ± 190.1 nm is obtained. Smaller aggregates are further observed at higher Tris concentrations (145.6 ± 28.3 and 114.2 ± 37.8 nm for 60.0 and 200 mM, respectively), until a nonaggregated sample of materials is again obtained at the high buffer concentration of 400 mM (85.9 ± 20.0 nm).

Based upon the observed trends of LSP band shifting, TEM images demonstrating aggregation, changes in the ζ-potential, and the DLS-based size/aggregation analysis, it is likely that the Au nanorods aggregated in an

uncontrolled fashion at intermediate Tris buffer concentrations. Furthermore, it is highly likely that electrostatic interactions, mediated by the buffer anions, are the driving force for the formation of aggregates in solution. For the two sample sets of Au nanorods studied, at low Tris buffer concentrations ($\leq$ 10.0 mM) little to no aggregation of materials exists. As the concentration of buffer increases to between 10.0 and 100 mM, a dramatic shift of the LSP band is observed, accompanied by a decreased ζ-potential and an increased aggregate size in solution. This is likely the result of electrostatic aggregation of the nanorods through the templating of buffer anions along the cationic nanorod surface, thus minimizing electrostatic repulsion and leading to aggregation and eventual precipitation. Over this concentration range, the LSP band is typically red-shifted, but at 50.0 mM, the peak position is actually blue-shifted as compared to the original position. El-Sayed and co-workers have previously demonstrated that end-to-end linkages of Au nanorods produces a red-shifted LSP band, while side-to-side aggregation of nanorods produces a LSP peak that is blue-shifted.[225] This is suggestive that side-to-side aggregation dominates in species dissolved in buffers that result in a blueshifted LSP peak (50.0 mM), but a more thorough analysis of the particles in solution is required to confirm this hypothesis. Such methods are currently unavailable.

The uncontrolled aggregation of the Au nanorods in solution is likely mediated by the polycationic surface of the materials due to the CTAB surfactant that is present, which is known to electrostatically interact with negatively charged polymers in solution.[289] The stability of nanorods in solution is dictated by two key factors: electrostatic repulsion between the charged materials and steric constraints, both of

which are attributable to the CTAB surfactant.[277] The surfactant is cationic under any condition due to the quaternary ammonium head group of the molecule. Dissolving of the materials in Tris buffer at pH 7.42 introduces monovalent anions to the species, which can electrostatically bind to the cationic surface. These anions include hydroxide ions present at pH 7.42, as well as chloride ions in the buffer. The chloride ions are present due to the HCl that was used to titrate the buffer. The ionic strength of solution has been demonstrated to result in self-assembly of Au nanorods as the solvent was evaporated based upon electrostatic interactions.[229] In that experiment, the evaporation process likely drove aggregation,[229,277] whereas in the present study, aggregation is occurring directly in solution. Upon electrostatic binding of the anions to the nanorod surface, the overall positive charge of the nanorod decreases as determined by ζ-potential analysis. By the partial shielding of the positively charged surface with the buffer anions, the electrostatic repulsion between the nanorods in solution is decreased.[217] Once the decrease in charge reaches a critical level, at approximately 15.0 mM Tris buffer, the materials are able to aggregate in solution. At this point, the effects of electrostatic repulsion have been overcome, thus allowing the materials to reach an interrod distance in which aggregation can occur. Additionally, once aggregated, mixing of the surfactant layers may occur,[277] which can account for the stability of the aggregates in solution. Indeed, precipitation of the materials with the most-shifted LSP bands is observed within 24.0 h. Furthermore, aggregation of the materials at high buffer concentrations is not observed. At such high concentrations of anions present in solution, >100 mM Tris buffer, a sufficient number of negative charges have bound to the surface of each individual nanorod,

resulting in neutralization of the surface potential. At this point, a charged double layer has been formed along a significant fraction of the Au nanorod surface. With the formation of a double layer, interrod repulsion is restored, thus restoring the solution stability of the nanorod.[290]

To test if the described buffer-mediated electrostatic aggregation theory results in the observed phenomenon, a set of control experiments was conducted; a NaCl solution, adjusted to pH 7.42 by NaOH, was used to determine if similar aggregation trends were observed. The UV-vis results are presented in Figure 4.5 with a complete UV-vis analysis presented in Appendix III (Figure A4.2). For this analysis, a very similar aggregation profile is observed as compared to the trend of Tris buffered solutions, except that a sharper aggregation transition is observed. Figure 4.5a specifically shows the UV-vis analysis for the aggregation of Au nanorods prepared using 2.00 μL of seeds in increasing concentrations of NaCl. The position of the LSP band is constant at 705 nm for solutions prepared using increasing concentrations of NaCl until the nanorods are dissolved in 20.0 mM NaCl. At this concentration, the LSP band red shifts to 900 nm consistent with uncontrolled aggregation of the nanorods. When the Au nanorods are dissolved in 30.0 mM NaCl, the LSP is still red-shifted by approximately 100 nm, consistent with aggregation of the nanorods in solution,[225] which is also similar to the trend of the Tris-buffered nanorods described above. At concentrations >30.0 mM NaCl, a trend toward the restoration of the unaggregated UV-vis spectra is observed. An identical tendency is observed for Au nanorods prepared using 4.00 μL of seeds, as shown in Figure 4.5b, demonstrating that electrostatic aggregation of nanorods in solution is possible, regardless of either
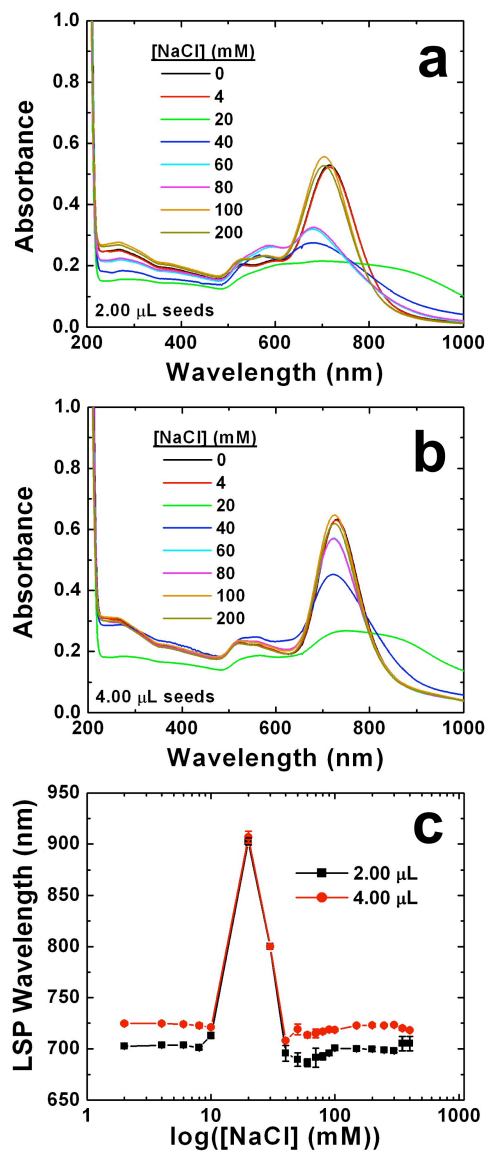
Figure 4.5 UV-vis analysis of the effects of the concentration of NaCl, pH 7.42, on Au nanorods in solution. Part (a) and (b) display the effects of individual salt concentrations on the shifting of the LSP band of Au nanorods fabricated using 2.00 and 4.00 μL of Au seeds, respectively. Part (c) demonstrates the dependence of the LSP peak position upon the concentration of the NaCl solution used to dissolve the materials.

161

the nanorod dimensions or the anionic species. A full UV-vis peak analysis is displayed in Figure 4.5c showing the direct comparison of the two species, which shows identical solution-based aggregation.

TEM analysis of the NaCl-mediated solution assembly of Au nanorods is presented in Figure 4.6. For the solution prepared using 4.00 mM NaCl, individualized Au nanorods are observed for the materials fabricated using 2.00 μL of Au seeds (Figure 4.6a). When these same nanorods are dissolved in a 20.0 mM NaCl solution (Figure 4.6b), large aggregates are observed on the TEM grid in the solid state. A mass-based aggregate structure is observed, which is identical to the uncontrolled assemblies observed from materials dissolved in 40.0 mM Tris. Materials obtained from a 20.0 mM solution of NaCl and 40.0 mM solution of Tris buffer were selected for TEM analysis as they demonstrated a large degree of aggregation as determined by UV-vis analysis. Identical assemblies at 4.00 and 20.0 mM NaCl are observed for the nanorods prepared using 4.00 μL Au seeds as shown in Figures 4.6c and d, respectively.

ζ-Potential and DLS analyses of the materials studied in the NaCl solutions are presented in Table 4.3. For the materials prepared using 2.00 μL of Au seeds, a linear decrease in the surface charge is again observed with increasing concentrations of NaCl. The surface charge approaches 0.00 mV as the NaCl concentration increases to 60.0 mM, as would be expected for electrostatic shielding of the cationic charge of the surface CTAB species. Note that this charge minimization trend is nearly identical to the one observed using Tris buffer. DLS analysis of these materials is also wholly consistent with the proposed aggregation trend as we observe no aggregation for Au
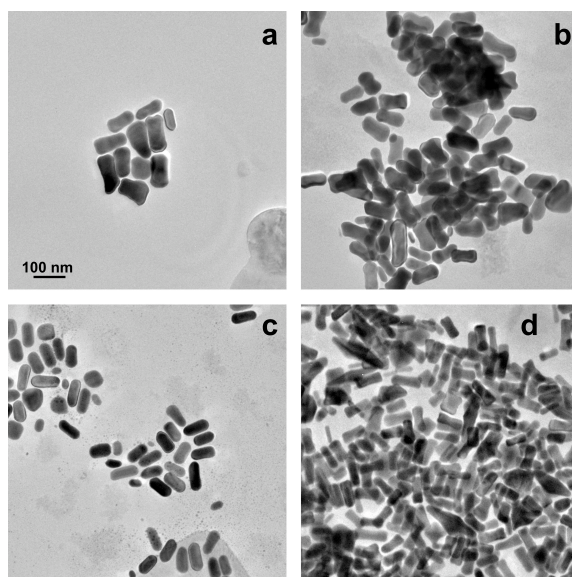
Figure 4.6 TEM images of the Au nanorods dissolved in aqueous NaCl solutions. Parts (a) and (b) demonstrate the 2.00 µLAu nanorods dissolved in 4.00 and 20.0 mM NaCl, respectively, while parts (c) and (d) were obtained from the 4.00 µL Au nanorods dissolved in 4.00 and 20.0 mM NaCl. Images obtained from nanorods dissolved in higher salt concentrations could not be obtained due to salt precipitation on the TEM grid. The scale bar in part (a) is 100 nm and is representative for all images.

163

Table 4.3 ζ-Potential and DLS Aggregate Size Comparisons for Au Nanorods Dissolved in Various Concentrations of NaCl

[NaCl]	2.00 μL Au nanorods		4.00 μL Au nanorods	
(mM)	ζ-potential (mV)	Size (nm)*	ζ-potential (mV)	Size (nm)*
0.00	52.4 ± 1.8	71.6 ± 6.9	50.4 ± 1.3	87.5 ± 13.7
4.00	44.8 ± 3.7	68.9 ± 30.2	43.3 ± 2.1	93.0 ± 35.6
20.0	10.2 ± 0.9	515.7 ± 89.0	10.2 ± 5.0	548.4 ± 117.9
60.0	1.93 ± 1.6	253.2 ± 30.3	1.68 ± 3.0	263.3 ± 32.9
200	---	119.6 ± 26.2	---	92.5 ± 36.7
400	---	107.3 ± 19.7	---	80.5 ± 20.5

* Represents the size of hydrated species in solution, either nanorods or aggregates, as determined by DLS.

nanorods dissolved in a NaCl solution of 4.00 mM; however, a large degree of aggregation is observed for materials dissolved in 20.0 mM NaCl (515.7 ± 89.0 nm). Note that this is the solution concentration that displays the maximum red-shifted LSP peak in the UV-vis and showed large area aggregates by TEM analysis. As the concentration of NaCl continues to increase, the aggregate size decreases linearly, as expected, thus demonstrating a smaller aggregate state at high NaCl concentrations.

Nearly identical results for ζ-potential and DLS analyses for the Au nanorods synthesized using 4.00 μL of Au seeds are observed. Again, a trend of decreasing surface charge is observed with increasing NaCl in solution, from 50.4 ± 1.3 mV at a solution concentration of 0.00 mM to 1.68 ± 3.0 for 60.0 mM NaCl, which is consistent with surface charge shielding. DLS analysis of the aggregates demonstrates the aggregation trend of minimal to no aggregation at low NaCl concentrations (< 20.0 mM) and maximal aggregation as expected at 20.0 mM, with an aggregate size of 548.4 ± 117.9 nm. As this concentration is increased, the nanorods become less aggregated, indicative of formation of a complete electronic double layer, which prevents undesired aggregation in solution. These aggregation trends for both species are consistent with the Tris-buffer-mediated trend described above, indicating that electrostatic aggregation is of concern for the cationically charged Au nanorods in solution.

4.5. Summary and Conclusions

Here we have demonstrated the stability and electrostatic aggregation of Au nanorods, which is mediated through the anions that are present in solution. We have chosen to study this effect using Tris-buffered media as biological applications of

nanomaterials are in high demand. At low buffer concentrations, no aggregation is observed, but significant aggregation is demonstrated at buffer concentrations ranging between 10.0 and 100 mM. While the mechanism of aggregation may vary based upon buffer concentration, the species that drives the process is likely to be the buffer anions, which can shield the surface charge of the Au nanorods that is used to prevent aggregation. Once a sufficient reduction in charge has been achieved, and thus interrod repulsion has been minimized, aggregation of the materials occurs. Eventually, at higher buffer concentrations, complete binding of the individual nanorod surface with anions is possible, resulting in the formation of an electronic double layer, which prevents aggregation and results in a decrease in the surface potential of the materials. These results were subsequently confirmed using a NaCl solution that was titrated to a pH of 7.42. Together, these results demonstrate that aggregation of Au nanorods can occur in solution based simply upon the anions of the solvent used. Additionally, we have shown that through judicious selection of the solution system, charge-based tuning of the nanorod surface is possible to allow for selective surface interactions to occur. Nanorods represent a material of interest for biological applications, both *in vitro* and *in vivo*; therefore, this study suggests that complete characterization of the aggregation state is required to optimize the system. Biological systems can be drastically different, so varying degrees of aggregation/uncontrolled assembly can be envisioned. By using materials in different states of aggregation, functionalization and activity would be expected to be different. These results are applicable to not only the individual systems studied but likely to any system to which the nanorods are being employed. As a result, this study suggests that optimization of the reaction system is needed to ensure maximal

reactivity. Instead, as discussed in next chapter, suitable information can be obtained from the aggregation patterns of Au nanorods in the presence of small biomolecules.

This Chapter has been reproduced with permission from the following publication: copyright ACS publications

Sethi, M.; Joung, G.; Knecht, M.R. Stability and Electrostatic Assembly of Au Nanorods for use in Biological Assays, *Langmuir* **2009**, *25*, 317-325.

Chapter 5: Linear Assembly of Au Nanorods Using Biomimetic Ligands

5.1. Overview of Study

The main goal of self-assembly processes is to arrange nanomaterials in specific orientations to produce designer three-dimensional architectures. These structures are produced in response to desired target systems where a specific arrangement of materials is required for structural, electronic, or optical applications. The level of complexity attained using present materials-based processes is relatively low, while highly complex structures are regularly produced in Nature through processes developed after millennia of evolution. By modeling biomimetic processes with current materials designs, production of highly structured and three-dimensionally assembled materials is possible. Simple amino acids represent starting bio-based systems to study the biomimetic assembly of nanomaterials in solution. In this study, evidence demonstrating that the assembly of Au nanorods into linear structures using the simple amino acid is controlled by both thiol and amine attachment to the tips of adjacent nanorods has been presented. This structural motif was isolated by studying the assembly process using cysteine and its biomimetic homologues 3-mercaptopropionic acid and cysteamine at a variety of solution pH values and ionic strengths. Understanding the fundamental mechanism of assembly for small biological molecules may prove useful in the development of assemblies based upon larger species such as peptides and proteins.

5.2. Introduction

Au nanoparticles represent targets for advanced applications ranging from biological and chemical sensors to therapeutics, with special emphasis on their assembled structures.[161,211,212] The interest in these materials arises from their unique properties that

are obtained based upon their size, including vibrant optical properties, a high surface-to-volume ratio, and simple surface functionalization.[165,212] These desirable properties can be enhanced and manipulated based upon their three-dimensional structural arrangement composed of nanoparticle building blocks.[211,291] A variety of methods have been developed through which self-assembly of the individual particles can occur, including DNA hybridization,[211] electrostatic interactions,[286,292] and crosslinkable surface ligands;[272] however, the control over the final assembled architecture is minimal. Recently, asymmetric functionalization of the nanoparticle surface has been studied, resulting in materials with a controlled surface ligand organization.[29,293] Assembly of these materials in solution can ultimately be controlled to a higher degree, resulting in specifically designed structures. The current challenge in the self-assembly process is two-fold: first, what is the mode of assembly and second, how can it be controlled to produce specific products. Understanding of these two key points will allow for integration of the assembly process into higher ordered architectures with additional functionality and durability.

Au nanorods are a unique subset of Au nanoparticles that have been of particular interest due to their anisotropic shape, resulting in enhanced optical properties.[161,227,228] Their unique architecture is prepared in solution using a seed-mediated method in which the cationic surfactant cetyltrimethylammonium bromide (CTAB) is attached to the long axis of the materials.[228] As a result of the synthetic conditions, materials with a variety of lengths can be prepared up to approximately 450 nm. The final materials possess a significant positive charge and are highly water-soluble, thus making them sensitive to the ionic strength of the selected media.[294] Based upon their metallic structure, nanorods

possess two distinct surface plasmon bands associated with their transverse (TSP) and longitudinal (LSP) axes.[225] The position of the LSP band is determined based upon the aspect ratio of the materials and is typically observed in the near-IR region of the electromagnetic spectra.[161,226] It is highly sensitive to changes near the particle surface, thus positioning nanorods as desirable optical materials.[225,273] Additionally, Au nanorods have been used for extensive applications, including biological sensors,[161,273] cellular targeting materials,[249,251,295] and substrates for surface enhanced Raman spectroscopy.[296,297]

Future applications for Au nanorods require their assembly in a highly controlled manner for signal propagation and electronic applications.[283] Within the past few years, extensive efforts have been made to assemble Au nanorods in a linear fashion,[272,274,275,298-300] whose chain-like structures may prove to be significant as device components. Linear nanochains are achieved by attachment of assembling ligands specifically to the nanorod tips. This region of the material is preferentially functionalized over the longitudinal nanorod facets due to the minimal surface concentration of CTAB present at this region.[275] A variety of linear assembly methods have been developed including biotin-streptavidin binding,[275] antigen-antibody binding,[274] hydrogen bonding,[213,301] α,Ω-alkanedithiol crosslinking,[272] and crown ether/cation recognition.[300]

Recently, the amino acid cysteine has been discovered to mediate the crosslinking of nanorods and other nanomaterials in a linear end-to-end fashion.[298,299,301] A variety of structures have been obtained including chains of nanorods, nanonecklaces, and alternating bipyramid-nanosphere chains.[298,299] The mechanism of formation is believed

to arise from thiol attachment to the Au nanorod tip followed by cross-linking via two-point electrostatic interactions of the exposed zwitterionic functionalities.[298,299] In this cooperative set-up, the positively charged amines and negatively charged carboxylates on a Au nanorod surface form electrostatic interactions with their oppositely charged counterparts on the adjacent Au nanorod tip to stabilize the assembled structure. Based upon the described mechanism, assembly of the materials is likely to be highly sensitive to the solution conditions, such as pH and ionic strength, which could prevent, alter, or aid in the assembly of the materials.

Recently, Sun *et al.* have demonstrated the assembly and disassembly of cysteine-assembled Au nanorods through changes in solution pH.[214] While the technological advantages of selectable assembly versus disassembly has applications ranging from components in electronic devices to structures for sensing capabilities, the exact mechanism of this process and what controls these interactions remains unclear. This unique ability thus positions cysteine as a key player in the subsequent device-based application of assembled Au nanorods. Surprisingly, assembly of the materials optimally occurred at low pH values, which approached the pKa of the α-carboxylate group.[214] At such pH conditions where the protonated acid is present, two point electrostatic interactions are unlikely. To develop control over the final materials architecture and functionality, which is based upon the assembling activity of cysteine, it is important to understand the mechanism of formation and what interactions dominate in the system. Overall, the effects of standard reaction conditions on the cysteine-mediated self-assembly process of Au nanorods are only scarcely understood; therefore, a clear

understanding of both the mechanism of formation and the final product's structure is currently unknown.

The study reveals occurance of non-electrostatic assembly of Au nanorods using cysteine and the homologues 3-mercaptopropionic acid (MPA) and cysteamine presented in Figure 5.1. Using simple changes in solution pH, it was observed that there occurs the formation of end-to-end assemblies of nanorods mediated by cysteine that is most active below the pKa value of the α-carboxylate group, as shown in Scheme 5.1, thus prohibiting two-point electrostatic assemblies. At higher pH values, where the zwitterionic structure exists, only independent Au nanorods are observed. To confirm these results, the cysteine homologues were used to study their assembly properties to isolate the structure-directing moieties. Taken together, the results indicate that the linking action of cysteine is likely to be mediated by attachment of both the thiol and α-amine functionality to adjacent nanorods. Attachment is preferential at pH values where the carboxylic acid is protonated, and the charged amine is no longer electrostatically interacting with neighboring moieties. Once free, the amine is able to bind to the surface of a second nanorod, resulting in a linear, one-dimensional assembly of materials. As multiple cysteine molecules are isolated at the nanorod tip, multiple cross-linkages can occur to stabilize the assembled structure. These results demonstrate the conditions that control the overall assembly process of Au nanorod using multiply charged species that may prove to be useful in fabricating assemblies involving larger biomolecules.
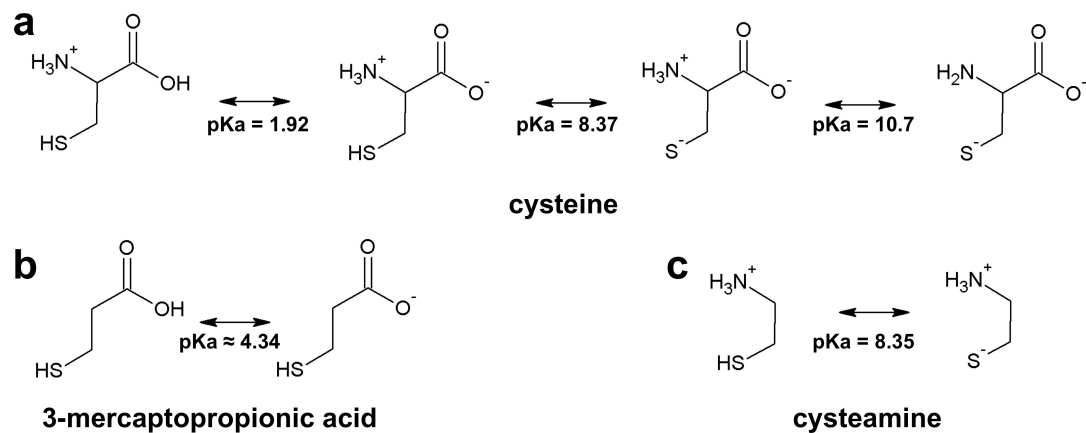
Figure 5.1 Bio-inspired molecules used in the assembly of Au nanorods: (a) cysteine, (b) 3-mercaptopropionic acid, and (c) cysteamine.
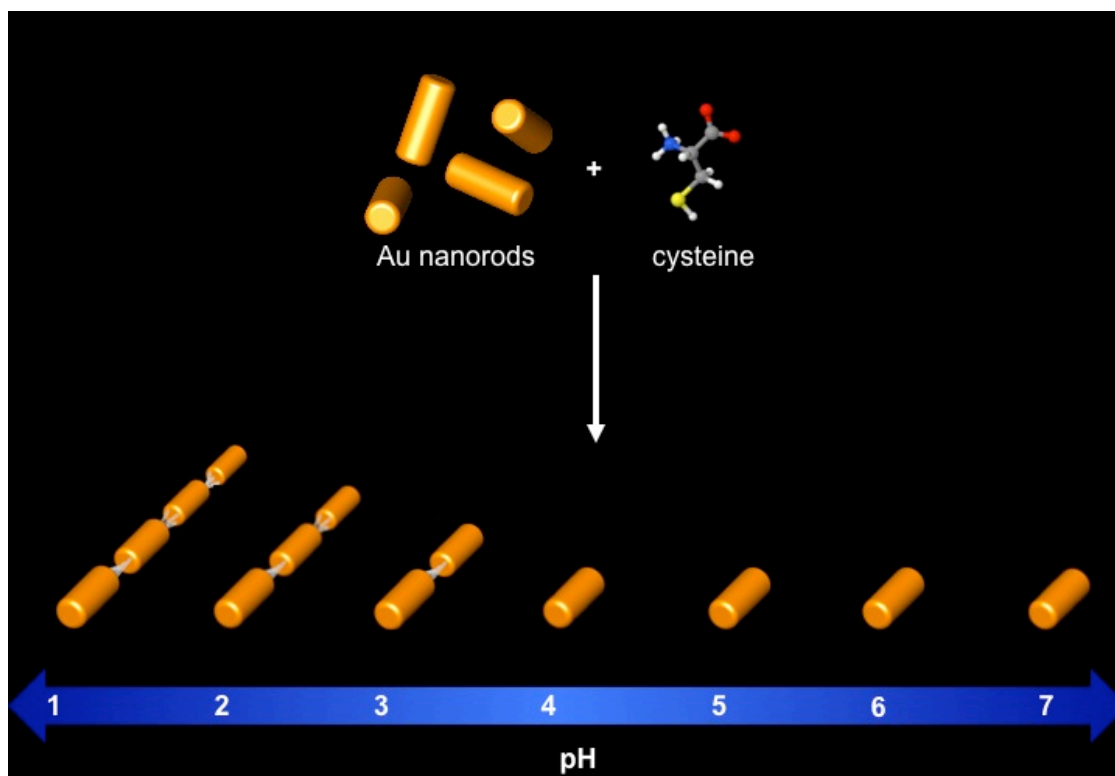
Scheme 5.1 Effect of pH on the cysteine-based assembly of Au nanorods.

5.3. Methods

5.3.1. Chemicals

HAuCl$_4$•3H$_2$O (99.999%), 3-Mercapto propionic acid (MPA) and CTAB (≥99.0%) were purchased from Sigma-Aldrich (St. Louis, MO). NaBH$_4$ (≥98%) was purchased from EMD (Gibbstown, NJ), ascorbic acid was purchased from J. T. Baker (Phillipsburg, NJ), AgNO$_3$ (ACS Grade) was purchased from BDH (VWR, Radnor, PA), cysteamine (2-aminoethanethiol) was purchased from Acros Organics, and cysteine (≥97%) was purchased from SAFC (Lenexa, KS). All chemicals were used as received. Milli-Q water (18 MΩ· cm) (Millipore, Bedford, MA) was used throughout.

5.3.2. Preparation of Au Seeds

Au nanorods were prepared using the seed-mediated method in water.[228] Au seeds were prepared as follows. First, 250 μL of a 10.0 mM HAuCl$_4$ solution was added to 7.50 mL of 100 mM CTAB in water that was kept at a constant temperature of 25.0 °C to prevent surfactant precipitation. The solution turned a deep orange color immediately upon addition. Second, after the solution was mixed by inversion, 600 μL of a freshly prepared 10.0 mM NaBH$_4$ solution was added at once. Upon addition of the reductant, the solution color turned pale brown. After gentle mixing, the solution was left undisturbed for at least 2.00 h before use and discarded 5.00 h postsynthesis.

5.3.3. Fabrication of Au nanorods

Upon seed production, growth of the Au nanorods was completed on a 100 mL scale. For this, 94.4 mL of 100 mM CTAB was added to a 250 mL glass bottle, to which 4.00 mL of 10.0 mM HAuCl$_4$ was added. Next, 600 μL of fresh 10.0 mM AgNO$_3$ and 640 μL of 100 mM ascorbic acid were added. After each reactant addition, mixing of the

solution by the inversion method was completed. Finally, 420 µL of Au seeds was added followed by gentle mixing by inversion about 10 times. The reaction was allowed to stand for approximately 2.0 h at 25.0 °C before use.

5.3.4. Nanorod Assembly

The assembly of Au nanorods using the amino acid cysteine and its biomimetic homologues was completed using solutions at various pH values. The aqueous solvent was obtained through titration of water to an appropriate pH (1.0 - 7.0) using HCl or NaOH as needed. All solutions were titrated to the exact pH without passing the desired end point to minimize addition of excess ions in solution.

For assembly experiments, 1.00 mL aliquots of the crude Au nanorods were centrifuged at 14,600 RPM for 10.0 min to pellet the materials. The supernatant of excess CTAB was discarded and the pellet was redissolved in 2.982 mL of water at the appropriate pH value. UV-vis analysis confirmed the stability of the nanorods. To the reaction, 18.0 µL of an aqueous 100 mM cysteine solution was added and mixed thoroughly. The progress of the reaction was then measured using UV-vis spectroscopy.

5.3.5. Characterization of the Au Nanorod Assembly

For each sample, time resolved UV-vis spectra were obtained using an Agilent 8453 UV-vis spectrometer that can support eight samples at a time. In each well, 3.00 mL quartz cuvettes of 1.00 cm path-length were used. Over a period of 4.00 h, spectra were recorded at 10.0 min intervals; however, for some pH values, the precipitation of the Au nanorods was found to occur as quickly as 10.0 min, so readings were obtained at 1.00 min intervals. For each pH value, a control was studied in which no cysteine was added to confirm the observed spectral changes. All spectra were background subtracted against

water, the solvent. The cysteine homologues, MPA and cysteamine, were studied in an identical manner.

To probe the assembly state, transmission electron microscopy (TEM) and dynamic light scattering (DLS) analysis were employed. TEM analysis of the Au nanorods was used to confirm their assembly state. 5.00 µL aliquots of each sample were pipetted onto 400 mesh Cu grids coated with a thin layer of carbon (EM Sciences), and were subsequently dried in a desiccator. The images were obtained on a JEOL 2010F TEM with a point-to-point resolution of 0.19 nm operating at 200 keV. Solution-based DLS analyses were completed on a Zetasizer Nano ZS System (Malvern Inc.). Solutions to be analyzed were allowed to react for 4.00 h prior to analysis and each reaction was monitored by UV-vis to correlate the assembly results.

5.4. Results and Discussion

5.4.1. Cysteine Mediated Nanorod Assembly

Au nanorods were fabricated via the seed-mediated method using CTAB as the surface passivant.[161,228] The Au seeds were prepared 2.00 h prior to their use in the nanorod growth solution to allow for complete reduction. Once added to the nanorod growth solution, the materials were incubated at 25 °C for 2.00 h from which the solution turned a deep purple-red color. UV-vis analysis was used to confirm nanorod production by observation of the LSP band. After fabrication, 1.0 mL of the crude material was centrifuged to produce a pellet and redissolved in 2.982 mL of water titrated to the appropriate pH. To this, 18.0 µL of a freshly prepared 100 mM cysteine solution was added and the formation of nanorod chains was monitored using UV-vis spectroscopy at

room temperature. Addition of this volume resulted in a 600 μM reaction concentration of cysteine, whose charge state is shown in Figure 5.1a depending upon the solution pH.

Initial analysis of the assembly process was studied using UV-vis spectroscopy. Such a technique is highly sensitive to the assembly state of the materials by shifts in the LSP peak.[213,214,225] Figure 5.2a displays the effect of cysteine, at a reaction concentration of 600 μM, upon the UV-vis spectra of the Au nanorods in solution at a pH value of 1.0. Note that at this concentration the cysteine molecule is positively charged due to protonation of the carboxylate group; the pKa of this moiety is ~2.0. At t = 0 min, immediately prior to the addition of cysteine, a LSP band was observed at 770 nm. Upon incubation with the amino acid, the intensity of the LSP peak begins to decrease with the formation of a new absorbance band at ~950 nm, with a clear isosbestic point at 835 nm. This peak continues to grow in intensity for 15.0 min, after which it begins to red shift to higher wavelengths. Eventually, once the newly formed absorbance reaches ~1060 nm, the intensity begins to decrease due to precipitation of the materials from solution.

Parts b and c of Figure 5.2 represent of the results obtained from the same experiment described above using a solution pH of 2.0 and 3.0, respectively. Similar results as to those attained at pH 1.0 were observed; however, the rate of formation of the 950 nm peak is clearly decreased with increasing pH values. At pH 2.0, the original LSP peak at 770 nm decreases over time upon the addition of cysteine, with formation of a new peak at 950 nm. The new peak continues to grow over the time period studied, 4.0 h, with no red shifting or precipitation as observed at pH 1.0. For the analysis at pH 3.0, changes to the UV-vis spectra are clearly noted; however, the rate of change is decreased as compared to pH 1.0 and 2.0. Upon cysteine addition, the LSP peak of the Au
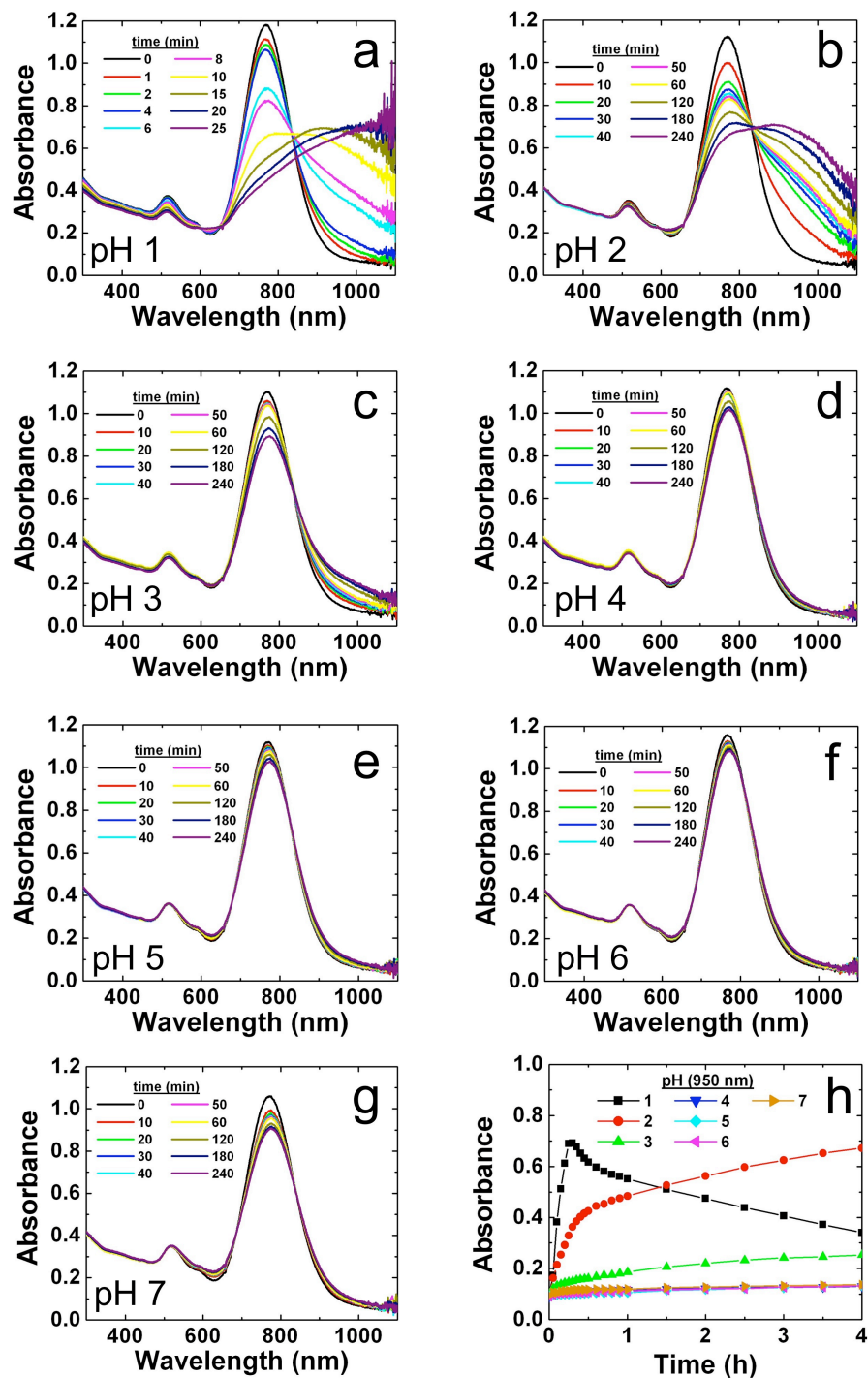
Figure 5.2 UV-vis analysis of the pH dependent cysteine mediated assembly of Au nanorods at (a) pH 1.0, (b) pH 2.0, (c) pH 3.0, (d) pH 4.0, (e) pH 5.0, (f) pH 6.0, and (g) pH 7.0. Part (h) displays the time evolution for the production of the assembled LSP peak at 950 nm for all pH values studied.

nanorods does decrease in intensity with an increase in absorbance at longer wavelengths, but a clear and defined peak is not observed at 950 nm. Similar to pH 1.0, an isosbestic point at 835 nm is observed for both reactions at pH 2.0 and 3.0. As shown in Figures 5.2 d-g, at all other pH values studied, between 4.0 and 7.0, no clear change in the absorbance spectra of the Au nanorods is observed over the time range studied.

For a full comparison, the growth of the 950 nm absorbance versus reaction time for all pH values studied is presented in Figure 5.2h. From this comparison, it is evident that the growth of this absorbance is inversely proportional to the solution pH such that as the pH decreases, an increased rate in spectroscopic change is observed. For pH 1.0, the 950 nm absorbance rapidly grows in intensity for 15.0 min, after which its intensity decreases due to the peak shifting described above. For pH 2.0 and 3.0, the absorbance intensity at 950 nm steadily grows; however the rate of formation is greater for pH 2.0 over 3.0. The absorbance intensity for these species remains on a positive slope as no shifting of 950 nm peak is observed during the time of analysis. Finally, no change in the absorbance at 950 nm is noted for those species studies at a pH $\geq$ 4.0.

The changes in the UV-vis spectra for the reactions at pH values between 1.0 and 3.0 are likely due to cysteine-based assembly of the Au nanorods. It is well documented that changes in the assembly state of Au nanomaterials results in significant alterations to their overall absorbance properties.[213,214,272,298,299] Using the discrete dipole approximation method, El-Sayed and coworkers have demonstrated that the directionality of the shift of the LSP peak of Au nanorods is directly linked to their specific assembly state: a blue shift is observed for side-to-side assembly, while a red shift is observed for tip-to-tip structures.[225] The number of nanorods per aggregate and their internanorod

180

distance controls the final position of the assembled peak.[225]   Similar results have recently been reported by Sun *et al.* using finite-difference time domain calculations.[214] Since our materials at low pH values demonstrate a clear red shift, it is likely that tip-to-tip nanorod assembly is occurring in solution mediated by cysteine. Note that at these low pH values, a significant fraction to nearly all of the amino acid species are positively charged and possess protonated carboxylic acid groups, which is a key point to understanding their assembly mechanism, as described below.

Three key points of the changes to the UV-vis spectra are suggestive of selected directional materials assembly and can be used to describe the process: the isosbestic point, the formation of a new and broad peak at 950 nm, and the subsequent shifting of this peak to higher wavelengths.[272]   First, the isosbestic point, in conjunction with the new absorbance at 950 nm, indicates that the Au nanorods exist in two different states. Through mechanistic studies using α,Ω-alkanedithiol, Thomas and coworkers have suggested that this initial transition is the formation of nanorod dimers from the individual units.[272]   In addition to dimers, it is likely that structures containing more than just two nanorods are produced due to the broadness of the assembled peak at 950 nm. Eventually, as the concentration of individual Au nanorods in solution is exhausted, which is observed by the lack of a peak at 770 nm (Figure 5.2a, t = 20.0 min), the dimer peak begins to red shift. This shifting is due to the oligomerization of the nanorod dimers in solution to form chains that are longer in length. Again, this shifting peak is quite broad, which, based upon theoretical calculations and dithiol mechanistic studies, suggests that a variety of chain lengths are present.[214,225,272]   This growth process continues in solution and is controlled by the concentration of linking molecules such that

at higher concentrations, longer chain lengths are produced.[272]   Eventually, a critical chain length is reached, resulting in precipitation of the materials as observed at pH 1.0. No shifting or precipitation was observed at pH 2.0 or 3.0, suggesting that the ability of the assembling species in solution is lower than at pH 1.0.

TEM analysis of the materials was used to confirm linear nanorod assemblies. Analysis of the unassembled materials demonstrated that the individual nanorods possessed dimensions of 51.5 ± 7.5 nm $\times$ 15.9 ± 2.5 nm with an average aspect ratio of 3.24 (Appendix IV, Figure A5.3). Figure 5.3a displays representative TEM images of the linear chains of Au nanorods prepared using cysteine at pH 1.0 at different magnifications (middle and right images). Statistical analysis of the aligned structures indicated that 85.4% of the nanorods were involved in end-to-end assemblies. Here, an end-to-end assembly was defined as materials with an inter-nanorod end-to-end distance of ≤ 1.0 nm. Control analysis of the materials subjected to the same condition in the absence of cysteine (left image of Figure 5.3a) demonstrated that only 9.8% of Au nanorods were aligned in an end-to-end fashion, which results from TEM sample preparation. Figures 5.3 b and c display the nanorod chains fabricated by cysteine for pH values 2.0 and 3.0, respectively. Under these conditions, 57.0% of the materials at pH 2.0 and 38.3% of the nanorods at pH 3.0 were involved in end-to-end assemblies. Such results are consistent with the spectroscopic results that suggested a lesser degree of aggregation for the higher pH values as compared to pH 1.0. Analysis of the nanorods incubated with cysteine at pH values ≥ 4.0 demonstrated mostly isolated species with <14.5% of the structures in an end-to-end assembly (Appendix IV, Table A5.1).
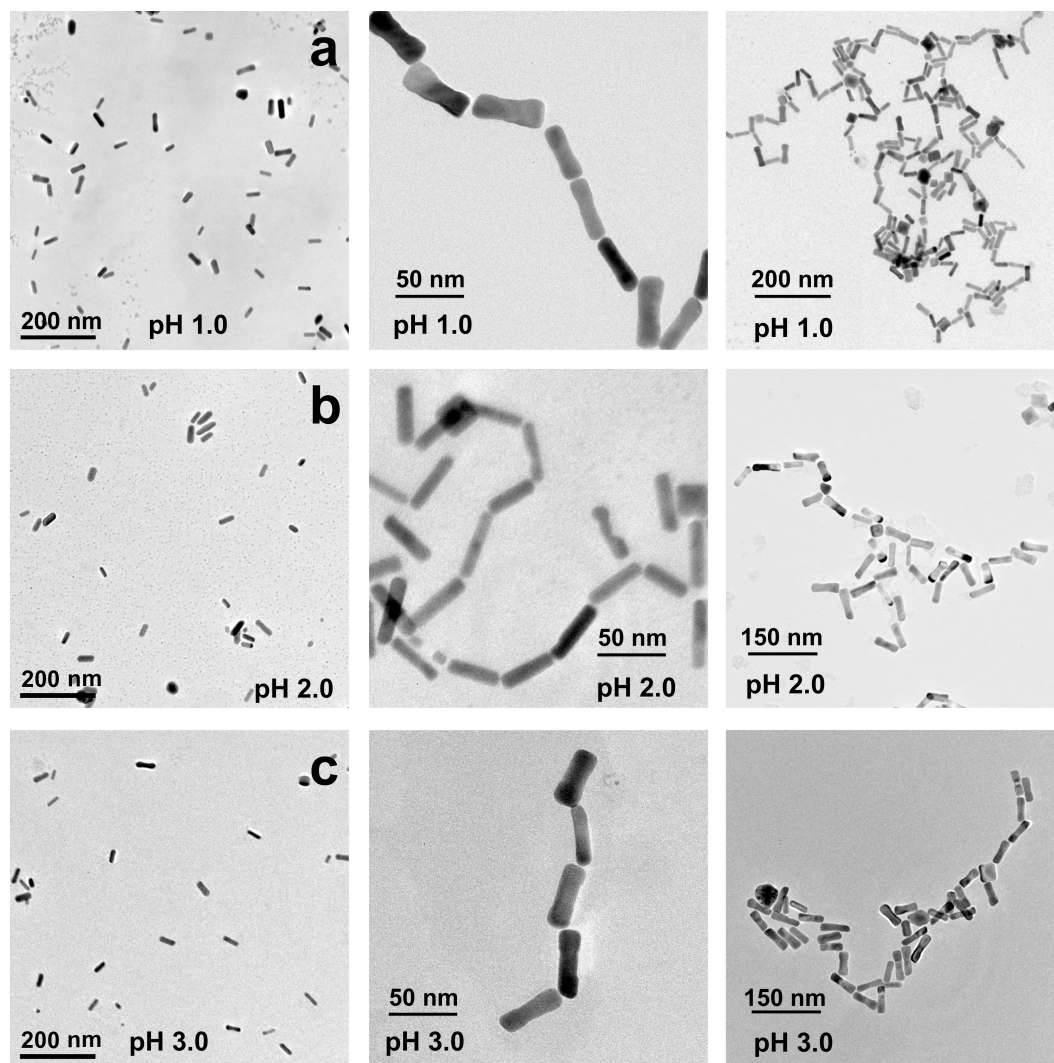
Figure 5.3 TEM micrographs of the cysteine assembled nanorods at (a) pH 1.0, (b) pH 2.0, and (c) pH 3.0. The image on the left is a representative TEM image of the materials at the appropriate pH in the absence of cysteine, while the middle and right representative images are in the presence of cysteine at different magnification levels.

To determine the extent of aggregation and aggregate size, analysis using TEM is difficult due to two specific reasons: only a small fraction of the materials are observed and mixing of the chains on the grid surface can artificially enhance the aggregate size. To overcome these limitations and address the actual aggregate dimensions, dynamic light scattering (DLS) analysis of the materials dispersed in solution was used. DLS allows for a more complete analysis of the degree of aggregation in which the whole sample set is analyzed, rather than a limited selection.[294] The sizes of the cysteine-derived aggregates in solution are presented graphically in Figure 5.4. At pH 1.0, an overall aggregate size of 598 ± 122 nm was observed for this sample set 10.0 min after cysteine addition. A short assembly time period was required due to the fast rate of spectrophotometric changes in the UV-vis analysis, and the resultant precipitation. As the pH was increased to 2.0 and 3.0, a smaller average aggregate size of 113 ± 10.9 nm and 131 ± 12.2 nm, respectively, was observed after 4.0 h of incubation with cysteine. For all other pH values (≥ 4.0), an overall size range of 43.4-55.2 nm was observed, which is consistent with the unassembled species in solution (*vide infra*). This suggests a lack of aggregation for the solutions at higher pH values, consistent with the UV-vis and TEM analysis.

To confirm that the observed results were the effect of cysteine and not associated strictly with the pH of the reaction environment, a set of spectroscopic, TEM, and DLS control studies were analyzed. For these controls, identical reaction conditions were studied in which the nanorods were dissolved in water of the appropriate pH value (from1.0 to 7.0); however, cysteine was not added to the system. Using these conditions, no shift or change in the UV-vis spectra of the materials at any pH value was observed;
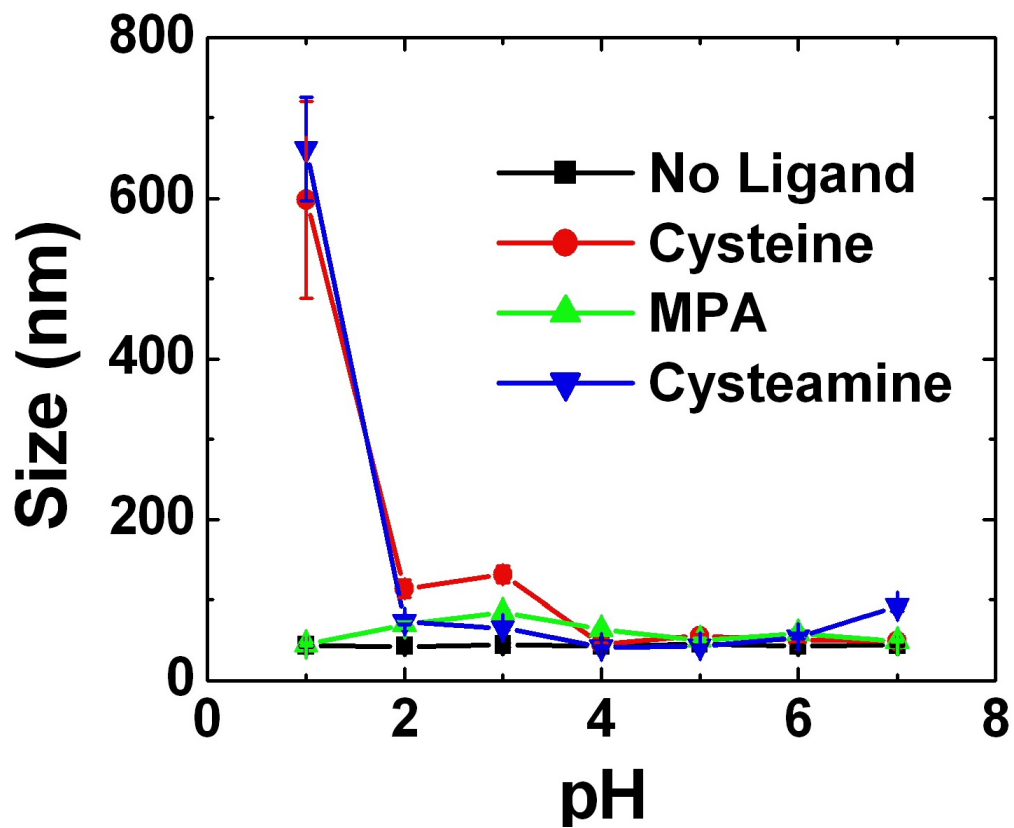
Figure 5.4 DLS analysis for the assembly of Au nanorods in the absence of assembling ligands (black curve) and in the presence of 600 μM cysteine (red curve), MPA (green curve), or cysteamine (blue curve).

the LSP peak remained constant at 770 nm over the 4.0 h reaction study (Appendix IV, Figure A5.1). TEM analysis of these materials demonstrated that the nanorods were unassembled and assumed a random orientation after solvent evaporation with a low fraction in an end-to-end arrangement (<10.5% for all pH values from 1.0 - 7.0; Appendix IV, Figure A5.2 and Table A5.1). Finally, DLS analysis at each pH value indicated that a particle size of between 43.0 and 44.2 nm was observed, with statistically overlapping degrees of error as shown in Figure 5.4. These results indicate that the changes in spectral properties and assembly observed for pH values 1.0 – 3.0 are indeed the effect of cysteine and not controlled by the pH of the solution only. This effect was surprising in light of the requirement of the zwitterionic species for the self-assembly process as has been suggested previously.[298,299]

5.4.2. 3-Mercaptopropionic Acid and Cysteamine Mediated Au Nanorod Assembly

To determine the mode of organization of cysteine, the assembly process using the cysteine homologues MPA and cysteamine was studied. The first UV-vis spectral analysis, shown in Figure 5.5, is for MPA. MPA has been shown to assemble Au nanorods through hydrogen bonding of the surface stabilized species;[213] therefore, assembly at low pH values was expected to be seen. Indeed, as shown in Figure 5.5b and c, spectroscopically observed assembly of the nanorods occurred at pH 2.0 and 3.0, which is below the carboxylate pKa value of 4.3; however, this assembly appears to be quite minimal as compared to cysteine. Based upon the UV-vis analysis, assembly of the nanorods occurred at a higher rate at pH 3.0, which decreased when studied at pH 2.0.
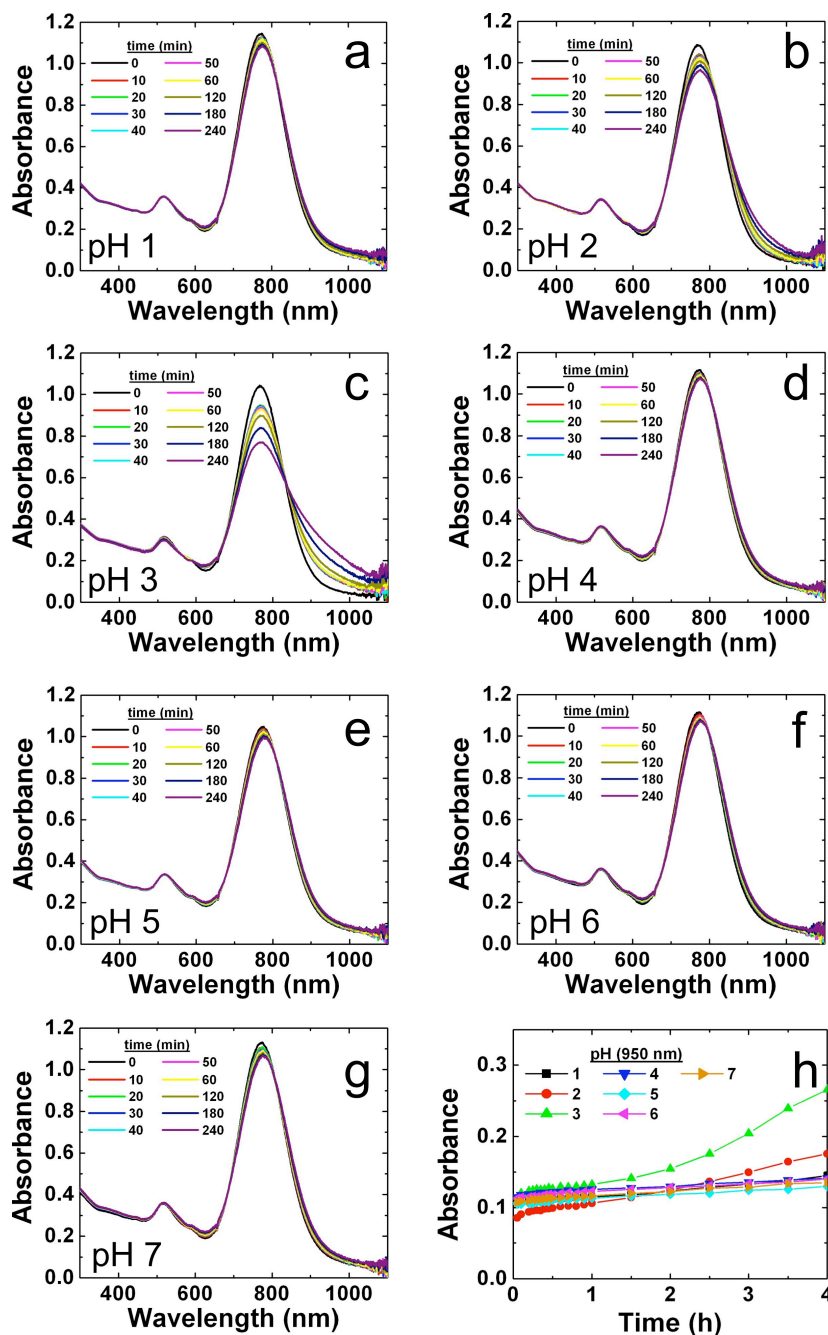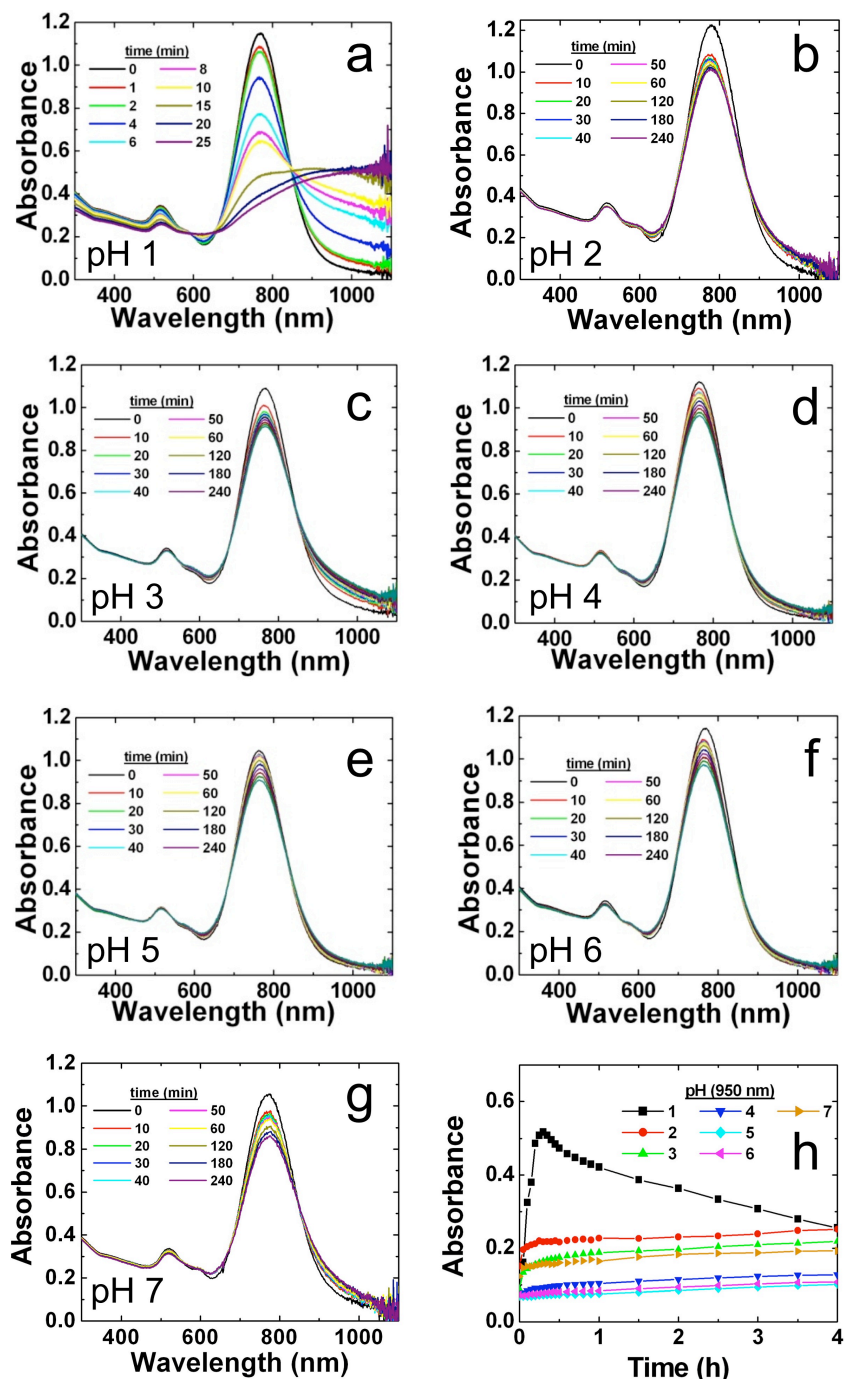
Figure 5.5 UV-vis analysis of the pH dependent MPA mediated assembly of Au nanorods at (a) pH 1.0, (b) pH 2.0, (c) pH 3.0, (d) pH 4.0, (e) pH 5.0, (f) pH 6.0, and (g) pH 7.0. Part (h) displays the time evolution for the production of the assembled LSP peak at 950 nm for all pH values studied.

Surprisingly, no spectral assembly was observed for the materials at pH 1.0. Note that maximal activity was observed for cysteine-mediated assembly at pH 1.0. TEM analysis of the materials produced at pH 2.0 and 3.0 (Figures 5.6a and b, respectively) confirms the aggregation state. Statistical analysis of the TEM images indicates that 33.1% and 35.3% of the nanorods were assembled in a linear fashion at pH 2.0 and 3.0, respectively. As observed by DLS in Figure 5.4, no formation of self-assembled structures was noted for samples at pH values > the pKa or at pH 1.0, with only small assembly sizes of 70.2 ± 4.97 nm at pH 2.0 and 85.1 ± 2.8 nm at pH 3.0, consistent with the UV-vis and TEM results. The lack of assembly at pH 1.0, where all of the carboxylate groups are protonated, is likely due to the solution ionic strength interfering with hydrogen bonding between the nanorod tips.[302] Under these conditions, the thiol moiety of the MPA is able to bind to the nanorod tip; however, the solution concentration of ions are able to screen the formation of the network of hydrogen bonds required for assembly. At pH 1.0, 2.0, and 3.0, the concentration of HCl, which was used as the titrating species, is ~ 0.10 M, 0.01 M, and 0.001 M, respectively. The absorbance intensities at 950 nm for the assembly of Au nanorods at these specific pH values after 4.0 h of assembly were 0.12, 0.17, and 0.28 respectively, which shows a directly proportional relationship, consistent with screening of hydrogen bond formation as the pH decreased (i.e. increasing ionic strength).

With an understanding of the effects of the acid functionality, which shows divergent assembly abilities as compared to cysteine, the effects of the amine functionality were studied using cysteamine. Cysteamine is a cysteine homologue sans
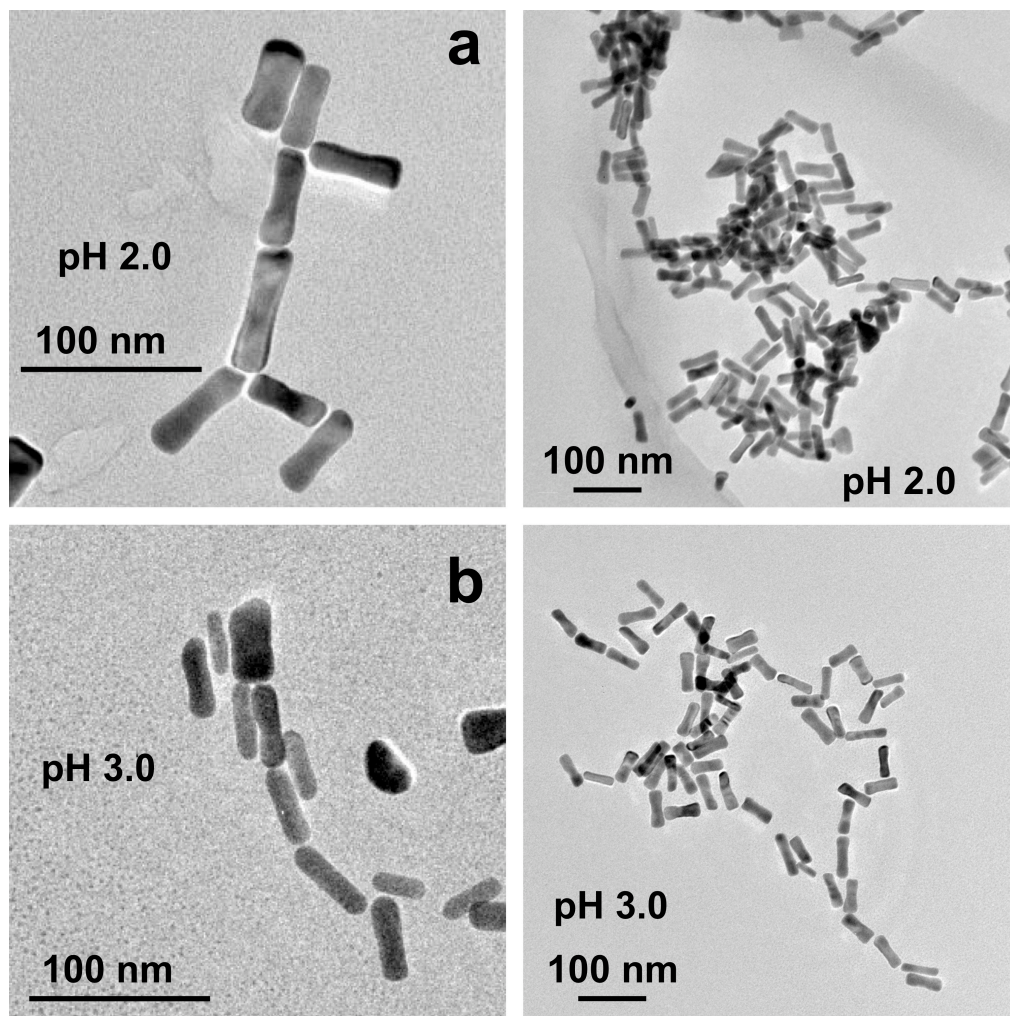
Figure 5.6 TEM micrographs of the MPA assembled nanorods at (a) pH 2.0 and (b) pH 3.0. Representative TEM images are presented at different magnification levels for a complete analysis.

the α-carboxylate functionality (Figure 5.1c). Primary amines, such as the amine of both cysteine and cysteamine, are able to bind to the surface of Au nanoparticles and cause the crosslinking of Au nanomaterials in solution.[212,223] Figure 5.7 displays the results obtained for the cysteamine-based assembly of Au nanorods at pH values between 1.0 and 7.0. The pKa values of the cysteamine functional groups are > 7.0; therefore no change in molecular charge or material assembly based upon pH is expected. Interestingly, as shown in Figures 5.7, nanorod chain formation occurs quickly at pH 1.0, with a sharp decrease in assembly activity for pH 2.0 and 3.0. Between a pH value of 4.0 and 6.0, no notable shifts or changes in the UV-vis spectra indicative of linear assembly occurs; however, assembly becomes evident, albeit rather slowly, at pH 7.0. TEM analysis of the materials, as shown in Figure 5.8 for pH 1.0 and 7.0 and in the Appendix IV, Figure A5.9 for all other values, confirmed cysteamine-based chain formation. For the nanorods assembled with this ligand, the percent of nanorods in an end-to-end arrangement varied from 69.5% for pH 1.0 to 29.3% for pH 7.0 (Appendix IV, Table A5.1). Finally, DLS analysis, as shown in Figure 5.4, confirms the assembly ability observed both spectroscopically and by TEM analysis. This divergent cysteamine-based assembly can be attributed to the solution ionic strength and the pKa values of the molecule's functional groups as discussed below. Overall, this analysis demonstrated two key points: cysteamine is able to cross-link the nanorods and the rate of formation is sensitive to the reaction solution. Note that nanorod chain formation is observed at pH 1.0 for both cysteine and cysteamine, but not MPA. Additionally, based upon the molecular structure of cysteamine, no electrostatic interactions are envisioned; therefore, a cross-linkage via amine-Au binding is highly probable.

Figure 5.7 UV-vis analysis of the pH dependent cysteamine mediated assembly of Au nanorods at (a) pH 1.0, (b) pH 2.0, (c) pH 3.0, (d) pH 4.0, (e) pH 5.0, (f) pH 6.0, and (g) pH 7.0. Part (h) displays the time evolution for the production of the assembled LSP peak at 950 nm for all pH values studied.
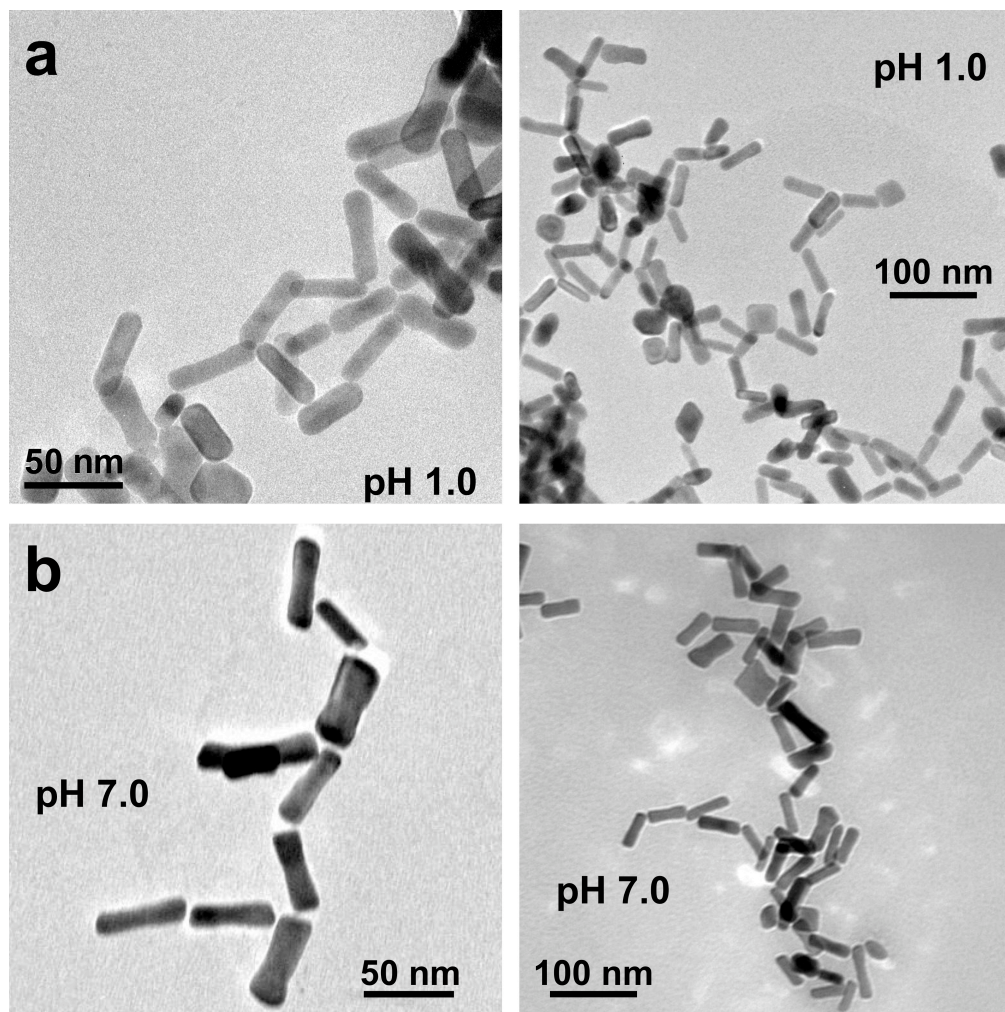
Figure 5.8 TEM micrographs of the cysteamine assembled nanorods at (a) pH 1.0 and (b) pH 7.0. Representative TEM images are presented at different magnification levels for a complete analysis.

From the assembly results, a more descriptive mechanism concerning cysteine-based assembly can be developed. The results suggest that the cysteine thiol is able to bind to the Au nanorod tip, followed by amine binding of an adjacent nanorod tip. This step is consistent with the fact that cysteine mediated assembly is observed at or below the pKa of the α-carboxylate, where cysteine is positively charged and is consistent with previous studies based upon cysteine assembly of spherical Au nanoparticles.[223] At this pH regime, the majority of acid groups are protonated, thus preventing two-point electrostatic interactions. This thiol/amine cross-linking is also supported by the fact that while hydrogen bond formation of Au nanorod chains was observed for MPA with protonated carboxylic acids, at pH 1.0, no assembly was observed due to the ionic strength of the solution and only minor assembly was observed overall. It is known that the solution ionic strength, which is at its highest point at pH 1.0 in the present study, is able to screen and prevent hydrogen bonding.[302] This suggests that the acid group of cysteine is not involved in assembly at pH 1.0 as this assembly motif would be prevented by the ions in solution as was observed for the MPA. Additionally, cysteamine, which possess a terminal thiol and amine only, is able to cross-link the nanorods at both low and mid-range pH values, with maximum activity at pH 1.0, similar to cysteine. The cysteamine results strongly suggest amine-based assembly that is translatable to the method used by cysteine.

For cysteine at low pH values, cross-linking of the nanorods occurs via amine attachment to an adjacent nanorod; however at higher pH values no assembly is observed. At these pH values, the cysteine structure is in a zwitterionic state in which the carboxylic acid is negatively charged and the amine functionality is positively charged. These

moieties are exposed along the surface of the Au nanorod tip and are able to interact with the other charged functionalities that are immediately adjacent to them on the surface. Indeed, *intra*surface hydrogen bonding and electrostatic interactions have been observed for cysteine passivated onto nanoparticle surfaces that subsequently prevents their self-assembly in solution.[222-224] By protonating the carboxylic acid, this network is disrupted, thus releasing the amine functionality for interactions with a secondary Au nanorod surface, resulting in a linear chain.

Additionally, the assembly process is also likely to be influenced by the solution ionic strength as the charge on the nanorods is known to influence their stability.[294] For all three species studied, cysteine, MPA, and cysteamine, the ionic strength of the solution changed the rates of assembly. For instance screening of hydrogen bond formation for MPA prevents nanorod assembly at pH 1.0. Additionally, the rate of formation for the cysteamine changed drastically based upon the pH, and thus ionic strength, while the positive charge state of the molecule was nearly constant. At the low pH value, the ions of the species in solution are able to screen the surface positive charge of the nanorods, thus preventing electrostatic repulsion of the positively charged cysteamine and allowing for a more rapid assembly rate.[294] At higher pH values, the ionic strength is minimized, thus yielding less screening of the system and increasing the repulsion of the cysteamine. By being repulsed from the system electrostatically, the assembly rate of the nanorods would also decrease, consistent with the obtained results. Assembly activity was partially restored at pH 7.0, which approaches the pKa of the cysteamine thiolate to produce an electronically neutral species that can have greater surface interactions with the Au nanorod tip. This effect suggests that electrostatics may

play a role in the lack of cysteine-based assembly at a pH > 3.0. As discussed above, the species is zwitterionic and electrostatically ordered on the surface of a single nanorod tip, thus preventing the amine interaction with other nanorods. The network was not formed at low pH values via acid protonation; however, screening of the electrostatic interactions on the surface via a high ionic strength solution could disrupt the charged network and restore assembly activity.

To determine the validity of the described crosslinking mechanism, a set of control experiments was performed and is presented in Figure 5.9. As shown in Figure 5.9a, a sample of cysteine assembled Au nanorods was prepared at pH 1.0. The rods were allowed to assemble in solution for 30.0 min, which was confirmed by UV-vis. Once assembled, the sample was heated at 60.0 $^{\circ}$C for 10.0 min in a glass vial. Heating of the solution would result in disruption of non-covalent interactions and a restoration of the non-assembled UV-vis spectra.[303] After heating, virtually no spectral change was observed; a small peak at 970 nm developed after heating, which is likely due to nanorod degradation.[282] This suggests that the assembly is robust to temperature changes; however, Sun *et al.* have demonstrated disassembly of the Au nanorod chains through changes in solution pH.[214] Under their study, assembly was observed at pH 2.8, while disassembly occurred when the solution was titrated to pH 9.8 after extended sonication. This suggests reformation of the *intra*surface electrostatic network among the newly deprotonated acid groups and positively charged amines, resulting in degradation of the chained structure and reformation of independent nanorod species.

Further, the effects of solution ionic strength, which likely plays a role in the assembly process through charge screening were studied as discussed in last chapter.[294]
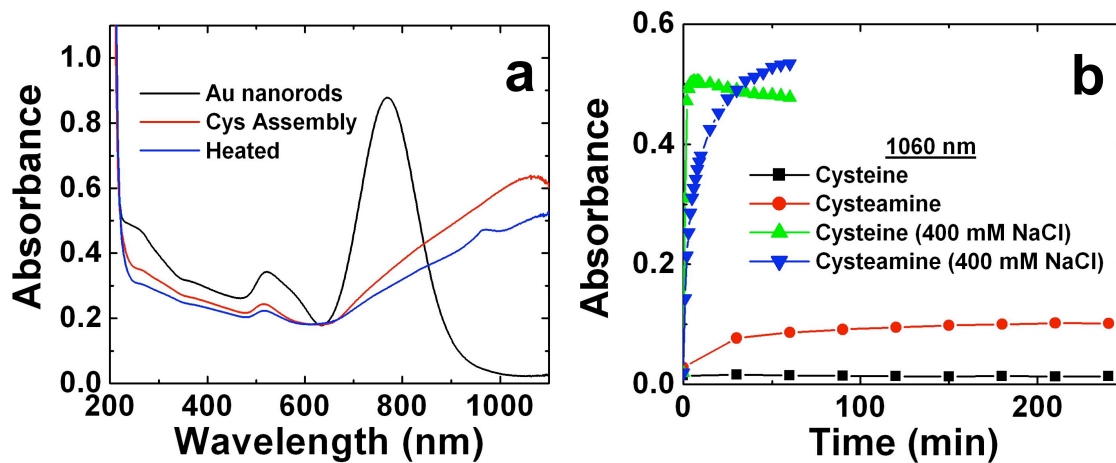
Figure 5.9 Control analyses of the cysteine-based assembly process. Part (a) displays the effects of heat on the assembled nanorods, while part (b) demonstrates the effects on the solution ionic strength on the assembly of the nanorods for cysteine and cysteamine at pH 7.0.

At pH 1.0, chain formation for the positively charged cysteine and cysteamine is fastest, yet these species should be repelled by the cationic nanorods; however, at this pH value, the concentration of anions is high, which can electrostatically neutralize the nanorod surface.[13,18] This effect would minimize repulsion and result in the observed increased rate of chain formation. Additionally, a high ionic strength medium is likely to prevent formation of the *intra*surface electrostatic network formed by the zwitterionic cysteine species,[222,224] thus allowing for linear chain formation. To support this fact, restoration of the cross-linking activity for both cysteine and cysteamine at pH 7.0 had been achieved. Note that no activity was observed for cysteine at pH 7.0 in water, and that a sharply decreased activity was observed for cysteamine. For this experiment, Au nanorods were dissolved in 400 mM NaCl, pH 7.0, and were stable as previously demonstrated.[294] From there, either cysteine or cysteamine was added and the assembly of nanorod chains was monitored. As shown in Figure 5.9b, nanorod chain formation activity was completely restored for both species. Under these conditions, the ions in solution are able to effectively screen and shield the charges on the surface of the nanorods, resulting in minimization of electrostatic repulsion and promoting efficient thiol attachment. Once attached, the amine functionalities of the two species are able to cross-link via amine-gold bond formation.

For cysteine, the effects of the high ionic strength (400 mM NaCl) resulted in assembly of the materials at pH 7.0. It was shown above that assembly of these materials in a low ionic strength, pH 7.0 solution was prevented. This was hypothesized to arise from a network of electrostatic interactions between the zwitterionic groups on the surface of a single tip, as is consistent with other systems.[222-224] However, under the high

ionic strength system, this network is likely to be disrupted by screening of the charges by the large concentration of ions in solution. As a result, the amines are now liberated from the *intra*surface network and allows for their binding to a secondary surface, thus resulting in the formation of Au nanorod chains. Overall, this indicates that amine-Au binding is the dominant mode of interaction for the chain formation.

Taken together, the results suggest that the mode of interactions dictating cysteine-based nanorod assembly is via thiol and amine binding of adjacent nanorod species. For this to occur, the amine moiety must be independent from the surface so as to allow for the formation of the amine-Au interactions with the adjacent nanorod. Based upon simple calculations using the thiol footprint of 0.214 nm^2,[163,272] ~928 cysteine molecules can bind to the tips of each Au nanorod assuming a total surface area of 2.97 × 10^3 nm^2, with 397 nm^2 of surface area arising from the tips. As a result, multiple cysteine species are present at the nanorod interface to facilitate assembly. The main inhibiting factor for this to occur is that under most conditions, the cysteine species is in the zwitterionic state with the adjoining negatively charged carboxylate group. In this state, a network of electrostatic interactions along the surface of a single nanorod tip prevents the amine from inducing assembly of the materials. To allow for assembly, the electrostatic network needs to be disengaged, thus liberating the amine for subsequent activity. To achieve this, two methods have been developed: protonation of the acid group and the use of a high ionic strength medium. The first method using a protonated COOH group prevents formation of the electrostatic network and thus frees the amine for cross-linking. The second method uses the ions of the solution to effectively screen the electrostatic

interactions, thereby disrupting the electrostatic network. Once disrupted, the amine is now able to cross-link the nanorods in solution.

5.5. Summary and Conclusions

In conclusion, it has been demonstrated that cysteine-based assembly of Au nanorods is caused by attachment of both the thiol and the amine moieties to adjacent materials. Through the pH-based analyses, no assembly of nanorods was observed at pH values where cysteine would be in the zwitterionic state. Formation of linear chains of nanorods is only observed near or below the pKa value of the α-carboxylate group. In fact, the rate of chain formation is fastest at pH 1.0, which is likely controlled by the solution ionic strength. These results were confirmed through the assembly characteristics of both MPA and cysteamine at various pH values and solution ionic strengths. Determining the mode of assembly is critically important for the fabrication of assembled architectures of nanomaterials, especially for bio-inspired techniques. By understanding simple structures, relevant design criteria can be examined and possibly adapted for larger and more complex biological cross-linking agents. Further examination of these processes may lead to fabrication of linear structures with a higher degree of control over the final product from a bottom-up approach.

This Chapter has been reproduced with permission from the following publication: copyright ACS publications

Sethi, M.; Joung, G.; Knecht, M.R. Linear Assembly of Au Nanorods Using Biomimetic Ligands, *Langmuir* **2009**, *25*, 1572-1581.
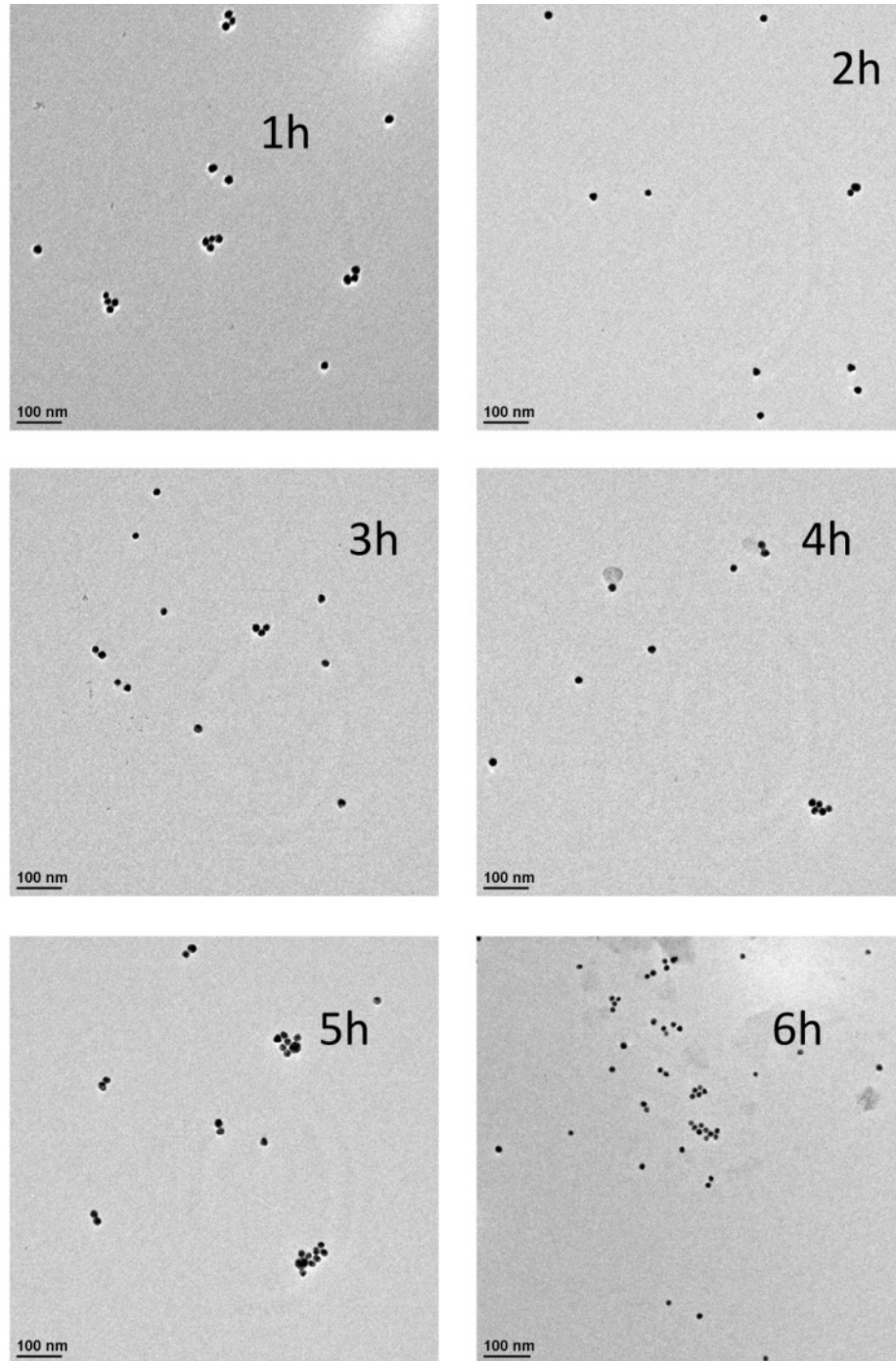
Figure A2.1 TEM analysis of the 0K Arg assembly process at time points of 1.0 h, 2.0 h, 3.0 h, 4.0 h, 5.0 h, 6.0 h.
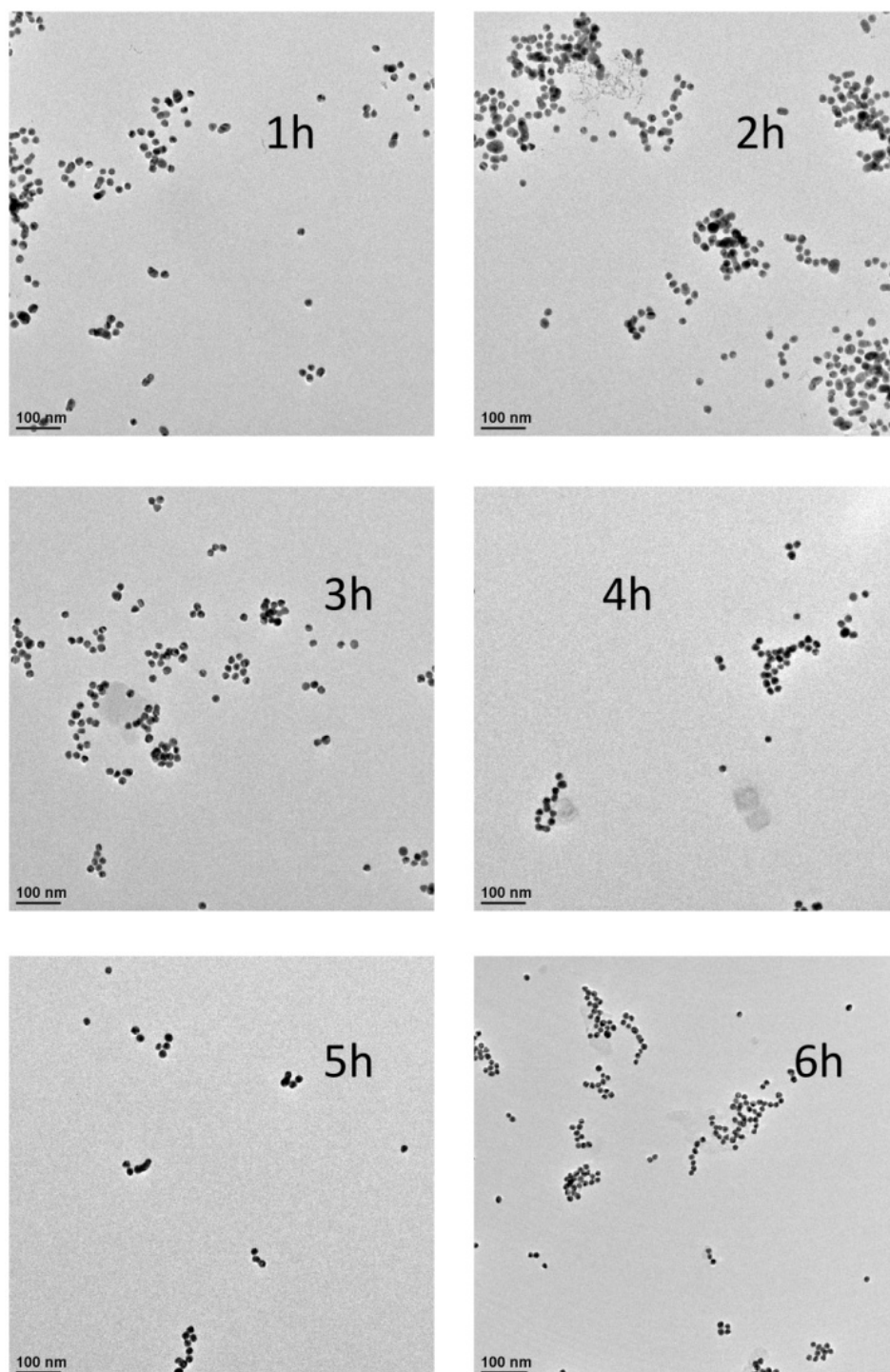
Figure A2.2 TEM analysis of the 20K Arg assembly process at time points of 1.0 h, 2.0 h, 3.0 h, 4.0 h, 5.0 h, 6.0 h.
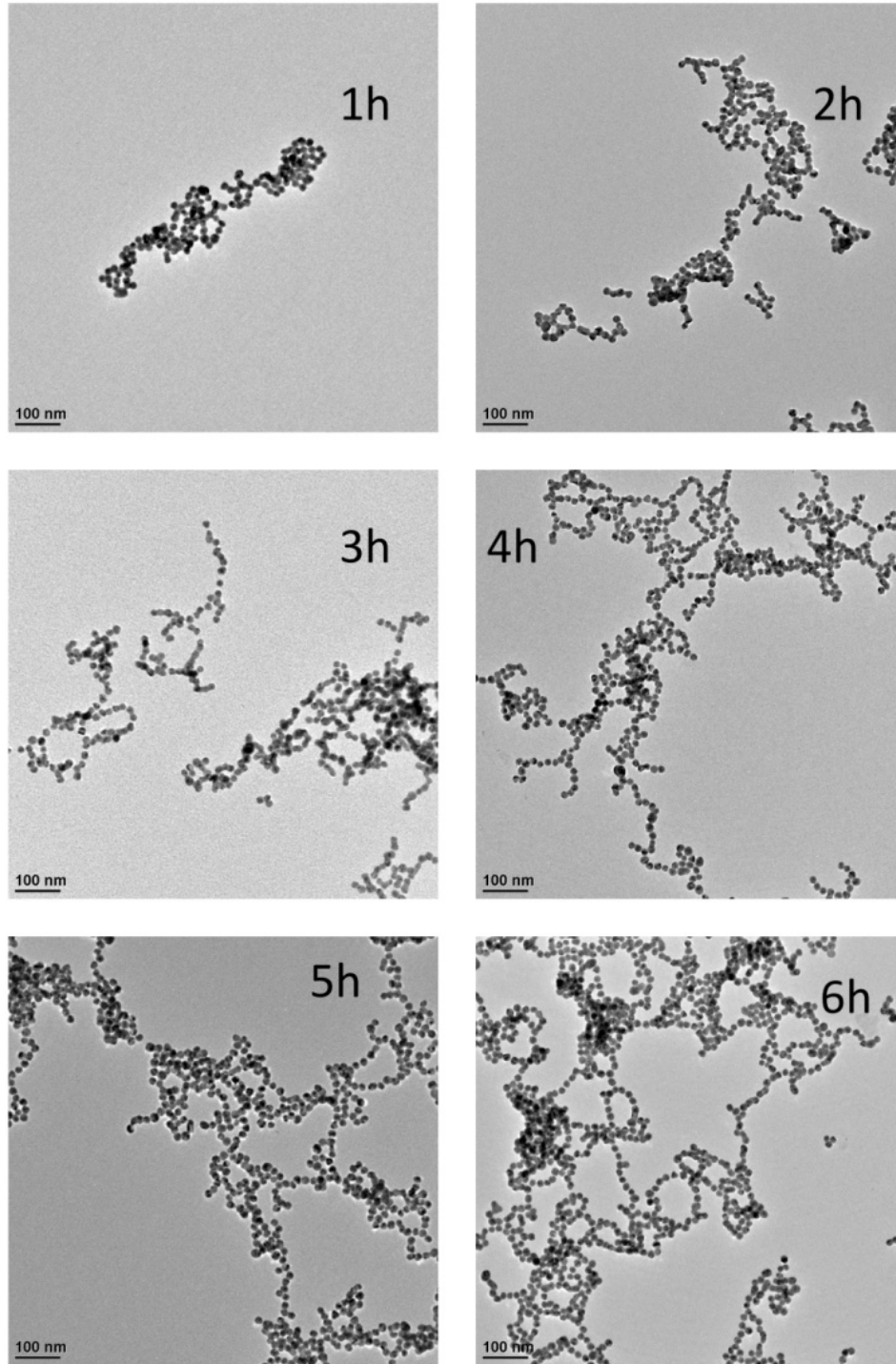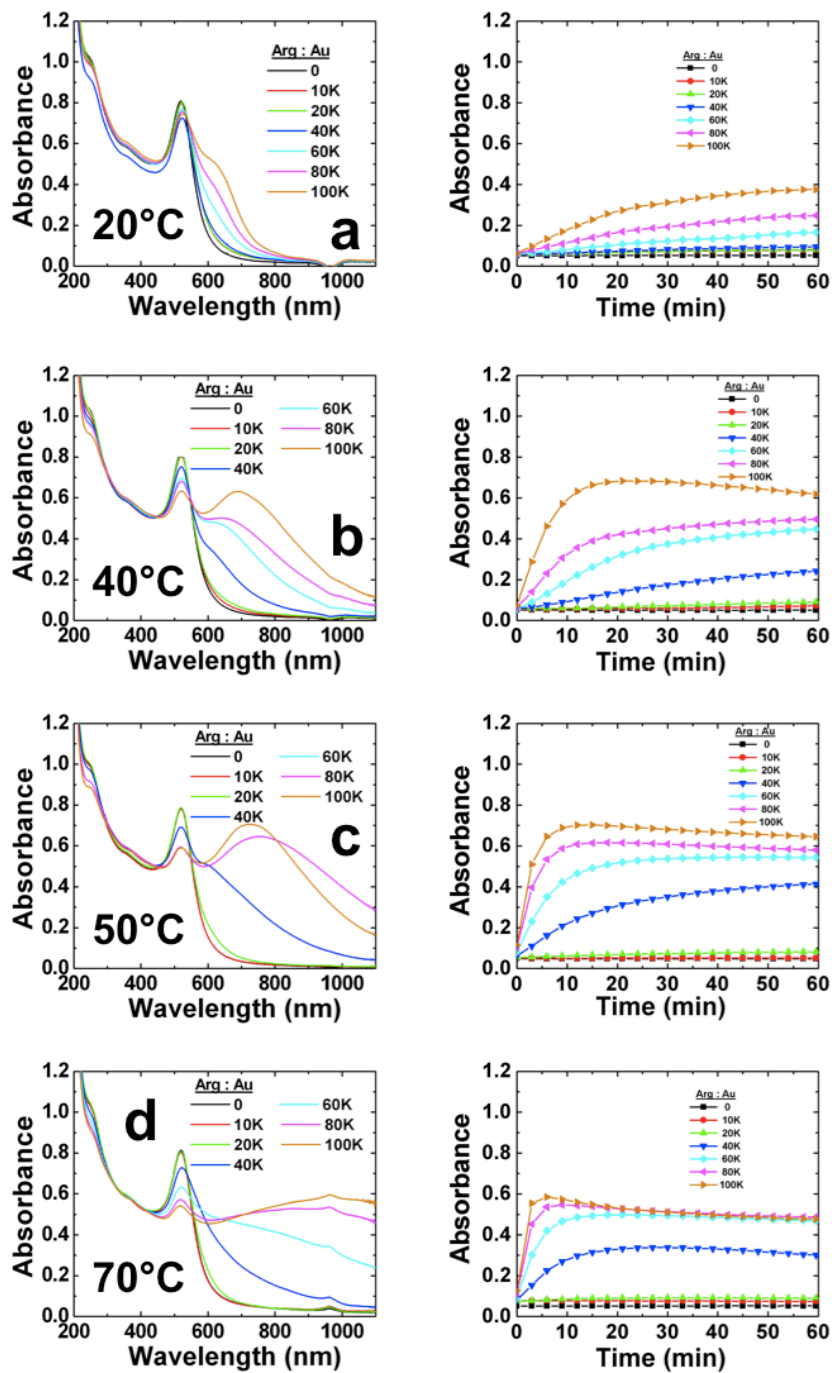
Figure A2.3 TEM analysis of the 60K Arg assembly process at time points of 1.0 h, 2.0 h, 3.0 h, 4.0 h, 5.0 h, 6.0 h.
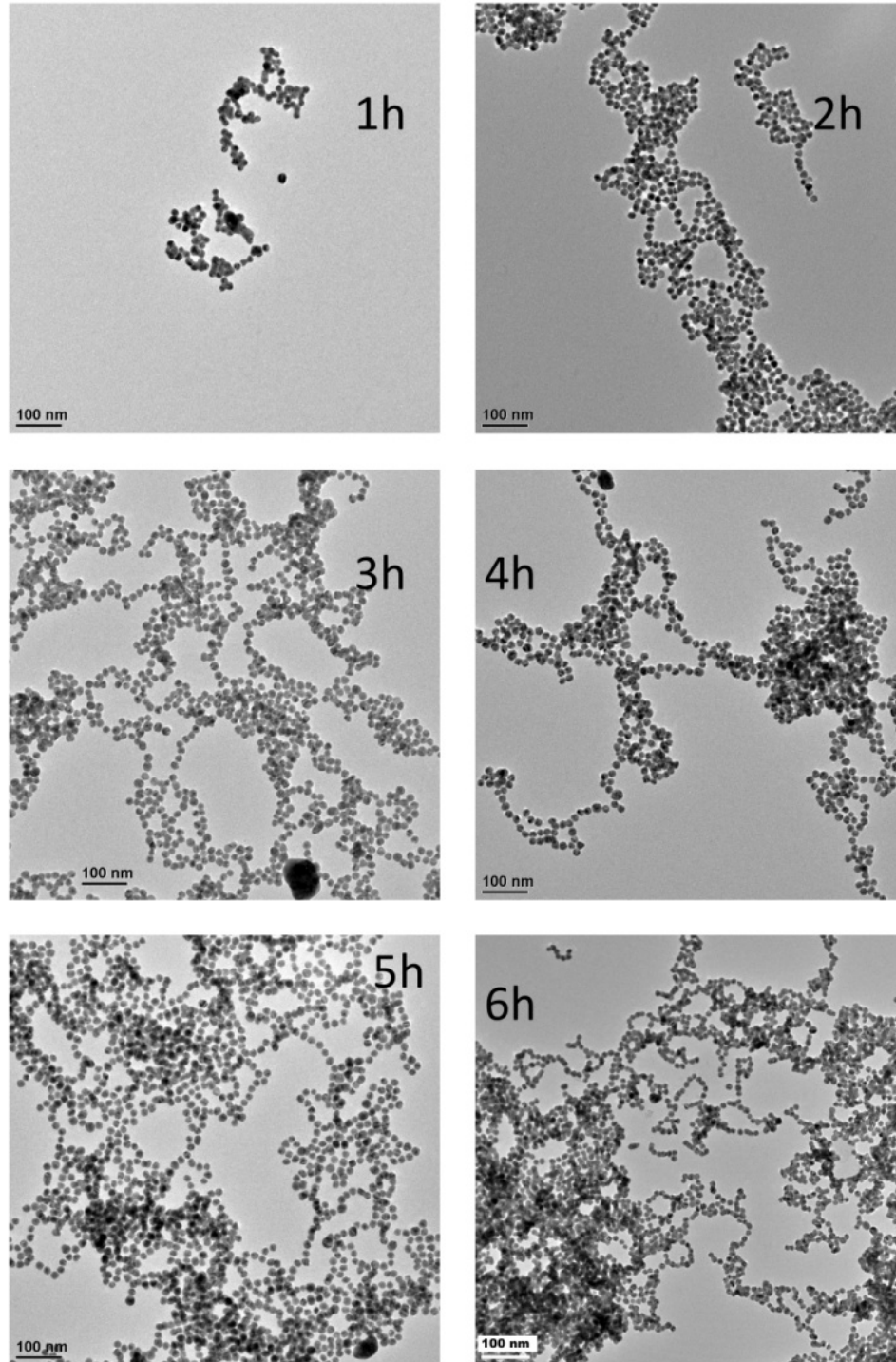
Figure A2.4 TEM analysis of the 80K Arg assembly process at time points of 1.0 h, 2.0 h, 3.0 h, 4.0 h, 5.0 h, 6.0 h.
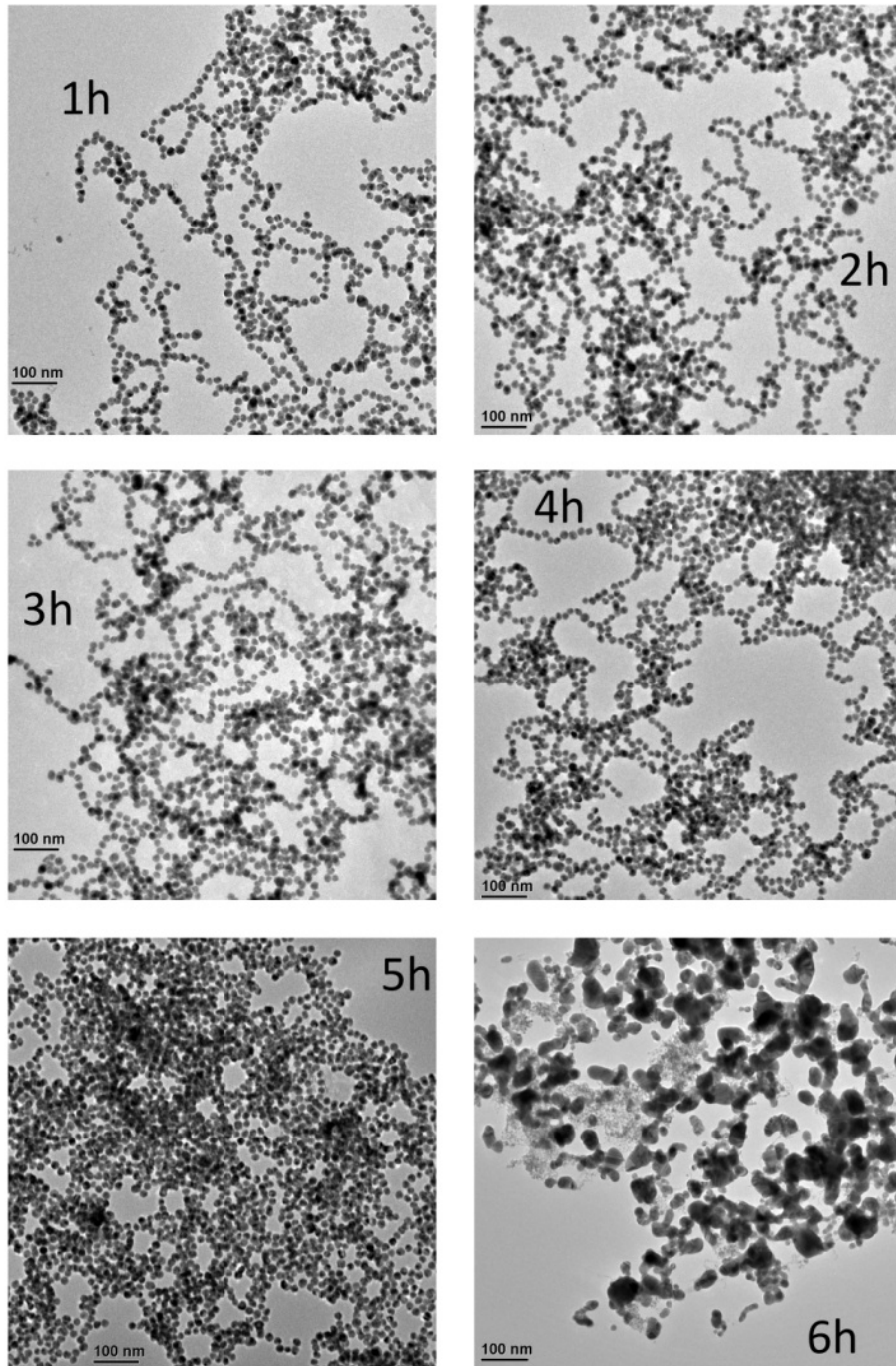
**Figure A2.5 TEM analysis of the 100K Arg assembly process at time points of 1.0 h, 2.0 h, 3.0 h, 4.0 h, 5.0 h, 6.0 h.**

Figure A2.6 UV-vis analysis of the temperature effects on the Arg concentration dependent assembly of Au nanoparticles studied at (a) 20.0 °C, (b) 40.0 °C, (c) 50.0 °C, and (d) 70.0 °C. The plots on the left demonstrate the UV-vis spectra obtained after 1.00 h of reaction for each Arg: Au nanoparticle ratio studied, while the plots on the right present the absorbance intensity of the 665 nm peak as a function of time.
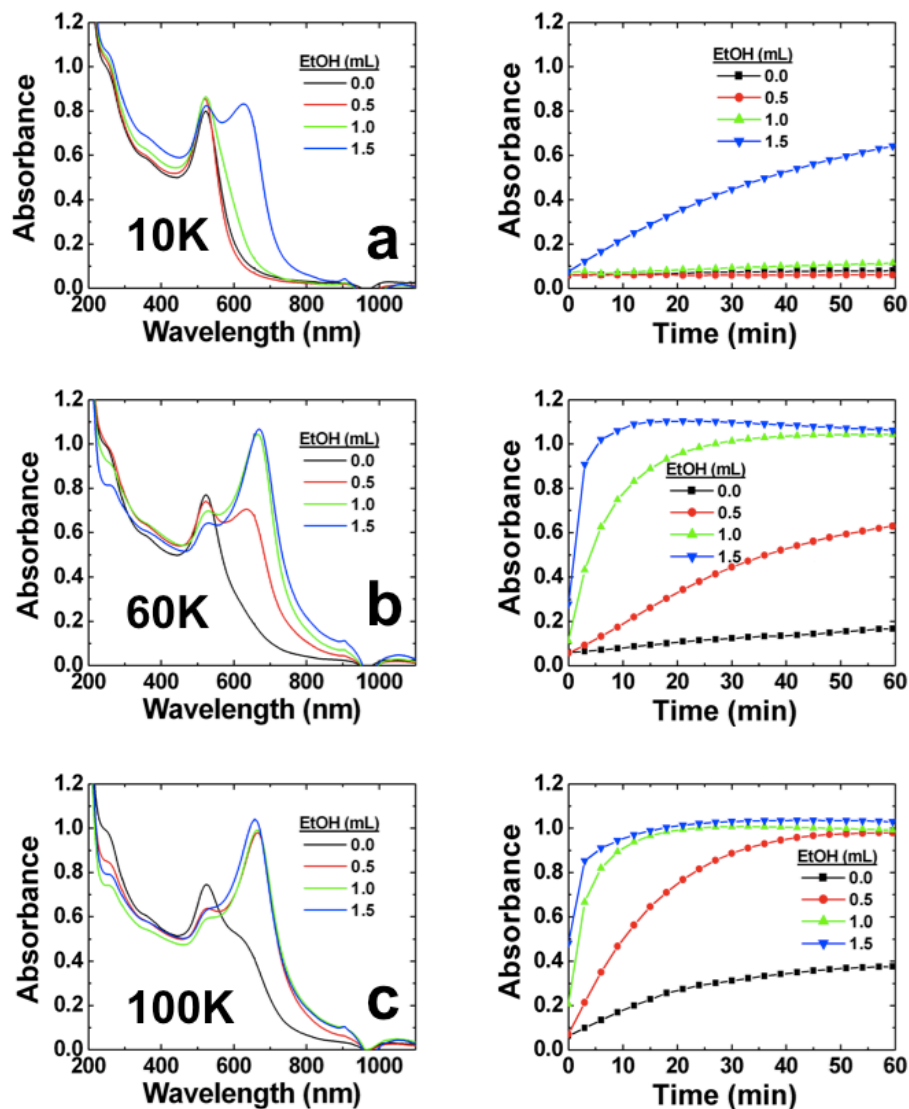
Figure A2.7 UV-vis analysis of the effects of the amount of EtOH added to the reaction system for the assembly of Au nanoparticles using the (a) 10K, (b) 60K, and (c) 100K samples. The plots on the left demonstrate the UV-vis spectra obtained after 1.00 h of reaction for each volume of EtOH studied, while the plots on the right present the absorbance intensity of the 665 nm peak as a function of time.
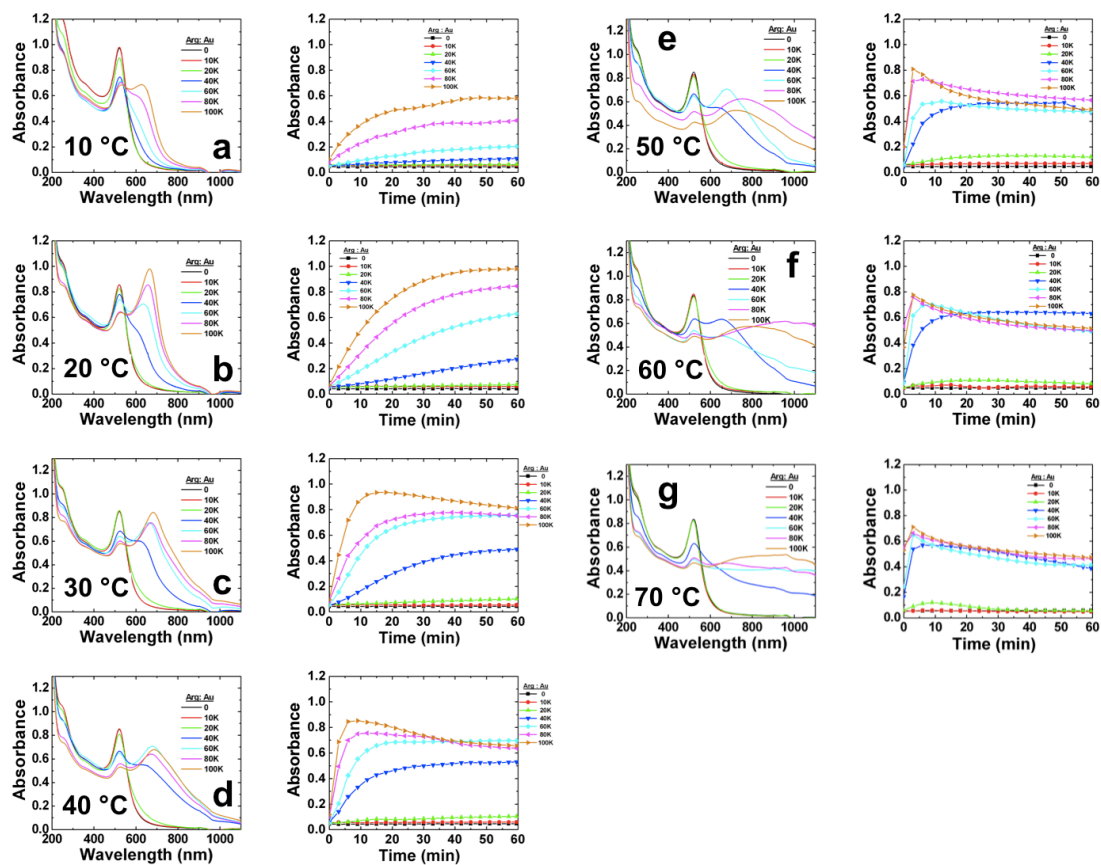
Figure A2.8 UV-vis analysis of the temperature effects on the Arg concentration dependent assembly of Au nanoparticles in the presence of 0.50 mL of EtOH studied at (a) 10.0 °C, (b) 20.0 °C, (c) 30.0 °C, (d) 40.0 °C, (e) 50.0 °C, (f) 60.0 °C, and (g) 70.0 °C. The plots on the left demonstrate the UV-vis spectra obtained after 1.00 h of reaction for each Arg: Au nanoparticle ratio studied, while the plots on the right present the absorbance intensity of the 665 nm peak as a function of time.
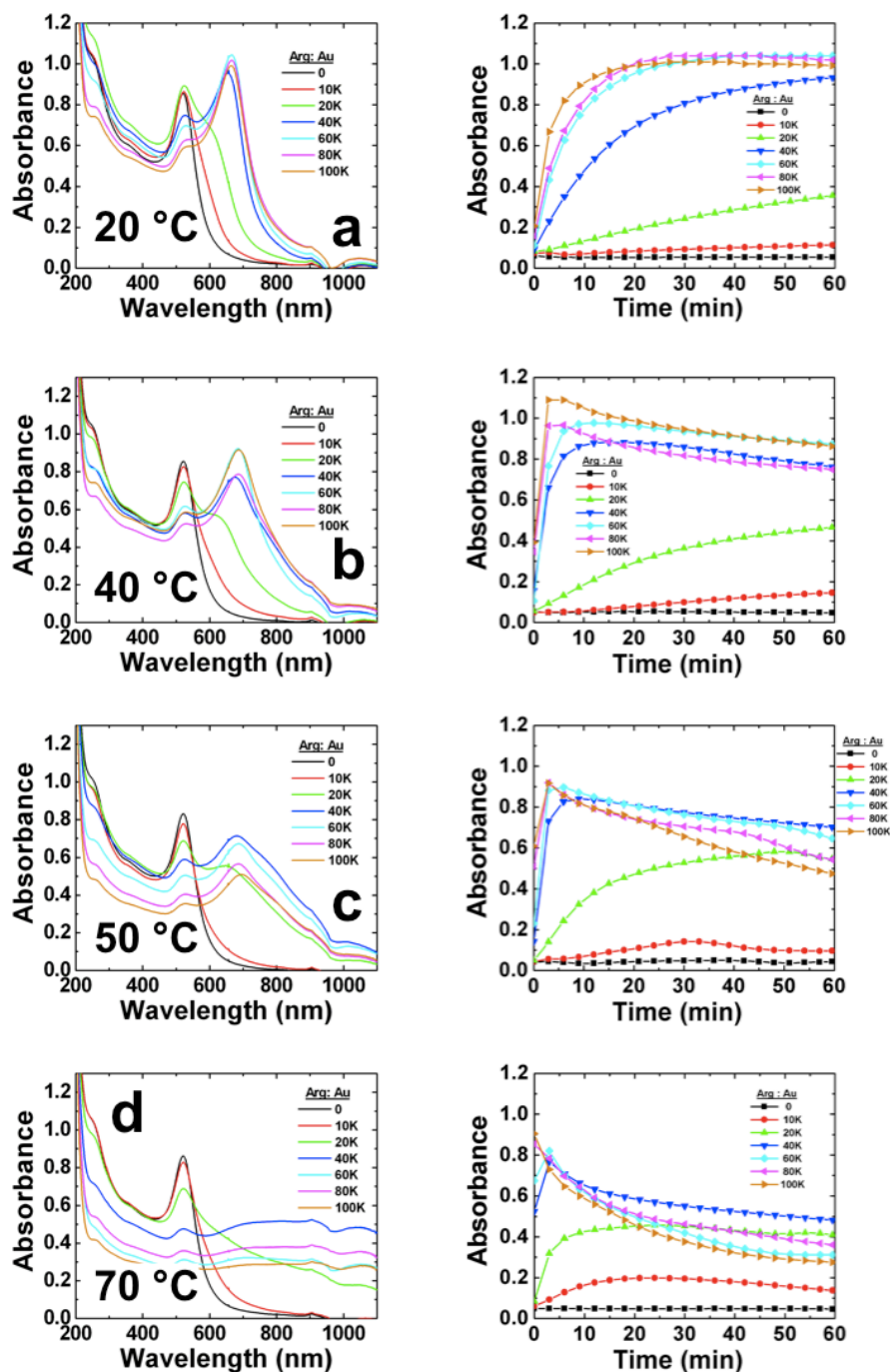
Figure A2.9 UV-vis analysis of the temperature effects on the Arg concentration dependent assembly of Au nanoparticles in the presence of 1.00 mL of EtOH studied at (a) 20.0 °C, (b) 40.0 °C, (c) 50.0 °C, and (d) 70.0 °C. The plots on the left demonstrate the UV-vis spectra obtained after 1.00 h of reaction for each Arg:Au nanoparticle ratio studied, while the plots on the right present the absorbance intensity of the 665 nm peak as a function of time.
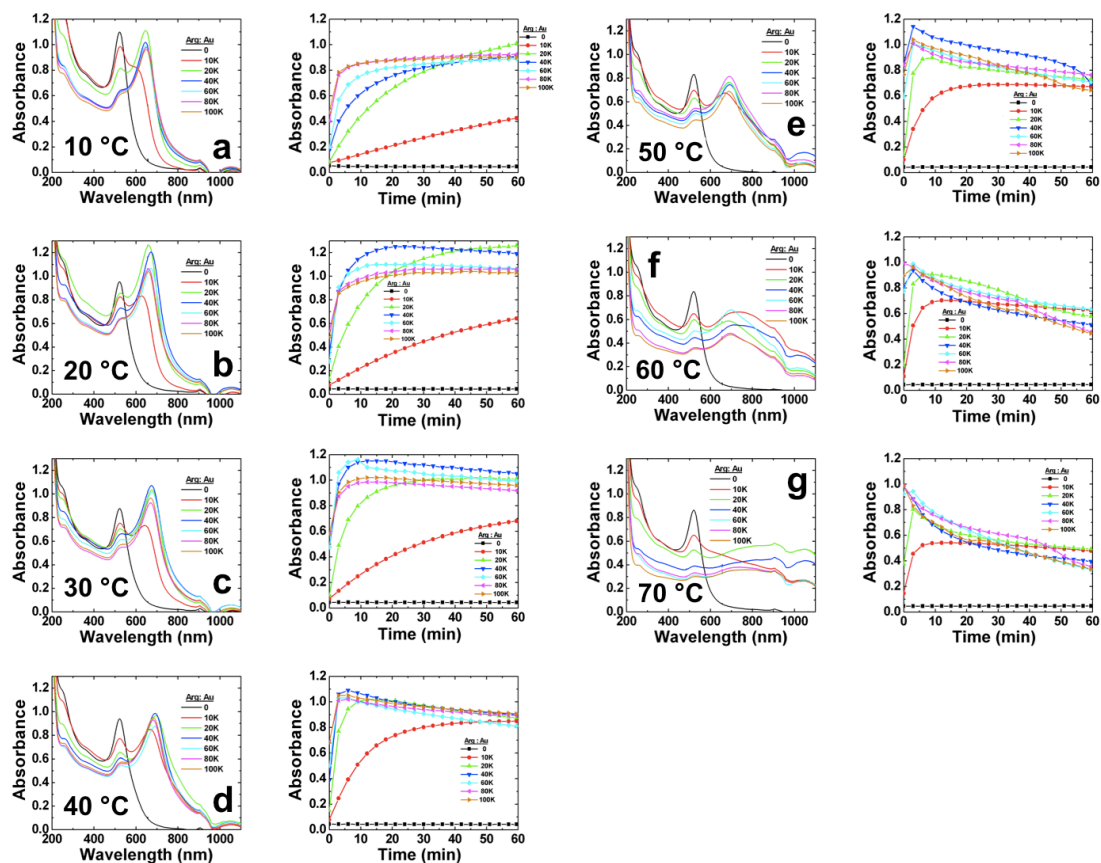
Figure A2.10 UV-vis analysis of the temperature effects on the Arg concentration dependent assembly of Au nanoparticles in the presence of 1.50 mL of EtOH studied at (a) 10.0 °C, (b) 20.0 °C, (c) 30.0 °C, (d) 40.0 °C, (e) 50.0 °C, (f) 60.0 °C, and (g) 70.0 °C. The plots on the left demonstrate the UV-vis spectra obtained after 1.00 h of reaction for each Arg: Au nanoparticle ratio studied, while the plots on the right present the absorbance intensity of the 665 nm peak as a function of time.
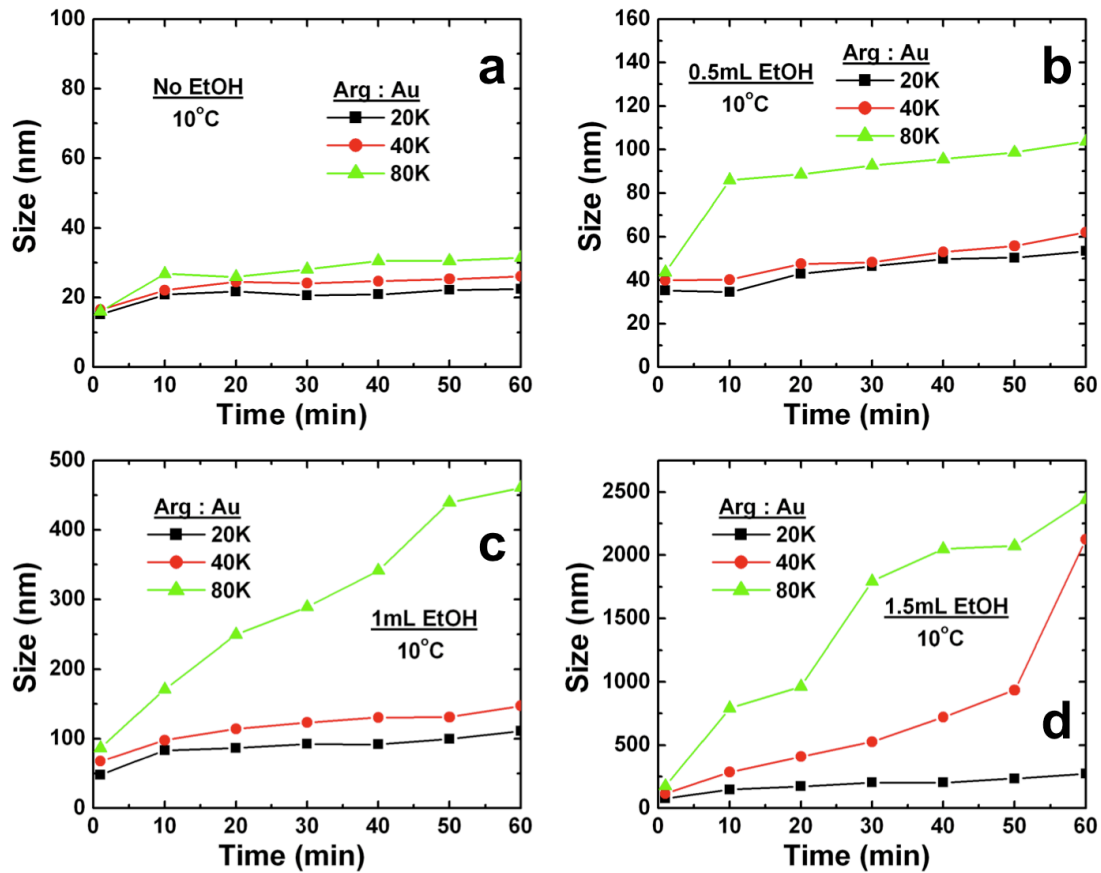
Figure A2.11 DLS aggregate size analysis for the 20K, 40K, and 80K samples as a function of time at 10.0 °C for (a) 0.00 mL, (b) 0.50 mL, (c) 1.00 mL, and (d) 1.50 mL of EtOH added to the system. Note the difference in scale.
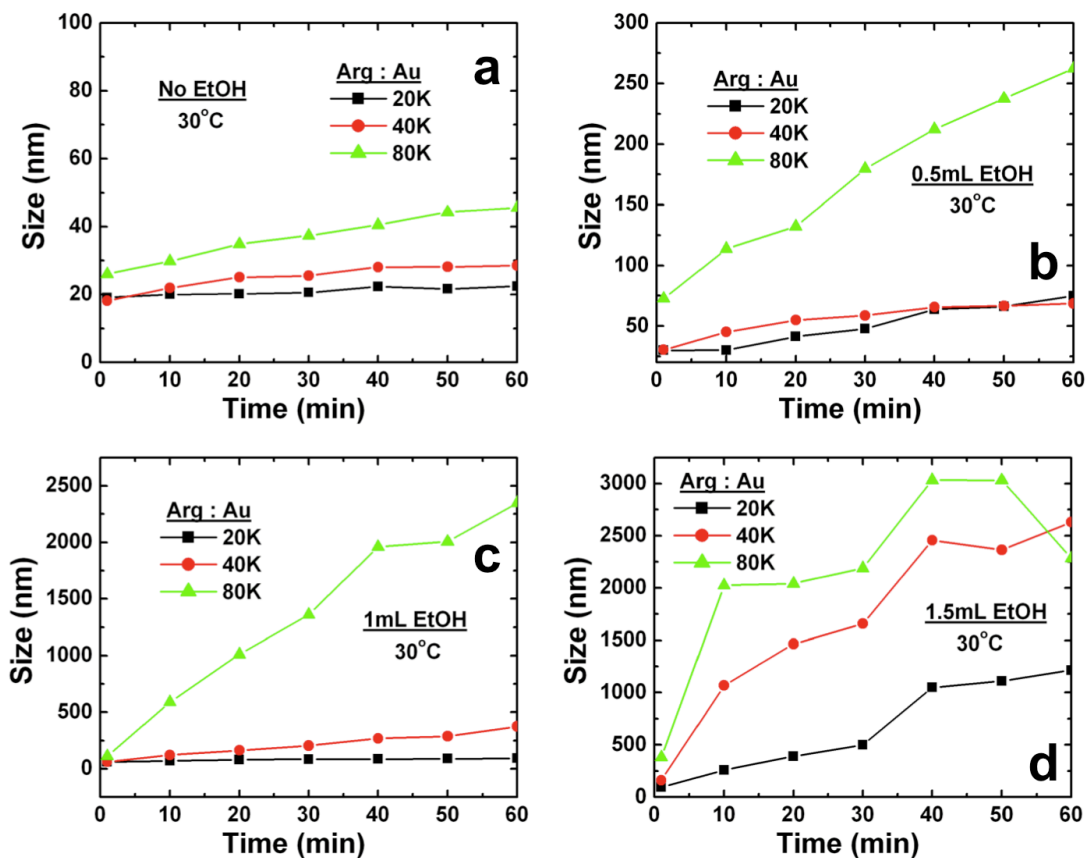
Figure A2.12 DLS aggregate size analysis for the 20K, 40K, and 80K samples as a function of time at 30.0 °C for (a) 0.00 mL, (b) 0.50 mL, (c) 1.00 mL, and (d) 1.50 mL of EtOH added to the system. Note the difference in scale.
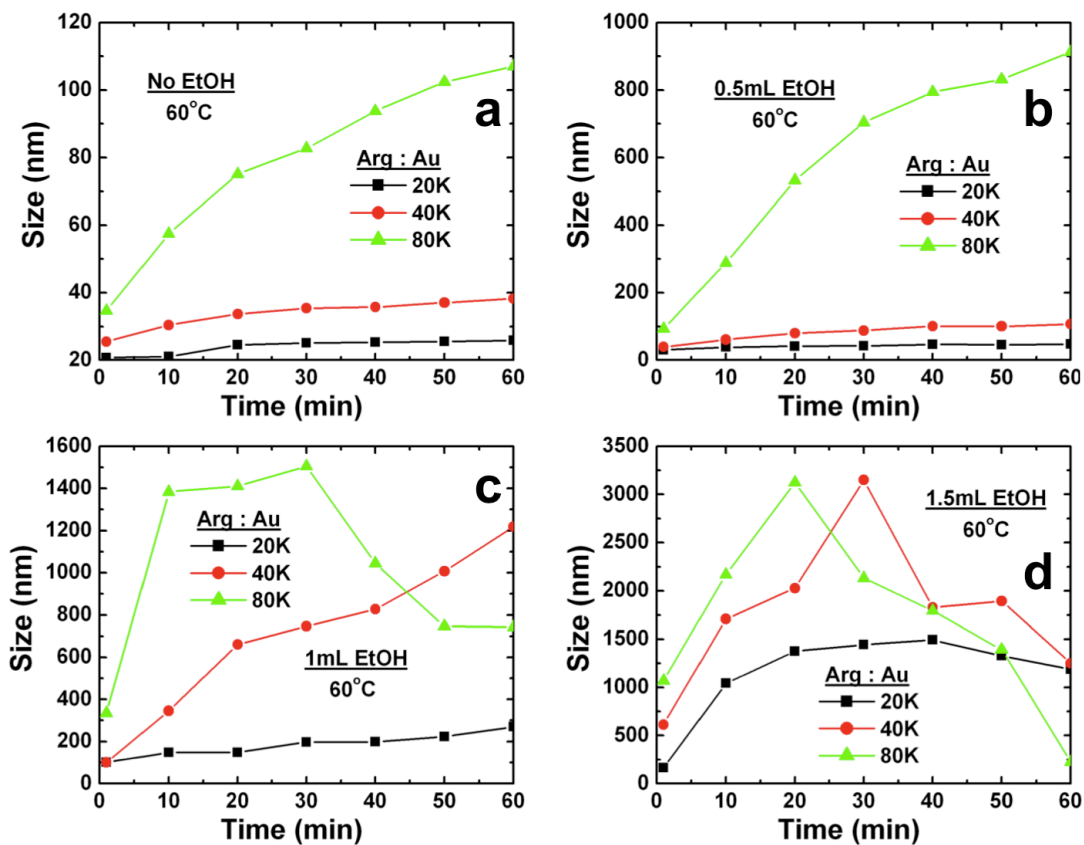
Figure A2.13 DLS aggregate size analysis for the 20K, 40K, and 80K samples as a function of time at 60.0 °C for (a) 0.00 mL, (b) 0.50 mL, (c) 1.00 mL, and (d) 1.50 mL of EtOH added to the system. Note the difference in scale.
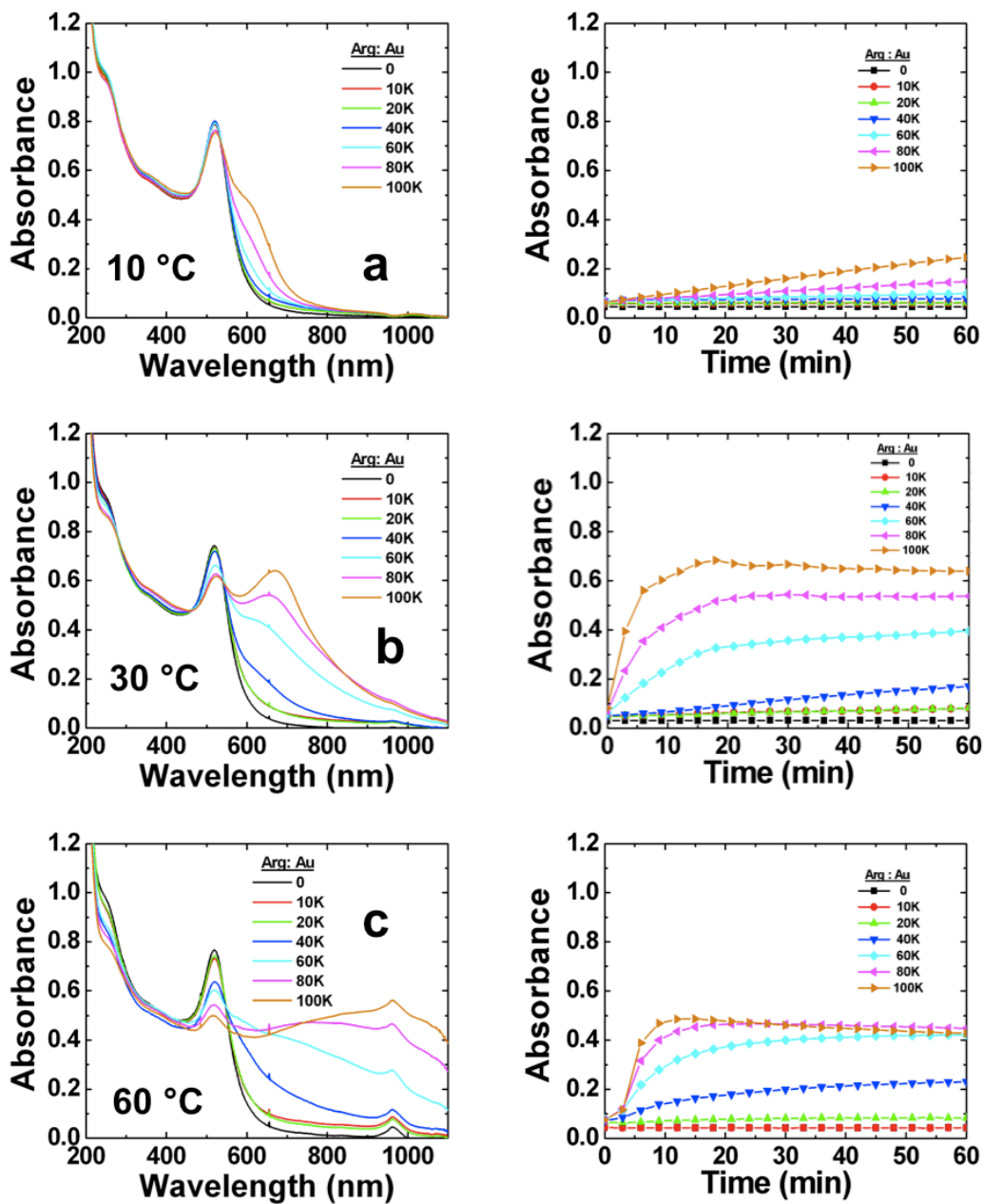
Figure A2.14 UV-vis analysis of the temperature effects on the Arg concentration dependent assembly of Au nanoparticles in the presence of 400 μM NaCl at (a) 10.0 °C, (b) 30.0 °C, and (c) 60.0 °C. The plots on the left demonstrate the UV-vis spectra obtained after 1.00 h of reaction for each Arg: Au nanoparticle ratio studied, while the plots on the right present the absorbance intensity of the 665 nm peak as a function of time.
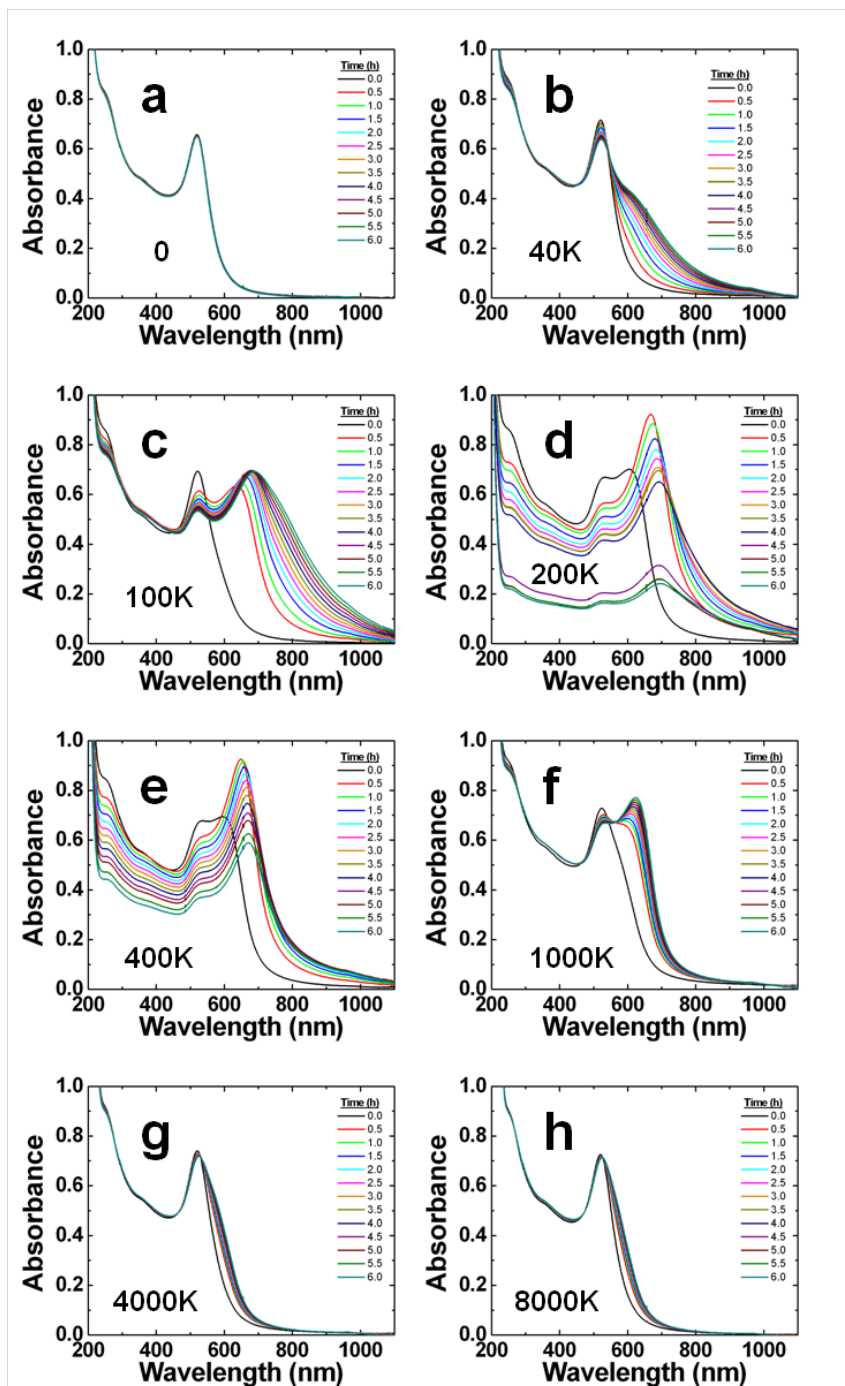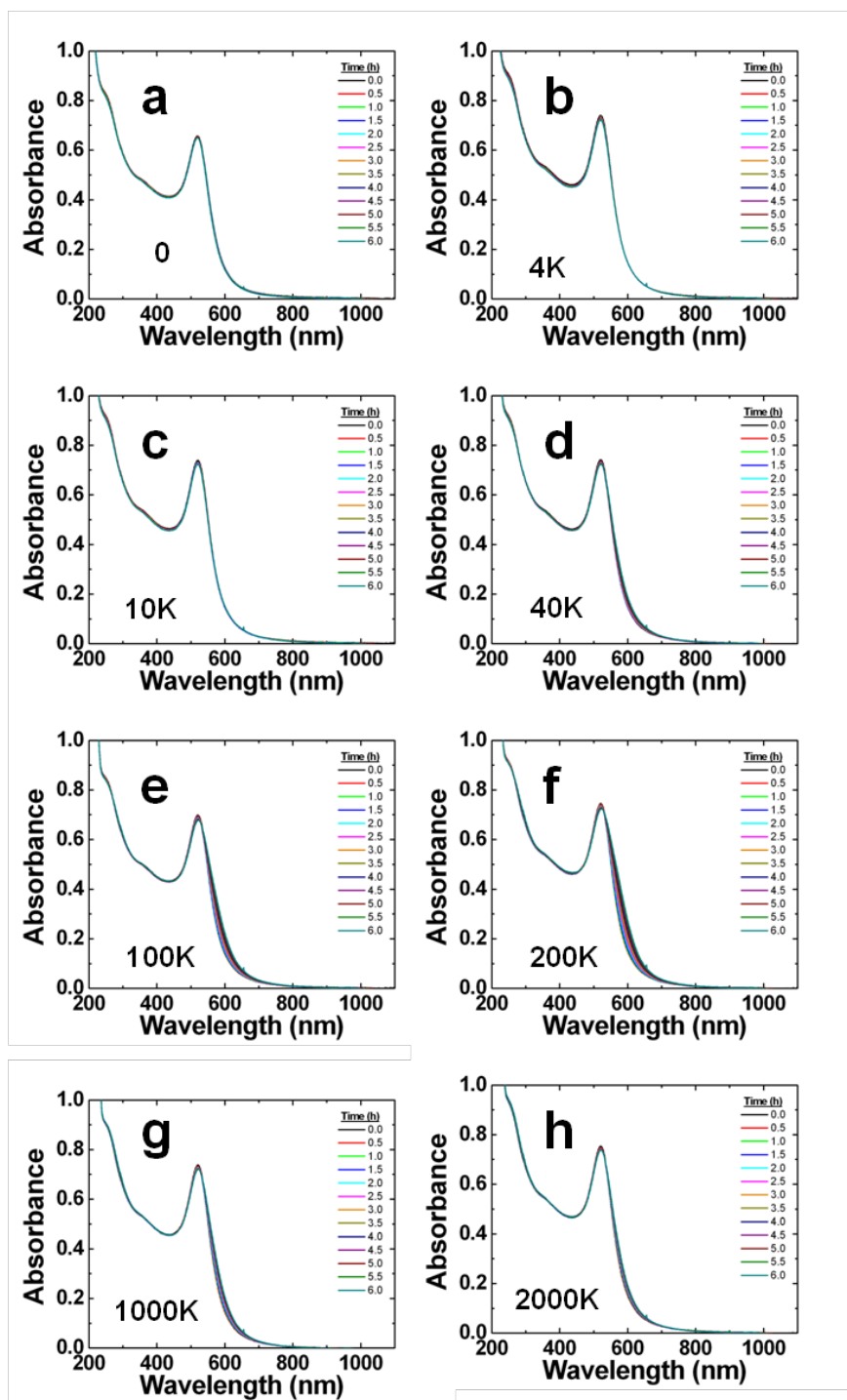
Figure A3.1. UV-vis analysis of the citrate-capped Au nanoparticles in the presence of Arg over the 6.00 h reaction time. For each analysis, the Arg:Au nanoparticle ratio employed was (a) 0, (b) 40K, (c) 100K, (d) 200K, (e) 400K, (f) 1000K, (g) 4000K, (h) 8000K.
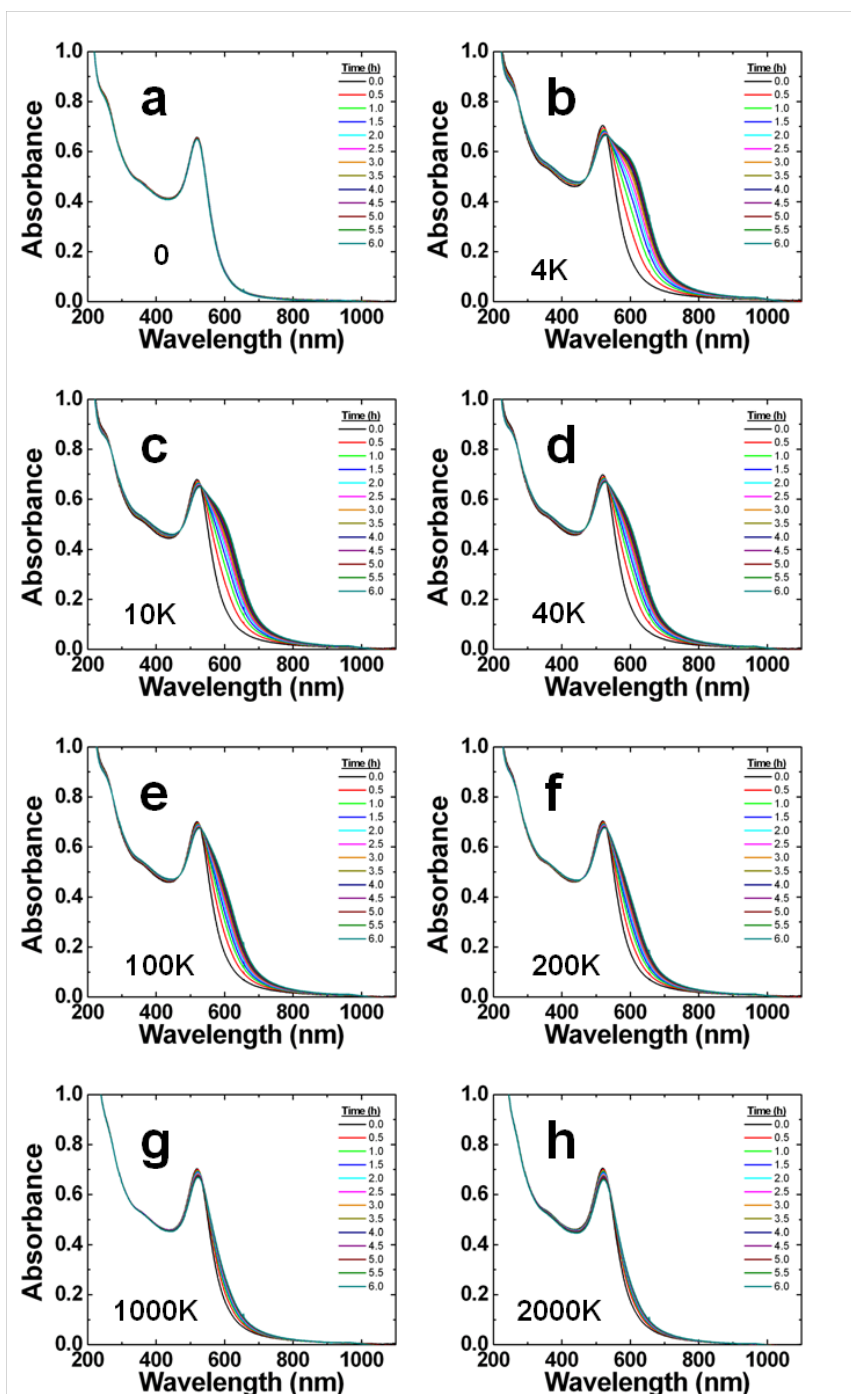
Figure A3.2. UV-vis analysis of the citrate-capped Au nanoparticles in the presence of Cys over the 6.00 h reaction time. For each analysis, the Cys:Au nanoparticle ratio employed was (a) 0, (b) 4K, (c) 10K, (d) 40K, (e) 100K, (f) 200K, (g) 1000K, (h) 2000K.

Figure A3.3. UV-vis analysis of the citrate-capped Au nanoparticles in the presence of His over the 6.00 h reaction time. For each analysis, the His:Au nanoparticle ratio employed was (a) 0, (b) 4K, (c) 10K, (d) 40K, (e) 100K, (f) 200K, (g) 1000K, (h) 2000K.
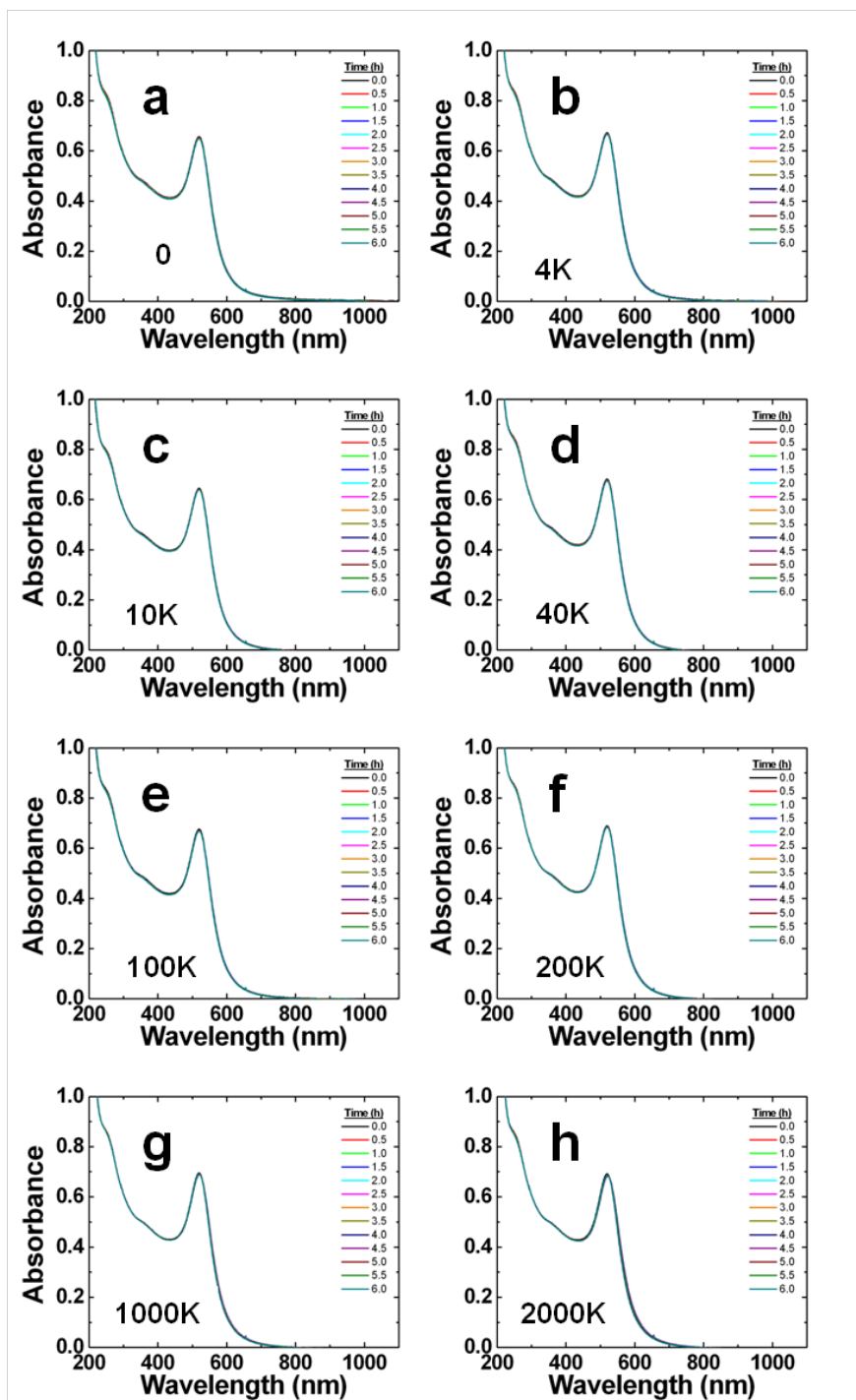
Figure A3.4. UV-vis analysis of the citrate-capped Au nanoparticles in the presence of Ala over the 6.00 h reaction time. For each analysis, the Ala:Au nanoparticle ratio employed was (a) 0, (b) 4K, (c) 10K, (d) 40K, (e) 100K, (f) 200K, (g) 1000K, (h) 2000K.
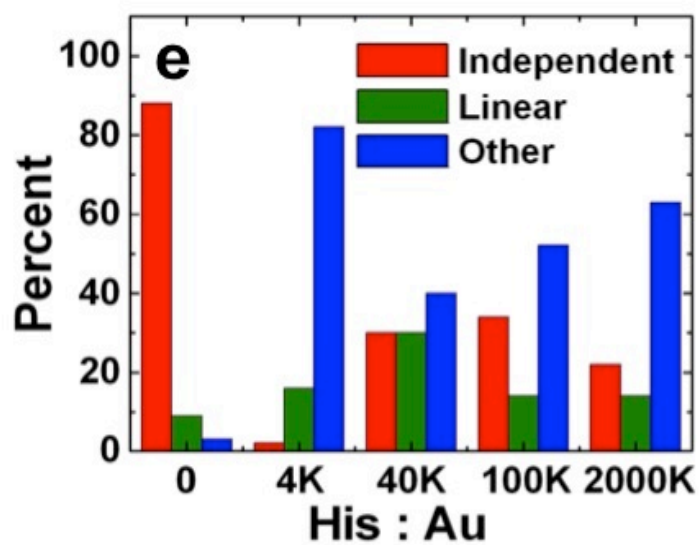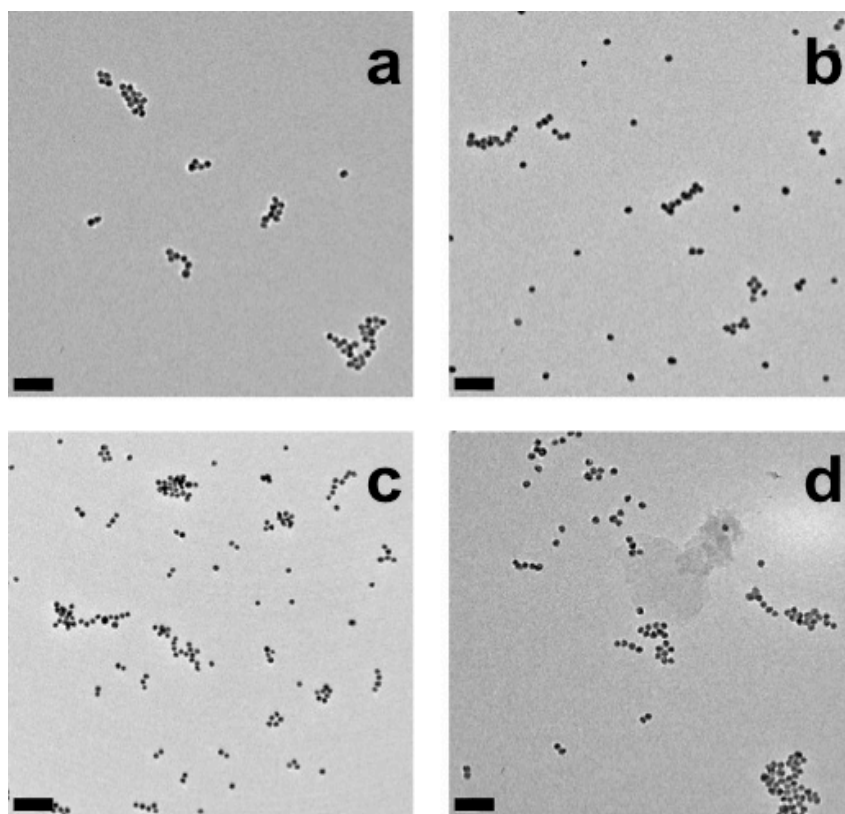
Figure A3.5. TEM analysis of the materials prepared at His:Au nanoparticle ratios of (a) 4K, (b) 40K, (c) 100K, and (d) 2000K. The scale bar represents 50 nm. Part (e) presents a statistical analysis of the assembly state based upon the TEM images.

Figure A3.6. TEM analysis of the materials prepared at Ala:Au nanoparticle ratios of (a) 4K, (b) 40K, (c) 100K, and (d) 2000K. The scale bar represents 50 nm. Part (e) presents a statistical analysis of the assembly state based upon the TEM images.
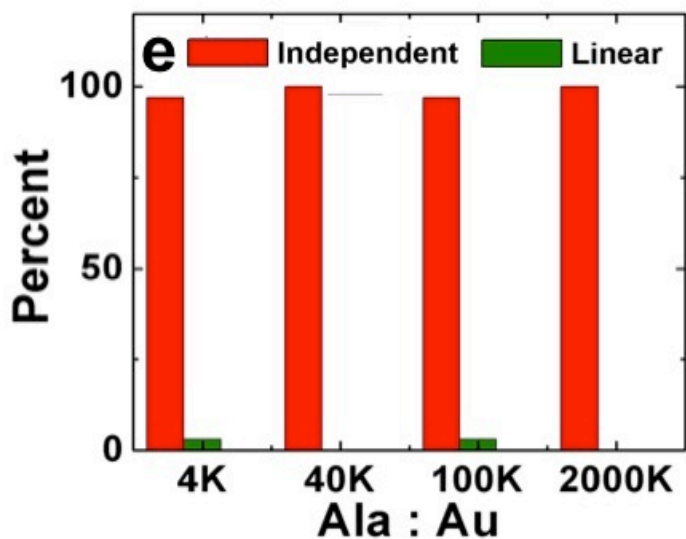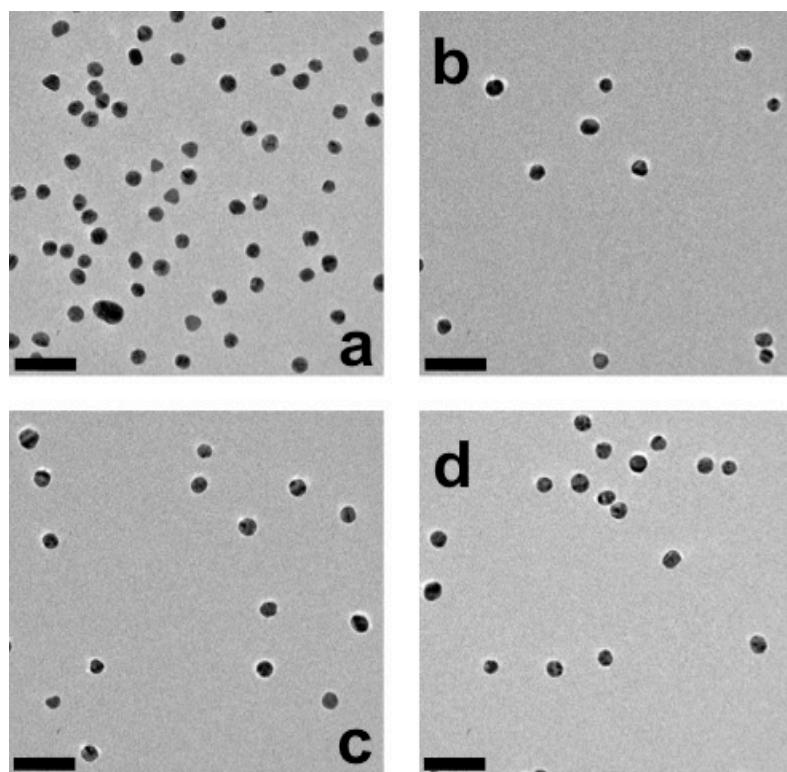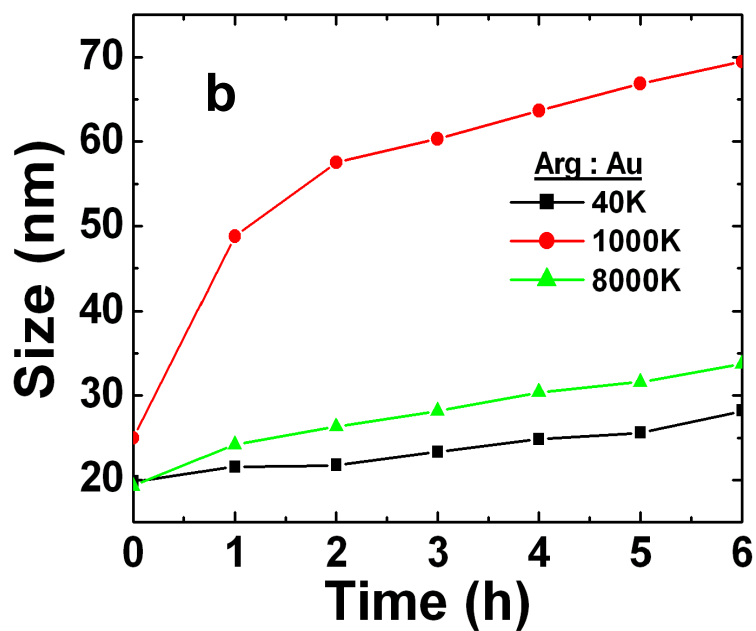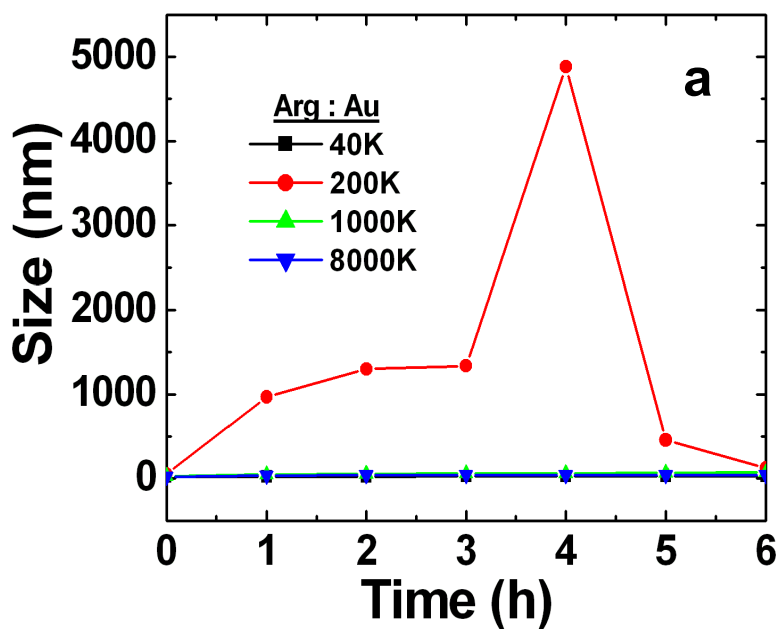
Figure A3.7. (a) DLS analysis of the assembly of Au nanoparticles in the presence of Arg. Part (b) presents an expanded analysis of the 40K, 1000K, and 8000K samples.

Figure A3.8. DLS particle size distributions for the Arg-assembled materials at Arg:Au nanoparticle ratios of (a) 40K, (b) 200K, (c) 1000K, and (d) 8000K.

Figure A3.9. DLS particle size distributions for the Cys-assembled materials at Cys:Au nanoparticle ratios of (a) 4K, (b) 40K, (c) 100K, and (d) 2000K.
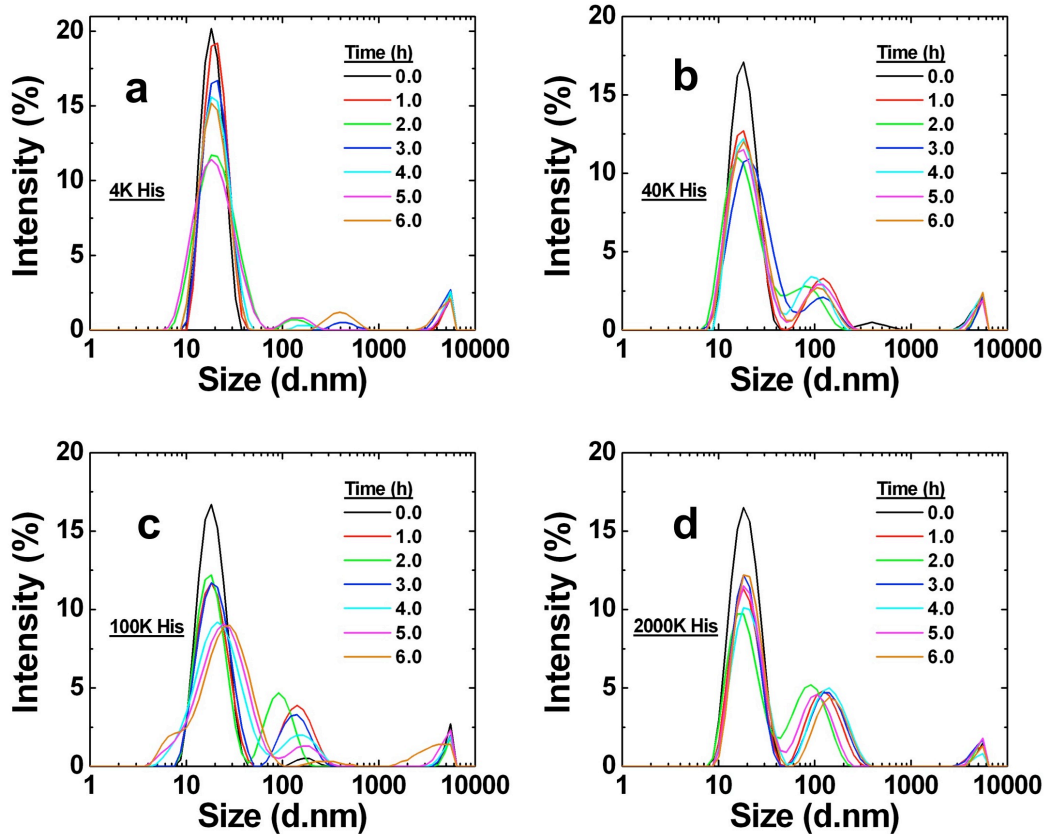
Figure A3.10. DLS particle size distributions for the His-assembled materials at His:Au nanoparticle ratios of (a) 4K, (b) 40K, (c) 100K, and (d) 2000K.
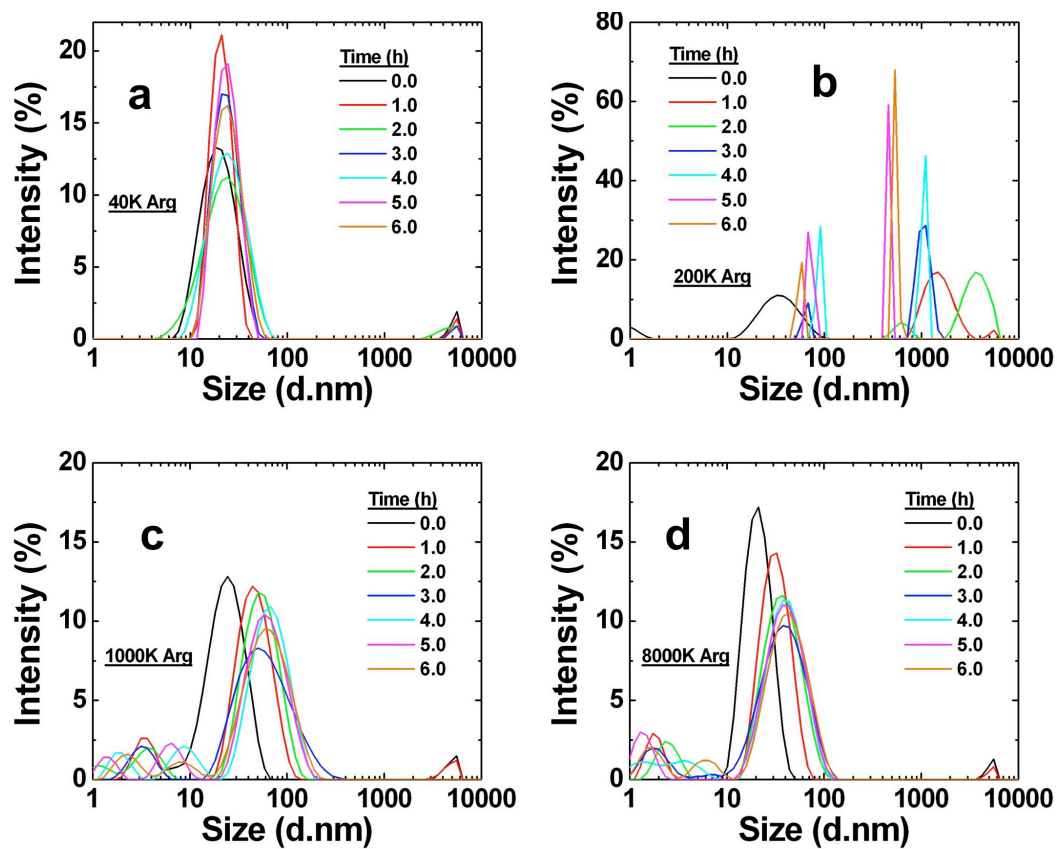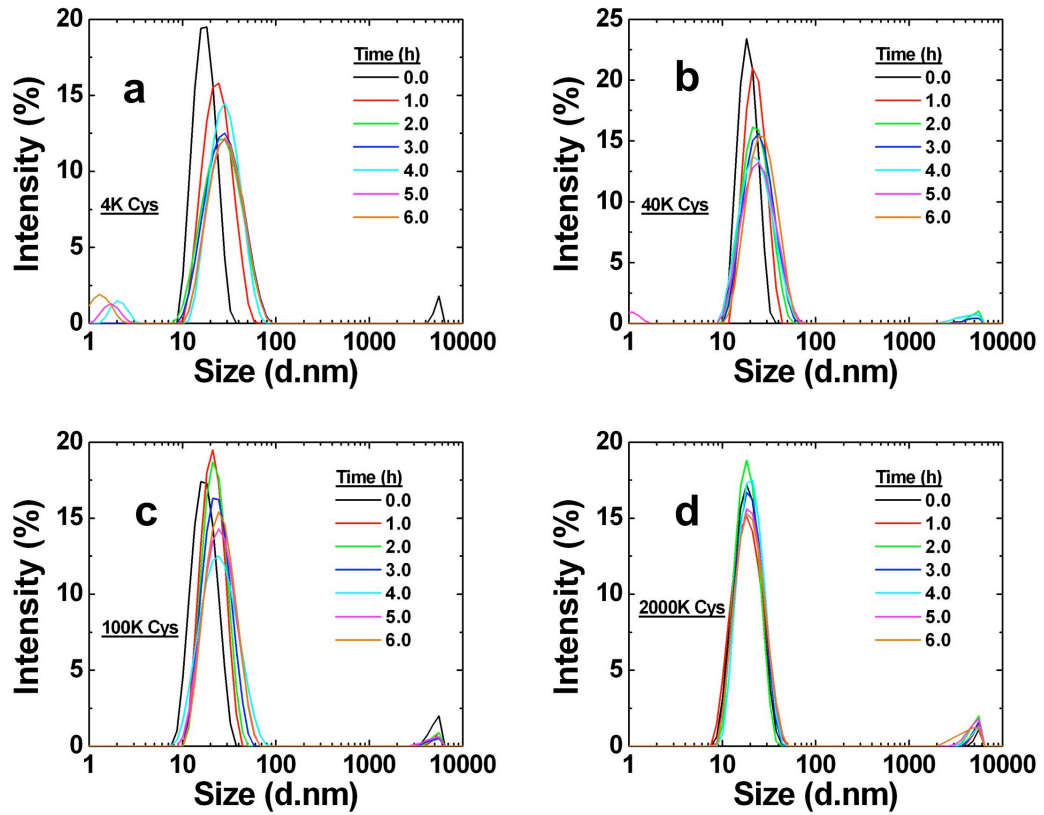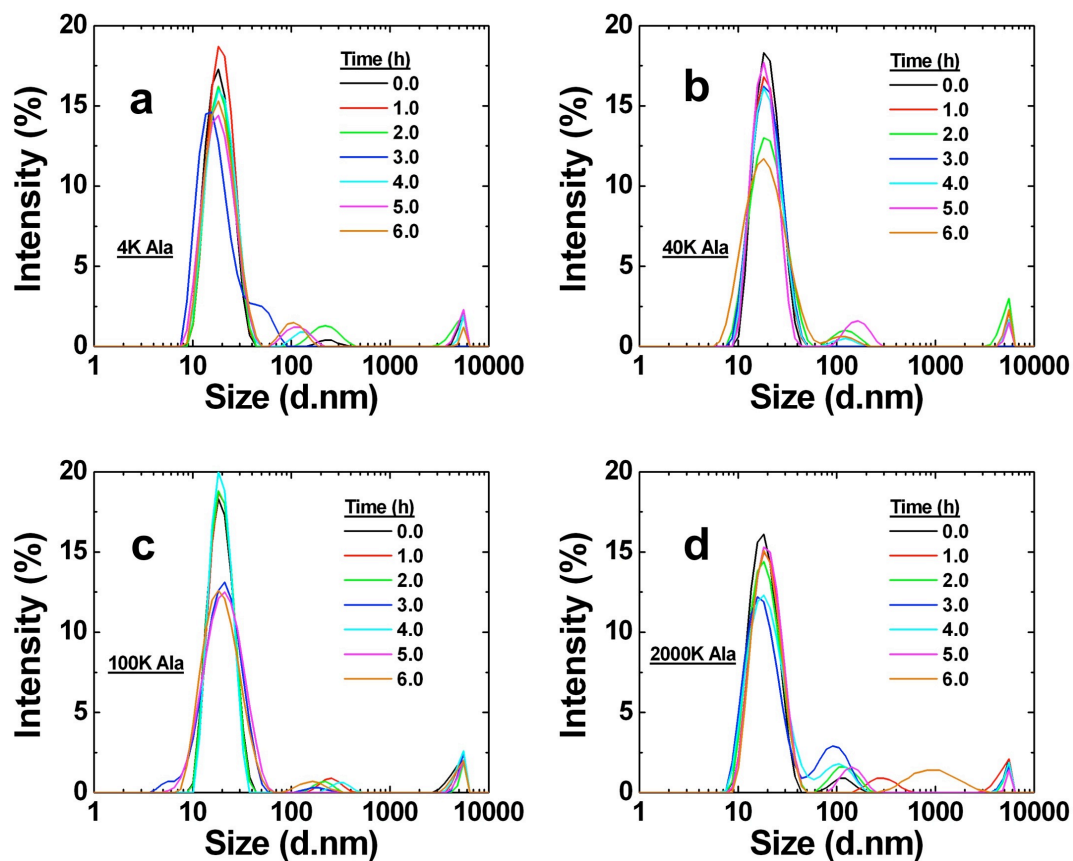
Figure A3.11. DLS particle size distributions for the Ala-assembled materials at Ala:Au nanoparticle ratios of (a) 4K, (b) 40K, (c) 100K, and (d) 2000K.
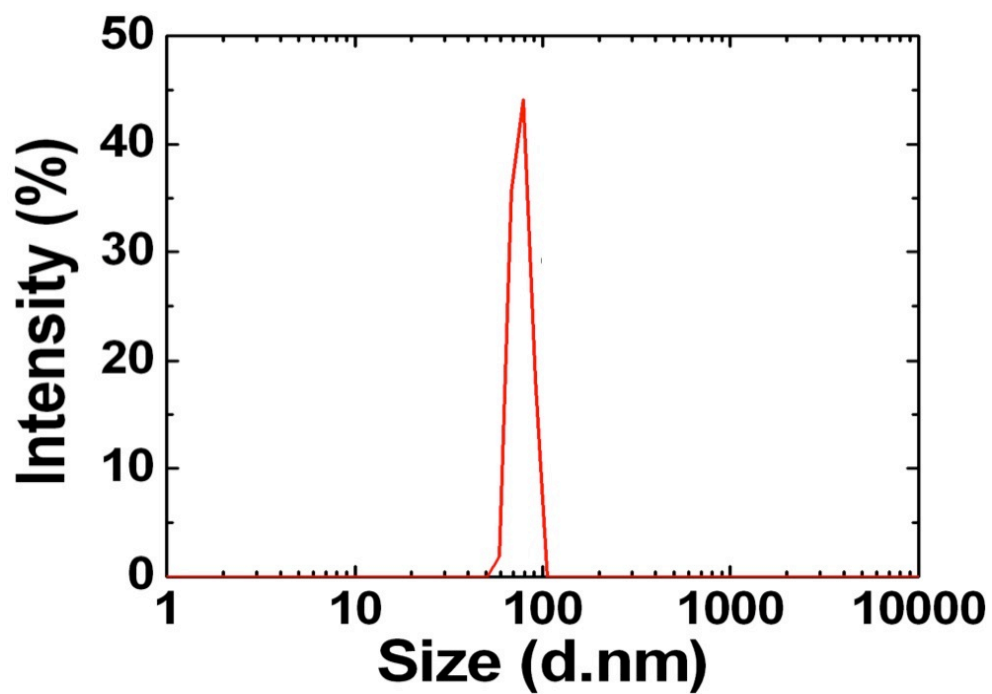
Figure A3.12. DLS analysis of 4.00 mM His in the presence of 19.4 mM citrate, which represents the reaction concentration of the two species in the 2000K His sample. As is evident, a peak is visible at ~100 nm, suggesting that some type of aggregated structure is generated under these conditions.
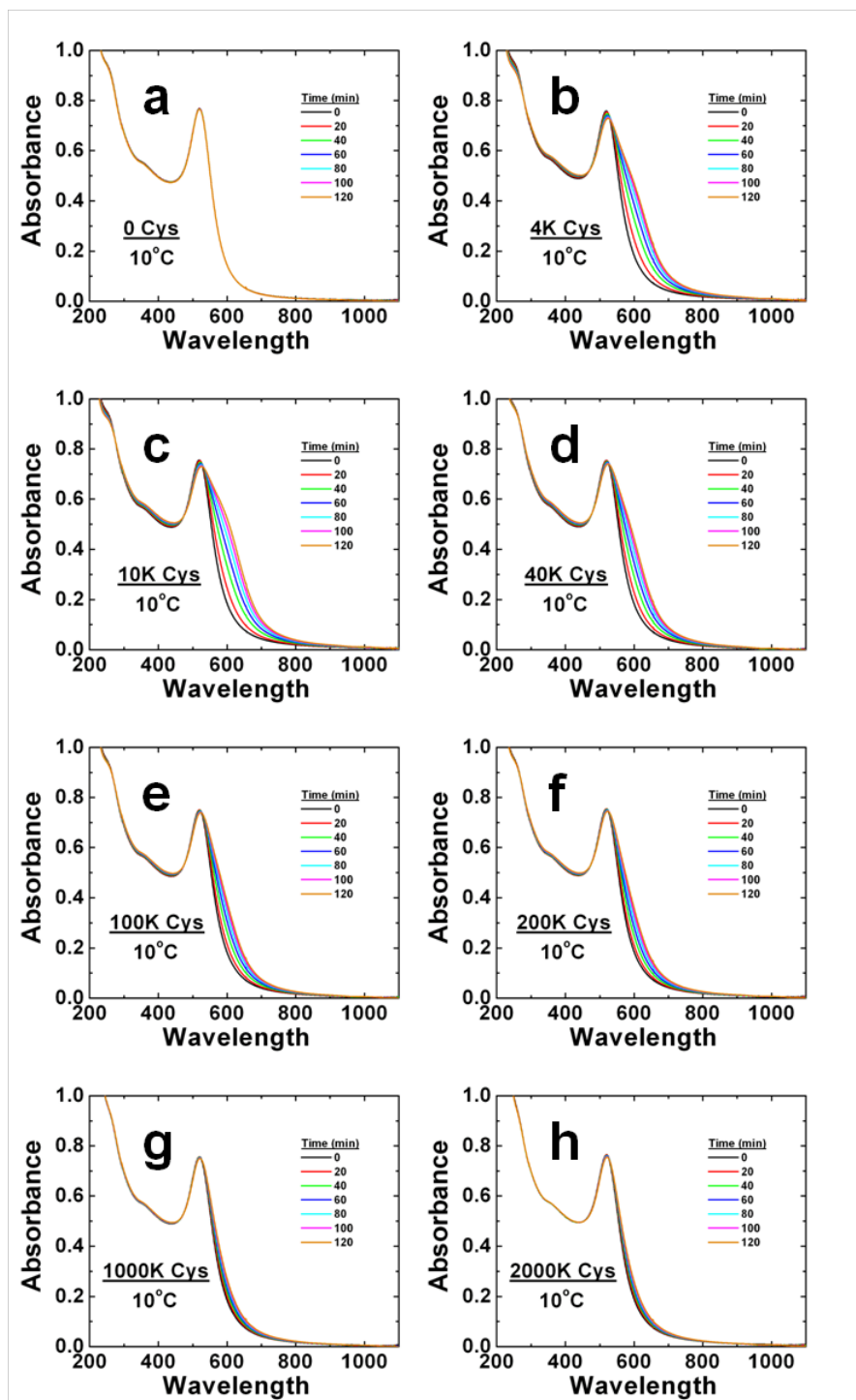
Figure A3.13. UV-vis analysis of the citrate-capped Au nanoparticles in the presence of Cys over the 2.00 h reaction time at 10.0 °C. For each analysis, the Cys:Au nanoparticle ratio employed was (a) 0, (b) 4K, (c) 10K, (d) 40K, (e) 100K, (f) 200K, (g) 1000K, (h) 2000K.
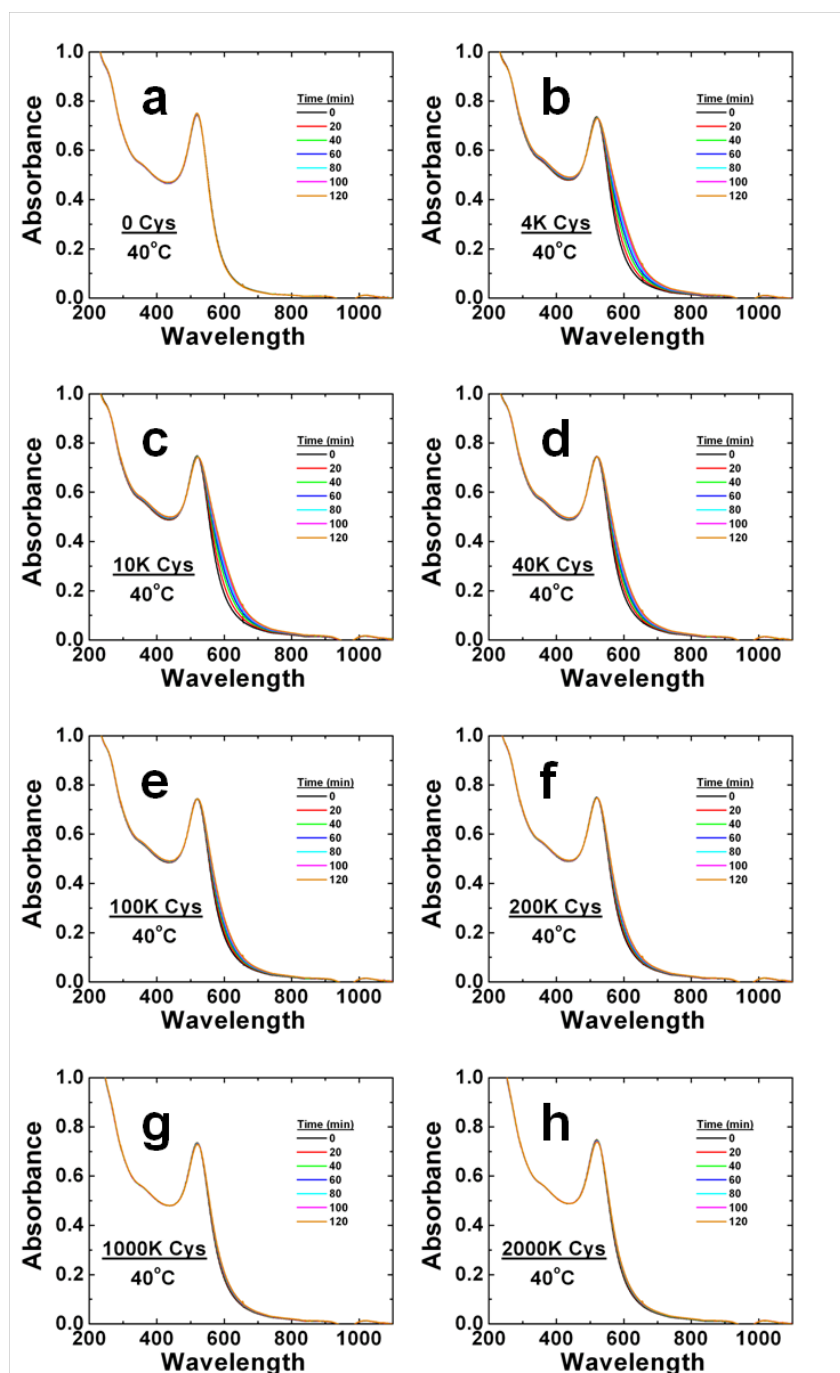
Figure A3.14. UV-vis analysis of the citrate-capped Au nanoparticles in the presence of Cys over the 2.00 h reaction time at 40.0 °C. For each analysis, the Cys:Au nanoparticle ratio employed was (a) 0, (b) 4K, (c) 10K, (d) 40K, (e) 100K, (f) 200K, (g) 1000K, (h) 2000K.
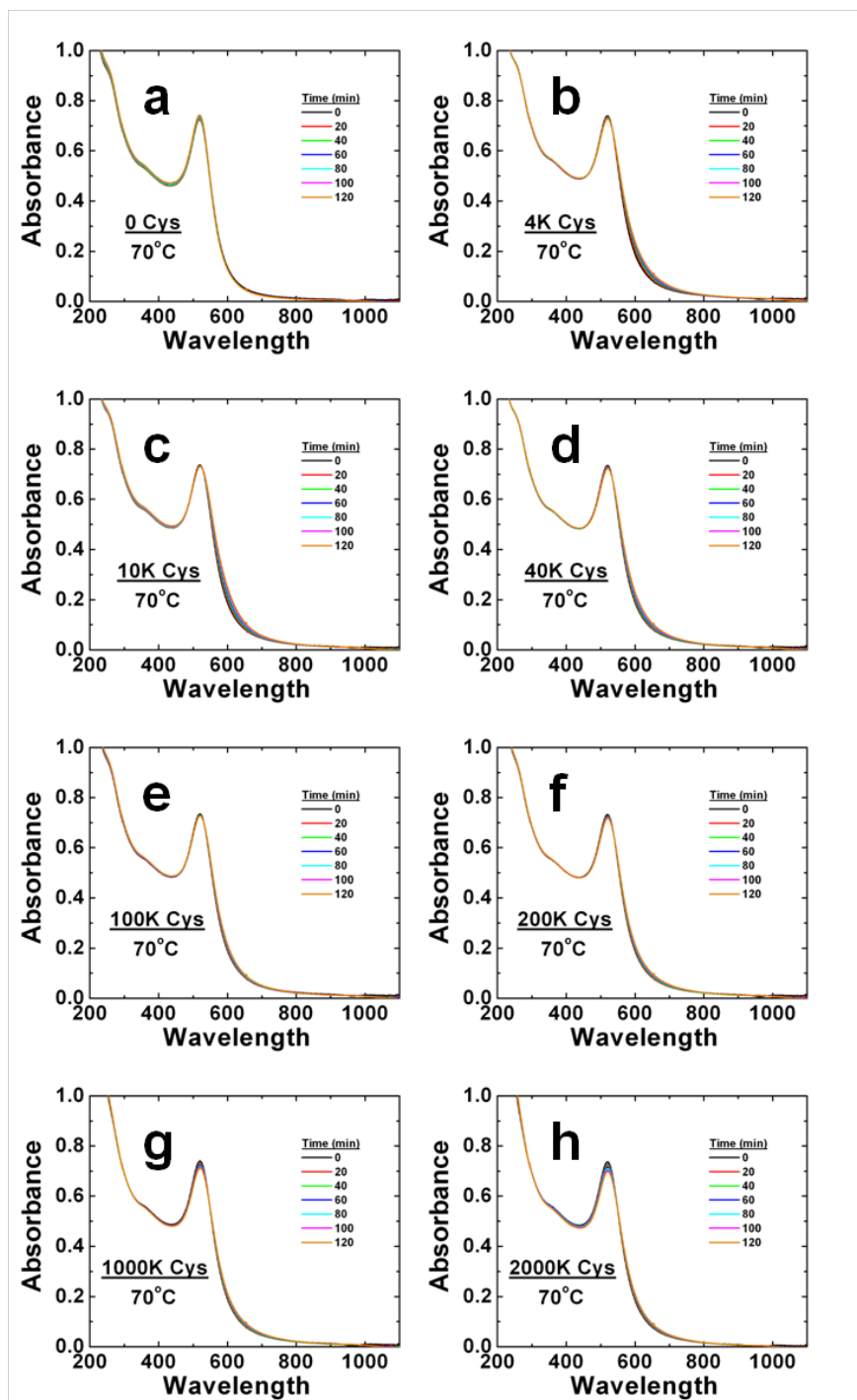
Figure A3.15. UV-vis analysis of the citrate-capped Au nanoparticles in the presence of Cys over the 2.00 h reaction time at 70.0 °C. For each analysis, the Cys:Au nanoparticle ratio employed was (a) 0, (b) 4K, (c) 10K, (d) 40K, (e) 100K, (f) 200K, (g) 1000K, (h) 2000K.
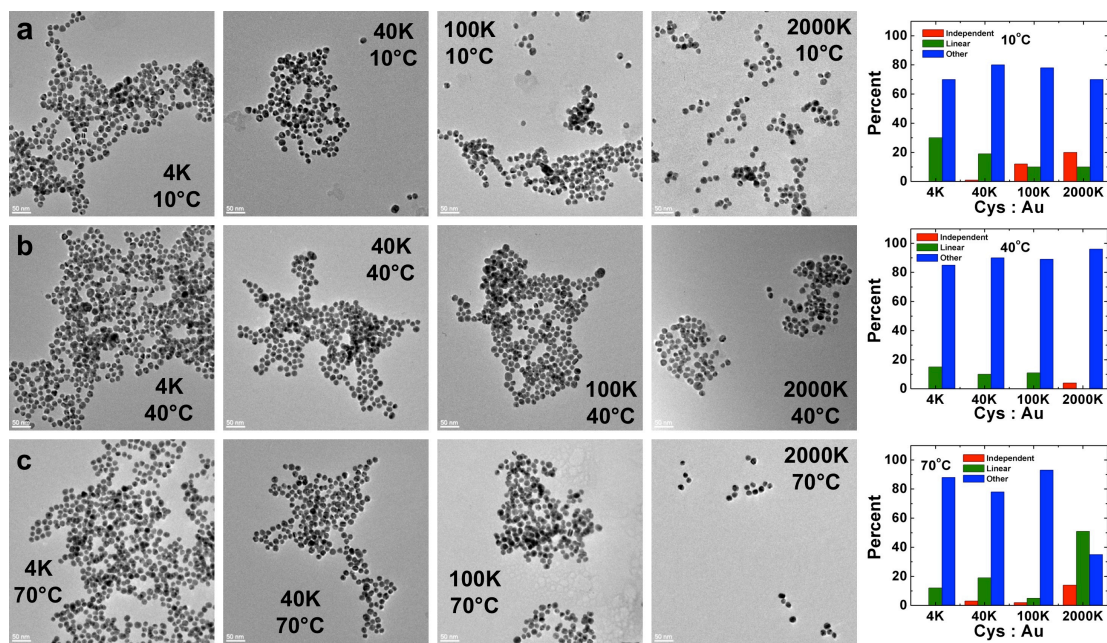
Figure A3.16. TEM analysis of the effects of reaction temperature on the cysteine mediated assembly of Au nanoparticles at temperatures of (a) 10.0 °C, (b) 40.0 °C, and (c) 70.0 °C at Cys:Au nanoparticle ratios of 4K, 40K, 100K, and 2000K. The graph on the right demonstrates a statistical analysis of the nanoparticle assembly state as determined from the TEM study of >100 nanoparticles.
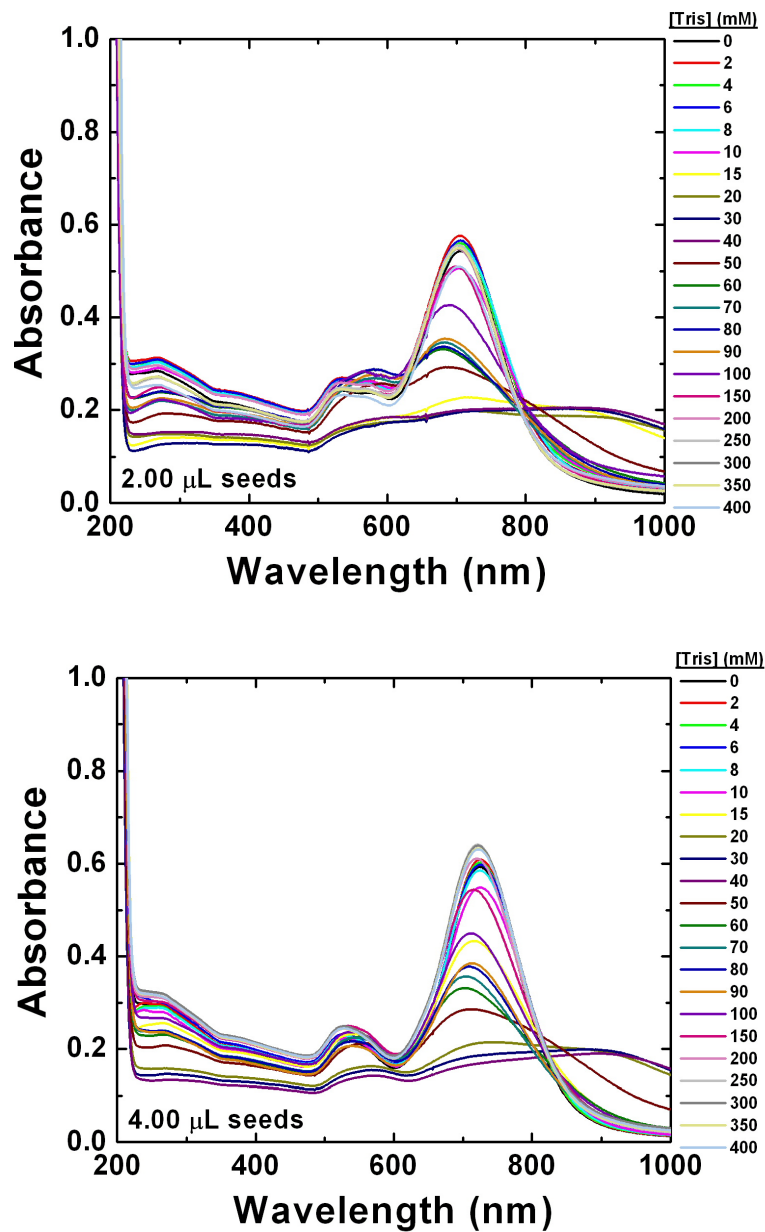
Figure A4.1. UV-vis spectra of Au nanorods dissolved in various concentrations of Tris buffer at pH 7.42. Part (a) corresponds to the materials prepared using 2.00 μL of Au seeds, while part (b) is for the materials produced using 4.00 μL of Au seeds.
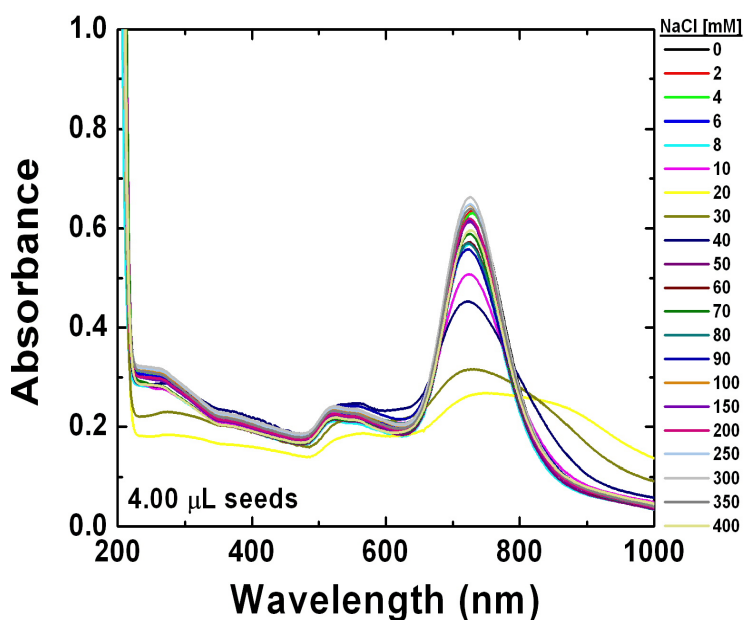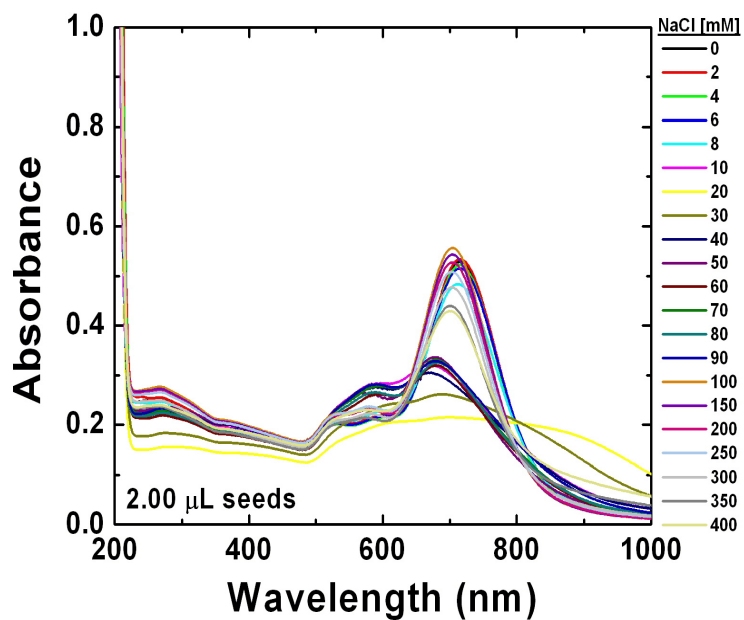
Figure A4.2. UV-vis spectra of Au nanorods dissolved in various concentrations of an aqueous NaCl solution titrated to pH 7.42. Part (a) corresponds to the materials prepared using 2.00 μL of Au seeds, while part (b) is for the materials produced using 4.00 μL of Au seeds.
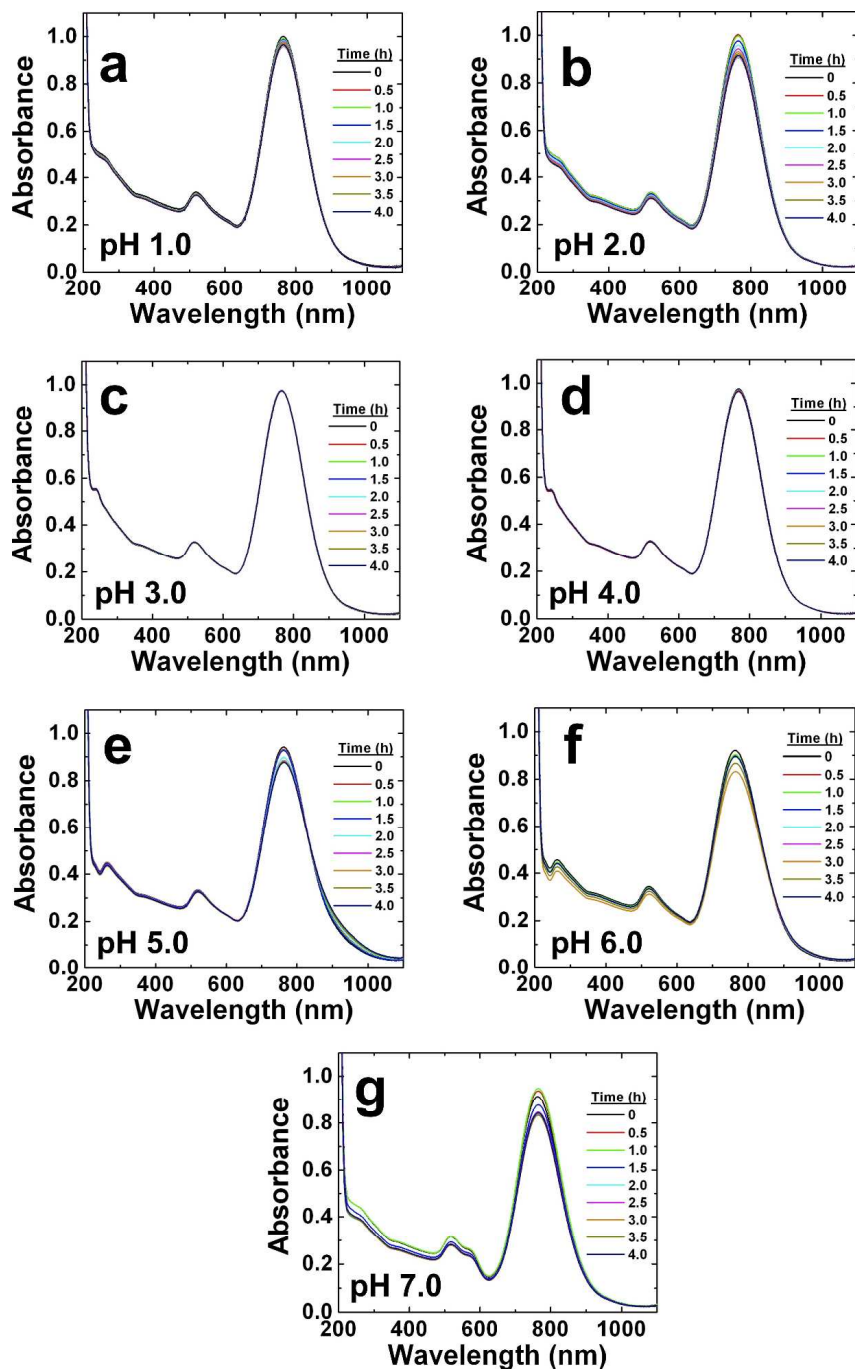
Figure A5.1. Stability analysis of the Au nanorods dissolved in water titrated to (a) pH 1.0, (b) pH 2.0, (c) pH 3.0, (d) pH 4.0, (e) pH 5.0, (f) pH 6.0, and (g) pH 7.0. No degradation or change in the nanorod structure or assembly is evident after 4.00 h in solution at any pH value studied.
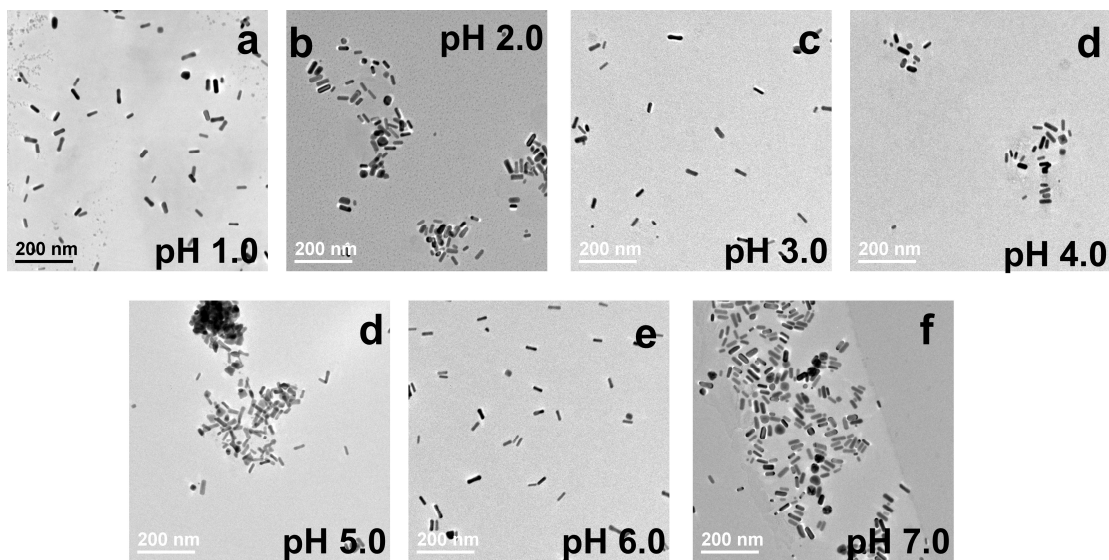
Figure A5.2. TEM images of the Au nanorods after being dissolved in water titrated to (a) pH 1.0, (b) pH 2.0, (c) pH 3.0, (d) pH 4.0, (e) pH 5.0, (f) pH 6.0, and (g) pH 7.0. No change in morphology is noted for the materials and only randomly oriented nanorods are observed by TEM analysis.

Table A5.1 Statistical Analysis of the End-to-End Assembly of Au Nanorods Based upon TEM Images

pH	No Ligand			Cysteine			MPA			Cysteamine		
	end-to-end	total	percentage	end-to-end	total	percentage	end-to-end	total	percentage	end-to-end	total	percentage
1.0	33	336	9.8%	405	474	85.4%	26	263	9.8%	244	351	69.5%
2.0	42	496	8.5%	200	351	57.0%	134	405	33.1%	43	212	20.3%
3.0	11	178	6.2%	140	366	38.3%	150	425	35.3%	78	349	22.3%
4.0	13	187	7.0%	78	919	8.5%	47	312	15.1%	59	454	12.9%
5.0	26	250	10.4%	63	462	13.6%	58	543	10.7%	53	346	15.3%
6.0	36	343	10.5%	86	611	11.1%	45	506	8.9%	34	388	8.8%
7.0	38	485	7.8%	16	112	14.3%	42	449	9.4%	99	338	29.3%
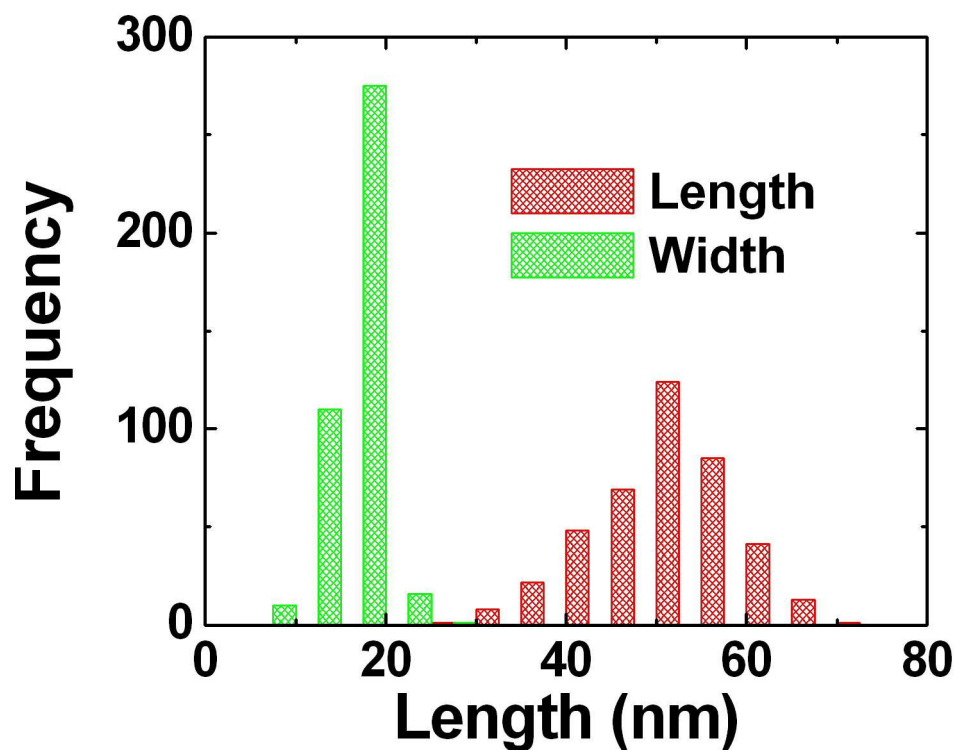
Figure A5.3. Particle size distribution analysis for the Au nanorods. Analysis of > 400 nanorods demonstrated an average dimensions of 51.5 ± 7.5 nm × 15.9 ± 2.5 nm, for an average aspect ratio of 3.24.
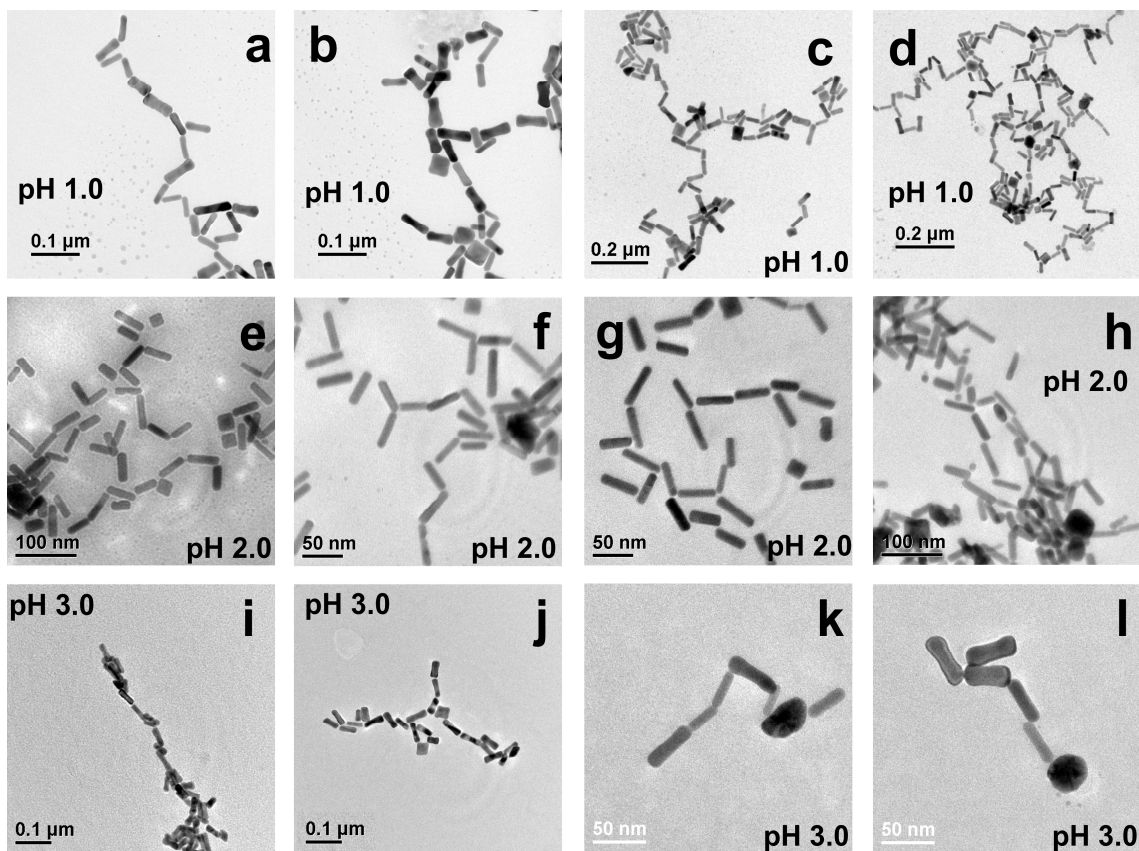
Figure A5.4. TEM images of linearly assembled Au nanorods using cysteine. Assembly was conducted at (a-d) pH 1.0, (e-h) pH 2.0, and (i-l) pH 3.0.
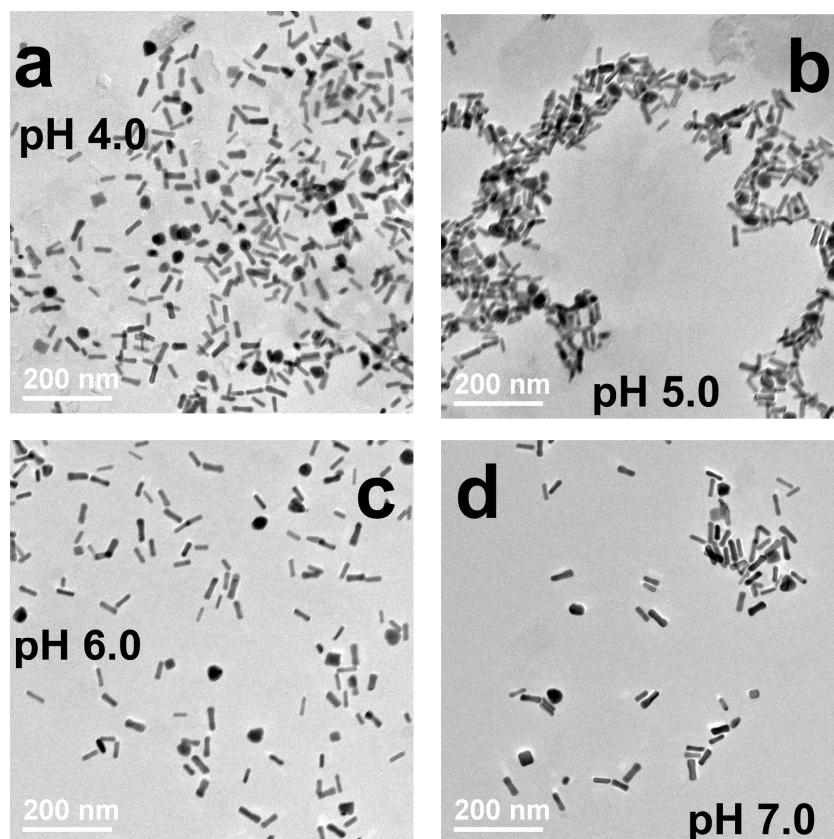
Figure A5.5. TEM images of the materials obtained after 4.00 h reaction between cysteine and the Au nanorods at (a) pH 4.0, (b) pH 5.0, (c) pH 6.0, and (d) pH 7.0. Only randomly oriented nanorods were observed with no evidence of materials assembly.
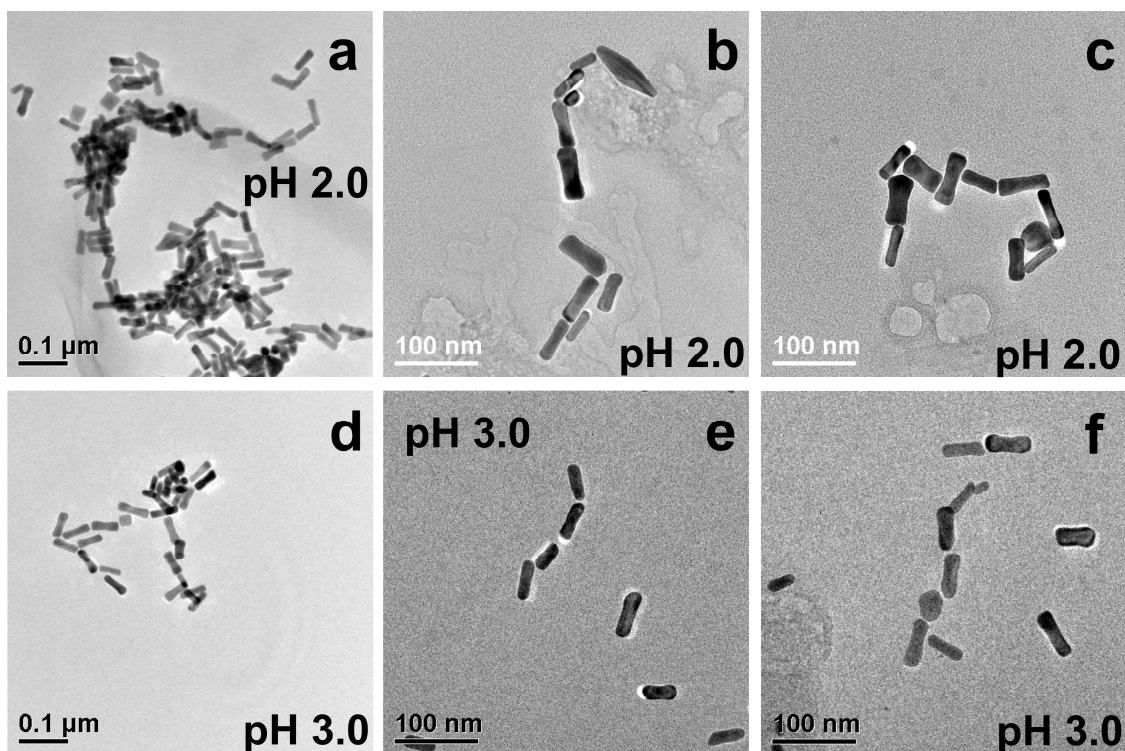
Figure A5.6. TEM images of linearly assembled Au nanorods using MPA. Assembly was conducted at (a-c) pH 2.0 and (d-f) pH 3.0.
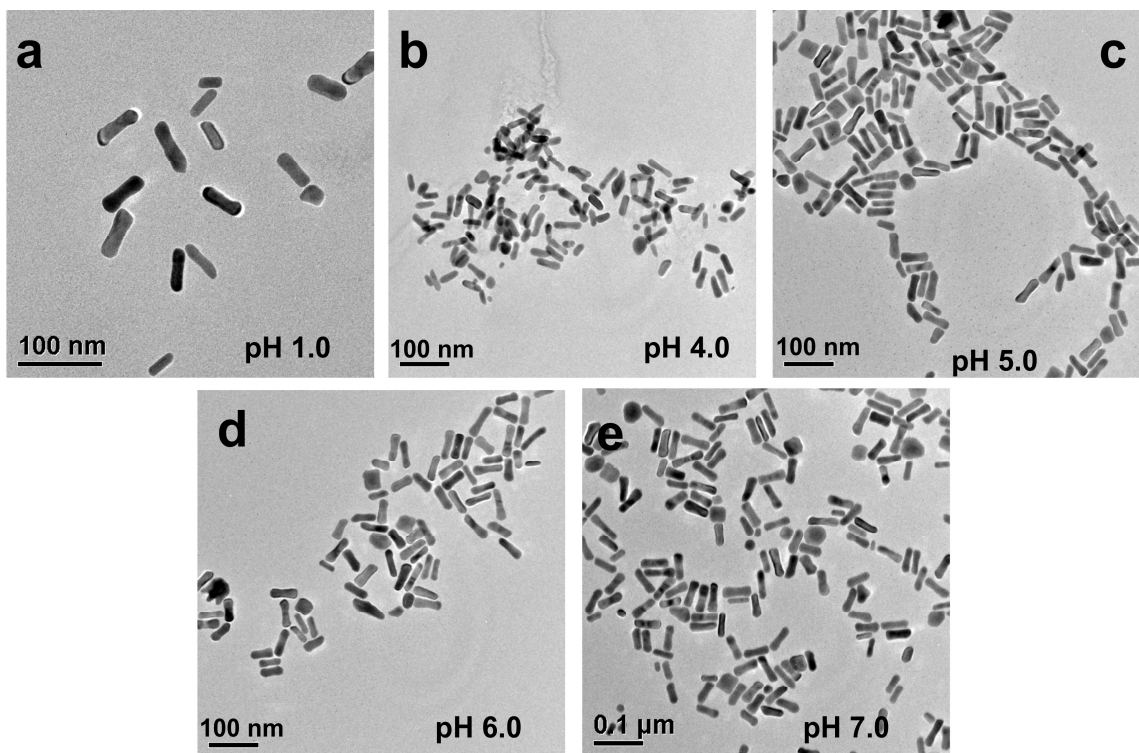
Figure A5.7. TEM images of the materials obtained after 4.00 h reaction between MPA and the Au nanorods at (a) pH 1.0, (b) pH 4.0, (c) pH 5.0, (d) pH 6.0, and (e) pH 7.0. Only randomly oriented nanorods were observed with no evidence of materials assembly.
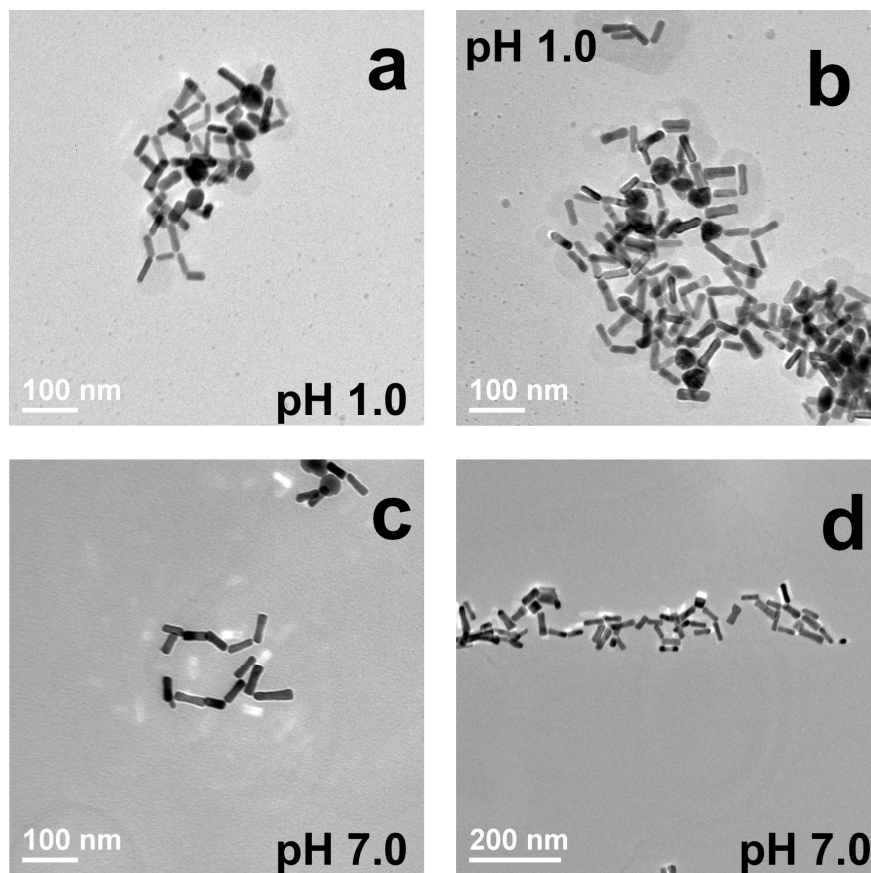
Figure A5.8. TEM images of linearly assembled Au nanorods using cysteamine. Assembly was conducted at (a-d) pH 1.0 and (e-h) pH 7.0. Note that obtaining dispersed Au nanorod chains at pH 1.0 was difficult due to the fast assembly rate at this pH value for cysteamine.
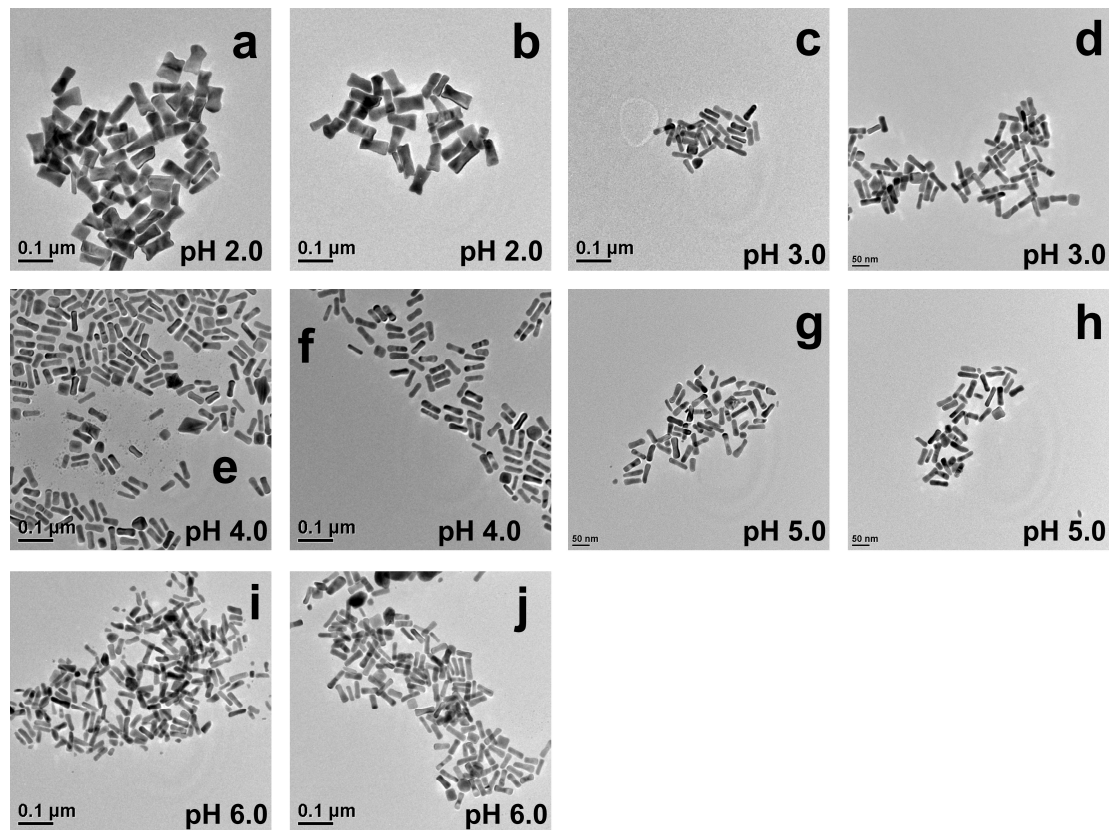
Figure A5.9. TEM images of the materials obtained after 4.00 h reaction between cysteamine and the Au nanorods at (a and b) pH 2.0, (c and d) pH 3.0, (e and f) pH 4.0, (g and h) pH 5.0, and (i and j) pH 6.0. Only randomly oriented nanorods were observed with no evidence of materials assembly.
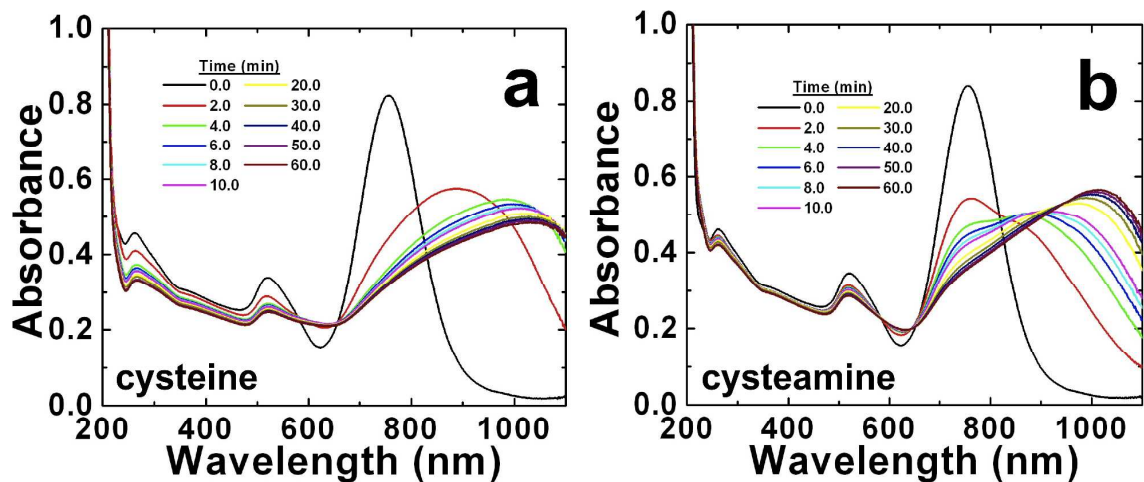
Figure A5.10. Assembly of Au nanorods at pH 7.0 in a solution of 400 mM NaCl mediated by (a) cysteine and (b) cysteamine.

References

(1)   Nano.gov 2011.

(2)   Cao, G.; Wang, Y. *Nanostructures and Nanoaterials: Synthesis, Properties and Applications*; 2 ed.; World Scientific Publishing Co. Pte. Ltd: Singapore, 2011; Vol. 2.

(3)   Henglein, A. *Chem. Rev.* **1989**, *89*, 1861.

(4)   Wang, Z. L. *Adv. Mater.* **1998**, *10*, 13.

(5)   Schmid, G. *Chem. Rev.* **1992**, *92*, 1709.

(6)   Schon, G.; Simon, U. *Colloidal Polym. Sci.* **1995**, *273*, 101.

(7)   Napper, D. H. *Polymeric Stabilization of Colloidal Dispersions*; Academic Press: New York, 1983.

(8)   Russel, W. B.; Saville, D. A.; Schowalter, W. R. *Colloidal Dispersions*; Cambridge University Press: Cambridge, 1991.

(9)   Somasundaran, P.; Markovic, B.; Krishnakumar, S.; Yu, X. *Colloid Systems and Interfaces - Stability of Dispersions Through Polymer and Surfactant Adsorption*; CRC Press: New York, 1997.

(10)   Hiemenz, P. C. *Principles of Colloid and Surface Chemistry*; Marcel Dekker: New York, 1977.

(11)   Faraday, M. *Phil. Trans. R. Soc.* **1857**, *147*, 145.

(12)   Turkevich, J.; Stevenson, P. C.; Hillier, J. *Discuss. Faraday Soc.* **1951**, *11*, 55.

(13)   Frens, G. *Nat. Phys. Sci.* **1973**, *241*, 20.

(14)   Parfitt, G. D. *Dispersion of Powders in Liquids with Special Reference to Pigments*; Applied Science: London, 1981.

(15)   Lieser, K. H. *Angew. Chem. Int. Ed.* **1969**, *8*, 188.

(16)   Ahmadi, T. S.; Wang, Z. L.; Green, T. C.; Henglein, A.; El-Sayed, M. A. *Science* **1996**, *272*, 1924.

(17)   Herron, N.; Wang, Y.; Eckert, H. *J. Am. Chem. Soc.* **1990**, *112*, 1322.

(18)   Sethi, M.; Joung, G.; Knecht, M. R. *Langmuir* **2009**, *25*, 1572.

(19)   Vos, J. G.; Forster, R. J.; Keyes, T. E. In *Interfacial Supramolecular Assemblies*; John Wiley & Sons, Ltd: 2003.

(20)   Schlenoff, J. B.; Li, M.; Ly, H. *J. Am. Chem. Soc.* **1995**, *117*, 12528.

(21)   Montalti, M.; Prodi, L.; Zacharoni, N.; Baxter, R.; Teobaldi, G.; Zerbetto, F. *Langmuir* **2003**, *19*, 5172.

(22)   *Nanoscale Materials in Chemistry*; 2nd ed.; Klabunde, K. J.; Richards, R. M., Eds.; John Wiley & Sons, Inc.: New Jersey, 2009.

(23)   Sethi, M.; Law, W.-C.; Fennell, W. A.; Prasad, P. N.; Knecht, M. R. *Soft Matter* **2011**, *7*, 6532.

(24)   Simard, J.; Briggs, C.; Boal, A. K.; Rotello, V. M. *Chem. Commun.* **2000**, *2000*, 1943.

(25)   Westenhoff, S.; Kotov, N. A. *J. Am. Chem. Soc.* **2002**, *124*, 2448.

(26)   Zubarev, E. R.; Xu, J.; Sayyad, A.; Gibson, J. D. *J. Am. Chem. Soc.* **2006**, *128*, 4958.

(27)   Song, T.; Dai, S.; Tam, K. C.; Lee, S. Y.; Goh, S. H. *Langmuir* **2003**, *19*, 4798.

(28)   Giljohann, D. A.; Seferos, D. S.; Patel, P. C.; Millstone, J. E.; Rosi, N. L.; Mirkin, C. A. *Nano Lett.* **2007**, *7*, 3818.

(29)   Huo, F.; Lytton-Jean, A. K. R.; Mirkin, C. A. *Adv. Mater.* **2006**, *18*, 2304.

(30)   Rosi, N. L.; Giljohann, D. A.; Thaxton, C. S.; Lytton-Jean, A. K. R.; Han, M. S.; Mirkin, C. A. *Science* **2006**, *312*, 1027.

(31)   Xu, X.; Rosi, N. L.; Wang, Y.; Huo, F.; Mirkin, C. A. *J. Am. Chem. Soc.* **2006**, *128*, 9286.

(32)   Hanszen, K. J. *Z. Phys.* **1960**, *157*, 523.

(33)   Sambles, J. R. *Journal of Physics and Chemistry of Solids* **1985**, *46*, 525.

(34)   Peters, K. F.; Chung, Y.-W.; Cohen, J. B. *Appl. Phys. Lett.* **1997**, *71*, 2391.

(35)   Gladkich, N. T.; Niedermayer, R.; Spiegel, K. *Phys. Stat. Sol.* **1966**, *15*, 181.

(36)   Blackman, M.; Curzon, A. E. *Structure and Properties of Thin Films*; Wiley: New York, 1959.

(37)   Boiko, B. T.; Pugachev, A. T.; Bratsykhin, Y. M. *Sov. Phys. Sol. State* **1969**, *10*, 2832.

(38)   Takagi, M. *J. Phys. Soc. Jpn.* **1954**, *9*, 359.

(39)   Deneen, J.; Carter, C. *Microsc. Microanal.* **2006**, *12*, 594.

(40)   Ferrer, D.; Blom, D. A.; Allard, L. F.; Mejia, S.; Perez-Tijerina, E.; Jose-Yacaman, M. *J. Mater. Chem.* **2008**, *18*, 2442.

(41)   Willets, K. A.; Van Duyne, R. P. *Annu. Rev. Phys. Chem.* **2007**, *58*, 267.

(42)   Kelly, K. L.; Coronado, E.; Zhao, L. L.; Schatz, G. C. *J. Phys. Chem. B* **2002**, *107*, 668.

(43)   Seker, U. O. S.; Wilson, B.; Sahin, D.; Tamerler, C.; Sarikaya, M. *Biomacromolecules* **2009**, *10*, 250.

(44)   Homola, J. In *Optical Chemical Sensors*; Baldini, F., Chester, A. N., Homola, J., Martellucci, S., Eds.; Springer Netherlands: 2006; Vol. 224, p 179.

(45)   Nenninger, G. G.; Piliarik, M.; Homola, J. *Meas. Sci. Technol.* **2002**, *13*, 2038.

(46)   Hong, G.; Heinz, H.; Naik, R. R.; Farmer, B. L.; Pachter, R. *ACS Appl. Mater. Interfaces* **2009**, *1*, 388.

(47)   Mie, G. *Ann. Phys.* **1908**, *25*, 377.

(48)   Knecht, M. R.; Sethi, M. *Anal. Bioanal. Chem.* **2009**, *394*, 33.

(49)   Sethi, M.; Knecht, M. R. *Langmuir* **2010**, *26*, 9860.

(50)   Sethi, M.; Knecht, M. R. In *Nanobiotechnology Protocols*; Humana Press: 2012.

(51)   Sethi, M.; Pacardo, D. B.; Knecht, M. R. *Langmuir* **2010**, *26*, 15121.

(52)   Link, S.; El-Sayed, M. A. *J. Phys. Chem. B* **1999**, *103*, 4212.

(53)   Kreibig, U.; Vollmer, M. *Optical Properties of Metal Clusters*; Springer-Verlag: New York, 1995.

(54)   Hostetler, M. J.; Wingate, J. E.; Zhong, C.-J.; Harris, J. E.; Vachet, R. W.; Clark, M. R.; Londono, J. D.; Green, S. J.; Stokes, J. J.; Wignall, G. D.; Glish, G. L.; Porter, M. D.; Evans, N. D.; Murray, R. W. *Langmuir* **1998**, *14*, 17.

(55)   Templeton, A. C.; Pietron, J. J.; Murray, R. W.; Mulvaney, P. *J. Phys. Chem. B* **2000**, *104*, 564.

(56)   Kim, T.; Lee, C.-H.; Joo, S.-W.; Lee, K. *J. Colloid Interface Sci.* **2008**, *318*, 238.

(57)   Murphy, C. J.; Sau, T. K.; Gole, A. M.; Orendorff, C. J.; Gao, J.; Gou, L.; Hunyadi, S. E.; Li, T. *J. Phys. Chem. B* **2005**, *109*, 13857.

(58)   Sethi, M.; Joung, G.; Knecht, M. R. *Langmuir* **2009**, *25*, 317.

(59)   *Nanomaterials Chemistry: Recent Developments and New Directions*; Rao, C. N. R.; Mu ̈ller, A.; Cheetham, A. K., Eds.; WILEY-VCH Verlag GmbH & Co. KGaA: Weinheim, 2007.

(60)   *Biomedical Nanostructures*; Gonsalves, K. E.; Halberstadt, C. R.; Laurencin, C. T.; Nair, L. S., Eds.; John Wiley & Sons, Inc.: Hoboken, N. J., 2008.

(61)   Naik, R. R.; Jones, S. E.; Murray, C. J.; McAuliffe, J. C.; Vaia, R. A.; Stone, M. O. *Adv. Funct. Mater.* **2004**, *14*, 25.

(62)   Jensen, G. J.; Newman, D. K.; Zhuo, L.; Komeili, A. *Science* **2006**, *311*, 242.

(63)   Bazylinski, D. A.; Frankel, R. B. *Nat. Rev. Microbiol.* **2004** *2*, 217.

(64)   Komeili, A. *Annu. Rev. Biochem.* **2007**, *76*, 351.

(65)   Dickerson, M. B.; Sandhage, K. H.; Naik, R. R. *Chem. Rev.* **2008**, *108*, 4935.

(66)   Scheffel, A.; Gruska, M.; Faivre, D.; Linaroudis, A.; Plitzko, J. M.; Schuler, D. *Nature* **2006**, *440*, 110.

(67)   Addadi, L.; Joester, D.; Nudelman, F.; Weiner, S. *Chem. Eur. J.* **2006**, *12*, 980.

(68)   Sollner, C.; Burghammer, M.; Busch-Nentwich, E.; Berger, J.; Schwarz, H.; Riekel, C.; Nicolson, T. *Science* **2003**, *302*, 282.

(69)   Addadi, L.; Raz, S.; Weiner, S. *Adv. Mater.* **2003** *15*, 959.

(70)   Aizenberg, J.; Sundar, V. C.; Yablon, A. D.; Weaver, J. C.; Chen, G. *Proc. Nat. Acad. Sci. U.S.A.* **2004** *101* 3358.

(71)   Muller, W. E. G.; Wendt, K.; Geppert, C.; Wiens, M.; Reiber, A.; Schroder, H. C. *Biosens. Bioelectron.* **2006**, *21*, 1149.

(72)   Baeuerlein, E.; Wiley-VCH Verlag GmbH & Co. KGaA: Weinheim, Germany, 2004.

(73)   Baeuerlein, E.; Wiley-VCH Verlag GmbH & Co. KGaA: Weinheim, Germany, 2007.

(74)   Sadowski, Z.; Jazdzyk, E.; Karas, H. *Miner. Eng.* **2003**, *16*, 51.

(75)   Sundar, V. C.; Yablon, A. D.; Grazul, J. L.; Ilan, M.; Aizenberg, J. *Nature* **2003**, *424*, 899.

(76)   W.E.G, M.; C., E.; K., K.; X., W.; U., S. m.; C., S.; S.E., W.; W., T.; H.C., S. *Cell Tissue Res.* **2007**, *329*, 363.

(77)   Cattaneo-Vietti, R.; Bavestrello, G.; Cerrano, C.; Sara, M.; Benatti, U.; Giovine, M.; Gaino, E. *Nature* **1996**, *383*, 397.

(78)   Round, F. E.; Crawford, R. M.; Mann, D. G.; Cambridge University Press: New York, 1990.

(79)   Lobel, K. D.; West, J. K.; Hench, L. L. *Mar. Biol.* **1996**, *126*, 353.

(80)   Xie, J.; Lee, J. Y.; Wang, D. I. C. *J. Phys. Chem. C* **2007**, *111*, 10226.

(81)   Chiu, T.-C.; Chiou, S.-H.; Hsieh, M.-M.; Chen, Y.-T.; Chang, H.-T. *J. Nanosci. Nanotechnol.* **2005**, *5*, 2128.

(82)   Singh, A. V.; Bandgar, B. M.; Kasture, M.; Prasad, B. L. V.; Sastry, M. *J. Mater. Chem.* **2005**, *15*, 5115

(83)   Shaw, C. F. *Chem. Rev.* **1999**, *99*, 2589.

(84)   Burt, J. L.; Gutierrez-Wing, C.; Miki-Yoshida, M.; Jose-Yacaman, M. *Langmuir* **2004**, *20*, 11778.

(85)   Zhou, Y.; Chen, W.; Itoh, H.; Naka, K.; Ni, Q.; Yamane, H.; Chujo, Y. *Chem. Commun.* **2001**, 2518

(86)   Shankar, S. S.; Rai, A.; Ankamwar, B.; Singh, A.; Ahmad, A.; Sastry, M. *Nat. Mater.* **2004**, *3*, 482.

(87)   Xie, J. P.; Lee, J. Y.; Wang, D. I. C.; Ting, Y. P. *Small* **2007**, *3*, 672.

(88)   Sumper, M.; Kroger, N. *J. Mater. Chem.* **2004**, *14*, 2059.

(89)   Muller, W. E. G.; Belikov, S. I.; Tremel, W.; Perry, C. C.; Gieskes, W. W. C.; Boreiko, A.; Schroder, H. C. *Micron* **2006**, *37*, 107.

(90)   Muller, W. E. G.; Krasko, A.; Le, P. G.; Schroder, H. C. *Microsc. Res. Tech.* **2003**, *62*, 368.

(91)   Weaver, J. C.; Morse, D. E. *Microsc. Res. Tech.* **2003**, *62*, 356.

(92)   Parmley, S. F.; Smith, G. P. *Gene* **1988**, *73*, 305.

(93)   Kehoe, J. W.; Kay, B. K. *Chem. Rev.* **2005**, *105*, 4056.

(94)   *Phage Display: A Practical Approach*; Clackson, T.; Lowman, H. B., Eds.; Oxford University Press: New York, 2004.

(95)   Barbaras, C. F.; Burton, D. R.; Scott, J. K.; Silverman, G. J.; Cold Spring Harbor Laboratory Press: Cold Spring Harbor, NY, 2001.

(96)   Bassindale, A. R.; Codina-Barrios, A.; Frascione, N.; Taylor, P. G. *Chem. Commun.* **2007**, *28*, 2956.

(97)   Smith, G. P. *Science* **1985**, *228*, 1315.

(98)   Naik, R. R.; Stringer, S. J.; Agarwal, G.; Jones, S. E.; Stone, M. O. *Nat. Mater.* **2002**, *1*, 169.

(99)   Brown, S.; Sarikaya, M.; Johnson, E. *J. Mol. Biol.* **2000**, *299*, 725.

(100)   Brown, S. *Nat. Biotechnol.* **1997**, *15*, 269.

(101)   Wang, Z.; Chen, J.; Yang, P.; Yang, W. *Appl. Organometal. Chem.* **2007**, *21*, 645.

(102)   Slocik, J. M.; Moore, J. T.; Wright, D. W. *Nano Lett.* **2002**, *2*, 169.

(103)   Slocik, J. M.; Stone, M. O.; Naik, R. R. *Small* **2005**, *1*, 1048.

(104)   Slocik, J. M.; Wright, D. W. *Biomacromolecules* **2003**, *4*, 1135.

(105)   Lévy, R.; Thanh, N. T. K.; Doty, C.; Hussain, I.; Nichols, R. J.; Schiffrin, D. J.; Brust, M.; Fernig, D. G. *J. Am. Chem. Soc.* **2004**, *126*, 10076.

(106)   Einhauer, A.; Jungbauer, A. *J. Biochem. Bioph. Methods* **2001**, *49*, 455.

(107)   Diamanti, S.; Elsen, A.; Naik, R.; Vaia, R. *J. Phys. Chem. C* **2009**, *113*, 9993.

(108)   Djalali, R.; Chen, Y.-F.; Matsui, H. *J. Am. Chem. Soc.* **2002**, *124*, 13660.

(109)   Djalali, R.; Chen, Y.-F.; Matsui, H. *J. Am. Chem. Soc.* **2003**, *125*, 5873.

(110)   Sano, K.-I.; Shiba, K. *J. Am. Chem. Soc.* **2003**, *125*, 14234.

(111)   Sano, K.-I.; Sasaki, H.; Shiba, K. *Langmuir* **2005**, *21*, 3090.

(112)   Yu, L.; Banerjee, I. A.; Matsui, H. *J. Am. Chem. Soc.* **2003**, *125*, 14837.

(113)   Yu, L.; Banerjee, I. A.; Matsui, H. *J. Mater. Chem.* **2004**, *14*, 739.

(114) Song, Y.; Challa, S. R.; Medforth, C. J.; Qiu, Y.; Watt, R. K.; Pena, D.; Miller, J. E.; Swol, F. v.; Shelnutt, J. A. *Chem. Commun.* **2004**, 1044.

(115) Jakhmola, A.; Bhandari, R.; Pacardo, D. B.; Knecht, M. R. *J. Mater. Chem.* **2009**, published online.

(116) Pacardo, D. B.; Sethi, M.; Jones, S. E.; Naik, R. R.; Knecht, M. R. *ACS Nano* **2009**, *3*, 1288.

(117) Naik, R. R.; Brott, L. L.; Clarson, S. J.; Stone, M. O. *J. Nanosci. Nanotechnol.* **2002**, *2*, 95.

(118) Kramer, R. M.; Li, C.; Carter, D. C.; Stone, M. O.; Naik, R. R. *J. Am. Chem. Soc.* **2004**, *126*, 13282.

(119) Dai, H.; Choe, W.-S.; Thai, C. K.; Sarikaya, M.; Traxler, B. A.; Baneyx, F.; Schwartz, D. T. *J. Am. Chem. Soc.* **2005**, *127*, 15637.

(120) Behrens, P.; Baeuerlein, E.; Wiley-VCH Verlag GmbH & Co. KGaA: Weinheim, Germany, 2007.

(121) Sano, K.-I.; Yoshii, S.; Yamashita, I.; Shiba, K. *Nano Lett.* **2007**, *7*, 3200.

(122) Iwahori, K.; Yamashita, I. *J. Cluster Sci.* **2007**, *18*, 358.

(123) Uchida, M.; Klem, M. T.; Allen, M.; Suci, P.; Flenniken, M.; Gillitzer, E.; Varpness, Z.; Liepold, L. O.; Young, M.; Douglas, T. *Adv. Mater.* **2007**, *19*, 1025.

(124) Sano, K.-I.; Sasaki, H.; Shiba, K. *J. Am. Chem. Soc.* **2006**, *128*, 1717.

(125) Slocik, J. M.; Naik, R. R. *Adv. Mater.* **2006**, *18*, 1988.

(126) McMillan, R. A.; Howard, J.; Zaluzec, N. J.; Kagawa, H. K.; Mogul, R.; Li, Y. F.; Paavola, C. D.; Trent, J. D. *J. Am. Chem. Soc.*, *127*, 2800.

(127) Hnilova, M.; Oren, E. E.; Seker, U. O. S.; Wilson, B. R.; Collino, S.; Evans, J. S.; Tamerler, C.; Sarikaya, M. *Langmuir* **2008**, *24*, 12440.

(128) Oren, E. E.; Tamerler, C.; Sarikaya, M. *Nano Lett.* **2005**, *5*, 415.

(129) Seker, U. O. S.; Wilson, B.; Dincer, S.; Kim, I. W.; Oren, E. E.; Evans, J. S.; Tamerler, C.; Sarikaya, M. *Langmuir* **2007**, *23*, 7895.

(130) Schravendijk, P.; Ghiringhelli, L. M.; Site, L. D.; van der Vegt, N. F. A. *J. Phys. Chem. C* **2007**, *111*, 2631.

(131) Willett, R. L.; Baldwin, K. W.; West, K. W.; Pfeiffer, L. N. *Proc. Nat. Acad. Sci. U.S.A.* **2005**, *102*, 7817.

(132) Seker, U. O. S.; Wilson, B.; Sahin, D.; Tamerler, C.; Sarikaya, M. *Biomacromolecules* **2009**, *10*, 250.

(133) Peelle, B. R.; Krauland, E. M.; Wittrup, K. D.; Belcher, A. M. *Langmuir* **2005**, *21*, 6929.

(134) Coppage, R.; Slocik, J. M.; Sethi, M.; Pacardo, D. B.; Naik, R. R.; Knecht, M. R. *Angew. Chem., Int. Ed.* **2010**, *49*, 3767.

(135) Tamerler, C.; Oren, E. E.; Duman, M.; Venkatasubramanian, E.; Sarikaya, M. *Langmuir* **2006**, *22*, 7712.

(136) Shao, Y.; Jin, Y.; Dong, S. J. *Chem. Commun.* **2004**, *9*, 1104.

(137) Selvakannan, P. R.; Mandal, S.; Phadtare, S.; Pasricha, R.; Sastry, M. *Langmuir* **2003**, *19*, 3545.

(138) Bhargava, S. K.; Booth, J. M.; Agrawal, S.; Coloe, P.; Kar, G. *Langmuir* **2005**, *21*, 5949.

(139) LaMer, V.; Dinegar, R. *J. Am. Chem. Soc.* **1950**, *72*, 4847.

(140)   Branden, C.; Tooze, J. *Introduction to Protein Structure*; 2nd ed.; Graland Publishing: New York, 1999.

(141)   Lee, S. Y.; Choi, J. W.; Royston, E.; Janes, D. B.; Culver, J. N.; Harris, M. T. *J. Nanosci. Nanotechnol.* **2006**, *6*, 974.

(142)   Rangnekar, A.; Sarma, T. K.; Singh, A. K.; Deka, J.; Ramesh, A.; Chattopadhyay, A. *Langmuir* **2007**, *23*, 5700.

(143)   Daniel, M.-C.; Astruc, D. *Chem. Rev.* **2004**, *104*, 293.

(144)   Aryal, S.; B.K.C, R.; Dharmaraj, N.; Bhattarai, N.; Kim, C. H.; Kim, H. Y. *Spectrochim. Acta, Part A* **2006**, *63*, 160.

(145)   Hoefling, M.; Iori, F.; Corni, S.; Gottschalk, K.-E. *Langmuir* **2010**, *26*, 8347.

(146)   Heinz, H.; Farmer, B. L.; Pandey, R. B.; Slocik, J. M.; Patnaik, S. S.; Pachter, R.; Naik, R. R. *J. Am. Chem. Soc.* **2009**, *131*, 9704.

(147)   Pandey, R. B.; Heinz, H.; Feng, J.; Farmer, B. L.; Slocik, J. M.; Drummy, L. F.; Naik, R. R. *PHys. Chem. Chem. Phys.* **2009**, *11*, 1989.

(148)   Slocik, J. M.; Govorov, A. O.; Naik, R. R. *Angew. Chem. Int. Ed.* **2008**, *47*, 5335

(149)   Johnson, C. R. *Acc. Chem. Res.* **1998**, *31*, 333.

(150)   Spreitzer, G.; Whitling, J. M.; Madura, J. D.; Wright, D. W. *Chem. Commun.* **2000**, 209.

(151)   Tsay, J. M.; Doose, S.; Pinaud, F.; Weiss, S. *J. Phys. Chem. B* **2005**, *109*, 1669.

(152)   Choi, Y.; Ho, N.-H.; Tung, C.-H. *Angew. Chem. Int. Ed.* **2007**, *46*, 707.

(153)   Sethi, M.; Joung, G.; Knecht, M. R. *Langmuir* **2009**, *25*, 317.

(154)   Elghanian, R.; Storhoff, J. J.; Mucic, R. C.; Letsinger, R. L.; Mirkin, C. A. *Science* **1997**, *277*, 1078

(155)   Aslan, K.; Lakowicz, J. R.; Geddes, C. D. *Anal. Biochem.* **2004**, *330*, 145.

(156)   Zhang, J.; Wang, L.; Pan, D.; Song, S.; Boey, F. Y. C.; Zhang, H.; Fan, C. *Small* **2008**, *4*, 1196.

(157)   Hurst, S. J.; Han, M. S.; Lytton-Jean, A. K. R.; Mirkin, C. A. *Anal. Chem.* **2007**, *79*, 7201.

(158)   Slocik, J. M.; Zabinski, J. S. J.; Phillips, D. M.; Naik, R. R. *Small* **2008**, *4*, 548.

(159)   Jain, P. K.; Eustis, S.; El-Sayed, M. A. *J. Phys. Chem. B* **2006**, *110*, 18243.

(160)   Jain, P. K.; Huang, X.; El-Sayed, I. H.; El-Sayed, M. A. *Acc. Chem. Res.* **2008**, *41*, 1578.

(161)   Murphy, C. J.; Gole, A. M.; Hunyadi, S. E.; Stone, J. W.; Sisco, P. N.; Alkilany, A.; Kinard, B. E.; Hankins, P. *Chem. Commun.* **2008**, 544.

(162)   Murphy, C. J.; Sau, T. K.; Gole, A. M.; Orendorff, C. J.; Gao, J.; Gou, L.; Hunyadi, S. E.; Li, T. *J. Phys. Chem. B* **2005**, *109*, 13857.

(163)   Hostetler, M. J.; Wingate, J. E.; Zhong, C.-J.; Harris, J. E.; Vachet, R. W.; Clark, M. R.; Londono, J. D.; Green, S. J.; Stokes, J. J.; Wignall, G. D.; Glish, G. L.; Porter, M. D.; Evans, N. D.; Murray, R. W. *Langmuir* **1998**, *14*, 17.

(164)   Ingram, R. S.; Murray, R. W. *Langmuir* **1998**, *14*, 4115.

(165)   Templeton, A. C.; Wuelfing, W. P.; Murray, R. W. *Acc. Chem. Res.* **2000**, *33*, 27.

(166)   Hostetler, M. J.; Templeton, A. C.; Murray, R. W. *Langmuir* **1999**, *15*, 3782.

(167)   Rosi, N. L.; Mirkin, C. A. *Chem. Rev.* **2005**, *105*, 1547.

(168)   Laaksonen, P.; Kivioja, J.; Paananen, A.; Kainlauri, M.; Kontturi, K.; Ahopelto, J.; Linder, M. B. *Langmuir* **2009**, *25*, 5185.

(169)   Lee, J.-S.; Han, M. S.; Mirkin, C. A. *Angew. Chem. Int. Ed.* **2007**, *46*, 4093.

(170)   Watson, K. J.; Zhu, J.; Nguyen, S. T.; Mirkin, C. A. *J. Am. Chem. Soc.* **1999**, *121*, 462.

(171)   Balci, S.; Noda, K.; Bittner, A. M.; Kadri, A.; Wege, C.; Jeske, H.; Kern, K. *Angew. Chem., Int. Ed.* **2007**, *46*, 3149.

(172)   Sethi, M.; Joung, G.; Knecht, M. R. *Langmuir* **2009**, *25*, 1572.

(173)   Astruc, D. *Inorg. Chem.* **2007**, *46*, 1884.

(174)   Diallo, A. K.; Ornelas, C.; Salmon, L.; Aranzaes, J. R.; Astruc, D. *Angew. Chem., Int. Ed.* **2007**, *46*, 8644.

(175)   Scott, R. W. J.; Wilson, O. M.; Crooks, R. M. *J. Phys. Chem. B* **2005**, *109*, 692.

(176)   Caswell, K. K.; Wilson, J. N.; Bunz, U. H. F.; Murphy, C. J. *J. Am. Chem. Soc.* **2003**, *125*, 13914.

(177)   Joseph, S. T. S.; Ipe, B. I.; Pramod, P.; Thomas, K. G. *J. Phys. Chem. B* **2006**, *110*, 150.

(178)   Thomas, K. G.; Barazzouk, S.; Ipe, B. I.; Joseph, S. T. S.; Kamat, P. V. *J. Phys. Chem. B* **2004**, *108*, 13066.

(179)   Sardar, R.; Heap, T.; Shumaker-Parry, J. S. *J. Am. Chem. Soc.* **2007**, *129*, 5356.

(180)   Mann, S. *Biomineralization: Principals and Concepts in Bioinorganic Materials Chemistry*; Oxford University Press: New York, 2002.

(181)   Faivre, D.; Schüler, D. *Chem. Rev.* **2008**, *108*, 4875.

(182)   Shimizu, K.; Cha, J.; Stucky, G. D.; Morse, D. E. *Proc. Natl. Acad. Sci.* **1998**, *95*, 6234.

(183)   Reiss, B. D.; Mao, C.; Solis, D. J.; Ryan, K. S.; Thomson, T.; Belcher, A. M. *Nano Lett.* **2004**, *4*, 1127.

(184)   Lee, Y. J.; Yi, H.; Kim, W.-J.; Kang, K.; Yun, D. S.; Strano, M. S.; Ceder, G.; Belcher, A. M. *Science* **2009**, *324*, 1051.

(185)   Lee, S.-W.; Mao, C.; Flynn, C. E.; Belcher, A. M. *Science* **2002**, *296*, 892.

(186)   Whaley, S. R.; English, D. S.; Hu, E. L.; Barbara, P. F.; Belcher, A. M. *Nature* **2000**, *405*, 665.

(187)   Mao, C.; Solis, D. J.; Reiss, B. D.; Kottmann, S. T.; Sweeney, R. Y.; Hayhurst, A.; Georgiou, G.; Iverson, B.; Belcher, A. M. *Science* **2004**, *303*, 213.

(188)   Nam, K. T.; Kim, D.-W.; Yoo, P. J.; Chiang, C.-Y.; Meethong, N.; Hammond, P. T.; Chiang, Y.-M.; Belcher, A. M. *Science* **2006**, *312*, 885.

(189)   Dickerson, M. B.; Jones, S. E.; Cai, Y.; Ahmad, G.; Naik, R. R.; Kröger, N.; Sandhage, K. H. *Chem. Mater.* **2008**, *20*, 1578.

(190) Dickerson, M. B.; Naik, R. R.; Stone, M. O.; Cai, Y.; Sandhage, K. H. *Chem. Commun.* **2004**, 1776

(191) Ahmad, G.; Dickerson, M. B.; Cai, Y.; Jones, S. E.; Ernst, E. M.; Vernon, J. P.; Haluska, M. S.; Fang, Y.; Wang, J.; Subramanyam, G.; Naik, R. R.; Sandhage, K. H. *J. Am. Chem. Soc.* **2008**, *130*, 4.

(192) Hong, G.; Heinz, H.; Naik, R. R.; Farmer, B. L.; Pachter, R. *ACS Appl. Mater. Interfaces* **2009**, *1*, 388.

(193) Seker, U. O. S.; Wilson, B.; Dincer, S.; Kim, I. W.; Oren, E. E.; Evans, J. S.; Tamerler, C.; Sarikaya, M. *Langmuir* **2007**, *23*, 7895.

(194) So, C. R.; Tamerler, C.; Sarikaya, M. *Angew. Chem., Int. Ed.* **2009**, *48*, 5174.

(195) Bonell, F.; Sanchot, A.; Dujardin, E.; Péchou, R.; Girard, C.; Li, M.; Mann, S. *J. Chem. Phys.* **2009**, *130*, 034702.

(196) Lin, S.; Li, M.; Dujardin, E.; Girard, C.; Mann, S. *Adv. Mater.* **2005**, *17*, 2553.

(197) Carney, R. P.; DeVries, G. A.; Dubois, C.; Kim, H.; Kim, J. Y.; Singh, C.; Ghorai, P. K.; Tracy, J. B.; Stiles, R. L.; Murray, R. W.; Glotzer, S. C.; Stellacci, F. *J. Am. Chem. Soc.* **2008**, *130*, 798.

(198) Hu, Y.; Uzun, O.; Dubois, C.; Stellacci, F. *J. Phys. Chem. C* **2008**, *112*, 6279.

(199) Jackson, A. M.; Myerson, J. W.; Stellacci, F. *Nat. Mater.* **2004**, *3*, 330.

(200) Singh, C.; Ghorai, P. K.; Horsch, M. A.; Jackson, A. M.; Larson, R. G.; Stellacci, F.; Glotzer, S. C. *Phys. Rev. Lett.* **2007**, *99*, 226106.

(201) Uzun, O.; Hu, Y.; Verma, A.; Chen, S.; Centrone, A.; Stellacci, F. *Chem. Commun.* **2008**, 196.

(202) Zhong, Z.; Patskovskyy, S.; Bouvrette, P.; Luong, J. H. T.; Gedanken, A. *J. Phys. Chem. B* **2004**, *108*, 4046.

(203) Hong, G.; Heinz, H.; Naik, R. R.; Farmer, B. L.; Pachter, R. *ACS Appl. Mater. Interfaces* **2009**, *1*, 388.

(204) Willett, R. L.; Baldwin, K. W.; West, K. W.; Pfeiffer, L. N. *Proc. Nat'l. Acad. Sci.* **2005**, *102*, 7817.

(205) Hnilova, M.; Oren, E. E.; Seker, U. O. S.; Wilson, B. R.; Collino, S.; Evans, J. S.; Tamerler, C.; Sarikaya, M. *Langmuir* **2008**, *24*, 12440.

(206) Brown, S.; Sarikaya, M.; Johnson, E. *J. Mol. Biol.* **2000**, *299*, 725.

(207) Nam, K. T.; Kim, D.-W.; Yoo, P. J.; Chiang, C.-Y.; Meethong, N.; Hammond, P. T.; Chiang, Y.-M.; Belcher, A. M. *Science* **2006**, *312*, 885.

(208) Sardar, R.; Shumaker-Parry, J. S. *Nano Lett.* **2008**, *8*, 731.

(209) Frens, G. *Nat. Phys. Sci.* **1973**, *241*, 20.

(210) Knecht, M. R.; Sethi, M. *Anal. Bioanal. Chem.* **2009**, *ASAP*.

(211) Rosi, N. L.; Mirkin, C. A. *Chem. Rev.* **2005**, *105*, 1547.

(212) Daniel, M.-C.; Astruc, D. *Chem. Rev.* **2004**, *104*, 293.

(213) Thomas, K. G.; Barazzouk, S.; Ipe, B. I.; Joseph, S. T. S.; Kamat, P. V. *J. Phys. Chem. B* **2004**, *108*, 13066.

(214) Sun, Z.; Ni, W.; Yang, Z.; Kou, X.; Li, L.; Wang, J. *Small* **2008**, *4*, 1287.

(215) Chow, M. K.; Zukoski, C. F. *J. Colloid Interface Sci.* **1994**, *165*, 97.

(216) Lin, S.; Li, M.; Dujardin, E.; Girard, C.; Mann, S. *Adv. Mater.* **2005**, *17*, 2553.

(217) Somasundaran, P.; Markovic, B.; Krishnakumar, S.; Yu, X. In *Handbook of Surface and Colloid Chemistry*; Birdi, K. S., Ed.; CRC Press: New York, 1997.

(218) Carney, R. P.; DeVries, G. A.; Dubois, C.; Kim, H.; Kim, J. Y.; Singh, C.; Ghorai, P. K.; Tracy, J. B.; Stiles, R. L.; Murray, R. W.; Glotzer, S. C.; Stellacci, F. *J. Am. Chem. Soc.* **2008**, *130*, 798.

(219) Hu, Y.; Uzun, O.; Dubois, C.; Stellacci, F. *J. Phys. Chem. C* **2008**, *112*, 6279.

(220) Jackson, A. M.; Myerson, J. W.; Stellacci, F. *Nat. Mater.* **2003**, *3*, 330.

(221) Uzan, O.; Hu, Y.; Verma, A.; S., C.; Centrone, A.; Stellacci, F. *Chem. Commun.* **2008**, 196.

(222) Zhong, Z.; Subramanian, A. S.; Highfield, J.; Carpenter, K.; Gedanken, A. *Chem. Eur. J.* **2005**, *11*, 1473.

(223) Zhong, Z.; Patskovskyy, S.; Bouvrette, P.; Luong, J. H. T.; Gedanken, A. *J. Phys. Chem. B* **2004**, *108*, 4046.

(224) Naka, K.; Itoh, H.; Tampo, Y.; Chujo, Y. *Langmuir* **2003**, *19*, 5546.

(225) Jain, P. K.; Eustis, S.; El-Sayed, M. A. *J. Phys. Chem. B* **2006**, *110*, 18243.

(226) Murphy, C. J.; Sau, T. K.; Gole, A. M.; Orendorff, C. J.; Gao, J.; Gou, L.; Hunyadi, S. E.; Li, T. *J. Phys. Chem. B* **2005**, *109*, 13857.

(227) Nikoobakht, B.; El-Sayed, M. A. *Chem. Mater.* **2003**, *15*, 1957.

(228) Sau, T. K.; Murphy, C. J. *Langmuir* **2004**, *20*, 6414.

(229) Nikoobakht, B.; Wang, Z. L.; El-Sayed, M. A. *J. Phys. Chem. B* **2000**, *104*, 8635.

(230) Mazo, R. M. *Brownian Motion: Flucuations, Dynamics, and Applications*; Oxford University Press: New York, 2002; Vol. 112.

(231) Mandal, S.; Gole, A.; Lala, N.; Gonnade, R.; Ganvir, V.; Sastry, M. *Langmuir* **2001**, *17*, 6262.

(232) Jakhmola, A.; Bhandari, R.; Pacardo, D. B.; Knecht, M. R. *J. Mater. Chem.* **2010**, *20*, 1522.

(233) Lee, Y. J.; Lee, Y.; Oh, D.; Chen, T.; Ceder, G.; Belcher, A. M. *Nano Lett.* **2010**, *10*, 2433.

(234) Slocik, J. M.; Naik, R. R. *Adv. Mater.* **2006**, *18*, 1988.

(235) Slocik, J. M.; Zabinsky, J. S.; Phillips, D. M.; Naik, R. R. *Small* **2008**, *4*, 548.

(236) Sethi, M.; Pacardo, D. B.; Knecht, M. R. *Langmuir* **2010**, *26*.

(237) Chen, C.-L.; Rosi, N. L. *J. Am. Chem. Soc.* **2010**, *132*, 6902.

(238) Chen, C.-L.; Zhang, P.; Rosi, N. L. *J. Am. Chem. Soc.* **2008**, *130*, 13555.

(239) Tamerler, C.; Oren, E. E.; Duman, M.; Venkatasubramanian, E.; Sarikaya, M. *Langmuir* **2006**, *22*, 7712.

(240) Sethi, M.; Knecht, M. R. *Langmuir* **2010**, *26*, 9860.

(241) Law, W.-C.; Markowicz, P.; Yong, K.-T.; Roy, I.; Baev, A.; Patskovsky, S.; Kabashin, A. V.; Ho, H.-P.; Prasad, P. N. *Biosens. Bioelectron.* **2007**, *23*, 627.

(242) Nikoobakht, B.; Wang, Z. L.; El-Sayed, M. A. *J. Phys. Chem. B* **2000**, *104*, 8635.

(243) Rosenthal, S. J.; Tomlinson, I.; Adkins, E. M.; Schroeter, S.; Adams, S.; Swafford, L.; McBride, J.; Wang, Y.; DeFelice, L. J.; Blakely, R. D. *J. Am. Chem. Soc.* **2002**, *124*, 4586.

(244) Kim, J. H.; Estabrook, R. A.; Braun, G.; Lee, B. R.; Reich, N. O. *Chem. Commun.* **2007**, 4342.

(245) Choi, J.-S.; Jun, Y.-W.; Yeon, S.-I.; Kim, H. C.; Shin, J.-S.; Cheon, J. *J. Am. Chem. Soc.* **2006**, *128*, 15982.

(246) Lee, I. S.; Lee, N.; Park, J.; Kim, B. H.; Yi, Y.-W.; Kim, T.; Kim, T. K.; Lee, I. H.; Paik, S. R.; Hyeon, T. *J. Am. Chem. Soc.* **2006**, *128*, 10658.

(247) Gole, A.; Murphy, C. J. *Langmuir* **2008**, *24*, 266.

(248) Seferos, D. S.; Giljohann, D. A.; Hill, H. D.; Prigodich, A. E.; Mirkin, C. A. *J. Am. Chem. Soc.* **2007**, *129*, 15477.

(249) Oyelere, A. K.; Chen, P. C.; Huang, X.; El-Sayed, I. H.; El-Sayed, M. A. *Bioconjugate Chem.* **2007**, *18*, 1490.

(250) Huang, X.; El-Sayed, I. H.; Qian, W.; El-Sayed, M. A. *Nano Lett.* **2007**, *7*, 1591.

(251) Norman, R. S.; Stone, J. W.; Gole, A.; Murphy, C. J.; Sabo-Attwood, T. L. *Nano Lett.* **2008**, *8*, 302.

(252) Hauck, T. S.; Ghazani, A. A.; Chan, W. C. W. *Small* **2008**, *4*, 153.

(253) Alivisatos, A. P.; Barbara, P. F.; Castleman, A. W.; Chang, J.; Dixon, D. A.; Klein, M. L.; McLendon, G. L.; Miller, J. S.; Ratner, M. A.; Rossky, P. J.; Stupp, S. I.; Thompson, M. E. *Adv. Mater.* **1998**, *10*, 1297.

(254) Kelly, K. L.; Coronado, E.; Zhao, L. L.; Schatz, G. C. *J. Phys. Chem. B* **2003**, *107*, 668.

(255) Nirmal, M.; Brus, L. *Acc. Chem. Res.* **1999**, *32*, 407.

(256) Liu, W.; Howarth, M.; Greytak, A. B.; Zheng, Y.; Nocera, D. G.; Ting, A. Y.; Bawendi, M. G. *J. Am. Chem. Soc.* **2008**, *130*, 1274.

(257) Bowers II, M. J.; McBride, J. R.; Rosenthal, S. J. *J. Am. Chem. Soc.* **2005**, *127*, 15378.

(258) Creighton, J. A.; Eadon, D. G. *J. Chem. Soc., Faraday Trans.* **1991**, *87*, 3881.

(259) Knecht, M. R.; Weir, M. G.; Frenkel, A. I.; Crooks, R. M. *Chem. Mater.* **2008**, *20*, 1019.

(260) Choi, M.-R.; Stanton-Maxey, K. J.; Stanley, J. K.; Levin, C. S.; Bardhan, R.; Akins, D.; Badve, S.; Sturgis, J.; Robinson, J. P.; Bashir, R.; Halas, N. J.; Clare, S. E. *Nano Lett.* **2007**, *7*, 3759.

(261) Gobin, A. M.; Lee, M. H.; Halas, N. J.; James, W. D.; Drezek, R. A.; West, J. L. *Nano Lett.* **2007**, *7*, 1929.

(262) Ryan, J.; Overton, K. W.; Speight, M. E.; Oldenburg, C. N.; Loo, L.; Robarge, W.; Franzen, S.; Feldheim, D. L. *Anal. Chem.* **2007**, *79*, 9150.

(263) Tkachenko, A. G.; Xie, H.; Coleman, D.; Glomm, W.; Ryan, J.; Anderson, M. F.; Franzen, S.; Feldheim, D. L. *J. Am. Chem. Soc.* **2003**, *125*, 4700.

(264) Connor, E. E.; Mwamuka, J.; Gole, A.; Murphy, C. J.; Wyatt, M. D. *Small* **2005**, *1*, 325.

(265) Dasog, M.; Scott, R. W. J. *Langmuir* **2007**, *23*, 3381.

(266) Singh, S.; Prasad, B. L. V. *J. Phys. Chem. C* **2007**, *111*, 14348.

(267) Tsung, C.-K.; Kou, X.; Shi, Q.; Zhang, J.; Yeung, M. H.; Wang, J.; Stucky, G. D. *J. Am. Chem. Soc.* **2006**, *128*, 5352.

(268) Gole, A.; Murphy, C. J. *Chem. Mater.* **2004**, *16*, 3633.

(269) Gao, J.; Bender, C. M.; Murphy, C. J. *Langmuir* **2003**, *19*, 9065.

(270) Smith, D. K.; Korgel, B. A. *Langmuir* **2008**, *24*, 644.

(271) Schatz, G. C.; Van Duyne, R. P. *Handbook of Bivrational Spectroscopy*; Wiley: New York, 2002.

(272) Joseph, S. T. S.; Ipe, B. I.; Pramod, P.; Thomas, K. G. *J. Phys. Chem. B* **2006**, *110*, 150.

(273) Yu, C.; Irudayaraj, J. *Anal. Chem.* **2007**, *79*, 572.

(274) Chang, J.-Y.; Wu, H.; Chen, H.; Ling, Y.-C.; Tan, W. *Chem. Commun.* **2005**, 1092.

(275) Caswell, K. K.; Wilson, J. N.; Bunz, U. H. F.; Murphy, C. J. *J. Am. Chem. Soc.* **2003**, *125*, 13914.

(276) Takahashi, H.; Niidome, Y.; Niidome, T.; Kaneko, K.; Kawasaki, H.; Yamada, S. *Langmuir* **2006**, *22*, 2.

(277) Sau, T. K.; Murphy, C. J. *Langmuir* **2005**, *21*, 2923.

(278) Jana, N. R. *Chem. Commun.* **2003**, 1950.

(279) Jana, N. R. *Angew. Chem. Int. Ed.* **2004**, *43*, 1536.

(280) Marinakos, S. M.; Chen, S.; Chilkoti, A. *Anal. Chem.* **2007**, *79*, 5278.

(281) Xu, X.; Cortie, M. B. *Adv. Funct. Mater.* **2006**, *16*, 2170.

(282) Gou, L.; Murphy, C. J. *Chem. Mater.* **2005**, *17*, 3668.

(283) Berry, V.; Gole, A.; Kundu, S.; Murphy, C. J.; Saraf, R. F. *J. Am. Chem. Soc.* **2005**, *127*, 17600.

(284) Stone, J. W.; Sisco, P. N.; Goldsmith, J. I.; Baxter, S. C.; Murphy, C. J. *Nano Lett.* **2007**, *7*, 116.

(285) Orendorff, C. J.; Hankins, P. L.; Murphy, C. J. *Langmuir* **2005**, *21*, 2022.

(286) Galow, T. H.; Boal, A. K.; Rotello, V. M. *Adv. Mater.* **2000**, *12*, 576.

(287) Knecht, M. R.; Sewell, S. L.; Wright, D. W. *Langmuir* **2005**, *21*, 2058.

(288) Knecht, M. R.; Wright, D. W. *Chem. Mater.* **2004**, *16*, 4890.

(289) Gole, A.; Murphy, C. J. *Langmuir* **2005**, *21*, 10756.

(290) Adamson, A. W.; Gast, A. P. *Physical Chemistry of Surfaces*; 6th ed.; Wiley: New York, 1997.

(291) Rosi, N. L.; Thaxton, C. S.; Mirkin, C. A. *Angew. Chem. Int. Ed.* **2004**, *43*, 5500.

(292) Hiramatsu, H.; Osterloh, F. E. *Langmuir* **2003**, *19*, 7003.

(293) Xu, X.; Rosi, N. L.; Wang, Y.; Huo, F.; Mirkin, C. A. *J. Am. Chem. Soc.* **2006**, *128*, 9286.

(294) Sethi, M.; Joung, G.; Knecht, M. R. *Langmuir* **2008**, accepted.

(295) Pissuwan, D.; Valenzuela, S. M.; Miller, C. M.; Cortie, M. B. *Nano Lett.* **2007**, *7*, 3808.

(296) Nikoobakht, B.; El-Sayed, M. A. *J. Phys. Chem. A* **2003**, *107*, 3372.

(297) Orendorff, C. J.; Gearheart, L.; Jana, N. R.; Murphy, C. J. *PHys. Chem. Chem. Phys.* **2006**, *8*, 165.

(298)   Zhang, S.; Kou, X.; Yang, Z.; Shi, Q.; Stucky, G. D.; Sun, L.; Wang, J.; Yan, C. *Chem. Commun.* **2007**, 1816.

(299)   Sudeep, P. K.; Joseph, S. T. S.; Thomas, K. G. *J. Am. Chem. Soc.* **2005**, *127*, 6516.

(300)   Nakashima, H.; Furukawa, K.; Kashimura, Y.; Torimitsu, K. *Chem. Commun.* **2007**, 1080.

(301)   Varghese, N.; Vivekchand, S. R. C.; Govindaraj, A.; Rao, C. N. R. *Chem. Phys. Lett.* **2008**, *450*, 340.

(302)   Lutkenhaus, J. L.; McEnnis, K.; Hammond, P. T. *Macromol.* **2007**, *40*, 8367.

(303)   Mukherjee, P.; Ahmad, A.; Mandal, D.; Senapati, S.; Sainkar, S. R.; Khan, M. I.; Ramani, R.; Parischa, R.; Ajayakumar, P. V.; Alam, M.; Sastry, M.; Kumar, R. *Angew. Chem. Int. Ed.* **2001**, *40*, 3585.

Scientific Publications

1. **Sethi, M**.; Law, W.C.; Fennell, W.A III; Prasad, P.N.; Knecht, M.R. Employing Materials Assembly to Elucidate Surface Interactions of Amino Acids with Au Nanoparticles. *Soft Matter* **2011**, *7*, 6532-6541.

2. **Sethi, M**.; Pacardo, D.B.; Knecht, M.R. Biological Surface Effects of Metallic Nanomaterials for Applications in Assembly and Catalysis. *Langmuir* **2010**, *26*, 15121-15134. (featured on the <u>cover</u> of the October 5, 2010 issue)

3. Pickin, K.A.; Ezenwajiaku, N.; Overcash, H.; **Sethi, M**.; Knecht, M.R.; Paumi, C.M. Suppression of YCF1P Function by CKA1P-Dependent Phosphorylation is Attenuated in Response to Salt Stress. *FEMS Yeast Res*. **2010**, *10*, 839-857.

4. **Sethi, M**.; Knecht, M.R. Understanding the Mechanism of Amino Acid-Based Au Nanoparticle Chain Formation, *Langmuir*, **2010**, *26*, 9860-9874. (This work was listed as <u>one of the most read article</u> in *Langmuir* for April 2010)

5. Coppage, R.; Slocik, J.M.; **Sethi, M.**; Pacardo, D.B. Naik, R.R.; Knecht, M.R. Elucidation of Peptide Effects that Control the Activity of Nanoparticles, *Angew. Chemie, Int. Ed*. **2010**, *49*, 3767-3770.

6. **Sethi, M**.; Knecht, M.R. Experimental Studies on the Interactions between Au Nanoparticles and Amino Acids: Bio-Based Formation of Branched Linear Structures, *ACS Appl. Mater. Interfaces* **2009**, *1*, 1270-1278. (This work was also listed as a <u>top 20 most read article</u> in *ACS Appl. Mater. Interfaces* for June 2009)

7. Pacardo, D.B.; **Sethi, M**.; Jones, S.E.; Naik, R.R.; Knecht, M.R. Biomimetic Synthesis of Pd Nanocatalysts for the Stille Coupling Reaction, *ACS Nano* **2009**, *3*, 1288-1296.

8. Knecht, M.R.; **Sethi, M**. Bio-Inspired Colorimetric Detection of Hg^{2+} and Pb^{2+} Heavy Metal Ions Using Au Nanoparticles, *Anal. Bioanal. Chem*. **2009**, *394*, 33-46.

9. **Sethi, M**.; Joung, G.; Knecht, M.R. Linear Assembly of Au Nanorods Using Biomimetic Ligands, *Langmuir* **2009**, *25*, 1572-1581.

10. **Sethi, M**.; Joung, G.; Knecht, M.R. Stability and Electrostatic Assembly of Au Nanorods for use in Biological Assays, *Langmuir* **2009**, *25*, 317-325.

Vita

Manish Sethi was born in Ludhiana, India on July 20th, 1984. He attented Sacred Heart Sr. Sec. School in Ludhiana and later went to New Delhi to earn his B.S. in Microbiology and M.S. in Biomedical Sciences from the University of Delhi, India. While in Delhi, he developed interest in the area of Nanotechnology that prompted him to contact Dr. Marc R. Knecht at the University of Kentucky's Chemistry Department in 2007. In Fall 2007, Manish was admitted to the Doctoral Program at the University of Kentucky and joined Dr. Knecht's Lab as his first student in Spring 2008. At Dr. Knecht's lab, he conducted research on understanding the biomolecular surface interactions on Au nanoparticles and published several articles in peer-reviewed journals.